Title
Simulation Analysis of Zero Mean Flow Edge Turbulence in LAPD

Author
Friedman, Brett

Publication Date
2013

Peer reviewed|Thesis/dissertation

University of California

Los Angeles

Simulation Analysis of Zero Mean Flow Edge Turbulence in LAPD

A dissertation submitted in partial satisfaction

of the requirements for the degree

Doctor of Philosophy in Physics

by

Brett Cory Friedman

2013

Abstract of the Dissertation

Simulation Analysis of Zero Mean Flow Edge Turbulence in LAPD

by

Brett Cory Friedman

Doctor of Philosophy in Physics

University of California, Los Angeles, 2013

Professor Troy A. Carter, Chair

I model, simulate, and analyze the turbulence in a particular experiment on the Large Plasma Device (LAPD) at UCLA. The experiment, conducted by Schaffner et al. [D. Schaffner et al., *Phys. Rev. Lett.* **109**, 135002 (2012)], nulls out the intrinsic mean flow in LAPD by limiter biasing. The model that I use in the simulation is an electrostatic reduced Braginskii two-fluid model that describes the time evolution of density, electron temperature, electrostatic potential, and parallel electron velocity fluctuations in the edge region of LAPD. The spatial domain is annular, encompassing the radial coordinates over which a significant equilibrium density gradient exists. My model breaks the independent variables in the equations into time-independent equilibrium parts and time-dependent fluctuating parts, and I use experimentally obtained values as input for the equilibrium parts.

After an initial exponential growth period due to a linear drift wave instability, the fluctuations saturate and the frequency and azimuthal wavenumber spectra become broadband with no visible coherent peaks, at which point the fluctuations become turbulent. The turbulence develops intermittent pressure and flow filamentary structures that grow and dissipate, but look much different than the unstable linear drift waves, primarily in the extremely long axial wavelengths

that the filaments possess. An energy dynamics analysis that I derive reveals the mechanism that drives these structures. The long $k_\parallel \sim 0$ intermittent potential filaments convect equilibrium density across the equilibrium density gradient, setting up local density filaments. These density filaments, also with $k_\parallel \sim 0$, produce azimuthal density gradients, which drive radially propagating secondary drift waves. These finite $k_\parallel$ drift waves nonlinearly couple to one another and reinforce the original convective filament, allowing the process to bootstrap itself. The growth of these structures is by nonlinear instability because they require a finite amplitude to start, and they require nonlinear terms in the equations to sustain their growth.

The reason why $k_\parallel \sim 0$ structures can grow and support themselves in a dynamical system with no $k_\parallel = 0$ linear instability is because the linear eigenmodes of the system are nonorthogonal. Nonorthogonal eigenmodes that individually decay under linear dynamics can transiently inject energy into the system, allowing for instability. The instability, however, can only occur when the fluctuations have a finite starting amplitude, and nonlinearities are available to mix energy among eigenmodes.

Finally, I attempt to figure out how many effective degrees of freedom control the turbulence to determine whether it is stochastic or deterministic. Using two different methods – permutation entropy analysis by means of time delay trajectory reconstruction and Proper Orthogonal Decomposition – I determine that more than a few degrees of freedom, possibly even dozens or hundreds, are all active. The turbulence, while not stochastic, is not a manifestation of low-dimensional chaos – it is high dimensional.

The dissertation of Brett Cory Friedman is approved.

Warren B. Mori

George J. Morales

Russel E. Caflisch

Troy A. Carter, Committee Chair

University of California, Los Angeles

2013

To my parents . . .

Table of Contents

List of Figures

List of Tables

Acknowledgments

This thesis culminates several years of hard work, and could not have been completed without the help of many individuals to whom I owe much thanks. First, I must thank my advisor, Professor Troy Carter, for giving me enough guidance throughout the process to help me constantly progress, and more importantly, for allowing me great freedom in following whatever courses of research I deemed most interesting. I could not have asked for a more knowledgeable, understanding, and helpful advisor and friend. Also, I thank Dr. Maxim Umansky from LLNL, who has acted as a mentor and a second advisor throughout my time at UCLA. While under no obligation to help, he has continuously given advice, support, knowledge, direct help, and friendship throughout the process. I would not have made nearly as much progress without him, and I greatly appreciate his mentorship while I briefly worked at Livermore. Furthermore, Dr. Pavel Popovich helped me start on this research, being increadibly patient while I tried to learn everything from Linux commands to plasma theory, asking him nearly every day a number of basic questions that he happily answered. He helped ease much of the frustration associated with starting a new field of research, and I owe him so much thanks.

I would also like to thank UCLA Professor George Morales for teaching me the basics of plasma physics. His methods instilled in me an appreciation for mathematical rigor, careful analysis, and the importance of in depth reading of papers. He has also made himself available to me for research questions and explanations of difficult theoretical topics. I thank Dr. James Maggs for helping explain to me concepts of chaos and stochasticity and providing me with code and information in order to fill out my chapter on chaos. Additionally, I acknowledge and thank York Professor Ben Dudson for writing the fantastic BOUT++ code, which has made my work so much easier. I also thank him for quickly and effectively answering all of my questions regarding the code, and for fixing some bugs that could

have set me back a long time.

I owe much appreciation to Professor Paul Terry of the University of Wisconsin for many useful discussions on a number of topics. He always pointed me in the right direction and often provided great insight into my results. Furthermore Dr. David Hatch spent a lot of time working with me on a proper orthogonal decomposition for my simulations, even writing code to decompose my data. Additionally, LLNL Dr. Ilon Joseph deserves thanks for carefully reading my work, discussing theory with me, teaching me a lot, and most importantly for suggesting a change to one of my equations that has greatly improved my work. Also, I thank LLNL Dr. Xueqiao Xu for our many helpful discussions, for helping create the BOUT++ community and bringing me into it, and for his help in advancing my career goals. Finally, Dr. David Schaffner has always provided me with all of the experimental data I could ever ask for and more, never making me wait.

I also must acknowledge the great friends I have made during my time at UCLA. Without them, I probably would have made much more progress and finished faster, but then again, I may not have made it out alive without them. Brandon, Scott, Dan, other Scott – their friendship has been invaluable. David, Tom, Derek, Erik, Gio, Seth, Mike, Yuhou, Danny – my plasma buddies, conference friends, people who let me ramble on about theory; I thank you all. I thank Eric and Mikhail for taking me in during my time at LLNL, making that experience truly enjoyable. I thank so many others at UCLA. And, of course, I thank my absolutely wonderful girlfriend, Alli for making my life so much better.

And last but not least, I thank my entire family, all of whom have always supported me, loved me, encouraged me, and raised me to be who I am today. I could not ask for better parents or a better sister. And I especially acknowledge my grandparents, who have given me all of the encouragement, love, and sustenance they could over the past several years.

Vita

2003-2007	Regent Scholar, University of California, Irvine.
2007	B.S. (Physics) Summa Cum Laude, UC Irvine.
2007	Chancellor's Fellow, University of California, Los Angeles.
2007-2009	Teaching Assistant, University of California, Los Angeles.
2009-2013	Research Assistant, University of California, Los Angeles.
2009-2012	ORISE FES Fellow, University of California, Los Angeles.
2012-2013	Dissertation Year Fellow, University of California, Los Angeles.

Publications

B. Friedman, T. A. Carter, M. V. Umansky, D. Schaffner, and I. Joseph, Nonlinear instability in simulations of Large Plasma Device turbulence, Phys. Plasmas 20, 055704 (2013).

D. A. Schaffner, T. A. Carter, G. D. Rossi, D. S. Guice, J. E. Maggs, S. Vincena, and B. Friedman, Turbulence and transport suppression scaling with flow shear on the Large Plasma Device, Phys. Plasmas 20, 055907 (2013).

B. Friedman, T. A. Carter, M. V. Umansky, D. Schaffner, and B. Dudson, Energy

dynamics in a simulation of LAPD turbulence, Phys. Plasmas 19, 102307 (2012).

D. A. Schaffner, T. A Carter, G. D. Rossi, D. S. Guice, J. E. Maggs, S. Vincena, and B. Friedman, Modification of Turbulent Transport with Continuous Variation of Flow Shear in the Large Plasma Device, Phys. Rev. Lett. 109, 135002 (2012).

S. Zhou, W. W. Heidbrink, H. Boehmer, R. McWilliams, T. A. Carter, S. Vincena, B. Friedman, and D. Schaffner, Sheared-flow induced confinement transition in a linear magnetized plasma, Phys. Plasmas 19, 012116 (2012).

B. Friedman, M. V. Umansky, and T. A. Carter, Grid convergence study in a simulation of LAPD turbulence, Contrib. Plasma Phys. 52, 412 (2012).

M. V. Umansky, P. Popovich, T. A. Carter, B. Friedman, and W. M. Nevins, Numerical simulation and analysis of plasma turbulence the Large Plasma Device, Phys. Plasmas 18, 055709 (2011).

P. Popovich, M.V. Umansky, T.A. Carter, and B. Friedman, Modeling plasma turbulence and transport in the Large Plasma Device, Phys. Plasmas 17, 122312 (2010).

P. Popovich, M.V. Umansky, T.A. Carter, and B. Friedman, Analysis of plasma instabilities and verification of the BOUT code for the Large Plasma Device, Phys. Plasmas 17, 102107 (2010).

S. Zhou, W. W. Heidbrink, H. Boehmer, R. McWilliams, T. A. Carter, S. Vincena, S. K. P. Tripathi, P. Popovich, B. Friedman, and F. Jenko, Turbulent transport of fast ions in the Large Plasma Device, Phys. Plasmas 17, 092103 (2010).

CHAPTER 1

Introduction

1.1 Motivation

Thermonuclear fusion has the potential to solve the world's energy problems. The fusion of a pair of light nuclei, such as deuterium and tritium, releases more energy than the fission of a uranium nucleus and much more energy than the chemical reactions involved in the burning of fossil fuels. Furthermore, the fusion products – unlike those from nuclear fission and fossil fuel burning– are relatively harmless to the environment, and fusion fuel sources are much more abundant than fossil fuels and fissionable uranium. The limiting component of deuterium-tritium fusion reactions is the tritium, which can be made from lithium. Yet there is enough lithium on Earth to power the world through nuclear fusion for at least a million years [Wes11].

Due to its great potential, scientists have been working on controlling fusion reactions for over half a century. The community has made much progress, but fusion is not yet a commercially viable energy source, and there are still several scientific and technological obstacles to overcome before it is. The main obstacle to achieving controlled fusion reactions is the confinement of the reaction fuel for a long enough time at sufficiently high temperatures and densities to achieve a self-sustaining reaction. One of the best ways to contain the fuel is to maintain it in a plasma state and restrict the motion of the plasma using magnetic fields. Possibly the best way to do this – and certainly the most intensely studied – is by

using a tokamak. Tokamaks around the world have already achieved temperatures and pressures necessary to produce fusion but have yet to confine the plasmas for long enough to achieve a self-sustained fusion reaction. Seemingly, this problem can be solved by making the tokamaks larger, although it's still unclear if the large tokamaks will be able to operate in a high confinement mode (H-mode), which will probably be necessary in order to keep the tokamaks economically viable. It's also unclear if the material walls of the larger tokamaks will be able to survive the large plasma fluxes.

The plasma confinement time, for a given sized tokamak, is inversely proportional to the rate of cross-field transport in the tokamak, so it's important to know how to minimize that transport. Now, while the energy transport must be minimized, fusion product alpha particles (and other non-intrinsic impurities) must be transported out of the core so particle transport must be kept sufficiently high. The cross-field particle and energy transport is primarily driven by microturbulence, which is driven by instabilities due to the presence of free energy sources. These free energy sources are due to non-Maxwellian velocity-space features of the distribution functions, spatial inhomogeneity of the distribution functions, and stored electromagnetic energy. These energy sources always exist in the normal operating conditions of a tokamak. For example temperature gradients must exist in tokamaks since the hot tokamak core cannot extend all the way to the walls, which are kept close to room temperature. In fact, we must take great care in order to prevent a high flux of extremely hot plasma from hitting the material walls, which can melt them or sputter atoms into the core. Transport can actually help in this regard by spreading out the plasma beam that crosses the last-closed-flux-surface so that its flux per unit area hitting material limiters and divertor targets is reduced. Altogether, turbulent transport is needed in some ways, but is detrimental in other ways. A balance may be key, or maybe clever techniques and engineering can be used to control the transport in the necessary ways. In either

case, it's important to be able to predict how the turbulence and the transport will react to changes in design or changes in operational parameters.

Predicting transport has been a long, slow research activity for some time. One large problem is that turbulence is not completely understood even in neutral fluids, let alone in tokamak plasmas. Nevertheless, at this point, many aspects of turbulence and transport in the tokamak core are fairly well-understood, largely due to the success of gyro-kinetic simulations. Turbulence in the edge, on the other hand, is not as well-understood for several reasons. One, the edge region contains complex magnetic field geometry, where the field lines range from open to closed, the open ones ending on material surfaces. Two, turbulent fluctuations are high, invalidating current forms of the gyro-kinetic equations, leaving no model to absolutely apply to the entire edge region. Three, the edge contains a zoo of potential instabilities that can drive the turbulence, and seemingly different instabilities exist in different tokamaks and in different operating regimes.

Numerical simulations have helped improve understanding of physical processes and spatial and temporal structures in all kinds of turbulent settings. However, experimental observations and analytic theory generally lead tokamak research, with simulations merely trying to confirm the ideas obtained from these more established methods. Nevertheless, simulations can produce more detailed results than analytic theory and more spatial information than experimental observation, making them valuable. Furthermore, the hope is that simulations can lead experiment, providing predictions before experiments are done, or at least providing enough physical insight to direct experimental efforts. In some instances, like in the cores of tokamaks, the community has made enough progress on simulations (specifically gyro-kinetic ITG simulations) that simulations have uncovered new unexpected physics (such as the Dimits shift of ITG turbulence [DBB00]). But in other instances, like in the edge of tokamaks, nonlinear turbulent simulations don't yet agree enough with experiment to provide good physical insight, let alone

predictive capabilities. A possible path to making progress on this problem is to reduce the problem to a simpler one, achieve simulation validation with that, and then slowly move up to more and more complex situations. A natural place to start is simulation of linear plasma devices.

Magnetic plasma devices that are simpler and colder than tokamaks, like the Large Plasma Device (LAPD) at UCLA [GPL91], have long been used to study basic plasma processes that are relevant to tokamaks. These machines, which generally produce plasma turbulence, offer a more experimentally accessible environment than a tokamak. They are also easier to understand due to their relative simplicity, especially with regard to their magnetic field configurations, which also reduces the number of instabilities present in them. Furthermore, they are colder and thus more collisional than tokamaks, making fluid equations more applicable than they are in tokamaks. It should be easier to produce a verified, validated simulation of turbulence in a linear machine like LAPD than in a tokamak. And any insight gained from analysis of the simulation may apply to tokamak edge turbulence as well, or at least provide methods of analysis or ideas that may be checked when tokamak simulations become more successful.

1.2 Dissertation Summary

This dissertation focuses on direct simulation and analysis of low frequency turbulent fluctuations in LAPD. Thus, in order to introduce important concepts that I will use, in Chapter 2, I briefly describe the modern paradigm of turbulence. I touch on the statistical Kolmogorov theory that has dominated the history of turbulence investigation, but I emphasize the newer deterministic turbulence theory that allows for the description of turbulence by a system of deterministic, dynamical, differential equations. The deterministic theory revolves around solution sets of the nonlinear differential equations called attractors, and in particular, strange

attractors, which give turbulence its random-looking properties. These attractors can have different phase space dimension, and when their dimension is high, the turbulence can be too difficult to describe with the deterministic theory, so that the statistical theory must be used. The statistical theory is based on different scales of fluctuations or eddies and how they interact with the background and with each other. I focus primarily on the instability interactions that drive the turbulence using the free energy contained in the equilibrium profile gradients. Since I find that the turbulence in LAPD is driven by a nonlinear instability with a subcritical flavor, I review the concept of subcritical instability.

After this brief introduction to turbulence concepts, I go on to describe the simulations that I use to reproduce the turbulence in LAPD. In Chapter 3, I review the plasma fluid model that I use in the LAPD simulations. Since LAPD has low temperature ($T_e \leq 10$ eV and $T_i \leq 1$ eV) and is very long, it is highly collisional, making it suitable for modeling with fluid equations. Thus, I use the Braginskii two-fluid model for the equations, but I use only four of the equations, neglecting ion temperature, sound waves, and magnetic field fluctuations. Then, in Chapter 4, I show the equations as they appear in the simulations, and I discuss my methods for numerically reproducing realistic LAPD turbulence. Specifically, I separate the independent variables into time-independent (equilibrium) and time-dependent (fluctuating) components. I then take the equilibrium density, electron temperature, and magnetic field profiles from experimental measurements, linearize the equations, and then insert back only the advective nonlinearities into the equations. I simulate a particular LAPD experiment conducted by Schaffner et al. [SCR12], in which they finely control the equilibrium radial electric field by biasing an azimuthal limiter. Although they access many plasma states with different electric field and pressure profiles, I only simulate and analyze the one state in which the radial electric field is nearly eliminated because this allows me to disregard the equilibrium electric field profile, simplifying the simulation

model. This plasma state, however, is different from the standard LAPD operating state – which has an intrinsic electric field. The null field state is more turbulent in that the fluctuations are larger and they extend further into the core. I actually do show simulation results of the non-zero radial electric field plasma states in Appendix B, but don't cover them in the main text. Furthermore, in the simulations, I use ad hoc density and electron temperature sources to maintain the equilibrium gradient drive over time, I use artificial diffusion and viscosity for saturation, and I use a number of different idealized axial boundary conditions. As for performing the simulations, I use the BOUT++ code, for which I provide details in Appendix A.

In Chapter 5, I overview the results of the simulations. I begin showing linear instability growth rate curves, move onto the space-time evolution of the turbulence, and finally show and discuss statistical properties of the turbulence. The analysis therein is simple, straight-forward, and model independent. I conclude from it that the simulations reproduce statistical turbulent fluctuations that are statistically similar to those of the experiment in both a qualitative and quantitative manner, which validates the simulation model. Figure 1.1 shows several statistical properties of the experimental and simulated turbulence that I also show in Chapter 5. The different curves – other than that labeled "Experiment" – correspond to simulations with different axial boundary conditions. It is clear that all but one of these simulations produces experimentally realistic turbulent fluctuation statistics. The one truly mysterious result, however, can be seen in Fig. 1.1 f). That is, all of the experimentally realistic simulations have axial wavenumber spectra that peak at $k_{\|} = 0$. The reason why this result is so interesting is because the only linear instability in the simulations – except for the Sheath simulation – is the linear drift wave instability, which has positive growth rate only for finite $k_{\|}$. The most unstable linear modes or waves generally dominate the structure of plasmas, but this isn't the case in these simulations.

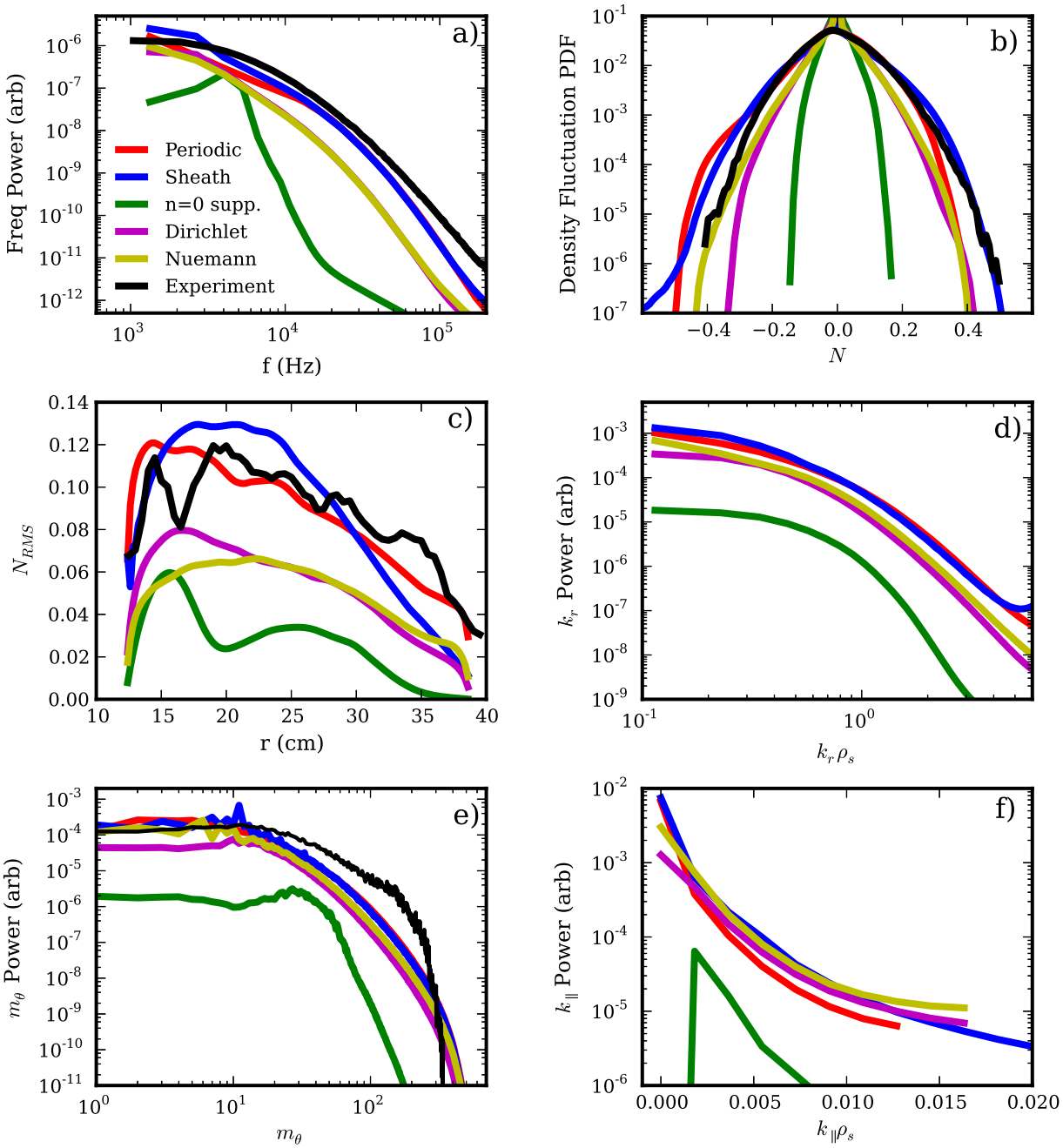

Figure 1.1: Experimental and simulation fluctuation statistics for the experiment and all simulations with different axial boundary conditions

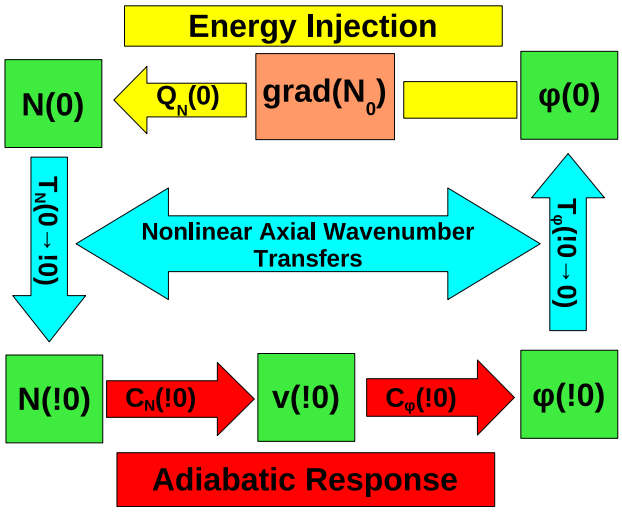

Figure 1.2: Nonlinear instability diagram

To determine the origin of this unusual result, I analyze the simulations using energy dynamics. Energy dynamics analysis use the simulation model as well as all of the spatial and temporal information output by the simulations to reveal dynamical processes such as energy injection into the fluctuations from the free energy equilibrium gradients, energy transfer between different waves or modes, energy transfer between potential and kinetic energy degrees of freedom, and energy dissipation of the fluctuations. In Chapter 6, I derive the energy dynamics equations for my simulation model and explain which terms in the model correspond to the different processes. Specifically, I show that the terms involving advection of equilibrium variables supply energy injection, the nonlinear advective terms cause mode to mode transfer, the adiabatic response terms transfer energy from potential to kinetic, and the collisional, diffusive, and viscous terms supply the dissipation. Furthermore, I decompose the turbulent fluctuations in two bases: a partial Fourier basis and a Proper Orthogonal basis, and I derive the energy dynamics equations for each of the basis functions.

Then in Chapter 7, by inputting the simulated turbulent results into the basis-decomposed energy dynamics equations, I uncover the primary mode-based processes that control the turbulence including that which supports the $k_\| = 0$ fluctuations. In fact, the nonlinear instability cycle that supports the $k_\| = 0$ fluctuations is the most dominant process controlling the turbulence. I show a diagram of the cycle in Fig. 1.2. The process begins with the "Energy Injection" step, in which $k_\| = 0$ convective filaments or flute-like structures advect density across the equilibrium density gradient, forming $k_\| = 0$ density fluctuations. These density fluctuations break up by axial three-wave transfer into finite $k_\|$ waves. An equivalent way to look at this step is that the azimuthal gradient that results from the density filaments drives radially propagating drift waves that have finite $k_\|$. These finite $k_\|$ drift waves – represented at the bottom of the diagram – have access to the adiabatic response, meaning they can transfer energy between potential energy of the density fluctuations N and the kinetic energy of the potential ϕ fluctuations. The resultant drift waves then transfer some of their kinetic energy back to the convective filaments. This process is self-sustaining and it is necessarily nonlinear because it requires finite amplitude fluctuations to begin, and the three-wave transfers from the $k_\| = 0$ density fluctuations to the drift waves and from the drift waves back to the convective cells are both purely nonlinear processes.

Despite the nonlinear nature of the instability cycle, linear effects are still important because the nonlinearities of the system are energetically conservative. This means that the energy that supports the process ultimately comes from a linear mechanism, specifically that in which the convective filaments advect density across the equilibrium density gradient. Such a process is unintuitive because all $k_\| = 0$ linear eigenmodes of the system are stable. This means that, individually, each $k_\| = 0$ eigenmode decays, losing energy to the equilibrium gradient rather taking it. Yet a linear process at $k_\| = 0$ still drives energy into the

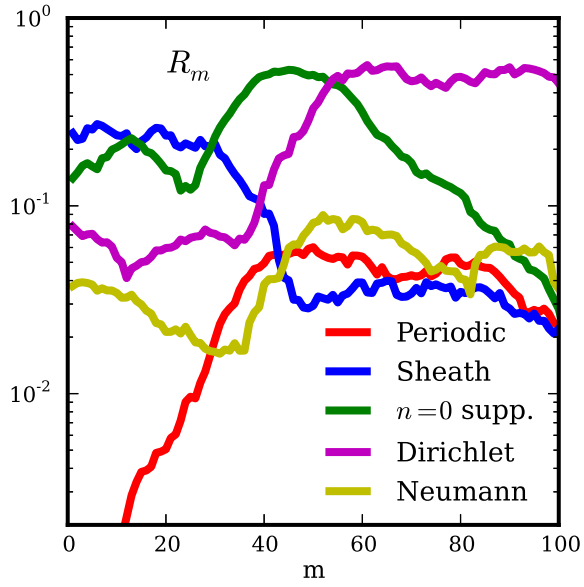

Figure 1.3: The ratio of energy contained in the most unstable eigenmodes to that in the turbulence

turbulent system. The process responsible for this is a transient growth mechanism unique to nonorthogonal stable linear eigenmodes. Because the linear system is non-normal, the linear eigenmodes are not orthogonal to one another. In fact, they are largely anti-parallel to each other. When this happens, even when all of the eigenmodes decay, the system as a whole may still grow, although only transiently. Nevertheless, this growth, when reinforced by nonlinear effects, can sustain itself, continuing to drive energy into the system. I discuss this first in Chapter 2, then again in Chapter 7. Interestingly, the nonlinear instability and the linear mechanism that drives it are analogous to those which drive turbulence in many subcritical neutral fluid flows.

While I focus only on the simulations that use periodic axial boundary conditions in Chapter 7, in Chapter 8, I generalize to the non-periodic simulations. These merit a separate discussion because without the axial periodicity, the linear eigenmodes can have non-sinusoidal axial structures, or put another way, each

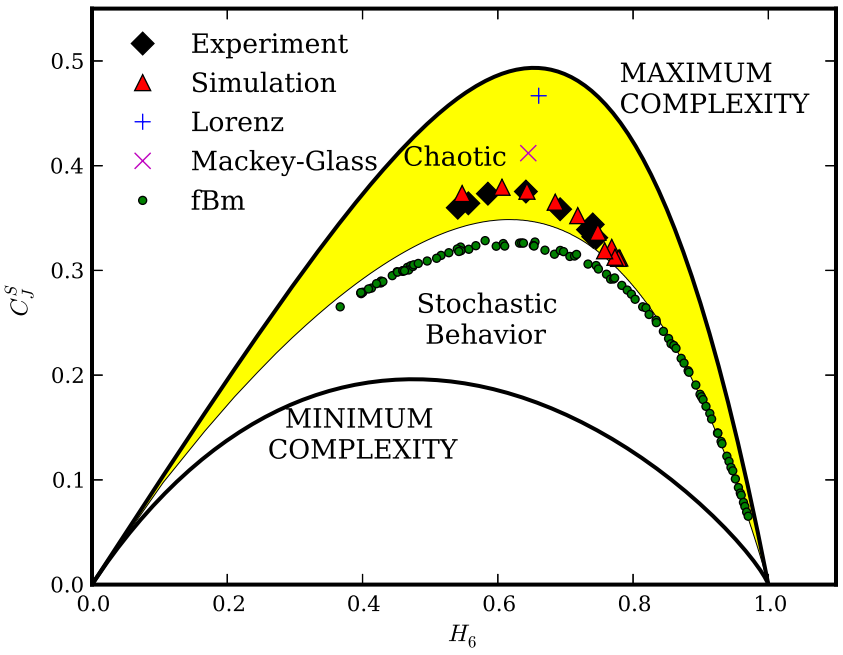

Figure 1.4: Location of chaotic, stochastic, and LAPD data in the complexity-entropy plane

eigenmode can have many non-zero Fourier coefficients, including the Fourier coefficient of $k_\parallel = 0$. And, since the nonlinear instability is dependent upon $k_\parallel = 0$ effects, it can be more difficult to differentiate between linear and nonlinear instability in this case. I present arguments and analysis, however, supporting the robustness of the nonlinear instability in the simulations with non-periodic axial boundary conditions. One such analytical technique I use is determining the fraction of turbulent energy contained in the most unstable linear eigenmode. I preview the result in Fig. 1.3, showing this fraction R_m as a function of m number. Except for a few places, the fraction is less than 0.1, indicating the small contribution of the linear instability in the turbulence.

Finally, in Chapter 9, I explore the deterministic, chaotic nature of the experimental and simulated turbulence. From Chapters 5-8, I use analytical techniques

based on the statistical and structural nature of turbulence. These require a lot of information that can only be obtained from well-validated simulations. But these don't answer deep questions regarding the solutions of the differential equations, like are they deterministic, and if so, what is the dimensionality of the attractor solution? In fact, if the attractors are low dimensional, meaning the turbulence is not stochastic, simpler analyses, highly reduced models, and non-simulation reconstruction techniques may be used to understand the turbulence. So, in Chapter 9, I attempt to find the deterministic nature of the turbulence and the dimensionality of the attractors. I do so first by exploring the temporal structure of time signals from experimental and simulation observables. The Lorentzian pulse structure of the time signals indicates that the turbulence is deterministic, but the range of Lorentzian pulse widths, the non-exponentiality of the power spectra, and more direct techniques reveal that the turbulence is high dimensional, containing many effective degrees of freedom. I show a result of one of these techniques – the permutation entropy – in Fig. 1.4, where I plot the permutation entropy against the permutation complexity for experimental and simulation time signals along with other representative signals. The other time signals come from two chaotic models – the Lorenz and Mackey-Glass models – and one stochastic model: fractional Brownian motion. Due to the relative location of the experiment and simulation in relation to the chaotic and stochastic models, it is evident that the LAPD turbulence is chaotic, but less so than the chaotic models, which is perhaps a manifestation of a multiple time-scale high-dimensional process. I further confirm the high dimensionality of the process with a Proper Orthogonal Decomposition, which shows that many degrees of freedom are active in the turbulence.

CHAPTER 2

Turbulence and Instability

Turbulence is a ubiquitous phenomenon in fluids that has been recognized and studied for centuries. It is often called the last unsolved problem in classical physics because we cannot predict in detail how or why turbulence occurs or fully predict its behavior. It is, however, extremely important to gain an understanding of it in laboratory plasmas and magnetically confined fusion devices because it causes increased particle and energy transport. This is not necessarily a good or bad property as far fusion devices are concerned on the whole – better energy confinement is needed in the core but not in the scrape-off-layer, while good particle confinement is needed in the scrape-off-layer but not in the core. Nevertheless, an enhanced understanding of plasma turbulence would allow for greater control to achieve the properties needed for fusion and would allow for greater prediction of future machine performance.

2.1 Paradigms of Turbulence

In the past, researchers thought that turbulence was a random process that could only be described in a statistical manner [TL72]. This is the classical view of turbulence. This view, however, contradicted the also widely-held belief that the Navier-Stokes equations can fully describe turbulent flow in neutral fluids [McD04]. This is contradictory because the Navier-Stokes equations are deterministic (assuming yet unproven existence of the solutions), so they cannot possibly describe a random flow. Apparently, some scientists in the first half of

the 20^{th} century didn't regard this as a problem, while others took this as a cue to abandon the fully equation-based approach to studying turbulence [TL72]. In any case, statistical theory dominated. Not until the 1970's was a modern deterministic theory of turbulence formulated. Nevertheless, the deterministic approach does not mean that turbulent statistics are useless because even though the turbulence is not random, it can still be stochastic. I note that random and stochastic are often used interchangeably, but formally, stochastic refers to a variable whose autocorrelation decays exponentially fast to zero. Thus, a deterministic system may be stochastic, but not random. Deterministic systems are stochastic when they are controlled by a large number of effective degrees of freedom. In stochastic systems, statistical tools are the only effective tools [McD04]. Even non-stochastic systems are often described statistically, although they often have more informative descriptions as well.

In any case, certain statistical descriptions are still widely accepted in the fluid and plasma communities. Perhaps the most important is Kolmogorov's theory (K41 theory) of high Reynolds number, small scale turbulence [Kol41, TL72]. It's based on the idea that large scale turbulent structures – generally eddies – are driven by instability at the largest scales: the system and integral scales. These then drive eddies of smaller scales in a cascading process. The cascade occurs in the inertial scale range, which has a power law spectrum with index of $-5/3$. When energy cascades down to the Kolmogorov scale, viscosity takes the energy away from the eddies, thermally transferring it to the fluid. I show a typical Kolmogorov spectrum in Fig. 2.1. The relative success of the Kolmogorov theory in describing some fluid flows has led to its widespread use [Man04].

The modern view of turbulence is that it is deterministic [SG81, McD04]. Most of the plasma community readily accepts this as evidenced by its use of deterministic equation sets and simulations used to model plasma turbulence. The first clue that deterministic equations could describe something as apparently

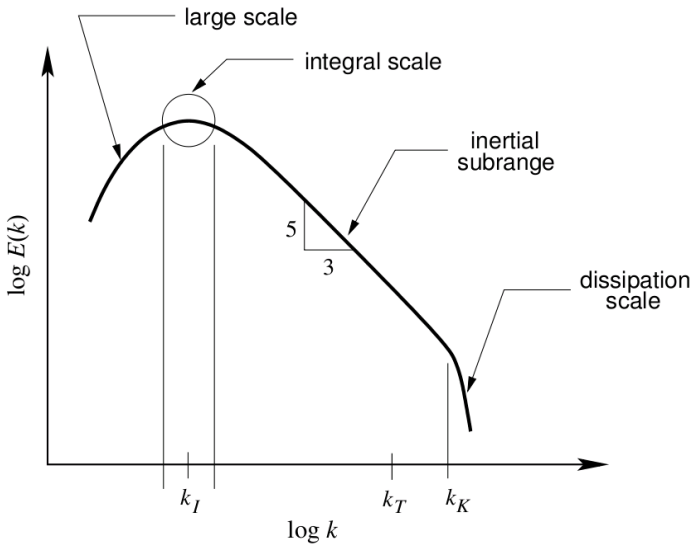

Figure 2.1: Diagram of the Kolmogorov energy spectrum

random as turbulence was provided by Lorenz in 1963 [Lor63]. He showed that a deterministic equation derived from the Navier-Stokes equations could exhibit random-looking behavior, and that it was sensitive to small changes in initial conditions. In 1971, Ruelle and Takens showed that the Navier-Stokes equations are capable of producing chaotic solutions that are sensitive to initial conditions and are associated with the mathematical concept of a strange attractor [RT71]. They also presented a sequence of transitions (bifurcations) that a flow undergoes as the Reynolds number is increased on its way to a chaotic state: steady $\rightarrow$ periodic $\rightarrow$ quasi-periodic $\rightarrow$ chaotic. This isn't the only possible bifurcation sequence; in fact, some flows like Poisueille pipe flow go straight from steady to chaotic. In any case, it's significant that the sequence is short and finite, meaning that turbulence may occur at finite Reynolds number, and it can be understood in terms of a strange attractor. Interestingly, Biskamp and Kaifen showed that a system of three plasma drift waves undergoes a Ruelle-Takens bifurcation sequence [BK85].

Under the deterministic viewpoint, chaotic solutions can have different degrees of complexity. The usual way to view turbulent solutions is in phase space (also called state space), rather than in coordinate space. While the phase space of real systems is infinite, the phase space orbits of solutions to dynamical differential equations generally lie on some manifold that covers only a subset of the phase space [Man04]. Thus, the dynamics are often effectively controlled by a finite number of degrees of freedom. When this effective number of degrees of freedom is small, the process is called low-dimensional chaos. When this number is greater than 3, it is called high-dimensional chaos or hyperchaos, though technically, hyperchaos must involve a system with more than one positive Lyapunov exponent. When the degrees of freedom approach infinity, the process is stochastic. A technique called time delay embedding, invented by Takens [Tak81], reconstructs the multi-dimensional solution to a deterministic process given a single time signal. This means that experimental data of a single observable at a single location can reveal information about other variables at multiple locations [BP02]. This technique cannot be used for stochastic processes. It is important, then, to determine whether turbulence is deterministic or stochastic.

2.2 Instability: Turbulent Drive

The main focus of this dissertation is on the specific process that drives turbulence in LAPD. Turbulence is dissipative and therefore needs a source of energy to sustain itself. Generally, this source comes from a gradient in a steady (equilibrium) variable such as a flow or a pressure. Fluctuations that take energy from these equilibrium gradients often develop certain unstable mode structures that continue to take energy indefinitely. The details of these instabilities are important for understanding the onset of turbulence and the structure of turbulence. Both the neutral-fluid community and the plasma community have studied instabilities

in great depth.

2.2.1 Linear Instabilities Abound in Plasmas

Linear instabilities are those that can grow from infinitesimally small fluctuations about an equilibrium. They can be calculated by linearizing a dynamical equation set about an equilibrium, where at least one equilibrium profile has a finite gradient. A linear dynamical system can be written in the form

$$\frac{\partial \mathbf{v}}{\partial t} = \mathbf{M}\mathbf{v} \tag{2.1}$$

where $\mathbf{v}$ is a vector of independent variables that describe the state of the system and $\mathbf{M}$ is a matrix of coupling coefficients and differential operators. If the equations are coupled, $\mathbf{M}$ is not diagonal. Assuming $\mathbf{v}$ has an exponential time dependence, this equation is an eigenvalue problem, with (generally complex) eigenvalues γ_i and eigenvectors $\boldsymbol{\xi}_i$, which are linearly independent. If any of the eigenvalues sit in the right half of the complex plane, their associated eigenvectors will grow exponentially from infinitesimal noise. In this case, the system is linearly unstable. Now, even though an equilibrium profile with a finite gradient is a necessary condition for linear instability, it is not sufficient. At least one of the eigenvalues must have a positive real part. This is why so much effort goes into testing plasma systems for linear instability.

In general, plasma physics has so many more types of equilibrium gradients and physical processes than neutral fluids, that there are many more linear plasma instabilities than linear neutral fluid instabilities. Plasmas have linear instabilities due to density gradients, temperature gradients, velocity gradients, current gradients, magnetic field curvature, and non-Maxwellian velocity-space features – to name a few [Wes11, Che06]. Linear plasma instabilities can be collisional, collionless, electrostatic, electromagnetic, ionization-related, sheath-induced, *etc.* The shear number of instabilities can be overwhelming. In physical systems, any

number of linear instabilities can be present at the same time, combining with each other, with some being more significant than others. Often times, it can take great effort to identify a particular linear instability with particular properties that is responsible for turbulence in a given situation. This can be important if one wants to create reduced models or if one wants to be able to predict the type of turbulence that will occur in future machines. Unfortunately, however, linear instability is just the tip of the iceberg because turbulence is inherently nonlinear, which opens the door for even more instabilities.

2.2.2 Supercritical Stability and Subcritical Instability

While the plasma community has focused much attention on linear stability of various plasma systems, the neutral-fluid community has long been aware that nonlinear stability effects are crucial to explaining observed transitions from laminar to turbulent flow [Kro99]. The foundations of the theory of nonlinear hydrodynamic stability were laid by Landau [Lan44, LL59]. While his ideas have required much elaboration, qualification, and application, they still contain many ingredients of modern day theory. I outline some of those ideas, following the treatment in Drazin and Reid [DR81].

Landau began with the linear theory of stability of a steady flow, which has a spectrum of linearly independent eigenmodes, each with growth rate σ. For some dimensionless parameter R (such as the Reynolds number), when $R < R_c$, all modes have $\sigma < 0$. As R increases above R_c, one mode becomes unstable with $\sigma > 0$, where $\sigma \sim R - R_c$ for $|R - R_c| \ll 1$. He described the evolution of the amplitude $|A|$ of the most unstable or least stable mode by what is now called the Landau equation:

$$\frac{d|A|^2}{dt} = 2\sigma|A|^2 - l|A|^4 \tag{2.2}$$

where l is the Landau constant and the $l|A|^4$ term is the nonlinearity. Landau's

equation admits an analytic solution given an initial condition, making it easy to explore. Several different qualitative scenarios arise depending on the signs and magnitudes of σ and l. If $l > 0, \sigma > 0$, as $t \to \infty, |A| \to (2\sigma/l)^{1/2}$ no matter the value of the intial condition A_0. This value of $A_e \equiv (2\sigma/l)^{1/2}$ is called a fixed point attractor with a basin of attraction consisting of all values of A_0 since any initial state asymptotically evolves to it. Attractors are important objects in the field of dissipative dynamical equations. Note that the linear problem is unstable because $|A| \to \infty$ as $t \to \infty$, but the nonlinear problem is stable in that it evolves to a finite value as $t \to \infty$. This is called supercritical stability. If $l > 0, \sigma < 0$, as $t \to \infty, |A| \to 0$ for both the linear and nonlinear problem. Here, the point $|A| = 0$ is the fixed point attractor. The situation is rather simple for $l > 0$ and the bifurcation diagram for this is shown in Fig. 2.2 a). The branching of the curve of the equilibrium solutions at $R = R_c, |A| = 0$ is called a bifurcation.

On the other hand, if $l < 0, \sigma > 0$, both the linear and the nonlinear problem are unstable with the nonlinear problem growing super-exponentially in time, becoming infinite at finite time. Such a situation is unphysical, and the Landau equation, which only has a single degree of freedom, is too simple in this case. The more interesting case is when $l < 0, \sigma < 0$. If $A_0 < A_e$, the solution decays to zero as $t \to \infty$. However, if $A_0 > A_e$, the solution is unstable and breaks down at finite time. This means that the system is unstable only when the initial condition has a finite amplitude, which is in contrast to a linear instability, which is unstable to infinitesimal initial perturbations. Finite amplitude instabilities are called nonlinear instabilities. Fig. 2.2 b) depicts the bifurcation diagram for the case of $l < 0$. In this figure, R_G represents a Reynolds number below which the unstable bifurcated solution doesn't exist. This isn't a part of the Landau equation, but Landau suggested that this should be the case.

Furthermore, unlike in the supercritical case, the subcritical case contains regions ($R > R_G$) where the unstable solution is not bounded by a higher region of

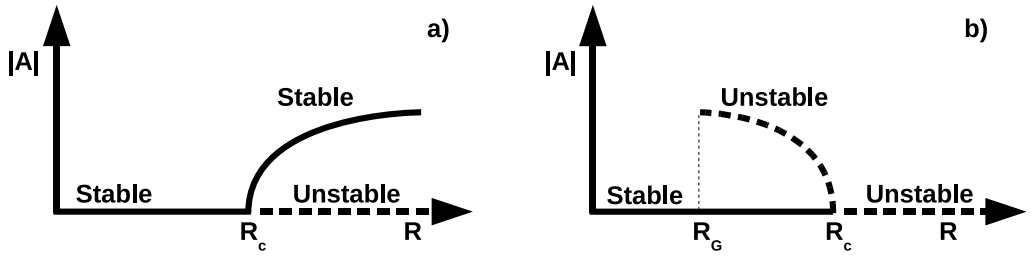

Figure 2.2: Supercritical and subcritical bifurcation diagrams

stability, indicating that the solutions become infinite. In reality, this is unphysical, and the simple Landau equation isn't sufficient to find the attractor solution. Now the subcritical case is so interesting because it allows for instability and turbulence when a system is linearly stable. This seems to be the case in several different kinds of flows. Landau asserted that Poiseuille pipe flow is an example of this [Lan44]. Poiseuille pipe flow, which is flow with a parabollic velocity profile, is linearly stable for all R, so that $R_c = \infty$. But experimentally, it is known that for $R = R_G \sim 2000$, it becomes unstable to finite disturbances. Plane Couette flow (flow with linear velocity profile between two infinite moving planes) is another example of this. Plane Poiseuille flow, also admits subcritical instability, but it has a finite R_c, so it's more representative of Fig. 2.2 b) [TTR93].

Since the Landau equation has only a single degree of freedom, its attractor solutions are always fixed points. When the governing equations contain more degrees of freedom, the attractors may have higher dimension, and bifurcations can change the dimension of the attractor. For instance, the Hopf bifurcation is one in which the attractor evolves from a fixed point to a one dimensional periodic limit cycle. A second Hopf bifurcation brings about a limit torus. Other bifurcations

can result in strange attractors, which have fractal dimension [Man04].

2.2.3 Non-normality, Transient Growth, and Subcritical Turbulence

Subcritical instability is especially unintuitive in the common case where the nonlinearities of the equation set are energetically conservative. Then, only the linear terms in the equations can extract energy from the equilibrium gradients. It seems reasonable that when all of the linear eigenmodes of a system are stable, there shouldn't be any instability. This makes subcritical instability a mysterious phenomenon. However, several neutral-fluid researchers in the early 1990's explained the linear mechanism behind nonlinear subcritical growth [Gus91, BF92, RSH93, RH93, TTR93, HR94, Hen96]. The mechanism requires that the eigenvectors of the linear system be nonorthogonal. In other words, the linear operator matrix (like $\mathbf{M}$ in Eq. 2.1) must be non-normal. Such non-normality is a necessary condition for sustained subcritical turbulence in systems with conservative nonlinearities.

I illustrate the mechanism behind sustained subcritical turbulence with a simple diagram in Fig. 2.3, which represents a two-dimensional two-state system. I start in Fig. 2.3 a) with two 2D linear eigenvectors that are not orthogonal to one another, but are largely anti-parallel with a 30° angle between them. I give them each a starting amplitude so that they form a leg and a hypotenuese of a 30-60-90 triangle. The sum of these vectors, which is the other leg, is the initial state of the system. The squared length of this is the energy of the system. Note that the total energy of the system is $|\mathbf{u}+\mathbf{v}|^2 = |\mathbf{u}|^2 + |\mathbf{v}|^2 + 2\mathbf{u}\cdot\mathbf{v}$. So since the eigenvectors are nonorthogonal, the total energy of the system is not just the sum of the individual energies of the eigenmodes ($|\mathbf{u}|^2 + |\mathbf{v}|^2$), but it includes an interaction term ($2\mathbf{u}\cdot\mathbf{v}$) that can be positive or negative.

Now, in Fig. 2.3 b), I show the result of purely linear evolution of the system.

Linearly, since the vectors are eigenvectors, they grow or decay exponentially at given rates γ_u, γ_v. And since I am interested in the subcritical case, I give both of the vectors negative growth rates. Furthermore, **u** has much smaller damping rate than **v**. After a certain amount of time, under purely linear action – where each vector decays at its characteristic decay rate – the system resides in the state shown in Fig. 2.3 b). Note that I have changed the scales on the axes because the triangle has become much smaller. Perhaps surprisingly, even though both vectors **u** and **v** have decayed and have smaller magnitudes than they did in Fig. 2.3 a), the total energy of the system (the green line) has grown! Clearly, the reason is that the interaction energy between the two vectors has become less negative. Moreover, if the system were to continue evolving linearly, the total energy would eventually decay as the vectors become smaller. Therefore, the growth of the total energy from a) to b) is called transient growth. One may wonder where this transient energy comes from. The answer is that the energy comes from the equilibrium gradients – the same place it comes from for unstable linear eigenvectors. So systems in which the fluctuations are made up of only nonorthogonal stable linear eigenvectors can transiently grow in energy before decaying. At small times, the growth has been shown to be algebraic, meaning it is proportional to time [Wal95]. This is in contrast to growth by unstable linear eigenmodes, which is exponential in time.

Now the linear growth in non-normal linearly stable systems is only transient, but the nonlinearities in the full nonlinear systems can take this transiently injected energy, mix it around, and sustain the fluctuation energy or sustain the turbulence indefinitely. In Fig. 2.3 c), I show how the nonlinearities, which conserve the total energy, can mix the energy between individual modes and the interaction energy. The nonlinearities can essentially prop up the linear eigenvectors' individual energies without injecting net energy into the system. Finally, Fig. 2.3 d) shows linear decay of the eigenvectors, bringing the system back to

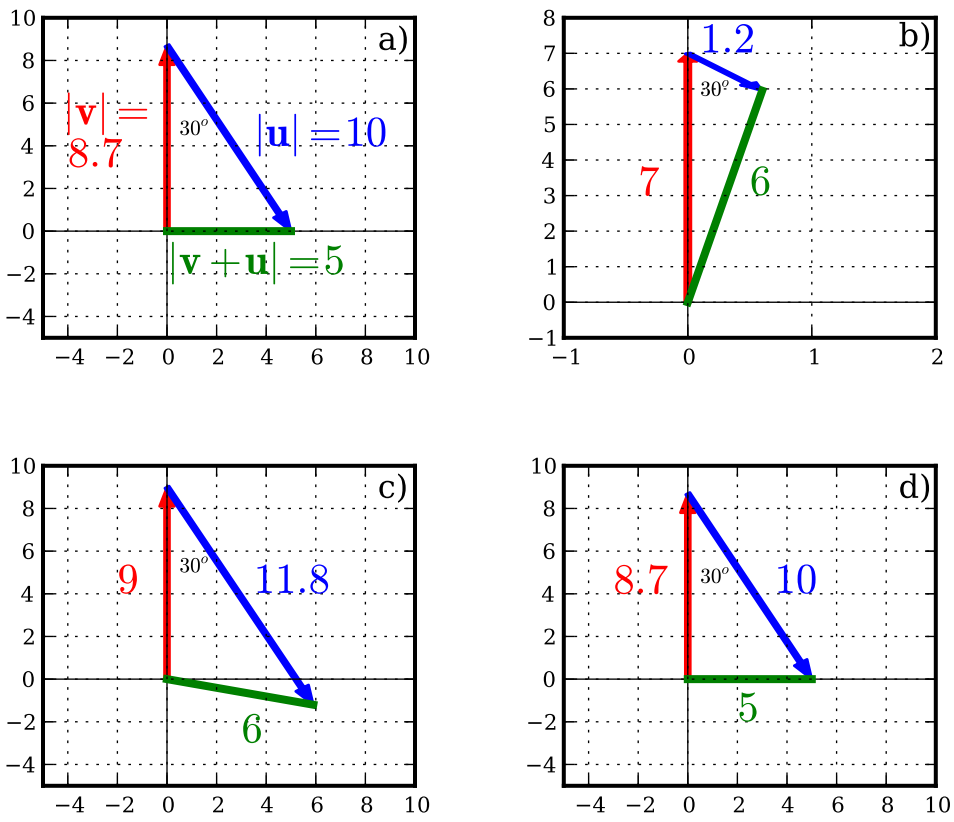

Figure 2.3: A simple diagramatic illustration of how non-orthogonal stable modes sustain themselves in subcritical systems

its original state with its original energy. Altogether, this is the basic mechanism of subcritical instability or self-sustained subcritical turbulence in systems with conservative nonlinearities. It is basically a linear mechanism, but it requires nonlinearity to sustain or bootstrap itself. Although my simple diagram makes it seem as though the transient growth mechanism is rather weak (amplifying the total energy from 25 to 36), the mechanism can amplify energies by factors of several thousand in realistic systems [Gus91, BF92].

CHAPTER 3

The Braginskii Fluid Model and LAPD

3.1 LAPD Suitability to the Braginskii Fluid Model

At a basic level, the state of a plasma is described by seven-dimensional distribution functions $f_j(\mathbf{x}, \mathbf{v}, t)$ for each species j. The behavior of the plasma is described by the system of kinetic equations (Boltzmann equations), which evolve the distribution functions forward in time:

$$\frac{\partial f_j}{\partial t} + \mathbf{v} \cdot \nabla f_j + \frac{e_j}{m_j}(\mathbf{E} + \mathbf{v} \times \mathbf{B}) \cdot \frac{\partial f_j}{\partial \mathbf{v}} = \left(\frac{\partial f_j}{\partial t}\right)_C . \tag{3.1}$$

$\left(\frac{\partial f_j}{\partial t}\right)_C$ is the change in the distribution function due to collisions. For plasmas, the collisions are Coulomb collisions, and the collision term takes the form of the Fokker-Planck operator. With this operator, Eq. 3.1 is called the Fokker-Planck equation. Now it is well known that the Fokker-Planck equation cannot be solved numerically for problems that require time intervals too much larger than the electron-cyclotron time due to computational time limitations. The phase space is just too large. Therefore, reduced equations, such as gyrokinetic, drift kinetic, or fluid equations have been derived to produce numerically tractable equations. These equations are all derived under certain physical assumptions such as strong guiding magnetic fields, small fluctuation levels, or slow spatial and/or time variations such that these different equations are best applied to different physical situations.

The equations that are arguably most suitable to describe waves and turbulence in LAPD – and fastest to solve numerically – are the fluid equations,

specifically those derived by Braginskii [Bra65]. In deriving his equations, Braginskii approximates the solution as $f_j = f_j^0 + f_j^1$ where the zero-order piece f_j^0 is a Maxwellian and the first-order piece f_j^1 is a perturbation on the zero-order distribution function: $|f_j^1| \ll f_j^0$. The equations are then derived by taking moments of the Fokker-Planck equation to create coupled equations of the independent variables, $n_j, \mathbf{v_j}$, and T_j. Now certain requirements must hold to justify the Braginskii approximation, all of which have the flavor that macroscopic quantities must vary slowly in time and space. This is generally caused by strong relaxation processes such as collisions, which keep the distribution functions close to Maxwellians. In general, for the Braginskii equations to be applicable, processes of interest must occur on time intervals much greater than the collision time and quantities should vary slowly over distances traversed by the particles between collisions.

Specifically, slow time variation requirement can be written as $\frac{d}{dt} \ll \nu$, where for electron drift wave turbulence, this is approximately $\omega_* \ll \nu_e$. Table 4.3.2, which displays typical LAPD operating parameters, shows that $\omega_*/\nu_e \sim 0.01$. The requirement that spatial quantities vary slowly compared to the collisional mean free path can be written simply for the direction parallel to the magnetic field as $\lambda_{ei} \sim \lambda_{ee} \ll L_\parallel$. For LAPD, $\lambda_{ei}/L_\parallel \sim 0.01$. For the direction perpendicular to the magnetic field, the same kind of relation $\lambda_{mfp} \ll L_\perp$ must also hold. However, due to the cyclotron motion of particles around the magnetic field, λ_{mfp} is really the Larmor radius, unless the collisional mean free path is less than the Larmor radius. For electrons, $\rho_e \ll \lambda_{ei}$ and $\rho_e/L_\perp \sim 10^{-4}$ where $L_\perp \sim 0.1$ m. For the ions, the ion cyclotron frequency is close to the ion collision frequency, meaning that either the ion Larmor radius or the ion mean free path may be used. Using the Larmor radius, $\rho_i/L_\perp \sim 0.01$. Therefore, the collisionality is high enough and the machine dimensions are large enough so that the Braginskii fluid model describing drift wave turbulence should be applicable to LAPD. Note that this doesn't apply to high frequency and high $k_\parallel$ waves.

3.2 The Braginskii Equations

The Braginskii fluid equations are as follows: the continuity equation for species j, electrons or ions, is [Wes11, Bra65]

$$\frac{\partial n_j}{\partial t} = -\nabla \cdot (n_j \mathbf{v}_j). \tag{3.2}$$

The momentum balance equation is

$$n_j m_j \frac{d\mathbf{v}_j}{dt} = -\nabla p_j - \frac{\partial \Pi_{j\alpha\beta}}{\partial x_\beta} + n_j e_j (\mathbf{E} + \mathbf{v_j} \times \mathbf{B}) + \mathbf{R}_j. \tag{3.3}$$

$p_j = n_j T_j$ is the pressure. $\Pi_{j\alpha\beta}$ is the stress tensor, which involves the products of viscosity coefficients and rate-of-strain tensor components. The viscosity coefficients are some of the several terms that are called transport coefficients. The transport coefficients are calculated by the Braginskii procedure in terms of n, $\mathbf{v}$, and T. $\mathbf{R}_j$, which involves several other transport coefficients, is the rate of collisional momentum transfer. The momentum transfer from ions to electrons is given by

$$\mathbf{R}_e = -m_e n_e \nu_e (0.51 u_{\parallel e} + \mathbf{u}_{\perp e}) - 0.71 n_e \nabla_\parallel T_e - \frac{3}{2} \frac{n_e \nu_e}{\omega_{ce}} \mathbf{b} \times \nabla T_e \tag{3.4}$$

where $\mathbf{u} = \mathbf{v}_e - \mathbf{v}_i$ and ν_e is the electron collision frequency with ions. $\mathbf{R}_e$ includes both the friction force and the thermal force. The thermal force, like the friction force, is due to electron-ion collisions, but its origin is in the gradient of the collisionality due to the temperature gradient. So, the thermal force terms are those proportional to the gradients of temperature. $\mathbf{R}_i = -\mathbf{R}_e$ in a fully ionized plasma with one ion species. However, LAPD has a significant neutral density. Collisions with neutrals are much more important for the ions [PUC10a]. So

$$\mathbf{R}_i = -\mathbf{R}_e - n_i m_i \nu_{in} \mathbf{v_i}. \tag{3.5}$$

The energy balance equation is

$$\frac{3}{2} n_j \frac{\partial T_j}{\partial t} = -n \mathbf{v}_j \cdot \nabla T_j - p_j \nabla \cdot \mathbf{v}_j - \nabla \cdot \mathbf{q}_j - \Pi_{j\alpha\beta} \frac{\partial v_j \alpha}{\partial x_\beta} + Q_j \tag{3.6}$$

where the term involving the stress tensor describes viscous heating. The electron heat flux (with more transport coefficients) is

$$q_e = n_e T_e \left(0.71 u_\parallel + \frac{3\nu_e}{2\omega_{ce}} \mathbf{b} \times \mathbf{u}\right)$$
$$+ \frac{n_e T_e}{m_e \nu_e} \left(-3.16 \nabla_\parallel T_e - \frac{4.66 \nu_e^2}{\omega_{ce}^2} \nabla_\perp T_e - \frac{5\nu_e}{2\omega_{ce}} \mathbf{b} \times \nabla T_e\right) \tag{3.7}$$

where the first part of this expression constitutes convection, while the second part is conduction. The ion heat flux is

$$q_i = \frac{n_i T_i}{m_i \nu_i} \left(-3.9 \nabla_\parallel T_i - \frac{2\nu_i^2}{\omega_{ci}^2} \nabla_\perp T_i - \frac{5\nu_i}{2\omega_{ci}} \mathbf{b} \times \nabla T_i\right). \tag{3.8}$$

The last transport coefficients are in the heating Q. The ion heating due to collisional heat exchange between ions and electrons is

$$Q_i = \frac{3 m_e}{m_i} n_e \nu_e (T_e - T_i) \tag{3.9}$$

while the electron heating is

$$Q_e = -\mathbf{R} \cdot \mathbf{u} - Q_i. \tag{3.10}$$

The electron heat exchange involves an ohmic heating contribution ($\mathbf{R} \cdot \mathbf{u}$) that is absent from the ion heating because electrons colliding with ions transfer very little momentum to the ions.

3.3 The Vorticity Equation

The Braginskii equations in the previous section contain electric and magnetic fields which must be self-consistently determined by the charges and currents that are evolved by the equations. This is done with the inclusion of Maxwell's equations. Two of those equations are used to write the fields in terms of potentials:

$$\mathbf{E} = -\nabla \phi - \frac{\partial \mathbf{A}}{\partial t} \tag{3.11}$$
$$\mathbf{B} = \nabla \times \mathbf{A}.$$

The vector potential $\mathbf{A}$ is strictly a fluctuating quantity, meaning it is not used to describe the guide field $\mathbf{B}_0$. The next equation,

$$\nabla \times \mathbf{B} = \nabla(\nabla \cdot \mathbf{A}) - \nabla^2 \mathbf{A} = \mu_0 \mathbf{j} \tag{3.12}$$

is used to relate the vector potential to the current, where the displacement current is neglected as is generally done in plasmas. Due to quasi-neutrality – $n_e = n_i \equiv n$ – it is difficult to keep track of the very small differences in the densities, so the Poisson equation is difficult to implement numerically for the main part of the plasma. A more useful equation that can be used instead is the conservation of charge (or ambipolarity condition), $\nabla \cdot \mathbf{j} = 0$. The vorticity equation is derived from this equation.

For the current, $\mathbf{j} = en(v_{\parallel i} - v_{\parallel e}) + en(\mathbf{v}_{\perp i} - \mathbf{v}_{\perp e})$. In LAPD, the parallel current is carried primarily by the light electrons, while the perpendicular current is primarily carried by the ions, which have larger Larmor radii. So the conservation of charge equation can be simplified to

$$\nabla_\parallel (n v_{\parallel e}) = \nabla_\perp \cdot (n \mathbf{v}_{\perp i}). \tag{3.13}$$

The perpendicular ion component of this equation is derived from Eq. 3.3 for the ions. Neglecting terms that have finite ion temperature (pressure and stress tensor), and solving for the ion velocity in the Lorentz force term, the perpendicular ion velocity has three terms [PUC10a, SC03]:

$$\mathbf{v}_{\perp i} = \mathbf{v}_E + \mathbf{v}_{pi} + \mathbf{v}_{\nu i} \tag{3.14}$$

where the $\mathbf{E} \times \mathbf{B}$ velocity is $\mathbf{v}_E = \mathbf{E} \times \mathbf{B}/B^2 = -\nabla_\perp \phi \times \mathbf{B}/B^2$, the polarization velocity is $\mathbf{v}_{pi} = (1/\omega_{ci})\mathbf{b} \times (\partial_t + \mathbf{v}_i \cdot \nabla)\mathbf{v}_i$, and the Pedersen velocity is $\mathbf{v}_{\nu i} = (\nu_{in}/\omega_{ci})\mathbf{b} \times \mathbf{v}_i$. The charge conservation equation then takes the form:

$$\nabla_\parallel (n v_{\parallel e}) = \frac{1}{\omega_{ci}} \nabla_\perp \cdot \left[n\mathbf{b} \times (\partial_t + \mathbf{v}_i \cdot \nabla + \nu_{in}) \mathbf{v}_i \right]. \tag{3.15}$$

Note that the $\mathbf{E}\times\mathbf{B}$ velocity doesn't contribute to the current due to the electrons producing an equal and opposite $\mathbf{E}\times\mathbf{B}$ current. I now employ the approximation $\mathbf{v}_i \sim \mathbf{v}_E$ to Eq. 3.15. This approximation wasn't appropriate of course for Eq. 3.14 due to the fact that $\mathbf{v}_E$ doesn't contribute to the current, but it is appropriate here. Then,

$$\nabla_\parallel(nv_{\parallel e}) = \frac{1}{\omega_{ci}}\nabla_\perp\cdot[n\mathbf{b}\times(\partial_t+\mathbf{v}_E\cdot\nabla+\nu_{in})\mathbf{v}_E]\rightarrow \tag{3.16}$$
$$\nabla_\parallel(nv_{\parallel e}) = -\frac{m_i}{eB^2}\nabla_\perp\cdot[n\mathbf{b}\times(\partial_t+\mathbf{v}_E\cdot\nabla+\nu_{in})\nabla_\perp\phi]\,.$$

Next, defining the vorticity as $\varpi\equiv\nabla_\perp\cdot(n\nabla_\perp\phi)$, the vorticity equation reads,

$$\frac{\partial\varpi}{\partial t} = -\mathbf{v}_E\cdot\nabla_\perp\varpi - \nabla_\perp\mathbf{v}_E:\nabla_\perp(n\nabla_\perp\phi) - \frac{eB^2}{m_i}\nabla_\parallel(nv_{\parallel e}) - \nu_{in}\varpi. \tag{3.17}$$

Finally, the term with the tensor product can be rewritten in a different form [PUC10a]:

$$\frac{\partial\varpi}{\partial t} = -\mathbf{v}_E\cdot\nabla_\perp\varpi + \frac{1}{2}(\mathbf{b}\times\nabla_\perp n)\cdot\nabla_\perp\mathbf{v}_E^2 - \frac{eB^2}{m_i}\nabla_\parallel(nv_{\parallel e}) - \nu_{in}\varpi. \tag{3.18}$$

3.4 Minimizing the Equation Set for LAPD Parameters

3.4.1 The Reduced Equations

The continuity equations 3.2 for electrons and ions do not have to both be used due to the quasi-neutrality condition $n_e = n_i \equiv n$. So, if one focuses on the electron continuity equation, then,

$$\frac{\partial n}{\partial t} = -\nabla\cdot(n\mathbf{v}_e). \tag{3.19}$$

Now, $\mathbf{v}_e = \mathbf{v}_{\perp e} + v_{\parallel e}$, where $\mathbf{v}_{\perp e} = \mathbf{v}_E + \mathbf{v}_{de} + \mathbf{v}_{pe}$, with the diamagnetic velocity $\mathbf{v}_{de} = \frac{\mathbf{b}\times\nabla p_e}{en_eB}$, which wasn't included for the ions in Eq. 3.14 due to the neglect of ion pressure. To a good approximation, the electron polarization velocity is smaller than the $\mathbf{E}\times\mathbf{B}$ velocity, so that $\nabla\cdot(n\mathbf{v}_{\perp e}) = \mathbf{v}_E\cdot\nabla n$ [PUC10a, SC03]. So, the continuity equation reads

$$\frac{\partial n}{\partial t} = -\mathbf{v}_E\cdot\nabla n - \nabla_\parallel(nv_{\parallel e}). \tag{3.20}$$

Next, the momentum equations (Eq. 3.3), of which there are six (three for electron velocity components and three for ion velocity components) are reduced to two here. The first is the vorticity equation (Eq. 3.18), in which I used the perpendicular momentum equations to derive it. The second is the equation for the parallel electron momentum. I neglect the parallel ion momentum equation since $v_{\|e} \gg v_{\|i}$ for LAPD. This eliminates ion sound waves from the model. The electron parallel momentum equation is then

$$nm_e \frac{\partial v_{\|e}}{\partial t} = -nm_e \mathbf{v}_E \cdot \nabla v_{\|e} - \nabla_\| p_e - enE_\| - 0.71 n \nabla_\| T_e - 0.51 m_e n \nu_e v_{\|e}, \quad (3.21)$$

where the viscous terms have been neglected. The conservation of energy equations (Eq. 3.6) are left. Since the ion temperature in LAPD is very low ($T_i \leq 1$ eV), the ion energy equation is neglected. The electron energy equation is [SC03]

$$\begin{aligned} \frac{3}{2} n \frac{\partial T_e}{\partial t} = &-\frac{3}{2} n \mathbf{v}_E \cdot \nabla T_e - p_e \nabla_\| v_{\|e} + 0.71 T_e \nabla_\| (n v_{\|e}) \\ &+ \nabla_\| (\kappa_{\|e} \nabla_\| T_e) + 0.51 m_e n \nu_e v_{\|e}^2 - 3 \frac{m_e}{m_i} n \nu_e T_e, \end{aligned} \quad (3.22)$$

where $\kappa_{\|e} = 3.16 \frac{n T_e}{m_e \nu_e}$.

3.4.2 The Electrostatic Justification

Plasma currents create magnetic fields in plasmas. The perturbed magnetic fields due to the perturbed currents that travel along or across the guiding magnetic field are Alfvén waves. Drift waves that carry a magnetic component are called drift-Alfvén waves. Often times, analytic and numerical calculations of plasma waves and turbulence neglect the time dependent magnetic field perturbations, focusing only on the electrostatic contribution to the waves, turbulence, and transport. In the reduced fluid equations of the previous subsection, the magnetic perturbation enters in two important ways. First, it enters the electric field term of Eq. 3.21 because $E_\| = -\nabla_\| \phi - \frac{\partial A_\|}{\partial t}$, where $A_\|$ is the parallel component of the vector potential. Second, it affects the parallel gradient operator, $\nabla_\| = \mathbf{b} \cdot \nabla$ where $\mathbf{b}$

is in the direction of the total magnetic field [SC03]. In the electrostatic limit, $A_\parallel \to 0$, so $E_\parallel = -\nabla_\parallel \phi$ and $\nabla_\parallel = \mathbf{b}_0 \cdot \nabla$. I take this limit in the remaining chapters, but how justified am I to do so?

As a first step in answering this question, examine Eq. 3.21. The four independent variables, $n, \phi, v_{\parallel e}$, and T_e, which each have their own evolution equation, are all present in Eq. 3.21. Taking the parallel projection of Eq. 3.12 gives

$$\nabla_\perp^2 A_\parallel = -\mu_0 j_\parallel = \mu_0 n e v_{\parallel e}. \tag{3.23}$$

So $A_\parallel \sim \mu_0 n e L_\perp^2 v_{\parallel e}$, where $\nabla_\perp^2 \sim 1/L_\perp^2$. Then, Eq. 3.21 can be approximately rewritten as,

$$n m_e \frac{dv_{\parallel e}}{dt} \sim -T_e \nabla_\parallel n + e n \nabla_\parallel \phi + \mu_0 e^2 n^2 L_\perp^2 \frac{\partial v_{\parallel e}}{\partial t} - 1.71 n \nabla_\parallel T_e - 0.51 m_e n \nu_e v_{\parallel e}. \tag{3.24}$$

The electromagnetic induction term, ($EM = en\frac{\partial A_\parallel}{\partial t}$) is now written in terms of $v_{\parallel e}$ as $EM = \mu_0 e^2 n^2 L_\perp^2 \frac{\partial v_{\parallel e}}{\partial t}$. It can therefore be directly compared to the other terms proportional to $v_{\parallel e}$ to test for its importance. The other terms are the inertial term, $M = n m_e \frac{dv_{\parallel e}}{dt}$ and the resistive term, $R = 0.51 m_e n \nu_e v_{\parallel e}$. A common way to compare these terms is to approximate the time derivative as the ion cyclotron frequency $\frac{\partial}{\partial t} \sim \omega_{ci}$ and the perpendicular length scale as the ion sound gyroradius $L_\perp \sim \rho_s$, where $\rho_s = c_s/\omega_{ci}$. Then the ratio of the three terms (obtained by dividing each term by $eBnv_{\parallel e}$) is:

$$M : EM : R = \frac{m_e}{m_i} : \beta : \frac{0.51 \nu_e}{\omega_{ce}}. \tag{3.25}$$

It can be seen from Table 4.3.2 that in LAPD, this ratio is $1 : 3.6 : 1.5$. Thus, all three terms are of the same order with the electromagnetic term slightly larger than the other two. It seems then quite unjustified to use an electrostatic approximation.

However, estimating $\frac{\partial}{\partial t} \sim \omega_{ci}$ isn't necessarily accurate. The equation set describes drift waves and so a more proper estimate might be $\frac{\partial}{\partial t} \sim \omega_*$. Under this

approximation, the ratio is $1 : 3.6 : 70$, meaning that the resistive term is more than an order of magnitude larger than the other two; however, the approximation $\frac{\partial}{\partial t} \sim \omega_*$ is still rough and the numerical value of ω_* in Table 4.3.2 is somewhat of an estimate itself. Moreover, one could also argue with the approximation of the perpendicular length scale as the sound gyroradius. This is probably too small, in which case the electromagnetic inductance has been underestimated. While it's clear that the inertial term is probably unimportant, the inductive term could be important.

Similarly, the contribution of $\tilde{\mathbf{b}} \sim A_\parallel$ in $\nabla_\parallel$ can be approximated in a similar manner with similar inconclusive results. Without a clear separation between the resistive and inductive terms, the best way to determine the validity of the electrostatic approximation is by direct numerical calculation of the turbulence with and without the electromagnetic contributions. Therefore, I simulated an electrostatic and two electromagnetic versions of LAPD turbulence. The details of the electrostatic code are described in Chapter 4 and in Appendix A.

The only difference between the electrostatic and the first electromagnetic simulation is the presence of the electromagnetic term $en\frac{\partial A_\parallel}{\partial t}$ in the parallel electron momentum equation (Eq. 3.21). Of course the Maxwell equation (Eq. 3.12) must also be included for the electromagnetic simulation. The second electromagnetic simulation includes not only the electromagnetic induction term but also the $A_\parallel$ contribution to $\nabla_\parallel$ in the parallel electron momentum equation.

Now, turbulence is best characterized and compared in a statistical and often spectral manner. More details of turbulence characterization and comparison will be discussed later, but for now, I make a few statistical comparisons between the electrostatic and electromagnetic simulation results. Figure 3.1 shows the results of the three simulations as well as the experiment – namely, a comparison of the frequency spectra, the probability distribution function (pdf), and the RMS level of the density fluctuations. The "Full Electromagnetic" curves are from the sim-

ulation including the $A_\parallel$ contribution to $\nabla_\parallel$, while the "Electromagnetic" curves just include the $A_\parallel$ contribution to $E_\parallel$. Clearly, the fluctuations are statistically similar in all cases and none of the simulations are inconsistent with the experiment. However, the electromagnetic effects are noticeable, and as I include more electromagnetic contributions in the simulations, the turbulent statistics more closely resemble those of the experiment. I make no quantitative comparison here, but rely only on a visual examination in making this conclusion.

Now, as mentioned above, I do not include any electromagnetic contributions in the simulations used in the following chapters. It seems rather unjustified to do so since I am clearly able to run electromagnetic simulations and they seem to reproduce experimental turbulence with slightly better accuracy than the electrostatic ones. One justification for my abandonment of electromagnetic simulations, however, is that electromagnetic simulations take a bit longer than electrostatic ones due to the extra relation in Eq. 3.12 that is used to solve for $A_\parallel$, which requires an inversion of the Laplacian. This takes extra computation. Another justification is that the electromagnetic equations make the energy dynamics analysis in Chapter 6 a bit more complicated. Both of these factors are mitigated, however, if the inertial term $nm_e\frac{dv_{\parallel e}}{dt}$ is dropped. Nevertheless, at the beginning of this work, I strived to find the simplest possible model to describe the turbulence in LAPD, and I determined that the electrostatic approximation was acceptable. At that time, I didn't have the results of Fig. 3.1. If I had the time, I would redo all of the simulations and analysis to include electromagnetic contributions, but drop the inertial term in Eq. 3.21. This is a clear route to take for future work. Nevertheless, I am confident that electromagnetics would not change any of my conclusions in this work. So for the remainder of this work, I will present theoretical calculations, simulation results, and conclusions using the electrostatic approximation.

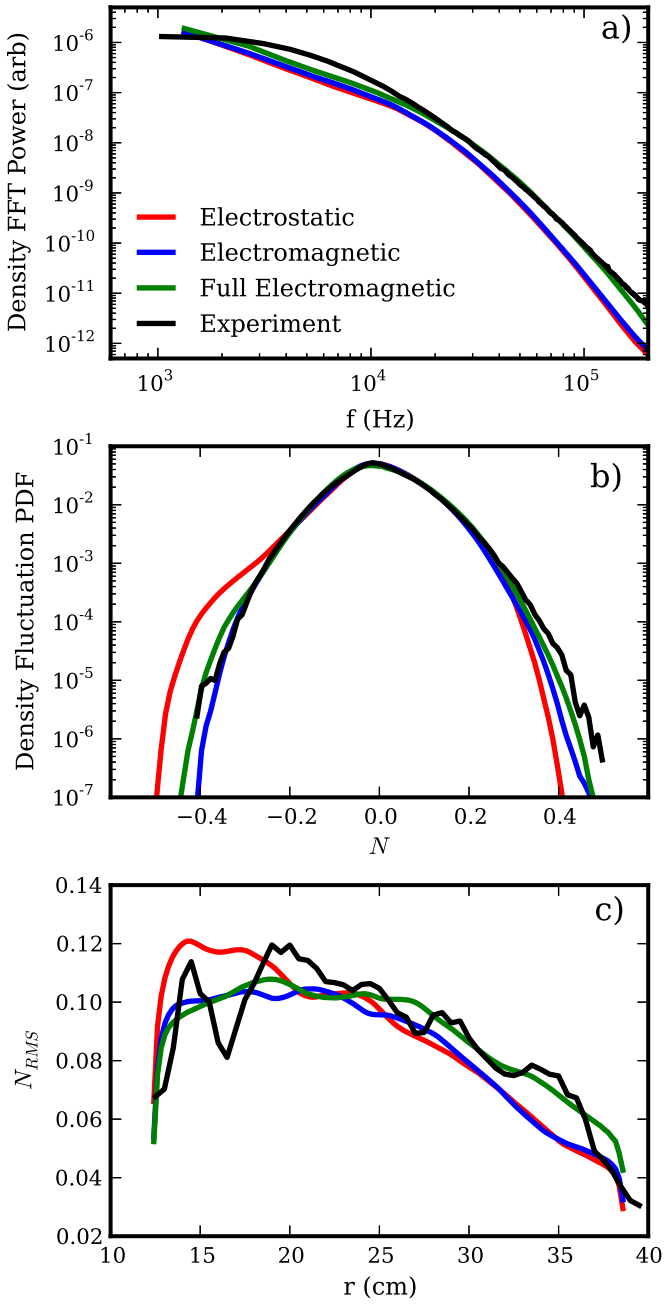

Figure 3.1: Statistical comparisons of turbulent electrostatic and electromagnetic simulations to each other and to the experiment

CHAPTER 4

Simulation and Experiment Details

I simulate the model equations using the BOUT++ code [DUX09], which I describe in Appendix A. There I discuss the nitty gritty aspects of the code and the specific numerical routines that I use. In this chapter, I state and explain the equations, boundary conditions, parameters, and profiles that I use in the LAPD simulations through a purely physics perspective. In all of the simulations hence forth (except for those in Appendix B), I use the same equations, parameters and profiles. I change only the axial boundary conditions between simulations, which I will discuss in Sec. 4.2. My goal is to simulate one particular LAPD experiment that I describe in Sec. 4.3 and fully analyze it, so I use only a single set of profiles and parameters. Scaling and sensitivity studies are beyond the scope of this work. Therefore, in this chapter, I explain all details of the model that I use to simulate and study the one particular experimental system.

4.1 The Equations

I use the Braginskii equations from Chapter 3 to model the LAPD turbulence. I separate all variables into time-independent equilibrium parts and time-dependent fluctuating parts so that I may use experimental time-independent profiles as input. This is called a Reynold's decomposition [McD04]. The alternative is to solve the full equations with no equilibrium/fluctuation separation and no experimental profile input. The difficulty in this is the need to specify realistic sources, sinks, and boundary conditions, which can be difficult to measure or estimate. This al-

ternative method has been undertaken by Rogers and Ricci [RR10]. My approach is easier to implement, and since the time-independent profiles are so important in driving the turbulence, inputting the experimentally measured profiles helps produce physically realistic turbulence. Because of my equilibrium/fluctuation separation technique, I can linearize the equations, keeping only one nonlinearity in each equation: the advective nonlinearity. While this isn't necessary, it does simplify the energy dynamics as formulated in Chapter 6. The justification is practical rather than mathematical, and the partially linearized equations produce fluctuations that are quite statistically similar to experimental fluctuations, which is shown in Chapter 5, so I feel justified in doing this.

In the equations below, all variables are dimensionless. I normalize all times to the inverse ion cyclotron frequency $\omega_{ci} = \frac{eB}{m_i}$, velocities to the ion sound speed $c_s = \sqrt{\frac{T_e}{m_i}}$, lengths to the sound gyro-radius $\rho_s = c_s/\omega_{ci}$, potentials to T_e/e, densities and temperatures to the density and temperature at the radial cylindrical axis. I take quantities such as c_s to be constant in these normalizations even though such quantities are radially dependent because of the radial dependence of their constitutive parts, i.e. the electron temperature. To calculate these constants, I take the values of their constitutive parts at the radial axis. The equations below appear the same whether or not the normalizations are constant or functions of radius, but the transport coefficients in the code do depend on this choice. Thus, the LAPD simulation equations are as follows:

$$\partial_t N = -\mathbf{v_E} \cdot \nabla N_0 - N_0 \nabla_\parallel v_{\parallel e} + \mu_N \nabla_\perp^2 N + S_N + \{\phi, N\}, \tag{4.1}$$

$$\partial_t v_{\parallel e} = -\frac{m_i}{m_e}\frac{T_{e0}}{N_0}\nabla_\parallel N - 1.71\frac{m_i}{m_e}\nabla_\parallel T_e + \frac{m_i}{m_e}\nabla_\parallel \phi - \nu_e v_{\parallel e} + \{\phi, v_{\parallel e}\}, \tag{4.2}$$

$$\partial_t \varpi = -N_0 \nabla_\parallel v_{\parallel e} - \nu_{in}\varpi + \mu_\phi \nabla_\perp^2 \varpi + \{\phi, \varpi\}, \tag{4.3}$$

$$\partial_t T_e = -\mathbf{v_E} \cdot \nabla T_{e0} - 1.71\frac{2}{3}T_{e0}\nabla_\parallel v_{\parallel e} + \frac{2}{3N_0}\kappa_{\parallel e}\nabla_\parallel^2 T_e$$
$$-\frac{2m_e}{m_i}\nu_e T_e + \mu_T \nabla_\perp^2 T_e + S_T + \{\phi, T_e\}. \tag{4.4}$$

Note that the advective nonlinearities in each equation appear as the Poisson

bracketed terms. Additionally, the only equilibrium profiles are N_0 and T_{e0}, which are only functions of radius. $\phi_0 = v_{\parallel e0} = 0$ in these equations. The linearized vorticity is $\varpi = \nabla_\perp \cdot (N_0 \nabla_\perp \phi)$. $N, v_{\parallel e}, \phi$, and T_e are fluctuating first-order quantities. These equations contain some terms not found in the equations of Chapter 3. First, there are the density and temperature sources S_N and S_T. I leave out momentum sources as well as the contribution of the density source to changes in the momentum and temperature. Second, I have included diffusive ($\mu_N \nabla_\perp^2 N$ and $\mu_T \nabla_\perp^2 T_e$) and viscous ($\mu_\phi \nabla_\perp^2 \varpi$) terms in Eqs. 4.1, 4.4, and 4.3 respectively.

4.1.1 Sources

The density source is actually a source/sink. It models both the ionization of neutral atoms as well as the recombination of ions and electrons. The sink action in LAPD is dominated by parallel (along $\mathbf{B}$) losses to materials at the machine ends because the magnetic field prevents rapid radial loss. It's also possible that a layer of neutral atoms near the end of the machine opposite the cathode cools the plasma enough so that recombination can be strong in this layer. The sink action occurs at all radii with finite plasma density, which constitutes regions both inside and outside of the limiter radius due to radial ion transport. If the sink action is primarily at the end plates, the sink can be calculated by $2 n_{se} c_s / L_\parallel$, where n_{se} is the density at the sheath edge in front of the end plate, c_s is the sound speed at the sheath edge, and the factor of 2 accounts for the two plates. n_{se} and c_s are functions of radius such that the sink is strongest at the cylindrical axis and decreases at larger radii. Calculation of the sink term requires knowledge of the density and temperature at the end of the machine, which is generally not measured experimentally.

The ionization source is strongest from the cylindrical axis out to the limiter radius. The source term may be calculated with $n_e n_n \langle \sigma v \rangle_{iz}$, where n_n is the neutral Helium density and $\langle \sigma v \rangle_{iz}$ is the ionization rate of Helium and is a strong

function of temperature. Because the primary electrons that boil off the cathode contribute significantly to the source, and the plasma temperature falls off outside of the limiter radius, ionization is restricted primarily to inside of the limiter radius. Ionization rates are readily available [Sta00], but the neutral density is not, making the source difficult to calculate. However, it is clear that if one were to sum up the source and sink and integrate axially, the region inside of the limiter radius must be a net source, while the region outside of it must be a net sink.

When I simulate the turbulence in LAPD without the source terms, turbulence drives radial transport such that the total flux-surface-averaged density gradient relaxes over time as seen in Fig. 4.1 a) until the radial transport ceases. One may notice that $\langle N_t \rangle_{fs} = \langle N_0 + N \rangle_{fs}$ doesn't become totally flat, but maintains a finite gradient. This is a result of the turbulent transport ceasing. Normally, however, when there is no turbulent transport, classical transport will further relax the gradient, but because I partial linearize the equations, specifically the diffusion term $\mu_N \nabla_\perp^2 N$, I prevent classical transport of the total density. Nevertheless, the strong profile relaxation is not physical because of the experimentally present source/sink mechanism, and when I include such a mechanism, the classical transport of the total density isn't significant.

Now, rather than developing a first principles source based on the theoretical source/sink expressions, I use ad hoc controlling sources. I estimate that $\langle N_t \rangle_{fs}$ remains relatively constant over time, and model the source using the integral portion of a PID controller. This means that I write an equation for the source:

$$\partial_t S_n = - \langle N \rangle_{fs} . \tag{4.5}$$

Therefore,

$$S_n(t) = - \int_0^t \langle N(\tau) \rangle_{fs} \, d\tau. \tag{4.6}$$

I show a typical time-averaged density source in Fig. 4.1 b). After a long enough time, the source reaches a quasi-steady state, making it somewhat physically

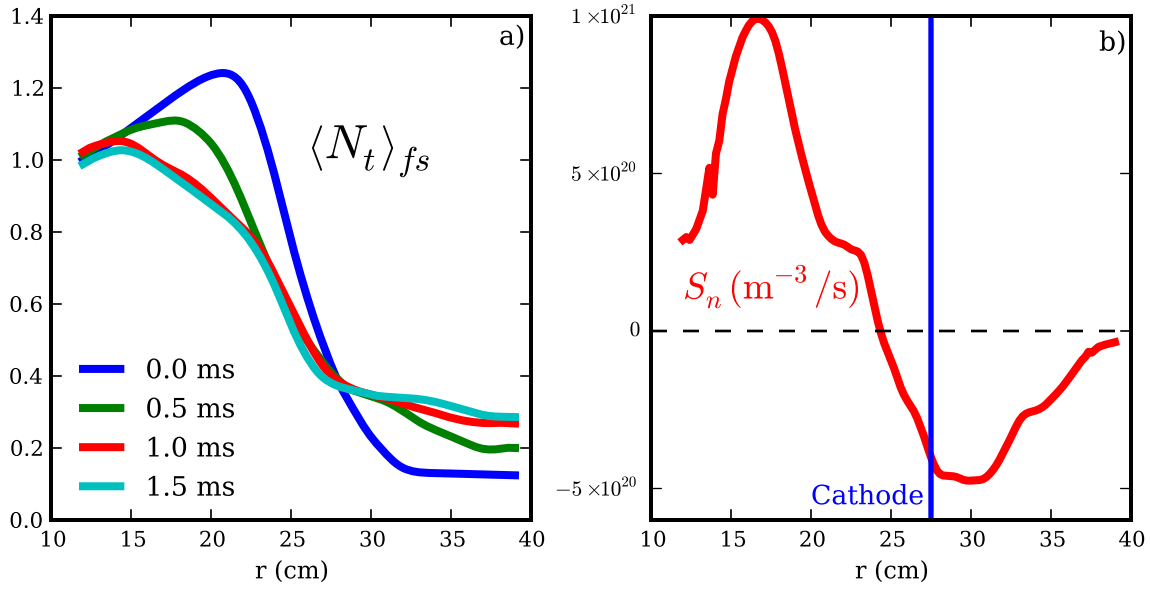

Figure 4.1: Sourceless profile relaxation and an evolved ad-hoc density source

realistic. The result is that $\langle N_t(t) \rangle_{fs} \simeq N_0$, but there is freedom for $\langle N_t(t) \rangle_{fs}$ to undergo some relaxation and buildup. Moreover, notice that the source in Fig. 4.1 b) is net positive inside of the cathode radius and negative outside of it, just as one would expect. I use the same method for the temperature source. The temperature source ultimately comes from the hot electrons that are boiled off of the cathode, which transfer their energy to the plasma through collisions. This heat transfer is mostly to the electrons of the plasma. The temperature sink is caused by collisions with ions and neutrals which line radiate and by heat loss to the sheath and end walls.

I emphasize that the sources are not first principle sources. They are constructed based on the simulated radial transport. The alternative first principle's approach was used by Rogers and Ricci for LAPD [RR10]. They use a stationary top-hat-like ionization source that models the physical density-producing process in LAPD. Furthermore, they do not separate equilibrium from fluctuations or in-

put equilibrium profiles. Their source feeds the density, which then transports itself until it comes to a quasi-equilibrium state (a sink is also present). This method solves for the full plasma state with very little experimental input. They input the sources and derive the plasma state. On the other hand, I input part of the plasma state and derive the sources. As I indicated before, my method has the advantage of using experimentally measured profiles. This experimental input allows me to more easily simulate turbulence that resembles that in the experiment, and therefore make conclusions on the fluctuation properties. I do not, however, evolve the equilibrium and gain the knowledge that comes from that.

Before I go on, I note that in the past, Pavel Popovich and I tried a number of different approaches to the source problem. One approach was to simply remove the flux-surface-averaged fluctuating density and temperature components at each time step. While similar to the technique I describe above, it cuts off of the flux-surface-averaged fluctuating components quicker because it doesn't preserve past history of the source. Another technique that we used was to derive a source like that in Fig. 4.1 b) in one simulation, and then start another simulation using that as a purely time-independent source. This supplied a slower cutoff of the flux-surface-averaged fluctuating components than the other two methods. Results of the evolution of the total density profile can be seen in Popovich et al. [PUC10b]. In any case, we didn't find any significant difference in the results when using these different source methods. While it's the most physically realistic, the time-independent source technique is just too slow to implement due to the need to run two simulations, so I do not generally use it. I prefer the PID source in general, and all simulations in this paper use it. Furthermore, I generally implement a condition with the PID source so that it does not drive the total density or temperature negative as I discuss in Appendix A.

4.1.2 Artificial Diffusion and Viscosity

Artificial diffusion or hyperdiffusion terms are ubiquitous in fluid simulations. They are generally intended to prevent high frequency or high wavenumber ringing caused by numerical advection schemes at steep interfaces. They can, however, cause unphysical smoothing in systems that are non-diffusive and non-viscous or cause over-smoothing if applied haphazardly. Some numerical advection schemes contain their own diffusion, called numerical diffusion. Other non-advective finite difference schemes also contain numerical diffusion or dispersion.

I use artificial diffusion and viscosity for several reasons. The first is to prevent artificial high-wavenumber oscillations due to the Arakawa advection scheme that I use [Ara66]. Second, it smooths out the solutions, preventing the total density and temperature from becoming negative at any point in space, which is obviously unphysical. Third, I can use it to prevent the need to go to very fine grid spacing at which physical diffusion and viscosity are important. Finally, I can use it to help saturate the turbulence at levels consistent with experiment. These reasons are all somewhat related, and I note that I performed an artificial diffusion and viscosity sensitivity study in Ref. [FUC12].

Diffusion and viscosity are real effects that are present in the non-reduced Braginskii equations. In Chapter 3, I made the approximation that $\nabla \cdot (n\mathbf{v}_{\perp e}) = \mathbf{v}_E \cdot \nabla n$, which neglected the polarization velocity part of $\mathbf{v}_{\perp e}$. However, the "full polarization velocity" [SC03] (from crossing Eq. 3.3 with $\mathbf{b}$ and neglecting the stress tensor) is

$$\mathbf{v}_{pe} = (1/\omega_{ce}) \left[\frac{d(\mathbf{b} \times \mathbf{v}_{\perp e})}{dt} + \nu_e \mathbf{b} \times \mathbf{v}_{\perp e} - \nu_e \mathbf{b} \times \mathbf{v}_{\perp i} - \frac{3}{2} \frac{\nu_e}{m_e \omega_{ce}} \nabla_\perp T_e \right]. \quad (4.7)$$

The part of this that causes collisional diffusive terms is $(\nu_e/\omega_{ce})\mathbf{b} \times \mathbf{v}_{\perp e}$. Since this term contains $\mathbf{v}_{\perp e}$ itself, closure necessitates that it be approximated as $\mathbf{v}_{\perp e} = \mathbf{v}_E + \mathbf{v}_{de}$. Only the diamagnetic drift part is important for the collisional diffusion, so the part of the polarization velocity that I focus on is $(\nu_e/\omega_{ce})\mathbf{b} \times \mathbf{v}_{de}$. Recall

that I want to use this in the continuity equation, so I am interested in the term $\nabla \cdot (n_e v_e) \rightarrow \nabla \cdot (n_e(\nu_e/\omega_{ce})\mathbf{b} \times \mathbf{v}_{de}) = -\nabla \cdot \frac{\nu_e m_e}{e^2 B^2} \nabla_\perp p_e$. Now defining $D = \frac{\nu_e m_e T_e}{e^2 B^2}$, I have $\nabla \cdot (n_e v_e) = -\nabla \cdot (D \nabla_\perp n)+$ lots of other terms. D is the classical diffusion coefficient, which is about $0.01\text{m}^2/\text{s}$ for LAPD parameters. One of the terms in $\nabla \cdot (D\nabla_\perp n)$ is $D\nabla_\perp^2 n$, which has the same form of the artificial diffusion term that I've added to Eq. 4.1. Of course, I have neglected many terms of the same order as this term in Eq. 4.1, but this shows that such a classical diffusion term is present in the Braginskii equations.

A similar treatment can be used for the energy conservation equation (Eq. 3.6), using the same procedure as for the continuity equation but with the $p_e \nabla \cdot \mathbf{v}_e$ term in Eq. 3.6. The result is $p_e \nabla \cdot \mathbf{v}_e = D n_e \nabla_\perp^2 T_e +$ lots of other terms. This has the same form as the temperature diffusion term in Eq. 4.4.

The viscosity in the vorticity equation comes from the ion stress tensor term $\frac{\partial \Pi_{i\alpha\beta}}{\partial x_\beta}$ that I neglected when deriving the vorticity equation because I neglected everything with finite ion temperature. If I had included this, a vorticity diffusion term (aka a viscosity) would have been appeared in the vorticity equation [PUC10b] as it is in other equation sets like the well-known Hasagawa-Wakatani equations [HW83]. The magnetized Braginskii viscosity coefficient is $\eta_1^i = \frac{3nT_i}{10\omega_{ci}^2 \tau_i}$, which is about 2×10^{-8} kg/m $\cdot$ s for LAPD. Since LAPD's ions are not necessarily magnetized due to the fact that $\omega_{ci}\tau_i \sim 1$, the unmagnetized ion viscosity is $\eta_0^i = 0.96 n T_i \tau_i$ [Bra65] which is about 4×10^{-7} kg/m $\cdot$ s.

For the artificial diffusion and viscosity coefficients in Eqs. 4.1-4.4, I use a single value of 1.25×10^{-3} – in normalized units – which is 0.075 m^2/s in real units. I find that this value produces turbulent fluctuation levels consistent with experimental levels. I use this as a free parameter in this sense. This value is much larger than the real classical diffusion D, but is smaller than $\frac{\eta_1^i}{n m_i} = 1\ \text{m}^2/\text{s}$. Nevertheless, I neglected a number of terms in Eqs. 4.1-4.4 such that there isn't justification to use the real diffusion and viscosity in these equations. Artificial

diffusion and viscosity terms, however, serve a numerical purpose.

4.2 Boundary Conditions

Boundary conditions are often difficult to determine in plasma devices. While the properties of the boundaries are usually known, the way that the plasma interacts with them can be complex. Plasma boundary physics is one of the main elements of present day fusion research [Sta00]. Often times there is uncertainty in the equations that need to be used in simulations, and once the equations are found, they can be difficult to implement in codes.

The boundary conditions in LAPD are difficult to determine. LAPD contains at one end, a hot emitting cathode behind a biased mesh anode. In front of the anode are biasable azimuthal limiters with radius about equal to the cathode radius, though the limiter radius may be changed [SCR12]. The far end contains a floating mesh plate. The cylinder is conducting and has a radius about 20 cm larger than the cathode radius. Rather than attempting to model all of these complex boundaries, I use a few simple boundary conditions, leaving the more physical modeling for future research.

4.2.1 Simple Boundaries

In all simulations, I use an annulus rather than a cylinder. Although the inner radius of the annulus may be arbitrarily small, I take the inner radius to be 12 cm. I take the outer radius to be 39 cm. This is the radial extent of the experimental probe measurements, so I don't have experimental information beyond these boundaries. Anyhow, the plasma fluctuations are nearly zero (when normalized to values at the cylindrical axis) outside of this annular region – as seen in Fig. 3.1 c). Therefore, I set the radial boundaries on all of the fluctuating variables ($N, \phi, v_{\|e}$, and T_e) to zero. It would be nice in the future to take data

spanning at least a few more cm and extend the simulation domain accordingly. But for now, the results use such an annular domain.

As for the axial boundaries, I use four different boundary conditions: periodic, zero-value (Dirichlet), zero-derivative (Neumann), and Bohm sheath. The only non-trivial one, Bohm sheath, is derived and described below. The others are all trivial to implement. Using the different trivial axial boundary conditions tests how important these boundaries are in controlling the nature of the turbulence.

4.2.2 Bohm Sheath Boundaries

Cold Bohm sheath boundary conditions are applicable when a plasma terminates at a conducting plate. I note that this is not necessarily the case in LAPD. The cathode/anode system is obviously much different from a simple floating or biased conducting plate. Furthermore, the mesh wall at the far end is not a solid wall. Moreover, it's not clear if the plasma is even attached to the far end mesh wall or if it becomes detached in the neutrals in front of it, where the plasma cools and recombines before interacting with the wall. In any case, it is still instructive to apply such an idealized boundary condition to LAPD because it is somewhat more realistic than the simpler boundary conditions, and it creates a new linear instability (see Sec. 5.1.2), which can be used to test the robustness of LAPD's nonlinear instability. Thus, here I derive a model for the Bohm sheath boundary condition.

To start, I note that a plasma bounded by a wall can be divided into two regions: the main plasma and the Debye sheath [Sta00]. The Debye sheath is a small region adjacent to the wall, generally several Debye lengths long. It has a net positive charge ($n_i > n_e$) that shields the negative charge on the wall. The sheath does not completely shield the negative wall, however, and a small electric field penetrates into the main plasma (the ambipolar field), which mostly serves to

accelerate the cold ions toward the wall, and slightly retard the electrons before entering the sheath. In the main plasma, the quasi-neutrality relation holds: $n_i = n_e$.

The well-known Bohm criterion along with other considerations restricts the ions to move into the sheath entrance at the sound speed $c_s = \sqrt{T_e/m_i}$. I consider here the case where there is no external biasing; in other words, the end plates are electrically isolated and floating. The wall can be set to an arbitrary potential, say $\phi_w = 0$, while the potential at the sheath entrance is then the positive floating potential ϕ_{sf}. This potential difference across the sheath reflects slow electrons that enter the sheath. The electrons approximately maintain a cutoff Maxwellian velocity distribution throughout the sheath, and at the wall, their velocity is retarded by a Boltzmann factor due to the floating potential. In total, the current to the wall is [BRT91, BCR93, XRD93]

$$J_\parallel = \pm en \left[c_s - \frac{(T_e/m_e)^{1/2}}{2\sqrt{\pi}} e^{\left(-\frac{e\phi_{sf}}{T_e}\right)} \right], \tag{4.8}$$

where the $\pm$ indicates that the plasma flux goes into the wall, which is in different directions for the different end plates. Note that there is a factor of $\sqrt{2}$ discrepancy between different reports on the expression used for the thermal velocity, which should have only a minor consequence. In this expression, all values are total (equilibrium + fluctuations).

To proceed, note that Eq. 4.8 is not only the current to the wall, but also the current going into the sheath edge, since the sheath is too small for there to be appreciable radial current loss or an ionization source within the sheath. All values, in fact, are taken to be those at the sheath edge. Furthermore, since the wall is electrically isolated, the equilibrium current at the wall vanishes. This sets the value for the floating potential to be $\phi_{sf} = \Lambda T_{e0}/e$ with $\Lambda = \ln\left(\frac{1}{2\sqrt{\pi}}\sqrt{\frac{m_i}{m_e}}\right)$. And since T_{e0} is a function of radius, ϕ_{sf} is also a function of radius. Thus, a radial temperature gradient produces a radial electric field, at least at the sheath edge

and likely penetrating axially into the main plasma. I acknowledge that $J_\parallel$ need not vanish on every field line since the end plates are conducting and charges can move around on the plate, however, the vanishing equilibrium current is generally a fair approximation [BCR93].

On the other hand, the fluctuating component of the current is allowed to vary between field lines. The first order fluctuating component is obtained by linearizing Eq. 4.8, giving the result:

$$J_\parallel = \pm e N_0 c_{s0} \left[\frac{e\phi}{T_{e0}} - \Lambda \frac{T_e}{T_{e0}} \right], \tag{4.9}$$

where now, $J_\parallel, \phi$ and T_e are fluctuating components, consistent with previous notation. This expression for the current sets the fluctuating axial boundary condition of the plasma and is often called the Bohm Sheath boundary condition. This current condition holds both at the wall and at the sheath entrance. So rather than taking the simulation domain all the way to the wall, simulations often end at the sheath entrance and employ this analytically derived boundary condition to the boundaries of the main plasma. Then one doesn't have to worry about the small spatial scales and the non-quasineutrality of the sheath. The corresponding boundary conditions for the other fluid variables such as the density and temperature have recently been derived by Loizu et al. [LRH12]. However, I simply take them to have zero-gradient – as most others have done – which isn't wholly inconsistent with Loizu's calculations.

Now while one may set the parallel current (or equivalently $v_{\parallel e}$) at the axial boundaries to the quantity on the right hand side of Eq. 4.9, I don't do that. I use Ohm's Law ($-\nabla_\parallel \phi = \eta_\parallel J_\parallel$) to set the boundary condition for the gradient of ϕ. I do this for practical reasons in the coding. Therefore, the boundary condition used in the code is (in our normalized units):

$$\nabla_\parallel \phi = \pm \frac{\nu_e m_e}{m_i} \left(\phi - \Lambda T_e \right). \tag{4.10}$$

4.3 Profiles and Parameters

4.3.1 The LAPD Biasing Experiment

As stated above, I take all equilibrium profiles and parameters from experimental measurements on one particular experiment. In this experiment, limiter biasing was used to essentially null out the mean radial electric field [SCR12]. I simulate this experiment so that I can neglect the mean potential profile in the equations (as is done in Eqs. 4.1-4.4), which simplifies the analysis.

In fact, in the experiment to which I refer, Schaffner et al. [SCR12] did not just produce a plasma state with a null radial electric field – zero azimuthal mean flow – but they produced many plasmas with varying mean flow and flow shear. In order to vary the $\mathbf{E} \times \mathbf{B}$ flow, they inserted a biasable azimuthal limiter into LAPD. The limiter had radius 26 cm, and could be biased with respect to the cathode. To understand why such a setup produced varying flow and flow shear, recall my discussion of the sheath in Sec. 4.2.2 where I described how the plasma potential is set by the current into the boundary plates and the temperature profile. I specifically considered the case for a floating conducting plate, in which, $\phi = \Lambda T_e/e$, with $\Lambda = \ln\left(\frac{1}{2\sqrt{\pi}}\sqrt{\frac{\mathrm{m_i}}{\mathrm{m_e}}}\right)$, where ϕ is the potential difference between the sheath edge and the conducting plate. Note that this relation holds not only at the sheath edge, but also in the main plasma [Sta00]. The situation in the biasing experiment is more complicated than this because there is not a single plate – there is both the cathode and the limiter – and the plates are not generally floating but are drawing currents. If a plate is drawing a current, the proportionality factor relating ϕ and T_e is different and not necessarily constant:

$$\Lambda(r) = \ln\left(\frac{1}{2\sqrt{\pi}}\sqrt{\frac{m_i}{m_e}}\frac{1}{1-\frac{J_\parallel}{enc_s}}\right). \tag{4.11}$$

When $J_\parallel$ is a strong function of r, the proportionality factor $\Lambda(r)$ can be a strong function of r such that ϕ does not have the same radial shape as T_e. And since the

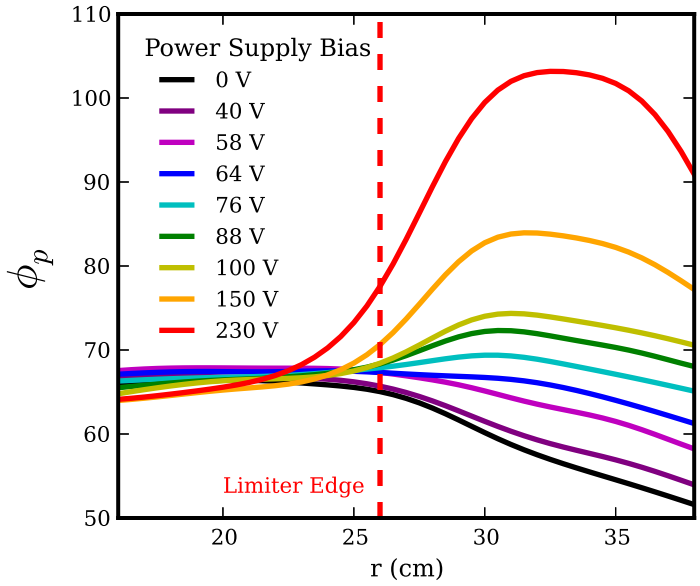

Figure 4.2: Experimentally measured mean radial potential for different limiter biases

radial derivative of ϕ is the radial electric field, which causes an azimuthal $v_{E\times B}$, the boundary currents influence the $\mathbf{E}\times\mathbf{B}$ flow and flow shear of the plasma.

In the biasing experiment, Schaffner et al. used a power supply to maintain a potential difference between the cathode and limiter, causing them to draw different currents, thus changing the plasma potential profile in accord with the above equations. I show in Fig. 4.2 the radial shape of ϕ for several different power supply voltages used in the experiment. Note the change from the unbiased state, in which the potential profile has a temperature profile-like shape to the highly biased state, where the potential profile is much different. Notice also how fine of a control over the profile that they obtained. They were able to incrementally change the flow and flow shear around the limiter edge with fine precision. I use this to my advantage in my simulations. Namely, I take the plasma state associated with the 64 V curve, in which the mean radial electric field is essentially zero for reasons

stated above. Note, then, that this is a very particular plasma state in LAPD that is not like all others. In fact, it is extreme in that it has the shallowest density gradient and the most turbulence of all of the biasing experiments [SCR12].

Before moving forward, allow me to discuss another way to see why the radial electric field changes when the cathode and limiter are biased. Picture the system as a circuit. The circuit runs from the limiter through the biasing source – maintaining a potential difference – through the cathode and finally through the plasma itself, which fills the region between the cathode and the limiter. The electrons in the plasma can carry the current along the magnetic field lines, but many of the field lines that terminate on the cathode are radially separated from the limiter field lines, so a radial current forms to complete the circuit. This radial current is primarily carried by ions. Recall from Sec. 3.3 that there are two contributions from the ions to the cross-field current: the polarization current and the Pederson current. The polarization current due to the ions, however, is

$$J_{pi} \approx en\vec{b} \times (\partial_t + \mathbf{v}_E \cdot \nabla)\, \mathbf{v}_E. \tag{4.12}$$

The time derivative term cannot contribute to the equilibrium current. Then, the radial part of the equilibrium polarization current is only

$$J_{pir} \approx \frac{en}{r} E_\theta \frac{\partial E_\theta}{\partial \theta}. \tag{4.13}$$

But there is no equilibrium E_θ, so $J_{pir} \approx 0$. It's likely that other terms that can contribute to the polarization current that I ordered out in Sec. 3.3 could produce a radial polarization current, but I do not try to derive them here. Rather, I attribute all of the equilibrium radial current to the Pederson current, which is driven by a time-independent radial electric field. Maggs et al. argued for the Pederson current as the main contributer as well [MCT07]. The radial electric field, therefore, is necessary to complete the circuit. Biasing then, through sheath properties and plasma currents, can change the radial potential profile. This, of course, produces mean azimuthal $\mathbf{E} \times \mathbf{B}$ flows that can have radial shear.

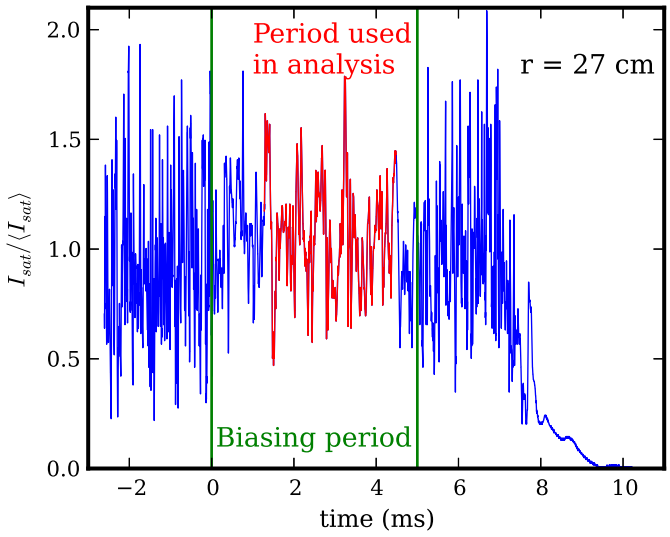

Figure 4.3: Ion saturation current time trace in the biasing experiment

4.3.2 Null Flow Profiles

In the biasing experiment, for all of the runs in which a finite power supply voltage is applied, the power supply is triggered several miliseconds after the start of the plasma discharge, which I show in Fig. 4.3. In this figure, I do not have data during the ramp-up phase of the discharge during which the density (and ion saturation current I_{sat}) grows. But I do have data before the biasing is triggered and after it is turned off, including part of the plasma after-glow phase during which the density falls rapidly. For all of my analysis, I use only the data collected during the time period from 1.5 ms after the biasing starts to 0.5 ms before the biasing ends. This produces about 3 ms of data, which is about 5000 data points. This ensures that the plasma is in a turbulent steady-state for all of my analysis.

The normalized profiles from the null flow experiment that I use in the simulations are shown in Fig. 4.4, and the parameters are tabulated in Table 4.3.2. The density profile that I use in the simulations is a polynomial fit to the experimental equilibrium density profile. The temperature profile that I use is a tanh function

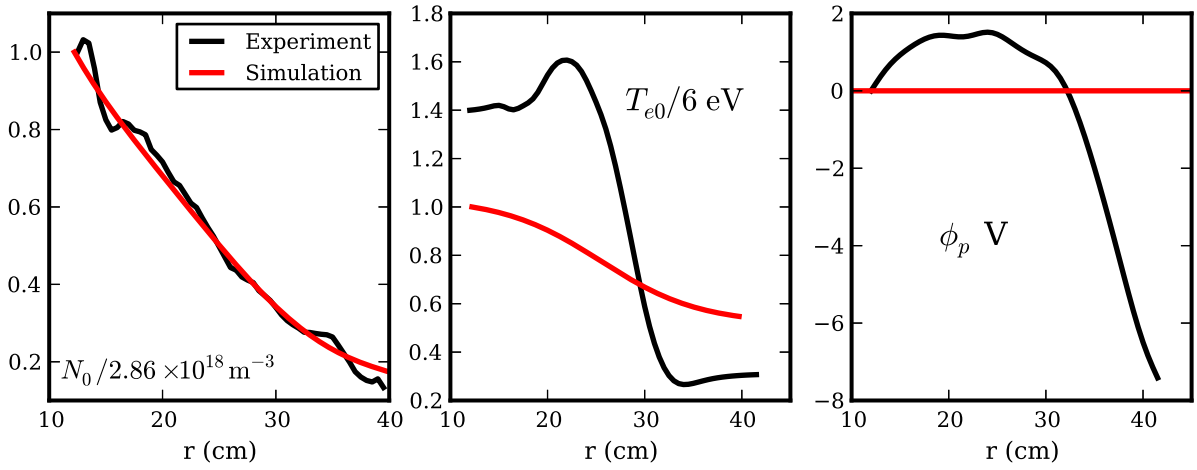

Figure 4.4: Equilibrium density, electron temperature, and potential profiles along with fits used in simulations

that does a very poor job of approximating the experimental electron temperature profile. The reason why the fit is so poor is that when I ran the simulations, I didn't have reliable temperature profile measurements, so I was forced to estimate what the profile might look like. Schaffner later reanalyzed his data to make the experimental profile in Fig. 4.4 b), but I didn't redo the simulations. Fixing this must await future study, but as I show in the following chapters, the agreement between experiment and simulation turbulence is already very good, so perhaps the temperature profile is not important in reproducing the turbulence. As for the potential, again, I use $\phi_0 = 0$, which is a good approximation for the experimental nulled out potential profile even though it does not appear so in Fig. 4.4 c) due to the compressed y-axis as compared to Fig. 4.2.

Moreover, the profiles that I use have no azimuthal or axial variation because I don't have the corresponding experimental measurements. So I assume that the equilibrium profiles are only functions of radius. It's likely, however, that there is some axial variation in the profiles and parameters. In LAPD, $\nu^* \equiv L_\parallel/\lambda_{ei} \sim 100$, which indicates that a parallel temperature gradient should exist

(depending on the locations of the sources and sinks) [Sta00]. Furthermore, if the Bohm sheath boundary condition is correct, the equilibrium potential must have a parallel gradient in order to accelerate the ions up to the sound speed at the sheath entrance. This ambipolar parallel electric field should exist between the location of the sheath entrance and an ion collision length into the main plasma – which is only about 10 cm, meaning that most of the plasma has no axial variation in the potential. The parallel electric field generated by the condition of Eq. 4.10 is not this equilibrium field. It is just the perturbed field that responds to electron temperature perturbations. So the lack of an equilibrium parallel electric field is not consistent with the Bohm Sheath boundary condition, but the high collisionality confines this effect to the very ends of the plasma column in any case.

Species	^{4}He
Z	1
n	2.86×10^{18} m^{-3}
T_e	6 eV
T_i	$\lesssim 1$ eV
B_0	0.1 T
$L_\parallel$	17 m
a	0.4 m
λ_D	10^{-5} m
ω_{ci}	2.4×10^6 rad/s
ω_{ce}	1.8×10^{10} rad/s
ρ_e	5.3×10^{-5} m
ρ_i	$\sim 1 \times 10^{-3}$ m
ρ_s	5×10^{-3} m
v_{te}	9.4×10^5 m/s
c_s	1.1×10^4 m/s
v_A	7×10^5 m/s
β	5×10^{-4}
m_e/m_i	1.4×10^{-4}
$\ln\Lambda$	11
ν_e	7.2×10^6 Hz
λ_{ei}	0.13 m
ν_i	$\sim 10^6$ Hz
ν_{in}	3×10^3 Hz
$\kappa_\parallel^e$	9.8×10^{23} eV/m^2 s
η_0^i	$\sim 10^{12}$ eV s/m^3
ω_*	$\sim 5 \times 10^4$ rad/s

Table 4.1: Plasma parameters used in LAPD simulations

CHAPTER 5

The Nature of LAPD Turbulence

Simulations can supplement experiment by providing detailed spatial data that is too difficult to obtain experimentally. This spatial data can be analyzed, revealing new properties of the experiment. In order for simulations to provide information, however, they must accurately represent the system which they model. Assessing the validity of simulations generally comes in two parts: verification and validation. Verification, the evidence that the code solves the equations correctly, will not be taken up here. I note, however, that my collaborators and I have done verification studies in the past, somewhat detailed in Popovich et al. [PUC10a]. We compared linear BOUT (the old version of BOUT++) and BOUT++ simulations to analytic solutions as well as to eigensystem solver solutions. On the other hand, I will focus parts of this chapter on our validation effort. Validation is the evidence that the simulation model accurately reproduces features of the experiment. Generally, the more features of the experiment that the model reproduces, the more valid the model. While this chapter focuses on simple analyses to describe the nature of the simulated turbulence, it will also make comparisons, where possible, to experimental data in order to show that the model is relatively well validated. First, however, I analyze the linear instabilities in the LAPD simulations, and this affords no experimental comparison.

5.1 LAPD Linear Instabilities

Linear instabilities are prevalent in plasma physics. They come from the linearization around an equilibrium of the plasma equations. Physically, if a plasma is in a time-independent steady state that is linearly unstable and a finite fluctuation of any size occurs, the fluctuation will grow exponentially. Linear instabilities often drive hydrodynamic and plasma turbulence. I therefore study the linear instabilities of the LAPD system before moving onto the turbulence because they can offer insight into the nature of the turbulence. The LAPD equations, parameters, and profiles described in Chapter 4 give rise to a couple of linear instabilities. They are both drift wave type instabilities, but they have different pressure/potential coupling mechanisms. One type couples through the adiabatic response, while the other couples through the sheath boundary response.

5.1.1 Drift Waves

Electron drift waves driven by an equilibrium density or pressure gradient that use the adiabatic response are usually just called drift waves. The electron drift wave mechanism is the following: an electron pressure fluctuation in the plasma is linked with a potential fluctuation through the adiabatic response. The adiabatic response is simply a parallel force balance between the pressure force and the electrostatic force. A simplified version of Eq. 3.3 can be written:

$$\nabla_\parallel p_e = en\nabla_\parallel \phi + Rv_{\parallel e}, \tag{5.1}$$

where the term $Rv_{\parallel e}$ represents effects such as electron inertia, resistivity, and electromagnetic induction. If $R = 0$, the electrons are said to be adiabatic, meaning $\nabla_\parallel p_e = en\nabla_\parallel \phi$. When T_e fluctuations are neglected and $\nabla_\parallel \neq 0$, this integrates to the Boltzmann expression:

$$n = n_0 e^{e\phi/T_e}. \tag{5.2}$$

For any R and T_e fluctuations, the parallel electron dynamics couple the pressure to the potential as long as the parallel wavelength $k_\parallel$ is finite. The perpendicular electric field associated with the potential fluctuation has a component in the azimuthal direction with $k_\perp \gg k_\parallel$. This creates a radial $\mathbf{E} \times \mathbf{B}$ drift that advects the pressure in the radial direction. Because of the radial pressure gradient, the fluctuation propagates azimuthally as a wave at the drift speed $v_{De} = \frac{T_e}{eB}\frac{\partial \ln N_0}{\partial r}$ [Che06] in the electron diamagnetic drift direction. If there is a small phase lag of the potential from the density of the wave – the result of $R \neq 0$ – the equilibrium pressure gradient will enhance the fluctuation, causing instability. Since $p_e = n_e T_e$, the pressure fluctuation may be due to either a density fluctuation, an electron temperature fluctuation, or both. The drift wave caused by a density gradient is commonly studied and given the name Resistive Drift Wave, but a temperature gradient driving a temperature fluctuation wave is also possible, and may be called a Thermal Drift Wave [MTK11]. It's not necessary, however, to separate them, and I will just refer to both of these as drift waves.

The LAPD equation set (Eqs. 4.1-4.4) supports such drift waves, which are unstable with the parameters and profiles used in the simulations. The growth rate as a function of the azimuthal wavenumber m is shown in Fig. 5.1 a) for the LAPD parameters in Table 4.3.2 and profiles in Fig. 4.4. I find the growth rates by simulating the linearized version of Eqs. 4.1-4.4 in BOUT++ with the three different simple axial boundary conditions: periodic, zero-value (Dirichlet), and zero-derivative (Neumann). The linear equations simply omit the advective nonlinearities and the source terms, though the source terms only affect constant flux-surface ($m = 0, n = 0$) modes, which are never unstable. I run the simulations for long enough so that the fastest growing modes can dominate the dynamics.

The solid curves in Fig. 5.1 derive from the simulation results using the formula, $\gamma_m = \frac{\partial E_m}{\partial t}/(2E_m)$ where E_m is the energy of the fastest growing linear eigenmode with azimuthal mode number m. The energy is defined in Chapter 6. The details

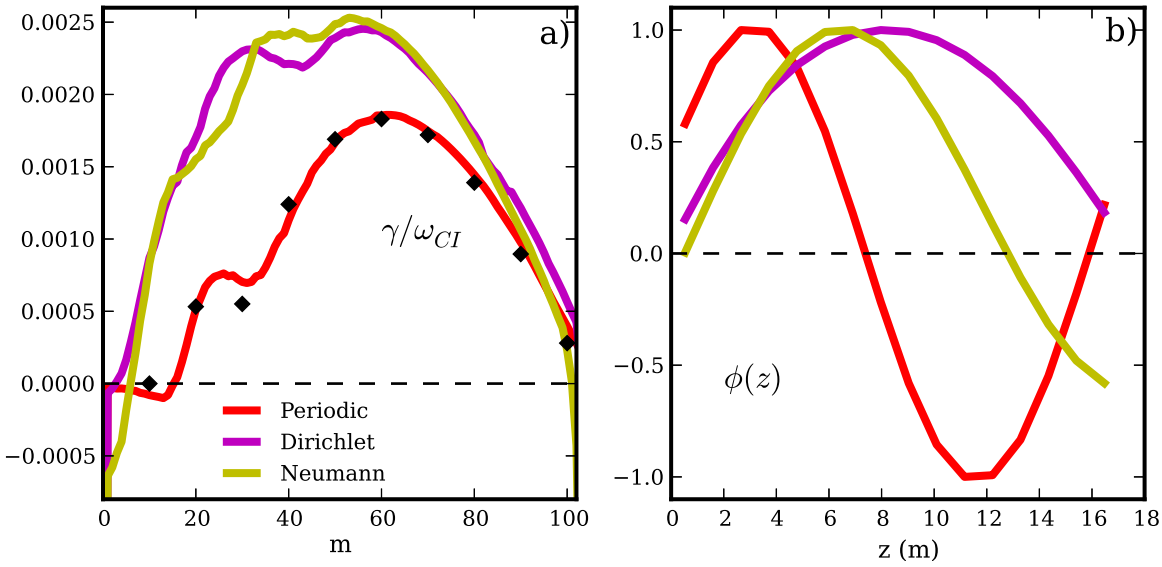

Figure 5.1: Linear drift wave growth rate spectra and axial structures of the fastest growing eigenmodes

of obtaining γ_m are explained in that chapter, but for now, it is sufficient to state that this procedure calculates γ_m at a particular time using only the structures of the fluctuating quantities: $N, \phi, v_{\|e}$, and T_e. An alternative way to calculate γ_m is to use BOUT++'s Fourier filtering capabilities and run many simulations where each one filters out a different azimuthal mode. Then, take the log of the envelope of one or several of the fluctuating quantities and calculate the slope of the line, which gives the growth rate for each particular simulation. This procedure uses the time signal of the fluctuations rather than their spatial structure to calculate the growth rate, thus providing a check on the first method. The results using this alternative method for the periodic case are shown with the black diamonds in Fig. 5.1 a), which agree well with the curve calculated using the alternative energetic structure-based calculation. I do this check with all of the simulations to ensure consistency. This second method is more time consuming, so I only sample a few values of m. Furthermore, it's difficult to get growth rates when

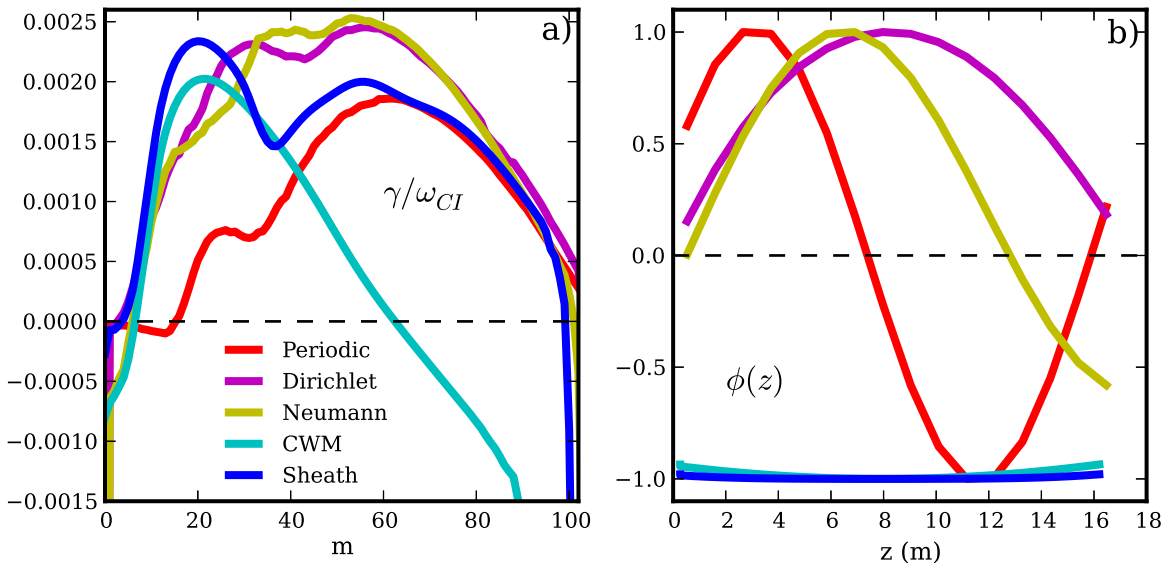

Figure 5.2: Linear conducting wall mode growth rates and axial structures along with those of the drift waves

$\gamma_m < 0$ using this second method.

The difference in the growth rate curves with the different boundary conditions is due to the different $k_\parallel = \frac{2\pi n}{L_\parallel}$ where n is the axial mode number. The periodic simulation restricts n to integer values, while the Dirichlet and Neumann simulations allow for any fractional n. The largest growth rate occurs for $n \sim 1/2$. The Dirichlet and Neumann axial structures for the most unstable m mode, shown in Fig. 5.1 b), reflect this. The periodic simulation, which has $n = 1$ structure, has a smaller growth rate, especially at low m. Note that in Fig. 5.1 b), I omit the axial boundaries. For example, I do not show the zero-valued boundary points for the Dirichlet simulation. Also, I plot the axial structures at one random point in the $r - \theta$ plane and at one time point, and I normalize them to their maximum value.

5.1.2 Conducting Wall Mode

I now consider the linear instability that can exist in a plasma bounded by two conducting walls on the boundaries where the magnetic field lines terminate – the axial boundaries. The instability is actually of the drift wave variety, but unlike the drift waves discussed above, the pressure-potential coupling mechanism is through the sheath boundary response rather than through the adiabatic response [BRT91, BCR93, XRD93]. The Bohm sheath boundary conditions that were derived in Sec. 4.2.2 can provide this coupling. As already noted, these boundary conditions are not necessarily the correct ones for LAPD, but are somewhat idealized. Yet, it is still instructive to apply such an idealized boundary condition to LAPD because it creates this new linear instability, which can be used to test the robustness of LAPD's nonlinear instability.

The conducting wall mode (CWM) instability – as it is called – that I study here is purely an electron temperature gradient instability, although other types of gradients can cause it [BCR93]. In it, electron temperature fluctuations are advected by electrostatic potential fluctuations and feed off the equilibrium electron temperature gradient as in the case of the Thermal Drift Waves. However, in contrast to the Thermal Drift Waves, the coupling between the temperature and potential fluctuations comes through the sheath boundary condition rather than through the adiabatic response. Furthermore, the CWM can have (nearly) $k_\parallel = 0$ flute-like behavior. The coupling mechanism is as follows: an electron temperature perturbation – say a positive constant fluctuation along a small flux tube – increases the sound speed and the electron thermal speed on the flux tube. Since the ions must enter the Bohm sheath at the sound speed by being accelerated by a parallel electric field, the temperature increase must coincide with an increase in the parallel potential gradient as derived in Eq. 4.10. Additionally, the increased electron thermal speed causes an increase in the floating potential along the flux tube. These serve to couple the electron temperature to the potential.

The CWM can be isolated from the drift waves by removing the adiabatic response from the full LAPD equation set, and of course using the Bohm sheath boundary condition of Eq. 4.10. Removal of the adiabatic response in this case means removal of the $\nabla_\parallel p_e$ and the $0.71\nabla_\parallel T_e$ terms in the parallel momentum equation (Eq. 4.2). This causes the density fluctuation N to become a passive scalar, so Eq. 4.1 can be removed as well with no consequence. So the isolated linear CWM equations are:

$$\partial_t v_{\parallel e} = \frac{m_i}{m_e}\nabla_\parallel \phi - \nu_e v_{\parallel e}, \tag{5.3}$$

$$\partial_t \varpi = -N_0 \nabla_\parallel v_{\parallel e} - \nu_{in}\varpi + \mu_\phi \nabla_\perp^2 \varpi, \tag{5.4}$$

$$\partial_t T_e = -\mathbf{v_E}\cdot\nabla T_{e0} + \frac{2}{3N_0}\kappa_{\parallel e}\nabla_\parallel^2 T_e - \frac{2m_e}{m_i}\nu_e T_e + \mu_T \nabla_\perp^2 T_e, \tag{5.5}$$

The CWM growth rate curve is shown in Fig. 5.2 a). The CWM is most unstable at values of $m \sim 20$, which is much lower than the $m \sim 60$ values of the drift waves. Furthermore, the CWM maximum growth rate is about equal to the drift wave growth rates. And from Fig. 5.2 b), the CWM axial structure is flute-like ($k_\parallel \simeq 0$). Finally, the growth rate curve of the full set of equations along with the sheath boundary condition is shown in this figure as the curve labeled "sheath." This set of equations contains the drift wave and CWM instabilities. From both Figs. 5.2 a) and b), it is clear that the sheath simulation is dominated by the CWM at $m \leq 20$, which in fact is where the growth rate is maximum. At $m \geq 40$, the drift waves dominate.

5.2 LAPD Turbulence: A Visual Examination

When I simulate the full LAPD equation set with the advective nonlinearities and source terms, I find that the simulation develops into a turbulent state. To start the simulation, I initialize each fluctuation quantity ($N, \phi, v_{\parallel e}$, and T_e) with a small random 3D spatial structure. This evolves until a coherent structure emerges – the fastest growing linear eigenvector – that grows exponentially in time. Once

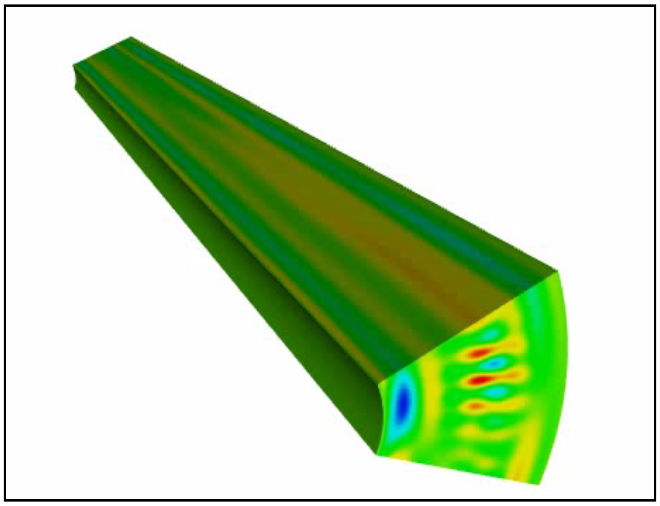

Figure 5.3: 3D turbulent simulation animation starting from a small random fluctuation

the normalized fluctuations reach values on the order of $0.01 - 0.1$, they saturate and become turbulent. A 3D animation of the density fluctuation N is shown in Fig. 5.3 (click to play). The animation consists of 1/8th of the simulated annulus, which makes the axial component of the annulus visible. The animation begins right before the fastest growing mode structure becomes dominant. The fastest growing mode dominates the structure for some time, where there is a clear coherent wave structure that simply propagates in the electron diamagnetic drift direction. This stage is called the linear stage since the linear terms in the equations dominate the evolution. Note that the axial structure in the linear stage has a finite wavelength about half of the length of the animation domain. The axial boundary conditions used here (Neumann) allow for such a structure.

Soon, the coherent eigenmode structure, which has been growing in magnitude, saturates and transitions to a turbulent-looking state that I call the turbulent stage. The evolution of the RMS fluctuation amplitude of the density and potential is shown in Fig. 5.4 a). The potential is separated into a flux-surface-averaged

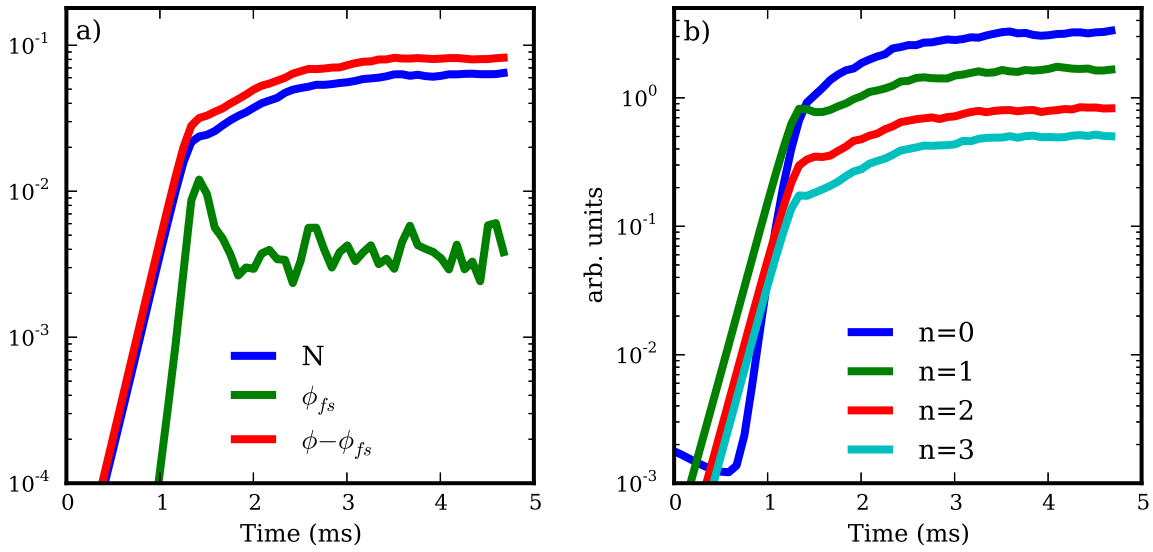

Figure 5.4: Volume-averaged RMS time evolution of a) different field fluctuations and b) axial Fourier mode numbers

component ϕ_{fs} and the remainder $\phi - \phi_{fs}$. ϕ_{fs} quantifies the amplitude in the zonal flow, which appears in Fig. 5.4 a) to have a role in the initial saturation because it becomes very large when the turbulence begins to saturate. However, the zonal flow has a relatively small magnitude in the turbulent stage, indicating that it is not so important here. For all the fluctuating fields, the exponential growth period during the linear stage is followed by saturation corresponding to the visual change from coherent to turbulent spatial structures in the animation. Upon transition to the turbulent stage, I notice in the animation that there is also a qualitative change in the axial mode structure. The axial structures elongate, looking more flute-like than in the linear stage. I confirm this by taking the axial Fourier transform of the density fluctuations and plotting the RMS values of the different axial mode numbers in Fig. 5.4 b). The linear stage is dominated by the $n = 1$ Fourier component, while the turbulent stage is dominated by the $n = 0$ flute mode component. I found this to be an interesting and unexpected transition

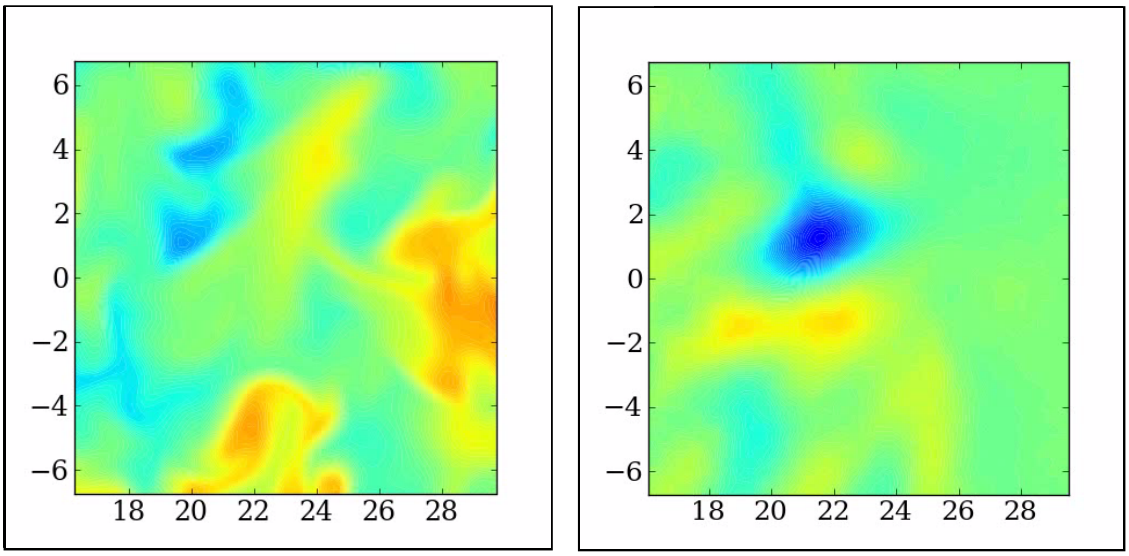

a) Simulation b) Experiment

Figure 5.5: Turbulent animations of a) density fluctuations from the simulation and b) mean-subtracted fluctuations from a fast optical camera viewing the experiment

when I first identified it. I will discuss why this is unexpected in the upcoming chapters, and I will show in detail what causes it. But take note now that this is an important result. This $n = 0$ dominance in the turbulent stage is the main subject of the remaining chapters. The physics that causes it is quite interesting!

However, before I jump into the analysis of the $n = 0$ mode dominance, I continue to look at simple and common turbulence analysis techniques to describe the nature of the turbulence and to validate the simulations. Continuing on with the visual examination, I show a couple of visual comparisons between the simulation and experiment. For the first experimental visual, I use a processed fast camera movie. The camera records the light intensity given off by the plasma. The light is primarily due to line radiation of the helium atoms and ions. It should be some function of plasma density, neutral density, and plasma temperature. Noting

that the comparison is certainly not exact, I show the experimental camera data next to corresponding simulation data of the density N signal during the turbulent stage. This is shown in Fig. 5.5. The animations cover the same spatial domain and proceed for equal time intervals – about 2 ms. Both are simply fluctuation data with the time-independent background not included – subtracted out from the camera data.

For the second visual comparison, in Fig. 5.6 I show fluctuating time signals for the experiment – Langmuir probe ion saturation current – and for the periodic simulation – density fluctuations. Although the quantities that I compare are not completely equivalent, as I explain in the next section, they are similar. All simulation data is taken during the turbulent steady-state phase of the simulation. Visual comparisons like these are certainly not quantitative, and at best they reveal that both simulation and experiment appear turbulent and contain similarly sized spatial and temporal structures. Furthermore, such comparisons are generally only useful when one has a lot of experience looking at such data, and even then the viewer is often biased by his previous experiences. Unbiased comparisons can be made more easily through statistical analysis.

Although the camera data can be a valuable tool since it provides so much simultaneous spatial data – something that is difficult to do with probes – I do not proceed here with detailed statistical analysis of the camera data or any quantitative comparisons between the camera and simulation. This work is left for future studies. Rather, I henceforth focus on statistical analysis of the simulation and experimental Langmuir probe data.

5.3 LAPD Turbulence: A Statistical Examination

Ergodic systems are often described statistically using such tools as spectra, pdfs, and spatial and temporal correlations [TL72]. This is probably the most com-

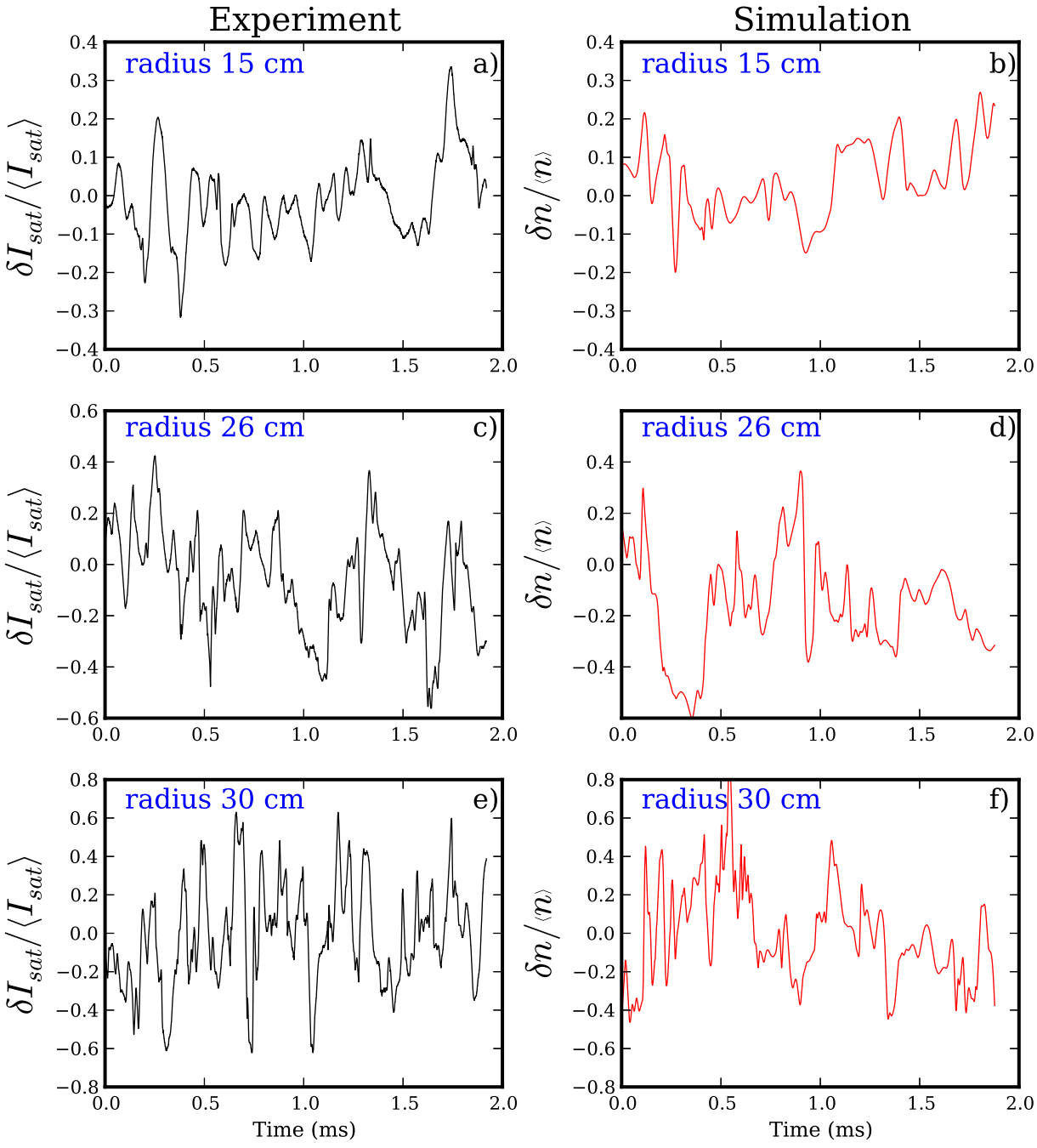

Figure 5.6: Normalized and mean-subtracted experimental probe and simulation temporal fluctuations

mon way to describe stochastic systems, but it is also common to describe chaotic systems this way as well [SG81]. The goal is to be able to characterize the fluctuations. At the very least, this provides a good way to compare simulations to the experiment in order to validate the simulation model. In a stronger way, different theories of turbulence make different predictions regarding statistics, making such a characterization important for confirming or disreputing theories. In this section, I focus mostly on simple comparisons between simulation and experiment, but I also point out some characteristics that relate to certain theoretical predictions. But before I proceed with statistical data comparisons to qualify and quantify the agreement between the simulations and experiment, I must first explain how I can extract equivalent information from the simulations and experiment. In general, this hinges upon experimental measurement theory.

5.3.1 Experimental Probe Data

There are many different kinds of experimental measurements, but I focus here only on Langmuir probe measurements. The Langmuir probes in LAPD generally provide time series data although I do have some two-probe data that provides certain spatial information. Langmuir probes do not directly measure any of the independent state or flux variables of the simulation $(N, \phi, v_{\parallel e}, T_e)$, but they can measure quantities that are functions of these variables. The probes are biased to a known potential – with respect to a reference like the cathode potential – and the current they draw from the plasma is measured. As long as the probes are biased sufficiently below the plasma potential so as to repel most electrons, they develop sheaths around them in the same way as the conducting plates considered in Sec. 4.2.2. The ion current to the probe is [Hut02]

$$I_i \sim \frac{1}{2} e A_s n c_s \tag{5.6}$$

where A_s is the sheath area, approximately equal to the probe area, and the factor of $\frac{1}{2}n$ is the reduction of density at the sheath edge compared to the main plasma. The probe may be biased negatively enough so that all electrons are repelled. The current collected is just that of Eq. 5.6, called the ion saturation current, I_{sat}. As the probe voltage is swept positively from this point, more electrons are collected. The total current to the probe then takes the form [Hut02]

$$I = eA_s n c_s \left[\frac{1}{2} - \left(\frac{m_i}{2\pi m_e} \right)^{1/2} e^{eV_p/T_e} \right], \tag{5.7}$$

where V_p (which is negative) is the potential of the probe with respect to the plasma potential. When $I = 0$, the probe potential is at the floating potential: $\frac{e(V_f - \phi)}{T_e} = \frac{1}{2}\ln\left(\frac{\pi m_e}{2m_i}\right)$. The temperature can be obtained by sweeping the probe potential to get $\frac{\partial I}{\partial V_p}$, which is an exponential function of V_p. So the logarithm of this function produces a straight line. Then, the temperature is:

$$T_e = e(I - I_i)/\frac{\partial I}{\partial V_p}. \tag{5.8}$$

The sweeping process is used to obtain temperature profiles, but it's too slow to measure temperature fluctuations. Therefore, it's not possible to find the exact density and potential fluctuations, N and ϕ. The probes only produce I_{sat} and V_f fluctuation data. Nevertheless, the simulations produce N, ϕ, and T_e fluctuations, which can be used to calculate the I_{sat} and V_f simulation values using the relations: $I_{sat} = \frac{1}{2}eA_s n c_s$ and $V_f = \phi + \frac{T_e}{2e}\ln\left(\frac{\pi m_e}{2m_i}\right)$. So rather than manipulating probe data to find the experimental N and ϕ fluctuations, I can use the simulation data to calculate experimentally-accessible quantities. The derived simulation quantities are called synthetic diagnostics. Synthetic diagnostics are model-dependent and bind together some of the fundamental underlying data. For instance, two measurements (I_{sat} and V_f) comprise three fundamental state variables (N, ϕ, and T_e), so the synthetic diagnostics bind the temperature fluctuations to the density and potential fluctuations. Nevertheless, synthetic diagnostics provide a way to make apples-to-apples comparisons between simulation and experimental data.

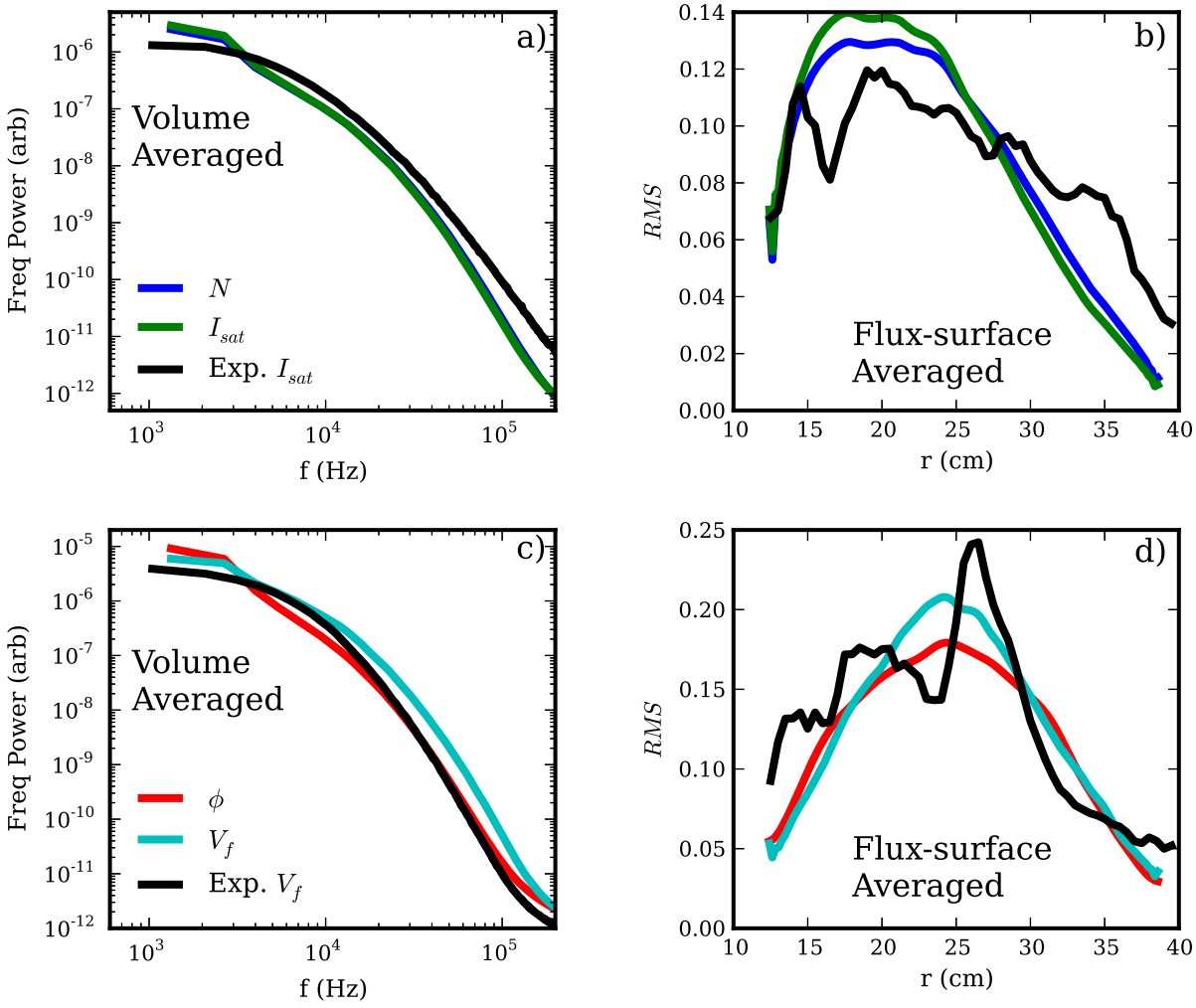

Figure 5.7: I_{sat} and V_f statistical data using synthetic diagnostics for the simulation data

I show in Fig. 5.7, a statistical comparison between I_{sat} and V_f fluctuations from simulation and experiment. The simulation uses the full nonlinear equation set along with Bohm sheath axial boundary conditions. I also show simulation statistics for N and ϕ fluctuations so that they may be compared to the simulation statistics of the synthetic I_{sat} and V_f, respectively. Figs. 5.7 a) and b) compare the volume averaged (from 15 to 35 cm) frequency spectra and radial RMS amplitudes of experimental and simulation I_{sat} fluctuations along with N fluctuations from the simulation. Figs. 5.7 c) and d) compare the same statistical properties, but this time of V_f fluctuations along with ϕ fluctuations from the simulation. The I_{sat} fluctuations from the simulation have nearly identical statistical properties as the N fluctuations because I_{sat} is proportional to density but only weakly dependent on temperature (square root dependence). V_f fluctuations are also somewhat similar to ϕ fluctuations, but to a lesser degree due to the large dependence of V_f on T_e. Furthermore, the simulation and experiment have very similar statistical properties, which I expand upon below.

5.3.2 Statistical Density Comparisons

A comparison of statistical properties of the experimental and simulation density fluctuations is displayed in Fig. 5.8. I actually compare the N fluctuations for the simulations to the I_{sat} fluctuations of the experiment, but as seen in Fig. 5.7, I_{sat} and N statistics are nearly identical. Fig. 5.8 contains results from five different simulations that all use the full nonlinear LAPD equation set (Eqs. 4.1-4.4) but differ in the axial boundary conditions as follows: 1) Periodic – uses periodic axial boundary conditions. 2) Sheath – uses Bohm sheath boundary conditions (Eq. 4.10). 3) $n = 0$ suppressed – uses axial boundary conditions, however, the axial average ($k_\parallel$ or $n = 0$) density, temperature, and potential fluctuation components are artificially removed from the simulation. 4) Dirichlet – uses zero-value axial boundary conditions. 5) Neumann – uses zero-first-derivative axial

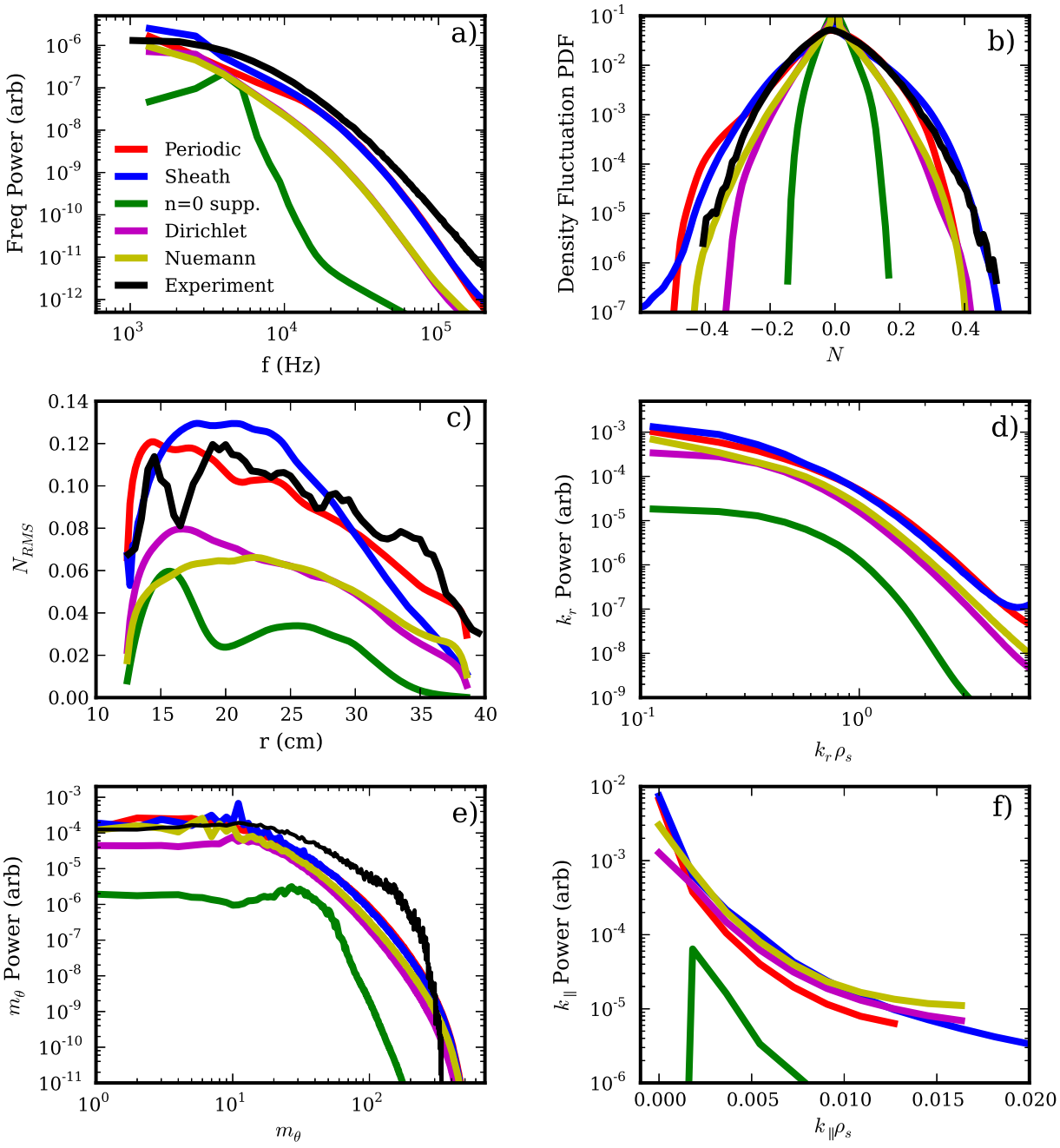

Figure 5.8: Density statistics of the experiment versus all simulations

boundary conditions. I will discuss the $n = 0$ suppressed simulation more in Chapter 7, but for now it is sufficient to say that this simulation does not contain the nonlinear instability and is thus a control case by which to compare the others. It still contains the same linear instabilities as the Periodic simulation, however.

Fig. 5.8 a) shows the frequency power spectrum of the density fluctuations. I use a sliding Hamming window on the time series data and take the FFT, then take a volume average from 15 to 35 cm to get each simulation curve. I use the same technique for the experimental density fluctuation data, except I only have probe data at one location in the $\theta - z$ plane. The axial location is near the center of the machine. I plot the frequency spectrum in a log-log format to emphasize the low-frequency comparison, which is where most of the power is located, but I also show the spectrum in a log-linear format in Fig. 5.11, and discuss this more later. Furthermore, since there are so many curves in each plot of Fig. 5.8, I replot only the experimental and Periodic simulation curves in Fig. 5.9 to make the simulation/experiment comparison easier to see.

Fig. 5.8 b) shows the probability distribution function (PDF) of the density fluctuations, while I provide the first four PDF moments in Table 5.3.2, which characterize the shape of the PDFs, and most importantly their non-Gaussianity. I make the distribution functions out of points at all radii. Fig. 5.8 c) displays the RMS amplitude of the density fluctuations as a function of radius, while Fig. 5.8 d) shows the radial k_r power spectrum of the simulations. I don't have experimental radial spectra data, which requires multiple probes at different radii. Fig. 5.8 e) is the volume-averaged azimuthal m_θ power spectra. Two probes separated azimuthally are used to obtain the experimental spectra. Finally Fig. 5.8 f) is the axial $k_\parallel$ spectra. Again, I don't have experimental axial spectra due to the difficulty of aligning two probes along a field line a significant distance from each other, which is required because of the long axial wavelengths of the modes.

Fig. 5.8 and Table 5.3.2 contain a lot of information about the simulations and

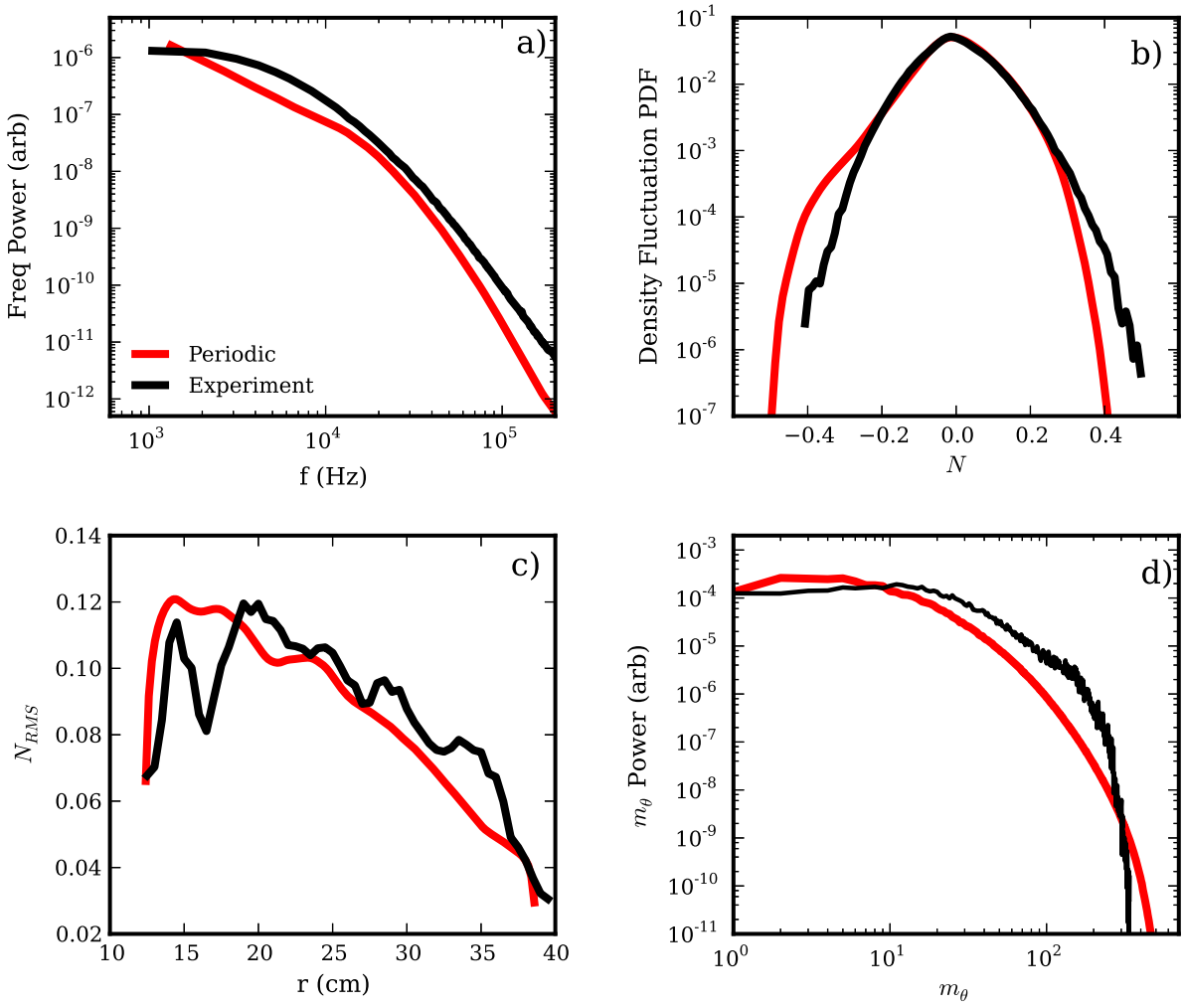

Figure 5.9: Density statistics of experiment versus only the Periodic simulation

Dataset	Mean $\overline{N}$	STD $\sigma^2 = \overline{N^2}$	Skewness $S = \overline{N^3}/\sigma^3$	Kurtosis $K = \overline{N^4}/\sigma^4$
Periodic	-3.2×10^{-8}	8.4×10^{-3}	-0.17	3.9
Sheath	1.0×10^{-4}	9.5×10^{-3}	0.14	3.9
$n = 0$ suppressed	-4.7×10^{-6}	9.6×10^{-4}	0.17	4.5
Dirichlet	6.2×10^{-4}	3.4×10^{-3}	0.18	5.2
Neumann	2.2×10^{-5}	3.5×10^{-3}	0.045	5.8
Experiment	-2.4×10^{-6}	8.2×10^{-3}	0.18	3.5

Table 5.1: PDF moments of the density fluctuations

experiment. The first obvious result is that the $n = 0$ suppressed simulation is statistically much different than all of the other simulations and the experiment. The density fluctuations of this simulation are a factor of 2-3 lower than those of the other simulations and the experiment. Furthermore, this simulation has peaks in the frequency, m_θ, and $k_\parallel$ spectra that are unique. The frequency and m_θ peaks are inconsistent with the experiment. Its spatial spectra peak at $m_\theta \sim 30$ and $k_\parallel \rho_s \sim 0.002 \rightarrow n = 1$, which is somewhat consistent with the linear growth rate spectra of Fig. 5.1, although the m_θ peak location is somewhat less than the maximum linear growth rate value of m_θ, which is around 60 when the axial boundaries are periodic. This differs significantly from all of the other simulations and the experiment which have peaks at $m_\theta \leq 10$ (if they peak at all). And again, as was clear from Fig. 5.4 b), all of the other simulations are strongly dominated by $n = 0$ axial mode numbers, which is a result of the nonlinear instability as I will explain in the upcoming chapters.

Moreover, all of the simulations other than the $n = 0$ suppressed simulation have qualitatively and semi-quantitatively similar statistical properties, which are also consistent with the statistical properties of the experiment. For instance,

they all possess broadband frequency and wavenumber spectra of the same general shape, they all have similarly shaped radial fluctuation amplitudes, and the fluctuations all have kurtosis greater than 3, meaning that their PDFs have tail off slower than does a Gaussian distribution. I note that on a quantitative level, the Dirichlet and Neumann simulations have fluctuation levels about 1.5 times less than the Periodic and Sheath simulations. I don't fully understand the reason for this, but note that the axial wavenumber spectra in Fig. 5.8 f) are shallower for the Dirichlet and Neumann simulations. This certainly affects the energy injection and energy dissipation, as will be seen in the following chapters. Nevertheless, even though their fluctuation levels are too low, I don't claim that the Dirichlet and Neumann simulations are less consistent with the experiment than the Periodic and Sheath simulations. The reason is that I have a free parameter, namely the artificial diffusion coefficient, which affects the overall fluctuation level without significantly affecting the shapes of the spectra. I tuned this parameter to be 1.25×10^{-3} (see Chapter 4) to match the fluctuation level of the Periodic simulation with experiment. Had I tuned this parameter with the Dirichlet or Neumann simulations in mind, the Periodic and Sheath simulations would have fluctuation levels that seem too large. So, in fact, all four of these simulations are qualitatively consistent with the experiment, and they are also quantitatively consistent when I correctly tune the free parameter, though this is a weaker statement of consistency. Moreover, I don't provide any error analysis to quantify the agreement between simulation and experiment, but rather just use an eye test. The fact that several different statistical properties of several fields (see Fig. 5.7) agree between simulation and experiment provides the evidence for my claim that the simulation model is relatively well validated.

Before moving forward, I note that the volume averaging procedure used to obtain many of the plots in Fig. 5.8 can obscure some important physics, namely, the physics that controls the shape of the power and wavenumber spectra. There-

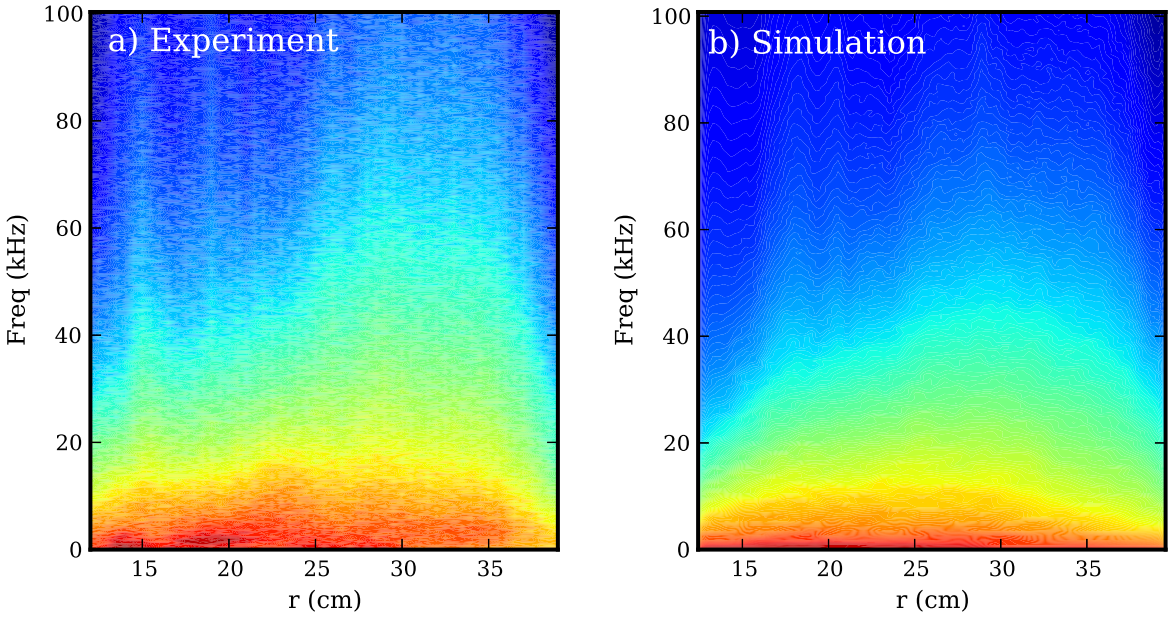

Figure 5.10: Radially dependent power spectra comparison for the experiment and simulation

fore, in Figs. 5.10 and 5.11, I show non-volume-averaged power spectra for the experiment and Periodic simulation. Furthermore, I don't use any window functions to obtain the plots because window functions distort temporal structures that can affect the spectra. Fig. 5.10 provides contour plots of the frequency spectra as a function of radius to include information at all radii. The spectra for both the simulation and experiment have no strong coherent features, meaning that the turublence is broadband everywhere. Since it is difficult to see the shapes of the spectra from contour plots, I show line plots of the spectra at a few radii in Fig. 5.11. First, notice how similar the spectra are at each radius, which is quite validating evidence for the simulation model. Second, notice that the spectra are neither exponential nor power law in shape for either the experiment or simulation at any radii. One may be able to fit multiple exponentials or power laws to the spectra, but theories rarely predict spectra with more than two fitting regions. This doesn't bode well for statistical Kolmogorov-type theories,

nor does it conform to theories based on low-dimensional chaos, which I discuss in Chapter 9.

Another statistical property that is of utmost importance is the radially convective flux – both particle and heat flux – which ultimately dominates the transport in turbulent magnetic confinement devices. I show the particle flux, $\Gamma = \langle N v_r \rangle$, and energy flux, $Q = \langle N T_e v_r \rangle$, in Fig. 5.12, where V_r is the radial $\mathbf{E} \times \mathbf{B}$ velocity due to the fluctuating potential. Although this transport is convective, many write the flux in terms of diffusion coefficients based on Fick's Law: $\Gamma = -D \nabla N_0$ and $Q = -N_0 \chi \nabla T_{e0}$. For the largest fluxes in Fig. 5.12 – those corresponding to the Sheath simulation – the maximum diffusion coefficients are $D_{max} \approx 5$ m^2/s and $\chi_{max} \approx 7 \times 10^5$ s^{-1}. For comparison, the Bohm diffusion coefficient for these simulations is $D_{Bohm} \approx 3$ m^2/s. So the transport in the simulations other than the $n = 0$ suppressed simulation is consistent with the Bohm value.

Another statistical measurement that may be compared between simulation and experiment is the spatial and temporal correlation. Experimentally, the spatial correlation can be found by fixing one probe at a certain location and moving another probe around and measuring the correlation between the two I_{sat} signals. The second probe scans the $r - \theta$ plane at an axial location close to the first probe. The results of the simulated spatial correlation compared to the experimental correlation are presented in Fig. 5.13. For the simulation, I show only the result from the Periodic simulation. The darkest red point, which has a correlation value of 1 represents the location of the stationary probe. The black line marks the $1/e$ contour, where the distance from the stationary probe to this contour is the correlation length. The simulation correlation length – which is about 1 cm – is about half of that of the experimental correlation length. Furthermore, neither the experimental nor simulated fluctuations have completely isotropic correlation structure. The slight divergences from isotropy are not that similar, though. Nevertheless, neither have coherent-mode-like correlation structures or any long range

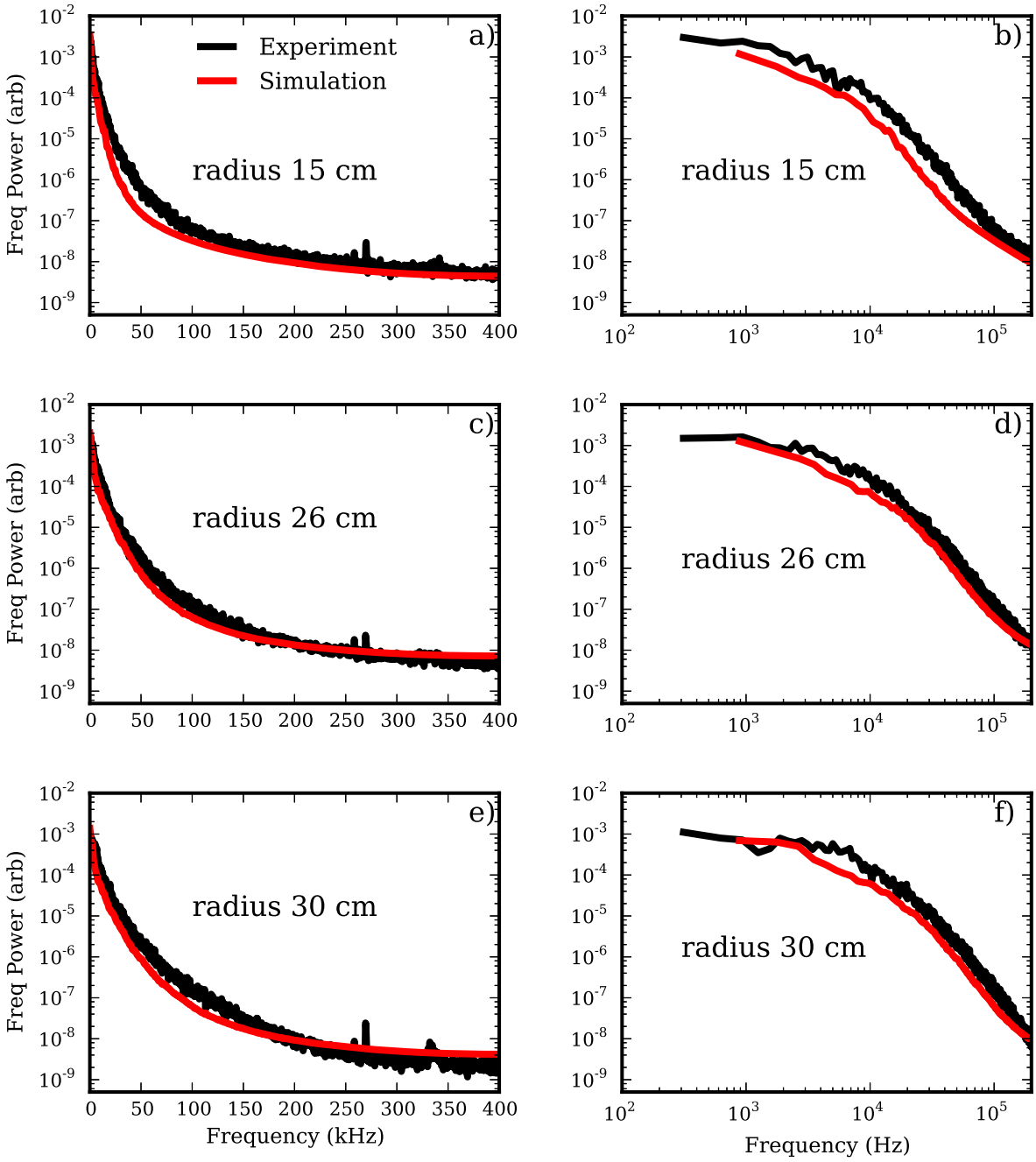

Figure 5.11: Line power spectra at certain radii of experiment and simulation

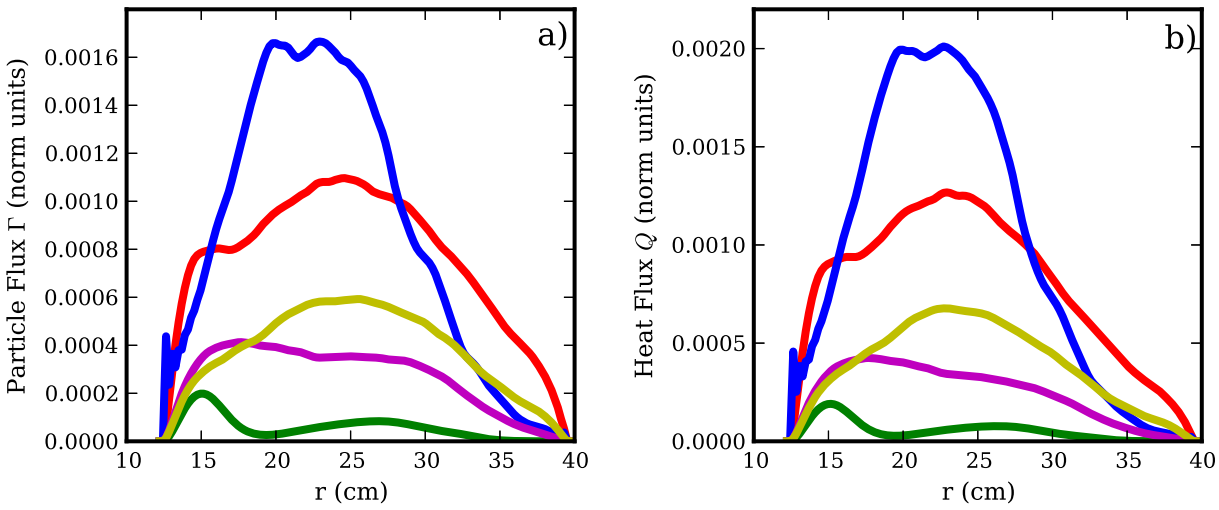

Figure 5.12: Radial particle and heat flux as a function of radius

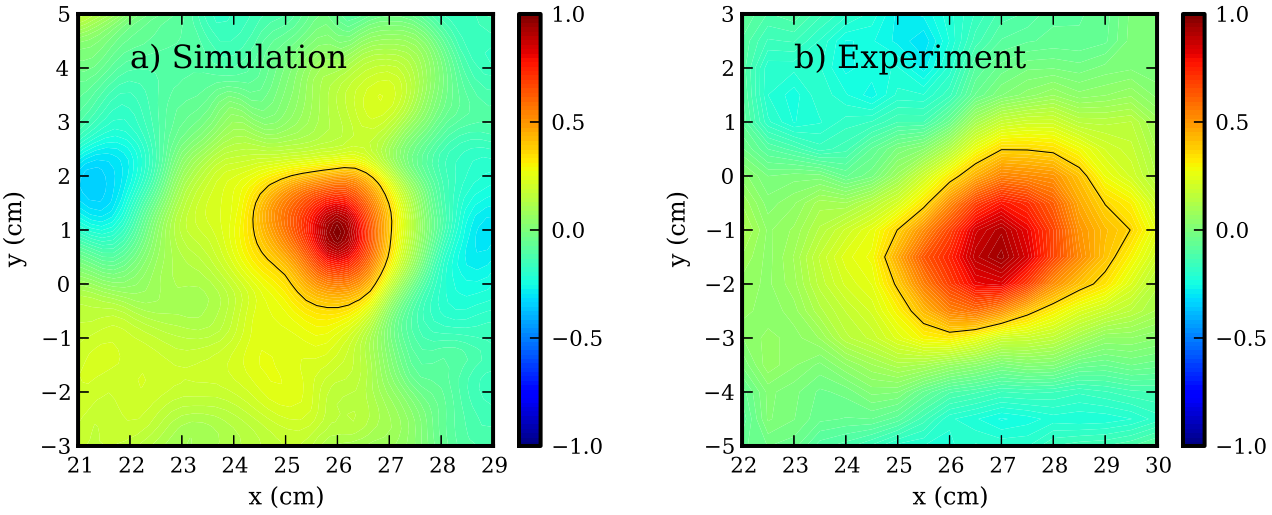

Figure 5.13: Spatial density two-probe correlations of the experiment and Periodic simulation with the 1/e contour indicated in black

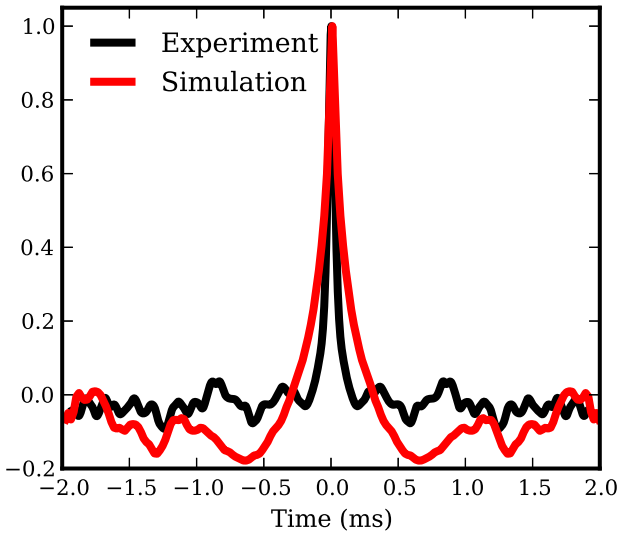

Figure 5.14: Temporal density autocorrelations of the experiment and Periodic simulation

correlation at all.

The experimental temporal autocorrelation is obtained with a single stationary probe. I show the autocorrelation results of the experiment and a simulation in Fig. 5.14. Both have autocorrelations that recede exponentially (confirmed by a semilog plot), but the simulation has a smaller slope and also contains longer correlation structure than the experiment. This is not surprising given the visually longer lived structures in the simulation (seen in Fig. 5.5).

CHAPTER 6

Energy Dynamics Formalism

In the last section of the previous chapter, I analyzed the experimental and simulated turbulence using simple and common statistical methods. Never did I assume any kind of model for the turbulence, nor did I take full advantage of the wealth of spatial information provided by the simulations. In the next few chapters, I do use the simulated physics model along with the turbulent spatial structures to analyze the nature of the turbulence from an energy dynamics perspective. The energy dynamics provide direct information about energy injection into the turbulence from the equilibrium gradients, energy transfer among different fields and between different normal modes, and turbulent energy dissipation. This information reveals the mysterious mechanism that drives the $n = 0$ fluctuations so strongly in the simulations (see Fig. 5.8 f)). The mechanism is a nonlinear instability. I will provide evidence for this in the next chapter, but in this chapter, I derive the dynamical energy equations and explain what they mean.

6.1 Total Energy and Dynamics

First, I consider the total, volume-averaged energy and energy dynamics. The total volume-averaged energy of the fluctuations (in normalized units) is:

$$E = \frac{1}{2}\int_V \left[P_0 \left((N/N_0)^2 + \frac{3}{2}(T_e/T_{e0})^2 \right) + N_0 \left(\frac{m_e}{m_i} v_{\|e}^2 + (\nabla_\perp \phi)^2 \right) \right] dV, \quad (6.1)$$

where $P_0 = N_0 T_{e0}$ is the equilibrium pressure. The $\frac{1}{2}P_0(N/N_0)^2$ term is the potential energy due to density fluctuations, $\frac{3}{4}P_0(T_e/T_{e0})^2$ is the electron temperature

fluctuation potential energy, $\frac{1}{2}N_0\frac{m_e}{m_i}v_{\parallel e}^2$ is the parallel electron kinetic energy, and $\frac{1}{2}N_0(\nabla_\perp\phi)^2$ is the $\mathbf{E}\times\mathbf{B}$ perpendicular kinetic energy. The energy contained in the electric field is smaller than the perpendicular kinetic energy by a factor of $(v_A/c)^2$ and is therefore neglected.

I obtain the dynamical energy evolution $\partial E/\partial t$ using Eqs. 4.1- 4.4 in the following way: first, I take Eq. 4.1, multiply both sides by $\frac{T_{e0}}{N_0}N$, and integrate it over the volume. The result is:

$$\frac{\partial E_N}{\partial t} = \left\langle -T_{e0}N\mathbf{v_E}\cdot\nabla\ln N_0 - T_{e0}N\nabla_\parallel v_{\parallel e} - \mu_N\frac{T_{e0}}{N_0}(\nabla_\perp N)^2 + \frac{T_{e0}}{N_0}NS_N\right\rangle, \quad (6.2)$$

where $E_N = \frac{1}{2}\left\langle P_0(N/N_0)^2\right\rangle$ with $\langle\rangle$ shorthand for the volume integral $\int_V dV$. Next, I multiply Eq. 4.2 by $N_0\frac{m_e}{m_i}v_{\parallel e}$, Eq. 4.3 by $-\phi$, and Eq. 4.4 by $\frac{3}{2}\frac{N_0}{T_{e0}}T_e$ and volume integrate, giving:

$$\begin{aligned}
\frac{\partial E_v}{\partial t} &= \left\langle -T_{e0}v_{\parallel e}\nabla_\parallel N - 1.71N_0v_{\parallel e}\nabla_\parallel T_e + N_0v_{\parallel e}\nabla_\parallel\phi - \frac{m_e}{m_i}N_0\nu_e v_{\parallel e}^2\right\rangle, & (6.3)\\
\frac{\partial E_\phi}{\partial t} &= \left\langle N_0\phi\nabla_\parallel v_{\parallel e} - \nu_{in}N_0(\nabla_\perp\phi)^2 - \mu_\phi\phi\nabla_\perp^2\varpi\right\rangle, & (6.4)\\
\frac{\partial E_T}{\partial t} &= \left\langle -\frac{3}{2}N_0T_e\mathbf{v_E}\cdot\nabla\ln T_{e0} - 1.71N_0T_e\nabla_\parallel v_{\parallel e} - \kappa_{\parallel e}/T_{e0}(\nabla_\parallel T_e)^2\right\rangle\\
&+ \left\langle -\frac{3m_e}{m_i}\frac{N_0}{T_{e0}}\nu_eT_e^2 - \frac{3}{2}\mu_T\frac{N_0}{T_{e0}}(\nabla_\perp T_e)^2 + \frac{3}{2}\frac{N_0}{T_{e0}}T_eS_T\right\rangle, & (6.5)
\end{aligned}$$

where $E_v = \frac{1}{2}\left\langle N_0\frac{m_e}{m_i}v_{\parallel e}^2\right\rangle$, $E_\phi = \frac{1}{2}\left\langle N_0(\nabla_\perp\phi)^2\right\rangle$, and $E_T = \frac{3}{4}\left\langle P_0(T_e/T_{e0})^2\right\rangle$.

Note that there are a few simplifications made in these equations. One simplification is that the term $\left\langle\mu_N\frac{T_{e0}}{N_0}N\nabla_\perp^2N\right\rangle$ is written approximately as $-\left\langle\mu_N\frac{T_{e0}}{N_0}(\nabla_\perp N)^2\right\rangle$ in Eq. 6.2. The fact that $\frac{T_{e0}}{N_0}\approx 1$ makes this approximation acceptable. In fact, I don't use this approximation when calculating such quantities from the simulations, but I write it here as it illuminates the fact that this energy term is negative. I use the same approximation with the $-\left\langle\frac{3}{2}\mu_T\frac{N_0}{T_{e0}}(\nabla_\perp T)^2\right\rangle$ and

$-\left\langle \kappa_{\|e}/T_{e0}(\nabla_\| T_e)^2 \right\rangle$ terms, although the latter contains the fraction $\kappa_{\|e}/T_{e0}$, which is not necessarily close to being constant.

Moreover, notice that none of the advective nonlinear terms are present in these energy dynamics equations. The reason is that $\langle f\{g,f\}\rangle = 0$, which holds as long as f and g have periodic boundary conditions, or if any boundaries are not periodic, then the boundaries must satisfy $f = 0$ and $\nabla g \cdot d\vec{S} = 0$. Now only Eq. 6.4 actually has this $\langle f\{g,f\}\rangle$ form for its nonlinearity because all of the other energy equations contain equilibrium profile quantities in the volume average (e.g. $\left\langle \frac{T_{e0}}{N_0} N\{\phi, N\} \right\rangle$ in Eq. 6.2). Nevertheless, the equilibrium profile quantities come as $\frac{T_{e0}}{N_0} \approx 1$ for Eq. 6.2 and $\frac{N_0}{T_{e0}} \approx 1$ for Eq. 6.5, while there is a factor of the electron to ion mass ratio multiplied by the nonlinearity in Eq. 6.3. This means that all of the nonlinearities approximately vanish in the energy equations. I have confirmed this by direct calculation of these terms. This is why I do not include the nonlinearities in Eqs. 6.2- 6.5.

I note that I could have used a different expression for the energy in order to absolutely conserve the nonlinearities. For instance, I could have set $E_N = \frac{1}{2}\langle N^2 \rangle$, neglecting the factor $\frac{T_{e0}}{N_0}$. In fact, I did this in one paper [FCU12]. However, even though such an expression has the nice property of conserving the nonlinearities, it does not conserve the adiabatic response (I show below how the energy I use does conserve the adiabatic response). Energy is a useful concept because of its conservation properties, but unfortunately, in this case, I have to choose which property to conserve. I choose here to use the physical energy – Eq. 6.1 – that conserves the adiabatic response for a few reasons (I also used the physical energy in another paper [FCU13]). First, the adiabatic-conserving energy is the same thing as the physical energy – meaning, it is the energy one would write down without knowledge of the equations. Second, the physical energy generally conserves the nonlinearities more than the nonlinearity-conserving energy conserves the adiabatic response. I have tested this using my simulations. And third, when

the adiabatic response is not conserved, the energy dynamics appear to deposit energy directly into the $v_{\|e}$ fluctuations, which is not standard.

Now, one may wonder why the physical energy doesn't absolutely conserve the advective nonlinearities when many other papers use a physical energy that does. For one, those other papers generally use local rather than global models. Additionally, I have partially linearized the simulation equations, eliminating certain conservation properties. Still though, this partial linearization makes the energy dynamics analysis simpler, and therefore more useful, although some may disagree.

Now Eqs. 6.2- 6.5 are still not incredibly revealing because they contain nearly as many terms as the original simulated equations. However, I can break each of these equations down in the following way:

$$\frac{\partial E_j}{\partial t} = Q_j + C_j + D_j. \tag{6.6}$$

The subscript j represents the individual field: (N, v, ϕ, T). Q_j represents energy injection from an equilibrium gradient. For example, Q_N represents the energy injected into E_N (the density fluctuation potential energy) taken from the free energy of the equilibrium density gradient ($\nabla_r N_0$). These terms are:

$$Q_N = \langle -T_{e0} N \mathbf{v_E} \cdot \nabla \ln N_0 \rangle , \tag{6.7}$$

$$Q_v = 0, \tag{6.8}$$

$$Q_\phi = 0, \tag{6.9}$$

$$Q_T = \left\langle -\frac{3}{2} N_0 T_e \mathbf{v_E} \cdot \nabla \ln T_{e0} \right\rangle . \tag{6.10}$$

Only the density and temperature fluctuations receive energy from the equilibrium density and temperature gradients, respectively. They do so by radial $\mathbf{E} \times \mathbf{B}$ advection, moving fluid or heat across the gradient where it can enhance or diminish the density and temperature fluctuations. I call the Q_j terms energy injection terms, but they can in fact dissipate fluctuation energy if the phase between the density (or temperature) and potential are stabilizing.

Next, the C_j terms, which constitute the adiabatic response, represent field transfer channels. They are:

$$C_N = \left\langle -T_{e0} N \nabla_\parallel v_{\parallel e} \right\rangle, \tag{6.11}$$

$$C_v = \left\langle -T_{e0} v_{\parallel e} \nabla_\parallel N - 1.71 N_0 v_{\parallel e} \nabla_\parallel T_e + N_0 v_{\parallel e} \nabla_\parallel \phi \right\rangle, \tag{6.12}$$

$$C_\phi = \left\langle N_0 \phi \nabla_\parallel v_{\parallel e} \right\rangle, \tag{6.13}$$

$$C_T = \left\langle -1.71 N_0 T_e \nabla_\parallel v_{\parallel e} \right\rangle. \tag{6.14}$$

Notice that $C_N + C_\phi + C_T = -C_v$ if the axial boundaries are periodic or zero value. Alternatively, $\sum_j C_j = 0$. This is what I mean by conservation of the adiabatic response. No energy is gained or lost in total from these terms when taken together. Energy does, however, transfer between the different fields: $N, T_e, \phi \leftrightarrow v_{\parallel e}$. All energy transfers through the parallel electron velocity. The density, temperature, and potential fluctuations all feed or draw energy from the parallel electron velocity. This means that the density and potential fluctuations, for instance, cannot transfer energy between each other directly. There are two minor points regarding the affect of the boundary conditions on the adiabatic response. First, the Neumann and sheath simulations don't exactly conserve the adiabatic response because of non-vanishing contributions from the boundaries. Second, the sheath boundary conditions allow energy transfer between the temperature and potential fluctuations that is completely independent of the adiabatic response. In fact, this is what allows for the CWM (see Sec. 5.1.2). The sheath energy transfer mechanism isn't represented by the C_j expressions. I don't account for that transfer mechanism in these energy dynamics equations. I leave it to future work.

Finally, the D_j terms represent dissipative energy loss from the fluctuations. They are:

$$D_N = \left\langle -\mu_N \frac{T_{e0}}{N_0} (\nabla_\perp N)^2 + \frac{T_{e0}}{N_0} N S_N \right\rangle, \tag{6.15}$$

$$D_v = \left\langle -\frac{m_e}{m_i} N_0 \nu_e v_{\parallel e}^2 \right\rangle, \tag{6.16}$$

$$
\begin{aligned}
D_\phi &= \left\langle -\nu_{in} N_0 (\nabla_\perp \phi)^2 - \mu_\phi \phi \nabla_\perp^2 \varpi \right\rangle, && (6.17)\\
D_T &= \left\langle -\kappa_{\|e}/T_{e0} (\nabla_\| T_e)^2 - \frac{3m_e}{m_i}\frac{N_0}{T_{e0}} \nu_e T_e^2 \right\rangle \\
&+ \left\langle -\frac{3}{2}\mu_T \frac{N_0}{T_{e0}} (\nabla_\perp T_e)^2 + \frac{3}{2}\frac{N_0}{T_{e0}} T_e S_T \right\rangle. && (6.18)
\end{aligned}
$$

Most of these terms have forms that illustrate that their negative definiteness. However, the source terms do not have a clear sign and the $\langle -\mu_\phi \phi \nabla_\perp^2 \varpi \rangle$ viscous term in Eq. 6.17 doesn't have a clear sign either. Recall, though, that the sources essentially remove the flux-surface averaged component of the density and temperature fluctuations, indicating that they remove the energy associated with these fluctuation components. Taking $S_N \approx -\langle N \rangle_{fs}$ from Eqs. 4.5 and 4.6, then the source contribution to D_N is $-\left\langle \frac{T_{e0}}{N_0} \langle N \rangle_{fs}^2 \right\rangle$, which is negative. The viscous term in Eq. 6.17 is less obviously negative, however, letting $\nabla_\perp \to -k_\perp^2$ makes the viscous term approximately $-\langle \mu_\phi N_0 k_\perp^4 \phi^2 \rangle$. So it's reasonable to conclude that all contributions in the D_j expressions are absolutely negative. My direct calculations have confirmed this.

6.2 Spectral Energy Dynamics

While the total energy dynamics can reveal some important information such as the amount of energy entering the density fluctuations vs. the temperature fluctuations, the direction of energy flow through the adiabatic response, and how much energy is dissipated by the various mechanisms, the total dynamics cannot show the mechanism of the nonlinear instability. In fact, the total energy dynamics are rather useless in revealing any nonlinear physics. Spectral or mode-decomposed energy dynamics, on the other hand, provide much more information regarding mode-specific processes like cascades and complex nonlinear processes.

When deriving mode-decomposed energy dynamics, one first has to choose a set of basis functions (modes) on which to decompose the fluctuations. This

is important because a good choice of basis functions can immediately reveal important dynamical information, while a poor choice can lead to a lot of wasted time and a muddled picture. Generally, basis functions are time-independent spatial structures that are linearly independent and span the whole computational space Ω. For example, a particular set of basis functions $\psi_i(\vec{r})$ can linearly sum to represent any 3D function on Ω:

$$f(\vec{r}) = \sum_i a_i \psi_i(\vec{r}). \tag{6.19}$$

In dynamical systems, the system is represented by a time-dependent 3D function, causing the amplitudes a_i to vary with time:

$$f(\vec{r}, t) = \sum_i a_i(t) \psi_i(\vec{r}). \tag{6.20}$$

Fourier modes or linear eigenvectors are common examples of basis functions. However, Fourier modes are not always a useful or a natural basis, and linear eigenmodes can be unwieldy when they are nonorthogonal to each other, which is the case for my dynamical system. In the next section, I discuss an alternative basis, namely that obtained by Proper Orthogonal Decomposition, but for now, I describe a basis upon which I base most of my results. That basis is a partial Fourier basis, which I have found useful in analyzing the simulations and uncovering interesting physics.

What I mean by partial Fourier basis is that I decompose the azimuthal and axial directions in Fourier series, leaving the radial direction undecomposed. For example, I decompose the density in the following way:

$$N(r, \theta, z, t) = \sum_{\vec{k}} n_{\vec{k}}(r, t) e^{i(m\theta + k_z z)}. \tag{6.21}$$

Here, $k_z = \frac{2\pi n}{L_\parallel \rho_s}$, where n is the axial mode number and m is the azimuthal mode number, and the $\vec{k}$ symbol is short for (m, n). The sum over $\vec{k}$ is in fact a double sum over m and n. Furthermore, positive and negative m and n are included in

the sums to ensure reality of N since $n_{-\vec{k}} = n^*_{\vec{k}}$. Similar decompositions are used for $v_{\|e}, \phi$, and T_e. Note that the radial part of the basis function $n_{\vec{k}}(r,t)$ isn't really a basis function in the general sense. First, it is time-dependent. Second, it doesn't span the radial domain. In fact, at a particular time, it only describes one very particular 1D (complex) function. Nevertheless, by not using a radial decomposition, I greatly reduce the number of modes of the problem, allowing me to focus on certain processes of interest.

Now, to derive the spectral energy equations, I first substitute the basis decompositions – Eq. 6.21 and those corresponding to the other fields – into Eqs. 4.1- 4.4. Using the density evolution equation as an example, I get:

$$\begin{aligned}
&\sum_{\vec{k}} \frac{\partial n_{\vec{k}}}{\partial t} e^{i(m\theta + k_z z)} = \\
&\sum_{\vec{k}} \left[-\frac{im}{r} \partial_r N_0 \phi_{\vec{k}} - i k_z N_0 v_{\vec{k}} + \mu_N (\partial_r^2 n_{\vec{k}} + \frac{1}{r} \partial_r n_{\vec{k}} - \frac{m^2}{r^2} n_{\vec{k}}) \right] e^{i(m\theta + k_z z)} \\
&+ \frac{1}{r} \sum_{\vec{k},\vec{k}'} (im n_{\vec{k}} \partial_r \phi_{\vec{k}'} - im' \partial_r n_{\vec{k}} \phi_{\vec{k}'}) e^{i(m+m')\theta + i(k_z + k'_z)z} + S_N. \qquad (6.22)
\end{aligned}$$

Note the double sum for the nonlinearity. Continuing on with just the density equation for now, I proceed to get the energy equation by multiplying through by $\frac{T_{e0}}{N_0} n^*_{\vec{k}''} e^{-im''\theta - ik''_z z}$ and integrating over space. The result is (with primes permuted):

$$\begin{aligned}
&\frac{1}{2} \left\langle \frac{T_{e0}}{N_0} \frac{\partial |n_{\vec{k}}|^2}{\partial t} \right\rangle = \\
&\left\langle -\frac{T_{e0}}{N_0} \frac{im}{r} \partial_r N_0 \phi_{\vec{k}} n^*_{\vec{k}} - i k_z T_{e0} v_{\vec{k}} n^*_{\vec{k}} + \frac{T_{e0}}{N_0} \mu_N (\partial_r^2 n_{\vec{k}} + \frac{1}{r} \partial_r n_{\vec{k}} - \frac{m^2}{r^2} n_{\vec{k}}) n^*_{\vec{k}} \right\rangle \\
&+ \left\langle \frac{T_{e0}}{r N_0} \sum_{\vec{k}'} \left(im' n_{\vec{k}'} \partial_r \phi_{\vec{k}-\vec{k}'} n^*_{\vec{k}} - i(m-m') \partial_r n_{\vec{k}'} \phi_{\vec{k}-\vec{k}'} n^*_{\vec{k}} \right) \right\rangle \\
&+ \left\langle \frac{T_{e0}}{N_0} S_N n^*_{\vec{k}} \delta_{\vec{k},0} \right\rangle, \qquad (6.23)
\end{aligned}$$

where the brackets now represent the reality operator and the radial integral $Re\left\{\int r dr\right\}$ because I have performed the azimuthal and axial integrations and

taken the real part of the equation. Breaking this up into specific parts:

$$\frac{\partial E_N(\vec{k})}{\partial t} = Q_N(\vec{k}) + C_N(\vec{k}) + D_N(\vec{k}) + \sum_{\vec{k}'} T_N(\vec{k},\vec{k}') \tag{6.24}$$

with

$$E_N(\vec{k}) = \frac{1}{2}\left\langle \frac{T_{e0}}{N_0}|n_{\vec{k}}|^2 \right\rangle \tag{6.25}$$

$$Q_N(\vec{k}) = \left\langle -\frac{im}{r}\frac{T_{e0}}{N_0}\partial_r N_0 \phi_{\vec{k}} n^*_{\vec{k}} \right\rangle \tag{6.26}$$

$$C_N(\vec{k}) = \left\langle -ik_z T_{e0} v_{\vec{k}} n^*_{\vec{k}} \right\rangle \tag{6.27}$$

$$D_N(\vec{k}) = \left\langle \frac{T_{e0}}{N_0}\mu_N(\partial_r^2 n_{\vec{k}} + \frac{1}{r}\partial_r n_{\vec{k}} - \frac{m^2}{r^2} n_{\vec{k}}) n^*_{\vec{k}} + \frac{T_{e0}}{N_0} S_N n^*_{\vec{k}} \delta_{\vec{k},0} \right\rangle \tag{6.28}$$

$$T_N(\vec{k},\vec{k}') = \left\langle \frac{T_{e0}}{rN_0}\left(im' n_{\vec{k}'}\partial_r \phi_{\vec{k}-\vec{k}'} n^*_{\vec{k}} - i(m-m')\partial_r n_{\vec{k}'}\phi_{\vec{k}-\vec{k}'} n^*_{\vec{k}}\right) \right\rangle \tag{6.29}$$

The new piece not in the total energy dynamics in Sec. 6.1 – $T_N(\vec{k},\vec{k}')$ – comes from the advective nonlinearity. It couples different Fourier modes, meaning it transfers energy between different $\vec{k}$ waves. It is not conserved for individual $\vec{k}$ modes, but is conserved on the aggregate: $\sum_{\vec{k},\vec{k}'} T_N(\vec{k},\vec{k}') \simeq 0$. Notice also that $Q_N(\vec{k})$ can be finite for $n = 0$, but $C_N(\vec{k})$ is zero for $n = 0$. Thus, flute modes may take energy from the equilibrium density gradient, but they cannot access the adiabatic response. This eliminates linear drift wave flute modes, but does not preclude nonlinear drift wave flute modes that transfer their energy to non-flute structures in order to access the adiabatic response.

For completeness, I write the rest of the spectral energy dynamics pieces here. The perpendicular kinetic energy dynamics pieces are:

$$E_\phi(\vec{k}) = \frac{1}{2}\left\langle N_0 \left|\frac{\partial \phi_{\vec{k}}}{\partial r}\right|^2 + N_0 \frac{m^2}{r^2}|\phi_{\vec{k}}|^2 \right\rangle \tag{6.30}$$

$$Q_\phi(\vec{k}) = 0 \tag{6.31}$$

$$C_\phi(\vec{k}) = \left\langle ik_z N_0 v_{\vec{k}} \phi^*_{\vec{k}} \right\rangle \tag{6.32}$$

$$D_\phi(\vec{k}) = \left\langle -\mu_\phi(\partial_r^2 \varpi_{\vec{k}} + \frac{1}{r}\partial_r \varpi_{\vec{k}} - \frac{m^2}{r^2}\varpi_{\vec{k}})\phi^*_{\vec{k}} - \nu_{in} E_\phi(\vec{k}) \right\rangle \tag{6.33}$$

$$T_\phi(\vec{k},\vec{k}') = \left\langle -\frac{1}{r}\left(im'\varpi_{\vec{k}'}\partial_r \phi_{\vec{k}-\vec{k}'}\phi^*_{\vec{k}} - i(m-m')\partial_r \varpi_{\vec{k}'}\phi_{\vec{k}-\vec{k}'}\phi^*_{\vec{k}}\right) \right\rangle \tag{6.34}$$

and for the electron temperature potential energy:

$$
\begin{aligned}
E_T(\vec{k}) &= \frac{3}{4}\left\langle \frac{N_0}{T_{e0}}|t_{\vec{k}}|^2 \right\rangle && (6.35)\\
Q_T(\vec{k}) &= \left\langle -\frac{3}{2}\frac{N_0}{T_{e0}}\frac{im}{r}\partial_r T_{e0}\phi_{\vec{k}}t^*_{\vec{k}} \right\rangle && (6.36)\\
C_T(\vec{k}) &= \left\langle -1.71ik_z N_0 v_{\vec{k}}t^*_{\vec{k}} \right\rangle && (6.37)\\
D_T(\vec{k}) &= \left\langle -\frac{\kappa_{\|e}}{T_{e0}}k_z^2|t_{\vec{k}}|^2 - \frac{3m_e}{m_i}\frac{N_0}{T_{e0}}\nu_e|t_{\vec{k}}|^2 \right\rangle \\
&+ \left\langle \frac{3}{2}\frac{N_0}{T_{e0}}\mu_T(\partial_r^2 t_{\vec{k}} + \frac{1}{r}\partial_r t_{\vec{k}} - \frac{m^2}{r^2}t_{\vec{k}})t^*_{\vec{k}} + \frac{3}{2}\frac{N_0}{T_{e0}}S_T t^*_{\vec{k}}\delta_{\vec{k},0} \right\rangle && (6.38)\\
T_T(\vec{k},\vec{k}') &= \left\langle \frac{3}{2r}\frac{N_0}{T_{e0}}\left(im' t_{\vec{k}'}\partial_r\phi_{\vec{k}-\vec{k}'}t^*_{\vec{k}} - i(m-m')\partial_r t_{\vec{k}'}\phi_{\vec{k}-\vec{k}'}t^*_{\vec{k}}\right) \right\rangle && (6.39)
\end{aligned}
$$

and for the parallel kinetic energy:

$$
\begin{aligned}
E_v(\vec{k}) &= \frac{1}{2}\frac{m_e}{m_i}\left\langle N_0|v_{\vec{k}}|^2 \right\rangle && (6.40)\\
Q_v(\vec{k}) &= 0 && (6.41)\\
C_v(\vec{k}) &= \left\langle -ik_z N_0 n_{\vec{k}}v^*_{\vec{k}} + ik_z N_0\phi_{\vec{k}}v^*_{\vec{k}} - 1.71ik_z T_{e0}t_{\vec{k}}v^*_{\vec{k}} \right\rangle && (6.42)\\
D_v(\vec{k}) &= \left\langle -\nu_e\frac{m_e}{m_i}N_0|v_{\vec{k}}|^2 \right\rangle && (6.43)\\
T_v(\vec{k},\vec{k}') &= \left\langle \frac{m_e}{m_i}\frac{N_0}{r}\left(im' v_{\vec{k}'}\partial_r\phi_{\vec{k}-\vec{k}'}v^*_{\vec{k}} - i(m-m')\partial_r v_{\vec{k}'}\phi_{\vec{k}-\vec{k}'}v^*_{\vec{k}}\right) \right\rangle. && (6.44)
\end{aligned}
$$

6.3 Proper Orthogonal Decomposition

6.3.1 Decomposition

As I alluded to above, there are many choices by which one can mode-decompose a turbulent system. Full Fourier decompositions and linear eigenmode decompositions are common. I choose not to use a radial Fourier decomposition for a couple of reasons. First, the radial Fourier modes are poor representatives of the turbulent structures. That is, too many radial Fourier modes have large coefficients upon decomposition, which makes simple modeling difficult. Second, the equilibrium profiles have radial dependence, and some of the differential operators

contain factors of the radius r. This means that the integration over the volume which eliminates the Fourier exponentials – like the step between Eq. 6.22 and Eq. 6.23 – does not work for the radial coordinate. This is more of an aesthetic consideration than a mathematical one; nevertheless, I prefer to avoid it.

The linear eigenmode decomposition is an attractive one because the dynamical energy expressions can be written elegantly (see Sec. 8.4), and it seems that the fastest growing linear eigenmodes should make up most of the turbulent amplitude. However, there is the practical difficulty in doing an eigenmode decomposition in that one has to somehow find all of the linear eigenvectors, which cannot be done with an initial value code like BOUT++. One must write or use an eigensystem code to do this. On a more fundamental level, however, dynamical systems with non-normal linear operators – gradient-driven systems – have nonorthogonal linear eigenvectors. Using a nonorthogonal basis decomposition can be too unwieldy for a decomposition analysis because the total energy contains contributions from each individual eigenmode plus contributions from cross terms. I showed a simple example of this in Sec. 2.2.3. The fact that the cross terms can have negative energies is undesirable and unmanageable. Using left and right eigenvectors to introduce some kind of orthogonality condition can partly simplify matters, but energies and the dynamical terms still contain cross terms, leaving still overly complicated results [KT10]. I, in fact, began this line of research using an eigenmode decomposition, but I eventually gave up that path because the results were too complicated and the interesting physics didn't depend on that particular decomposition.

Hatch et al. dealt with the nonorthogonal eigenvector problem using two distinct methods [HTJ11]. The first was to use a Gram-Schmidt orthogonalization procedure, retaining the most unstable linear eigenmode and orthogonalizing the others from this. The resulting orthogonal modes other than the most unstable linear eigenmode, however, are not linear eigenmodes after the procedure. They

more or less form an arbitrary orthogonal basis, leaving this method with limited applicability. The second method they used was Proper Orthogonal Decomposition (POD, aka Principle Component Analysis) to create orthogonal modes that best captured the dominant turbulent structures. The POD has properties that make it the most desirable decomposition for my dynamical system – other than the one in the previous section.

POD is a procedure for extracting an orthogonal basis from an ensemble of space-time signals. Its power lies in its generality, its linearity, and its creation of an "optimal" basis. A nice review of the properties of POD is given by Berkooz et al. [BHL93]. A less descriptive and less rigorous description of POD is given in Futatani et al. [FBC09], and I will follow their treatment to show how to construct the POD and to present some of its properties. Simply, the POD is a singular value decomposition (SVD) of the data given by

$$A(\vec{r}_i, t_j) = \sum_{q=1}^{N_{\mathrm{POD}}} \sigma_q u_q(\vec{r}_i) w_q(t_j) \tag{6.45}$$

where $A(\vec{r}, t)$ is the data. In my case, four independent variables $(N, \phi, v_{\|e}, T_e)$ comprise the data. These must be appended together to get the full matrix A. Furthermore, $N_{\mathrm{POD}} = \min[4 \times \mathrm{N_r} \times \mathrm{N}_\theta \times \mathrm{N_z}, \mathrm{N_t}]$. In other words, N_{POD} is the lesser of 4 times the number of total grid points – the degrees of freedom – and the number of time points. For me, $N_{\mathrm{POD}} = N_t$ because I choose to retain more spatial data than time data. Linear eigenmodes and full Fourier modes, on the other hand, always number $4 \times N_r \times N_\theta \times N_z$. This means that the spatial POD functions, $u_q(\vec{r})$, do not span the computational domain – any arbitrary function on the computational domain cannot be represented by a linear combination of the u_q POD functions. They do, however, span a subspace of the domain and every data signal that is used to derive the u_q POD functions can be represented by a linear combination of them.

Before I continue, I note a couple of practical considerations. First, I find it

useful at times to first Fourier decompose the data in the azimuthal and axial dimensions before performing the POD. In that case, the data for each Fourier pair $\vec{k} = (m, n)$ is only a function of the radial coordinate r and time: $A_{\vec{k}}(r, t)$. The spatial POD functions u_q are then 1D (complex) functions of radius. Second, if I do not Fourier decompose the data, I must make A a 2D matrix in order to take the SVD computationally. To do this, I simply unravel or collapse all of the spatial dimensions into a 1D vector. Then a single column of A is the unraveled spatial data at one particular instant in time, and the time varies from column to column. Furthermore, the non-Fourier spatial and temporal POD functions u_q and w_q are real, not complex. Third, whether or not I use a Fourier decomposition, A must be a 2D matrix and u_q must be a 1D vector, so performing the POD requires appending the four fields $(N, \phi, v_{\|e}, T_e)$ into a single vector.

Continuing on, the spatial POD u_q modes and the temporal POD w_q modes satisfy the following orthonormality conditions:

$$\sum_i u_q(\vec{r}_i) u_l^*(\vec{r}_i) = \sum_j w_q(t_j) w_l^*(t_j) = \delta_{ql}. \tag{6.46}$$

The positive real numbers σ_q are the singular values, and they are sorted in descending order, i.e., $\sigma_1 \geq \sigma_2 \geq \sigma_3 \cdots$. Then for $1 \leq h \leq N_{\text{POD}}$, I can define a rank-$h$ truncation of the dataset $A^{(h)}$ as

$$A_{ij}^{(h)} = \sum_{q=1}^{h} \sigma_q u_q(\vec{r}_i) w_q(t_j). \tag{6.47}$$

What makes the POD more optimal than any other decomposition is that this truncation approximation is better than any other rank-h approximations with other bases. Formally,

$$\|A - A^{(h)}\|^2 = \min \left\{ \|A - B\|^2 \right\}, \text{for rank}(B) = h. \tag{6.48}$$

where $\|A\| = \sqrt{\sum_{ij} \|A_{ij}\|^2}$ is the L_2 norm. In general, $\|A\|^2 = \sum_{q=1}^{N_{\text{POD}}} \sigma_q^2$ is the energy of the data and σ_q^2 represents the energy contained in the q^{th} POD

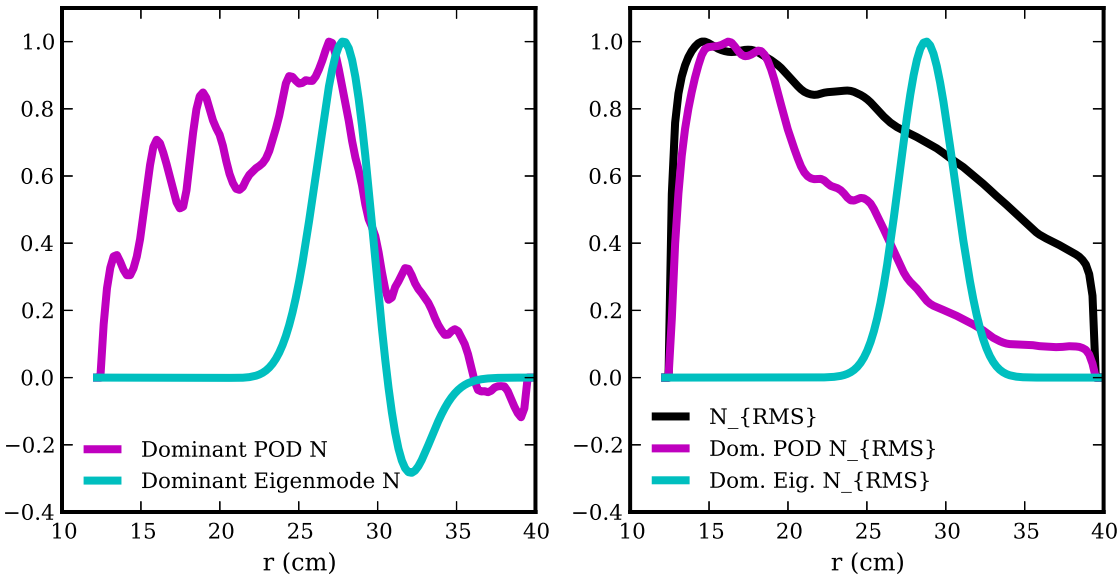

Figure 6.1: Comparison of the radial spatial structure of the fastest growing eigenmode and dominant POD mode along with the total turbulent fluctuation RMS

mode. In this sense, the POD is a decomposition of the data in terms of energy content. In other words, the modes with the highest σ_q comprise most of the energy of the data. If the σ_q's descend rapidly, as they often do, the truncated data reconstitution of Eq. 6.47 represents the original data quite well. This is obviously useful in energetics analyses.

To show an example of how the POD modes represent the turbulent data better than the linear eigenmodes, I perform a POD on the Periodic simulation with 300 time signals, giving 300 POD modes. Then, in Fig. 6.1 a), I compare the real part of the radial structure of the fastest growing linear eigenmode to the dominant POD mode – that with the highest σ_q. For both, I take only the density component of the modes. The eigenmode has mode numbers $n = 1, m \sim 60$, while the POD mode has much more complicated axial and azimuthal dependence because I don't do an (m, n) Fourier decomposition before performing the POD.

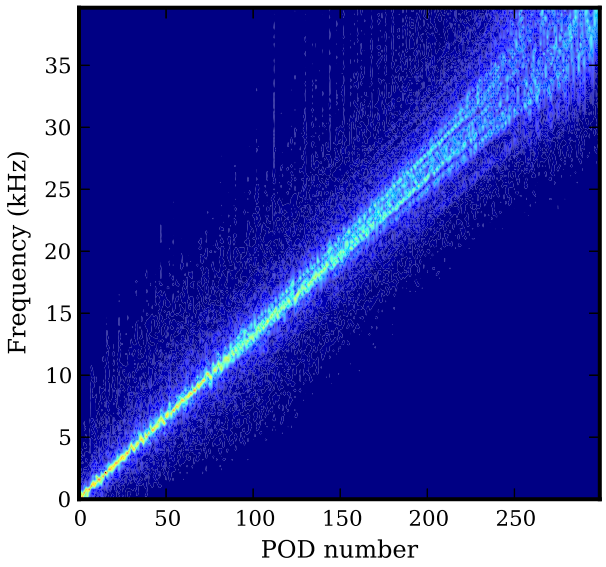

Figure 6.2: Frequency power spectrum for the temporal part of the POD modes

Because of the complex nature of the linear eigenmode and the non-trivial axial and azimuthal POD mode structures, it isn't that instructive to compare the real part of the linear eigenmode to the POD mode at a single point in the $\theta - z$ plane. Therefore, in Fig. 6.1 b), I take the RMS of the linear eigenmode and the RMS of the POD mode, averaging over θ and z. I further compare these to the RMS of the turbulent density fluctuations. Clearly, the dominant POD mode captures the turbulent fluctuations better than the linear eigenmode. This, along with the orthogonality of the POD modes, makes them better to use in certain situations than the linear eigenmodes.

Another interesting POD mode result is shown in Fig. 6.2, in which I plot the frequency spectrum of all of the temporal POD w_q modes. Surprisingly, each POD mode has a single frequency associated with it – although there is some spread, especially for the higher modes. This means that the POD is somewhat equivalent to a frequency decomposition in this case. This is not a typical property of the POD. In fact, I have not seen this in any other POD study. Perhaps this is a

consequence of the monotonic (non-peaked) frequency spectrum of the simulation. Nevertheless, this result requires further study that I leave to future work. It will not be applicable, in any case, to the POD energy dynamics.

6.3.2 POD Energy Dynamics

In order to construct the energy dynamics of the POD modes, I must first alter the data a bit because energy of the system in Eq. 6.1 is not simply given by $\|A\|^2$ if A is made up of the variables $(N, \phi, v_{\|e}, T_e)$ from which I constructed the POD above. The reason is that the energy contains equilibrium constants as well as the perpendicular gradient of ϕ rather than ϕ itself; the energy is not simply $E \neq \|A\|^2 = \left(N^2 + \phi^2 + v_{\|e}^2 + T_e^2\right)$. To fix this, I instead reconstruct A from the variables $(\sqrt{T_{e0}/N_0}N, \sqrt{N_0}\nabla_r\phi, \sqrt{N_0}\nabla_\theta\phi, \sqrt{N_0}\frac{m_e}{m_i}v_{\|e}, \sqrt{3N_0/2T_{e0}}T_e)$. This variable weighting provides the equality, $E = \frac{1}{2}\|A\|^2$. I then perform the POD with this A. The spatial POD modes u_q can be unweighted, broken apart, and unraveled to get back functions such as $n_q(\vec{r})$ which is the density part of the u_q POD mode. Let me give a name to this unweighted vector: $x_q = (n_q, \phi_q, v_q, t_q)$. The original data is still decomposed in terms of this vector,

$$(N, \phi, v_{\|e}, T_e) = \sum_{q=1}^{N_{\text{POD}}} \sigma_q x_q(\vec{r}) w_q(t) \tag{6.49}$$

and equivalently

$$N = \sum_{q=1}^{N_{\text{POD}}} \sigma_q n_q(\vec{r}) w_q(t) \tag{6.50}$$

but there is no orthogonality relation of these n_q or even the full x_q vectors, i.e.,

$$\sum_i n_q(\vec{r}_i) n_l^*(\vec{r}_i) \neq \delta_{ql}, \sum_i x_q(\vec{r}_i) x_l^*(\vec{r}_i) \neq \delta_{ql}. \tag{6.51}$$

Note that I construct the data that goes into the POD with 5 variables rather than 4 due to the need for both $-E_r = \nabla_r\phi$ and $-E_\theta = \nabla_\theta\phi$ in the energy expression and the requirement that A be a scalar. This is straight-forward enough to do,

but a potential complication arises when I unweight the u_q POD modes to recover $\phi_q(\vec{r})$. Seemingly, the unweighting recovers a $\phi_{r,q}$ and a $\phi_{\theta,q}$ that can be different, but in sum, $\sum_{q=1}^{N_{\rm POD}} \sigma_q \phi_{r,q} w_q = \sum_{q=1}^{N_{\rm POD}} \sigma_q \phi_{\theta,q} w_q = \phi$ must hold. Fortunately, however, the POD ensures that $\phi_{r,q} = \phi_{\theta,q}$ because each of the POD modes preserves any mathematical property of the original data such as the zero-curl nature of the electric field. I have confirmed this directly.

With this change of definition of A and the corresponding definitions for the POD modes, I can now construct the POD energy dynamics. Like in the previous sections, I start with Eqs. 4.1- 4.4. This time, I decompose the fields in terms of the POD modes. For example, I substitute $N(\vec{r},t) = \sum_{q=1}^{N_{\rm POD}} \sigma_q n_q(\vec{r}) w_q$ into N in the equations, and the same for the other independent variables $(\phi, v_{\|e}, T_e)$. Eq. 4.1 then becomes

$$\begin{aligned} \sum_{q=1}^{N_{\rm POD}} \sigma_q n_q \frac{\partial w_q}{\partial t} &= \sum_{q=1}^{N_{\rm POD}} \sigma_q w_q \left[-\frac{1}{r}\frac{\partial \phi_q}{\partial \theta}\frac{\partial N_0}{\partial r} - N_0 \frac{\partial v_q}{\partial z} + \mu_N \nabla_\perp^2 n_q \right] + S_N \\ &+ \frac{1}{r}\sum_{q,l} \sigma_q \sigma_l w_q w_l \left(\frac{\partial \phi_q}{\partial r}\frac{\partial n_l}{\partial \theta} - \frac{\partial n_q}{\partial r}\frac{\partial \phi_l}{\partial \theta} \right). \end{aligned} \tag{6.52}$$

Next, I multiply this equation through by $T_{e0}/N_0 \sigma_p n_p^* w_p^*$ and the other equations by their corresponding energy prefactors and POD's. The LHS of the density equation is

$$\sum_{q=1}^{N_{\rm POD}} \frac{T_{e0}}{N_0} \sigma_q \sigma_p n_q n_p^* w_p^* \frac{\partial w_q}{\partial t} \tag{6.53}$$

In Sec. 6.2, volume integrating this term at this point isolated $E_N(\vec{k})$. Volume integration of Eq. 6.53 will not produce the density energy of POD mode p: $E_N(p)$. The reason is that n_q and n_p^* are not orthogonal under volume integration as I pointed out in Eq. 6.51. They are not even orthogonal under volume integration with the appropriate energy prefactor. The reason is that n_q is only part of the total POD mode, which contains ϕ_q, v_q, and t_q as well. The orthogonality relation only holds when the energy of all of these are summed and the prefactors are added. That is, the orthogonality relation for the POD modes is a total energy

orthogonality. As a consequence, there is no meaning to an equation for $\frac{\partial E_N(p)}{\partial t}$. There is only meaning to an equation for the evolution of the energy of an entire POD mode: $\frac{\partial E_{tot}(p)}{\partial t}$. So, adding the four equations together and integrating over the volume results in a LHS of

$$\sigma_p^2 w_p^* \frac{\partial w_p}{\partial t} = \frac{1}{2} \frac{\partial \left(\sigma_p^2 |w_p|^2 \right)}{\partial t} = \frac{\partial E(p)}{\partial t}. \tag{6.54}$$

The RHS, on the other hand, does not simplify much at all upon summing the equations together and performing volume integration – other than the fact that the adiabatic response terms cancel each other due to the equation summation. Take the $-\mathbf{v}_E \cdot \nabla N_0$ term as an example. As it stands, the term appears as

$$-\int_V \left(\sum_{q=1}^{N_{\text{POD}}} \frac{1}{r} \sigma_q \sigma_p w_q w_p^* n_p^* \frac{\partial \phi_q}{\partial \theta} \frac{\partial N_0}{\partial r} \right) dV. \tag{6.55}$$

While such a term may be calculated as is, it is unfortunate that the sum over all of the POD modes remains. However, recall that the temporal w_q POD modes are orthogonal to each other upon time integration (Eq. 6.46). So if I time integrate the energy evolution equation, this term becomes

$$-\int_V \left(\frac{T_{e0}}{r N_0} \sigma_p^2 n_p^* \frac{\partial \phi_p}{\partial \theta} \frac{\partial N_0}{\partial r} \right) dV, \tag{6.56}$$

which is only a function of a single POD mode! This step is one of the reasons why the POD is preferable to other decompositions like the left/right linear eigenmode decomposition. One may notice, however, that time integration trivializes the LHS $\frac{\partial E(p)}{\partial t}$, which becomes approximately zero in the steady-state regime. Necessarily, the RHS must be zero as well. However, the goal is to understand the mode dynamics in the steady-state regime, and simply separating linear and nonlinear terms on the RHS, like what I did in Eq. 6.24 can give information regarding which POD modes inject energy into the system, which ones dissipate energy, and which modes transfer to which other modes. Specifically,

$$\int_t \frac{\partial E(p)}{\partial t} dt = L(p) + \sum_{q,l} T(p,q,l) = 0 \tag{6.57}$$

with the $L(p)/\sigma_p^2$ being the volume integral of

$$\begin{aligned} & \frac{T_{e0}}{N_0} n_p^* \left(-\frac{1}{r} \frac{\partial \phi_p}{\partial \theta} \frac{\partial N_0}{\partial r} + \mu_N \nabla_\perp^2 n_p \right) \\ + \quad & \frac{3N_0}{2T_{e0}} t_p^* \left(-\frac{1}{r} \frac{\partial \phi_p}{\partial \theta} \frac{\partial T_{e0}}{\partial r} + \mu_T \nabla_\perp^2 t_p + \frac{2\kappa_{\|e}}{3N_0} \nabla_\|^2 t_p - \frac{2m_e}{m_i} \nu_e t_p \right) \\ - \quad & \phi_p^* \left(\mu_\phi \nabla_\perp^2 \rho_p + \nu_{in} \rho_p \right) - \nu_e \frac{m_e}{m_i} N_0 |v_p|^2 \end{aligned} \tag{6.58}$$

where positive values of $L(p)$ indicate energy injection into the POD p-mode from the equilibrium gradients, while negative values indicate dissipation of energy. $L(p)$ of course, is the linear nonconservative part of the energy dynamics. The conservative nonlinear transfer term, unfortunately, cannot be simplified with the orthogonality relations due to the appearance of triple time products ($\int_t w_q w_l w_p^* dt$) and spatial products without the right form for orthogonality. I do not write it out explicitly here, but I note that $T(p, q, l)$ represents the energy transfer from POD modes q and l to POD mode p. To reiterate, Eq. 6.58 determines which POD modes inject energy into the fluctuation system, which ones dissipate energy, and how much they do so.

CHAPTER 7

Nonlinear Instability for the Periodic Simulation

In this chapter, I use the energy dynamics machinery developed in the last chapter to show where in wavenumber space and to which fields energy is deposited, how it's transferred, and where it's dissipated. I show that the linear instability plasma paradigm doesn't hold for the LAPD simulations, but rather, a complex nonlinear instability process dominates the energy dynamics. Furthermore, in this chapter, I consider only the simulations with periodic boundary conditions – the Periodic simulation and the $n = 0$ suppressed simulation. I analyze the remaining simulations (Dirichlet, Neumann, and Sheath) in the next chapter.

7.1 Energy Dynamics Applied to LAPD Turbulence

7.1.1 The Energy Spectra

Although I have already discussed the relative importance of the $n = 0$ fluctuation flute structures and shown evidence for this in Figs. 5.3, 5.4, and 5.8, I now use the energy expressions in Eqs. 6.25, 6.30, 6.35, and 6.40 to take a detailed look at the energy wavenumber spectra. The spectra for the four fields in (m, n) space are presented in Fig. 7.1. As expected from Figs. 5.3, 5.4, and 5.8, most of the density energy $E_N(\vec{k})$ is located at $n = 0$ (and $1 < m < 10$). This wavenumber location is much different from that of the fastest growing linear eigenmode, which is at $(n = 1, m = 60)$. Additionally, $E_T(\vec{k})$ and $E_\phi(\vec{k})$ have similar-looking spectra as $E_N(\vec{k})$, though the actual magnitudes of the energy are quite different for the three

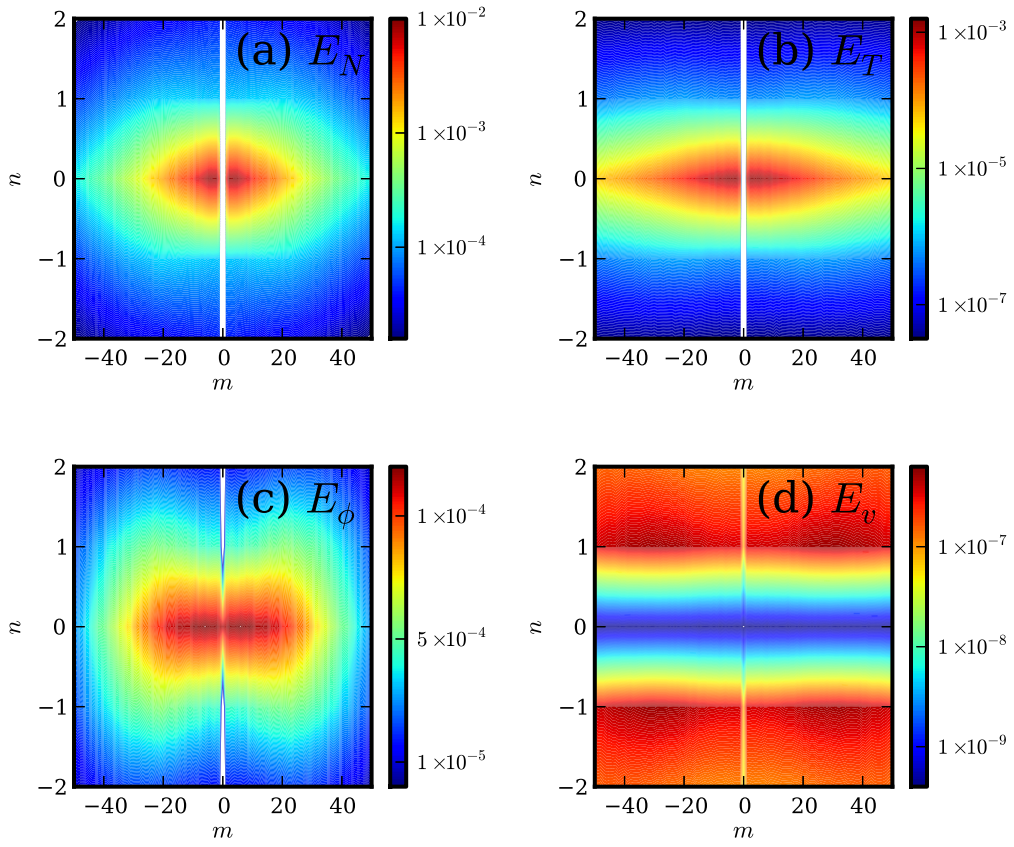

Figure 7.1: Energy k-Spectra of the different fields for the Periodic simulation

fields. Finally, $E_v(\vec{k})$ has a remarkably different energy spectrum than the other fields. Most of the energy is contained at $n \geq 1$ and $m \sim 30$, which is somewhat similar to the linear eigenmode growth rate spectrum, though m is lower.

Although these results seem contradictory to the notion that the most unstable linear eigenmode should pump energy into the turbulent system and thus dominate the energy, one might attribute the spectral results to a strong inverse cascade. In fact, in Ref. [UPC11], my collaborators and I posited and tested this hypothesis. Our specific hypothesis was that the most unstable linear eigenmode pumped energy into the system at its characteristic wavenumber and then proceeded to cascade energy forward and backward into other waves. The inverse cascade into $n = 0$ and low m would be particularly strong to account for all of the energy in the $n = 0$, low m Fourier components. Our test of this inverse cascade revolved around the use of a particular bicoherence three wave interaction, namely that between three density fluctuation Fourier modes of $(n, m) = (1, 25), (-1, -24)$ and $(0, 1)$ – not exactly local in m space as in a typical cascade picture. Note that in that study, we used a different set of profiles and smaller magnetic field for the simulation than the one I use here, so the dominant azimuthal mode numbers in that study were smaller than those in this dissertation. In any case, in Ref. [UPC11], we found a strong bicoherence amplitude for this three-wave interaction and assumed that this meant that the waves with $(n, m) = (1, 25)$ and $(-1, -24)$ coupled to transfer their energy to waves with $(0, 1)$. This fit within the standard linear instability paradigm because linear eigenmodes with $(n, m) \sim (\pm 1, \pm 25)$ were the most unstable for that system. Unfortunately, bicoherence is only a vague proxy for three-wave energy interaction, and it doesn't indicate a direction of energy transfer. As I later worked on energy dynamics calculations, I discovered, to my surprise, that we had the direction of energy transfer backwards! Our assumption regarding the direction of energy transfer was wrong. The paradigmatic plasma turbulence view led us astray.

7.1.2 Energy Dynamics Details

The full energy dynamics analysis using the machinery of Chapter 6 removes any ambiguity regarding the locations and magnitudes of energy injection into the fluctuations and direction of energy transfer between different Fourier modes. In fact, the full dynamics contains so much information that it can be difficult to digest it all. I therefore try to focus on the most important parts, especially those that are crucial to the nonlinear instability. First, in Fig. 7.2, I show values for some of the Q_j, C_j, and D_j terms in the energy dynamics equations for $n = 0, \pm 1$ and $0 \leq m \leq 100$, neglecting all dynamics with $|n| \geq 2$, which have relatively small values and are mostly insignificant. The dynamics curves are all averaged over a time period during the turbulent stage of the simulation where the dynamics processes have all reached a quasi-steady state. The label $n = \pm 1$ represents the addition of terms with $n = 1$ and $n = -1$. Fig. 7.2 a) displays the density potential energy injection (Q_N) and the adiabatic response transfer (C_N). I don't show the dissipation (D_N) in this figure, which is why the curves don't seem to add up to zero as they would if all dynamics were shown. Nevertheless, this figure immediately reveals that the majority of the energy is injected straight into the $n = 0$ fluctuations from the equilibrium density gradient rather than into the $n = \pm 1$ fluctuations! Looking at Eq. 6.26 again, and I reiterate, $Q_N(\vec{k})$ does not depend on n, so it is perfectly acceptable to inject energy straight into $n = 0$ fluctuations. However, $C_N(\vec{k})$ is dependent upon n (Eq. 6.27), so energy can only travel through the adiabatic response path in finite n structures. This is why the unstable linear eigenmodes have finite n – because eigenmodes with $n = 0$ cannot access the adiabatic response and thus have no field coupling. But with nonlinearities involved, there is nothing to prevent energy extraction at $n = 0$. Likewise, Fig. 7.2 b) reveals the same kind of story for the temperature potential energy, although the magnitudes are quite low compared to the density ones, indicating that the temperature fluctuations are relatively insignificant as a

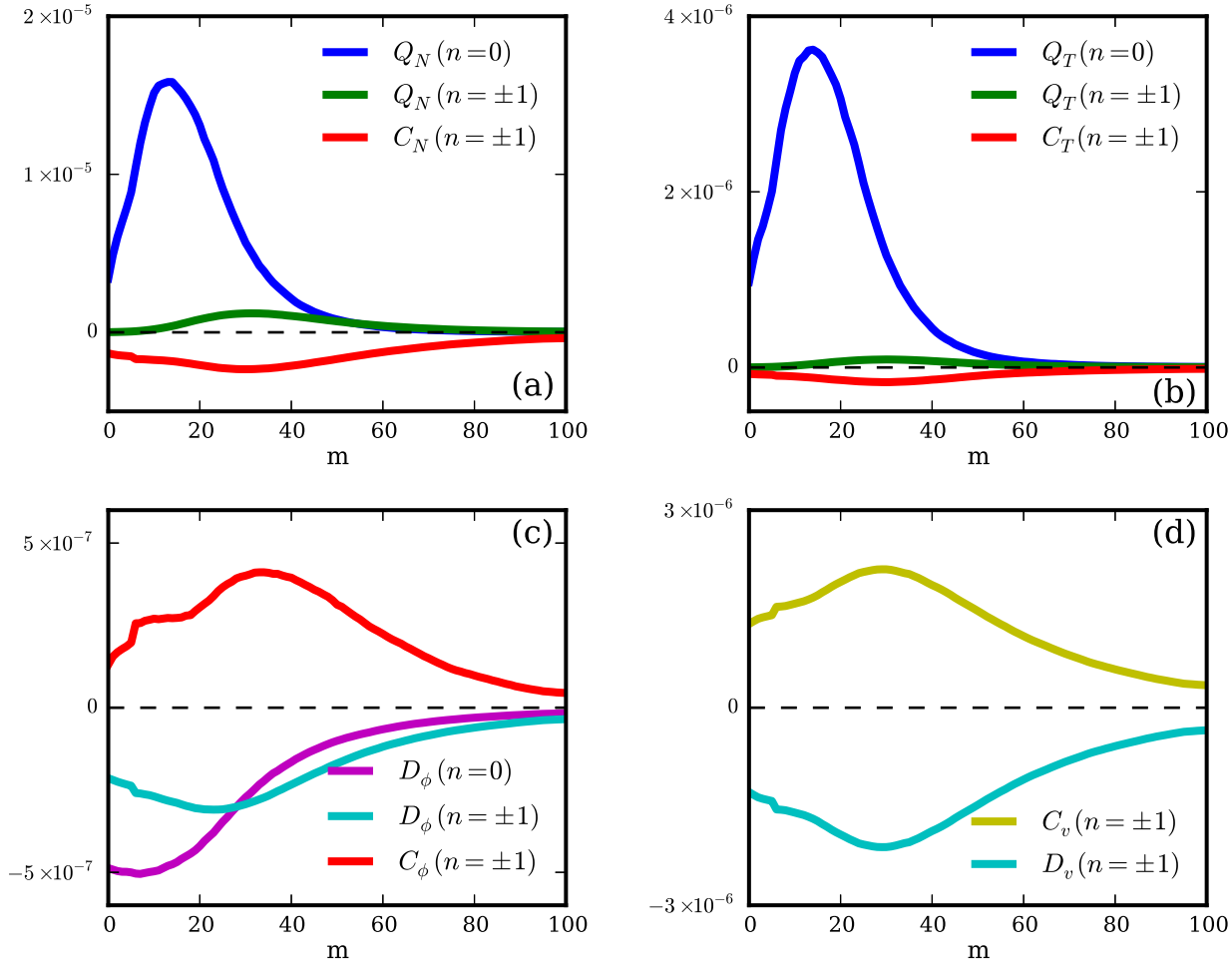

Figure 7.2: Most significant non-conservative energy dynamics results for dominant m and n numbers

player in the total energy dynamics.

Fig. 7.2 c) shows the perpendicular kinetic energy dynamics. Recall $Q_\phi = 0$, so there is no direct energy injection; rather, energy enters ϕ fluctuations via the adiabatic response (C_ϕ). Even though no energy enters ϕ at $n = 0$, flute-like dissipation $D_\phi(n = 0)$ is significant, foreshadowing the three-wave energy transfer into $n = 0$ ϕ fluctuations. Additionally, although I don't show $|n| \geq 2$ dynamics, they are somewhat important for C_ϕ and D_ϕ, accounting for the obviously unbalanced dynamics in this figure. Lastly, Fig. 7.2 d) reveals the parallel kinetic energy dynamics, which simply includes the adiabatic transfer (C_v) and electron-ion frictional dissipation (D_v). Recall that $C_N + C_\phi + C_T = -C_v$ for each $\vec{k}$. In other words, looking at the C_j terms altogether, one can see that energy is drawn from the density and potential fluctuations into the $v_{\parallel e}$ fluctuations and then moves onto the electrostatic potential ϕ fluctuations. That is only clear when looking at all of the C_j taken together.

Fig. 7.2 only shows the dynamical pieces due to the linear terms of Eqs. 4.1-4.4, and they therefore don't show the nonlinear transfer between different $\vec{k}$. The advective nonlinearities provide this transfer (the $T_j(\vec{k}, \vec{k'})$ terms), and they are essentially conservative, meaning they provide no net injection or dissipation with respect to the fluctuations. Now the $T_j(\vec{k}, \vec{k'})$ terms are each four dimensional, making them difficult to show. I choose to sum over some of the dimensions to show some of their aggregate properties. In Fig. 7.3 a), I sum over $\vec{k'}$ and n leaving them as only functions of m. Also note that I have divided $T_N(\vec{k}, \vec{k'})$ by 10 and multiplied $T_v(\vec{k}, \vec{k'})$ by 10 so that all of the T_j can be shown on one plot. Notice where T_N and T_T are positive and where they are negative. Negative values at a particular m indicate that the fluctuations with azimuthal wavenumber m are giving up net energy, while positive values correspond to fluctuations that are taking up net energy at that m. T_N and T_T transfer, on the aggregate, energy in the range $5 < m < 30$ to energy at all other values of m. This is not at all

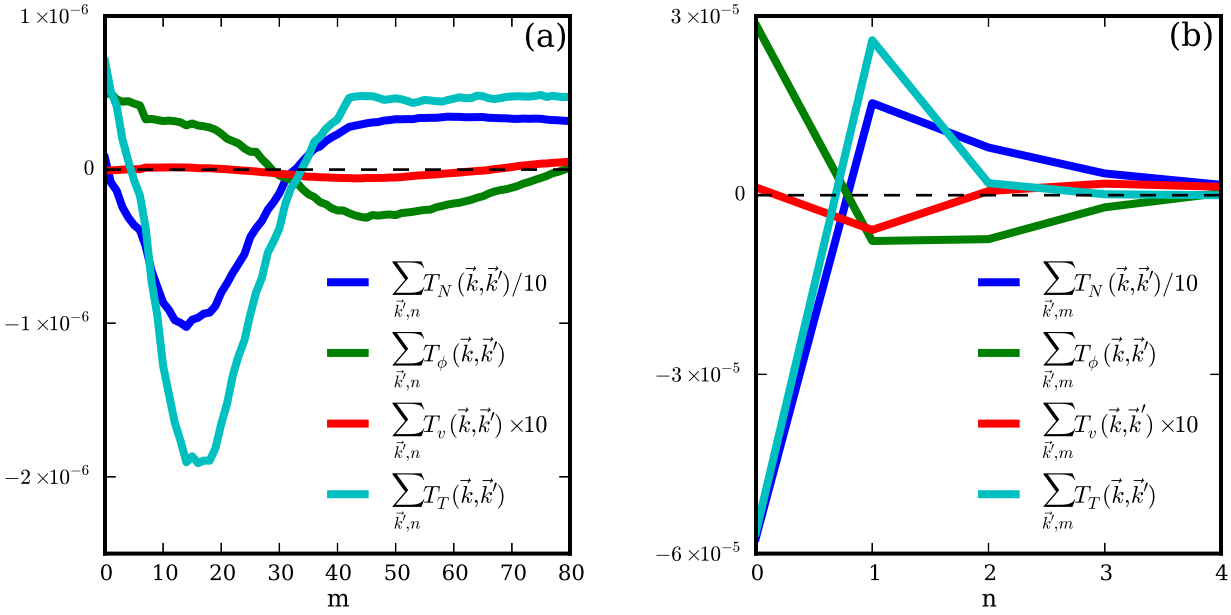

Figure 7.3: Periodic simulation conservative three-wave transfer dynamics

surprising because Q_N and Q_T are largest for $5 < m < 30$. This means that energy is injected from the equilibrium gradients at $5 < m < 30$ and then three-wave transferred into other azimuthal wave numbers in both forward and inverse cascades (mostly forward). Actually the summation I use hides the information regarding the locality of wavenumber transfer, so it's indeterminate from this figure whether the transfer process is by cascading or non-local transfer. On the other hand, T_ϕ and T_v have the opposite character of T_N and T_T, meaning that the transfer dynamics are the other way around. This is typical in similar systems, such as Hasegawa-Wakatani systems [HW83, CBS95] in which the density potential energy exhibits a forward cascade, while the perpendicular kinetic energy exhibits an inverse cascade. It was also obvious that this had to happen given the azimuthal asymmetry between C_ϕ and D_ϕ (see Fig. 7.2 c)).

More importantly, however, Fig. 7.3 b) shows the axial wavenumber transfers. Again T_N and T_T are similar. Both show energy transfer from $n = 0$ to $n \neq 0$. This

is truly important! It is the most direct evidence for the nonlinear instability. Our paradigmatic hypothesis in Ref. [UPC11] posited the opposite transfer direction. The most unstable linear eigenmodes have $n = \pm 1$ and all eigenmodes with $n = 0$ are stable, yet Fig. 7.3 b) shows that the dominant energy transfer is from $n = 0$ to $n \neq 0$, at least for N and T_e. Again, T_ϕ and T_v have the opposite character of T_N and T_T, as really they must, since ϕ and $v_{\|e}$ gain their energy through the adiabatic response.

It's still difficult to see the energy flow paths from Figs. 7.2 and 7.3 alone. So I have put the results in a flow diagram – Fig. 7.4. In order to do this, I've summed all quantities over m and n (including $|n| \geq 2$), except that I have left $n = 0$ components out of the sums and shown them separately. For instance, $Q_N(0)$ represents the density fluctuation energy injection at $n = 0$, while $Q_N(!0)$ represents the density fluctuation energy injection for all $n \neq 0$ summed together. Furthermore, the symbol $N(0)$ represents $\sum_m E_N(m, n = 0)$, $N(!0)$ represents $\sum_{m,n\neq 0} E_N(\vec{k})$, etc. Note that every term is summed over m.

The diagram starts at the top with the equilibrium density and temperature profile gradients in the orange boxes. They ultimately supply free energy for the fluctuations. Pointing out of them, the yellow Q_j's extract that energy, channeling it to the density and temperature fluctuations. The Q_j's are normalized so that they sum to 100 so that each one represents a percentage of energy brought into the system. Clearly, the $n = 0$ components dominate the energy injection from the equilibrium gradients, and the density injection is much stronger than the temperature injection. The blue T_N and T_T three-wave transfers both go in the direction of $n = 0$ to $n \neq 0$. Dissipation (the magenta arrows) acts on every fluctuation component and ultimately removes all of the injected energy from the system during the steady-state turbulent phase. Next, the red C_N and C_T transfer channels transfer energy from N and T_e to $v_{\|e}$, only at $n \neq 0$, which is the start of the adiabatic response. Actually, $C_T = 0$ because the parallel heat conduction

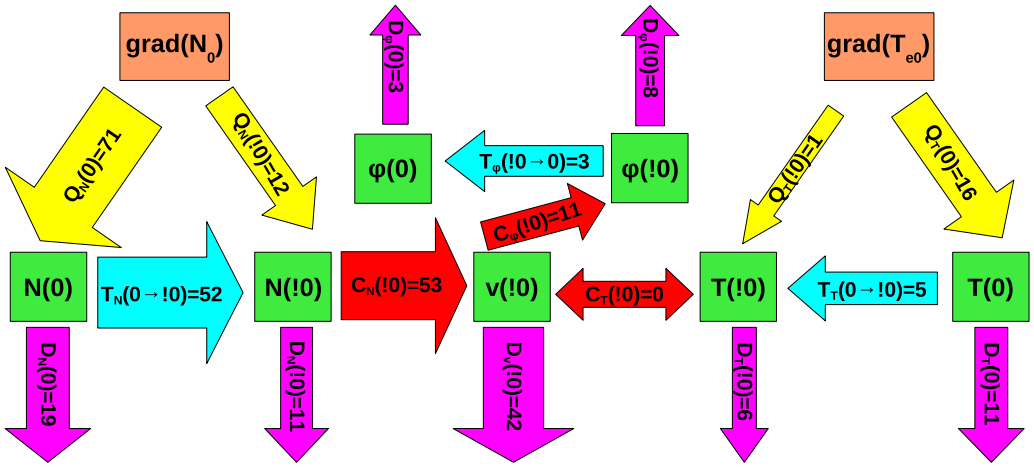

Figure 7.4: Periodic simulation energy flow diagram summed over m number and n number except for $n = 0$

is so dissipative. Completing the adiabatic response, C_ϕ transfers energy from $v_{\|e}$ to ϕ at $n \neq 0$. Finally, T_ϕ shows axial transfer into $n = 0$ ϕ components.

7.1.3 Nonlinear Instability

Fig. 7.4 provides a look at the way energy flows through the system. The nonlinear instability mechanism can be extracted from a subset of the steps in the flow diagram. I provide a reduced diagram in Fig. 7.5 to isolate the essential interactions of the nonlinear instability mechanism. Notice that I focus only on the density fluctuation side – as opposed to the temperature fluctuation side – because it's clear from the numbers in Fig. 7.4 that the density fluctuations are a much stronger drive for the system than the temperature fluctuations. Again, starting at the top, the $n = 0$ density fluctuations draw energy from the equilibrium density gradient by $n = 0$ fluctuating flow advection. Then, those density fluctuations nonlinearly transfer energy into $n \neq 0$ density fluctuations. Next,

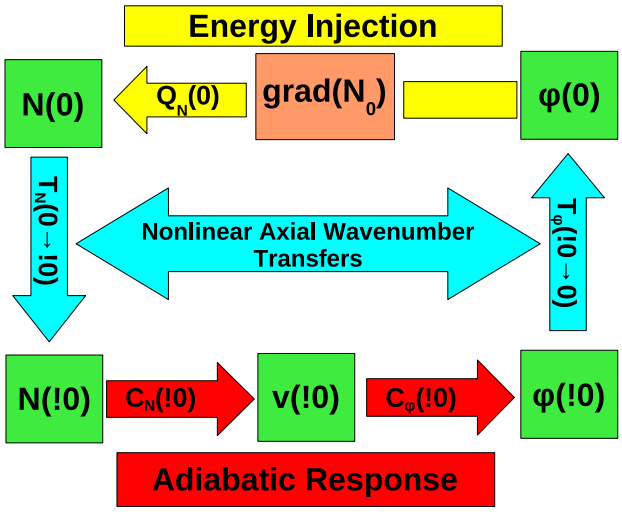

Figure 7.5: Nonlinear instability diagram that contains the pertinent and dominant parts of the energy dynamics

the adiabatic response acts to transfer some of that energy into $n \neq 0$ potential fluctuations, which finally nonlinearly transfer energy into the $n = 0$ potential fluctuations. Shown in this way, it's clear that the process is self-sustaining. It's also the dominant process by which the fluctuations get their energy from the equilibrium gradients, which is clear from the fact that $Q_N(n = 0)$ comprises 71% of all of the energy injection. Also, the net direction of T_N (from $n = 0$ to $n \neq 0$) and its large magnitude support this.

To me at least, this came as a big surprise due to my understanding of the unstable linear eigenmode drive paradigm. Given this paradigm, it seems counter-intuitive that energy can be injected into the fluctuations at $n = 0$, where only stable linear eigenmodes reside. The reason why stable regions in wavenumber space inject energy into the system is that the linear eigenmodes are nonorthogonal. Highly nonorthogonal stable eigenmodes may transiently draw energy from an equilibrium as I discussed in Sec. 2.2. To show that this happens in the sim-

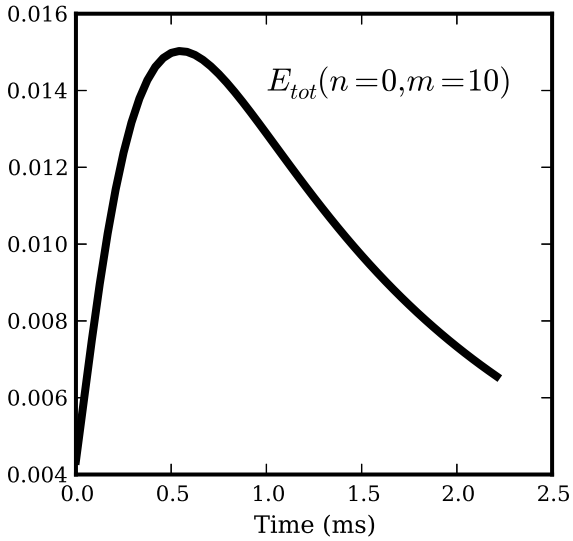

Figure 7.6: The transient linear growth of the $m = 10, n = 0$ energy component after the nonlinear simulation terms are turned off

ulation, I turn off the nonlinearities and observe the energy evolution. I show the total energy as a function of time after turning off the nonlinearities for the $n = 0, m = 10$ fluctuations in Fig. 7.6. At early time, the energy grows despite the fact that all of the linear eigenmodes with $n = 0$ are stable. Furthermore, it grows linearly (algebraically) at very early time, consistent with simple model calculations [Wal95]. At late time, the energy drops and doesn't recover because I have shut off the nonlinearities. As I discussed previously, the energy-conserving nonlinearities mix energy in the system, reinforcing structures which grow transiently, leading to a self-sustaining system of stable nonorthogonal linear eigenmodes. The key to this self-sustaining process is the ability of the linearly stable eigenmodes to transiently draw energy from the equilibrium, which happens in these simulations. This explanation does not take away the necessity of the $n \neq 0$ fluctuations, which are essential in this particular nonlinear instability for allowing access to the adiabatic response, another important step in the self-sustainment process.

7.1.4 POD dynamics

The transient growth mechanism due to the linear eigenmode nonorthogonality is quite unintuitive. It shows how difficult it is to gain intuition based on linear eigenmodes when they are nonorthogonal and how complicated their energetics analysis can be. This points to the need to use an orthogonal basis for mode decompositions. As I discussed in Sec. 6.3.1, the POD basis is ideal in many ways. Therefore, I perform a POD on the simulation following my treatment in Sec. 6.3.1 and calculate the energy dynamics following Sec. 6.3.2. However, before I perform the POD and the associated energy dynamics, I Fourier decompose the data axially and azimuthally to connect the results to those above. Since the axial dynamics proved essential in understanding the nonlinear instability, I use that to inform my POD analysis. Each complex spatial POD mode is a function of r, m, and n. I show an example of the radial structures of the first and fourth POD modes for $n = 0, m = 10$ in Fig. 7.7 a), where the solid line is the real part and the dashed line is the imaginary part. The lowest POD modes for a given (m, n) – those that contain the most energy, indicated by the highest values of σ_p – have relatively smooth radial structures, while the higher POD modes are more oscillatory.

Recall Eqs. 6.57 and 6.58, in which I defined the POD energy dynamics, specifically the nonconservative linear term $L(p)$. This term quantifies the time-integrated change of energy of POD mode p due to the linear terms of the equations. Of course, the nonlinear terms mix the energy between the different POD modes, so that in steady state turbulence, all of the POD modes retain a quasi-stationary level of energy. But in the Kolmogorov sense, it is informative to know which POD modes inject energy into the system and which dissipate energy. $L(p)$ gives this information. A compact way to show the nonconservative energy dynamics is through the effective POD growth rate: $\gamma(p) = L(p)/\sigma_p^2$ (more accurately $\gamma(m, n, p) = L(m, n, p)/\sigma_{mnp}^2$). I show this quantity, plotted against the square

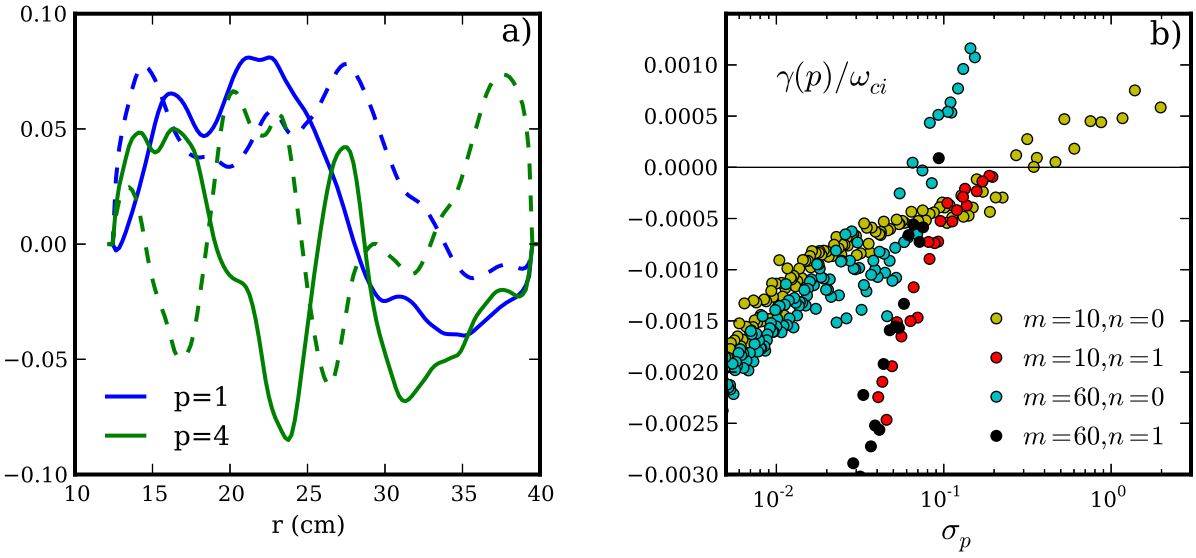

Figure 7.7: Representative POD radial structures and growth rates

root of the energy $\sqrt{E(p)} = \sigma_p$ for a large number of POD modes in Fig. 7.7 b). In this figure, I plot POD modes with four different values of (m, n), which I choose because they are particularly illustrative. First, I choose to show the $m = 10, n = 0$ POD modes because this is approximately where most of the energy is located in the turbulence (see Fig. 7.1). This manifests itself in the relatively large values of σ_p for some of these modes. Furthermore, the lowest $m = 10, n = 0$ POD modes – those with the highest σ_p – have positive growth rates, meaning these POD modes inject energy into the turbulence. This confirms the picture that I advocated in the previous sections, in which $n = 0$ structures inject fluctuation energy into the turbulence. It also confirms that orthogonal POD modes can provide better insight into turbulent processes than the linear eigenmodes of the system. This isn't surprising, given that the POD modes are derived from the turbulence, while the linear eigenmodes have no knowledge of nonlinear physics. Nevertheless, POD modes prove to be especially useful for non-normal systems.

Another set of POD modes that I plot in Fig. 7.7 b) are those with $m = 60, n = 1$ because this is the approximate location of the most unstable linear eigenmodes (see Fig. 5.1). These modes all have fairly low energy, and except for one mode that is just above marginal stability, they all have negative growth rates. This is also a non-normal effect, but it is opposite that which makes the $n = 0$ modes unstable. Again, this result is unintuitive and quite unexpected if one only considers linear eigenmodes. To compare to these two cases, I also show POD modes for $m = 60, n = 0$ and $m = 10, n = 1$. Again, some of the $n = 0$ modes have positive growth rates, while all of the $n = 1$ modes have negative growth rates. The linear eigenmodes have no bearing on the structure of the POD modes and therefore no obvious effect on the stability properties of the turbulent dynamics. The POD basis is dramatically more useful for understanding the turbulence than the linear eigenmode basis. Nevertheless, the POD basis is more difficult to obtain than the partial Fourier decomposition that I used in the previous sections, and it is probably worse in illuminating some turbulent processes like the nonlinear instability. I therefore leave it be for now.

7.2 n=0 Suppression

I previously introduced the $n = 0$ suppressed simulation in Sec. 5.3, where I discussed the nature of the simulation and some of its statistical properties. I claimed before that this simulation, in which I artificially remove the $n = 0$ components of the density, temperature, and potential fluctuations, eliminates the nonlinear instability. The details of the nonlinear instability mechanism described in the previous section should now make it obvious why removing these components eliminates the nonlinear instability. One may also consider other ways to remove the nonlinear instability while keeping the linear drift wave instability intact. For example, one could remove the $n = 0$ component of the linear drive terms or

remove one or more of the nonlinear advection terms, although this would affect quite a bit more than just the nonlinear instability. In any case, my method certainly removes the nonlinear instability mechanism while keeping the linear instability intact, allowing the simulation to act more in the paradigmatic manner.

Rather than showing another diagram of the energy flow for the $n = 0$ suppressed simulation, I construct a *spectral* growth rate from the spectral energy dynamics (those of Sec. 6.2). I emphasize, that I am not using the POD here. Thus, I define this growth rate as:

$$\gamma(\vec{k}) = \frac{\partial E_{tot}(\vec{k})}{\partial t}\Big|_{lin} \Big/ \left(2E_{tot}(\vec{k})\right) = \sum_j \left[Q_j(\vec{k}) + D_j(\vec{k})\right] \Big/ \left(2E_{tot}(\vec{k})\right). \quad (7.1)$$

Recall that $\sum_j C_j(\vec{k}) = 0$, so C_j does not appear in this sum. I also only include the linear contribution to $\frac{\partial E_{tot}(\vec{k})}{\partial t}$ so that the growth rate only involves the energy injection and dissipation at each wavenumber and not the three-wave transfers ($T_j(\vec{k}, \vec{k'})$). Adding the three-wave transfers would always make this sum about equal to zero in the turbulent quasi-steady state stage of the simulation anyway, rendering this quantity useless. In the *linear* stage of the simulations, this method reproduces the linear growth rate spectrum. I actually used this γ to generate the curves in Figs. 5.1 and 5.2, though I used other more common methods to confirm the accuracy of that calculation. γ can also be applied to the turbulent stage of the simulation – like I did with the POD modes in the previous section – where it describes the net energy injection into the system – or dissipation – at each $\vec{k}$ normalized by the steady-state energy at that given $\vec{k}$.

Fig. 7.8 shows the results of this calculation for three different cases. First, the light blue (cyan) curves represent $\gamma(m)$ for $n = 1$ (the solid line) and $n = 0$ (the dashed line) for the Periodic simulation during the linear exponential growth stage. The $n = 1$ curve is the same as that shown in Figs. 5.1 and 5.2. The $n = 0$ curve, on the other hand, is the linear growth rate of the $n = 0$ linear eigenmodes, which all have negative growth rates – since I take this after the

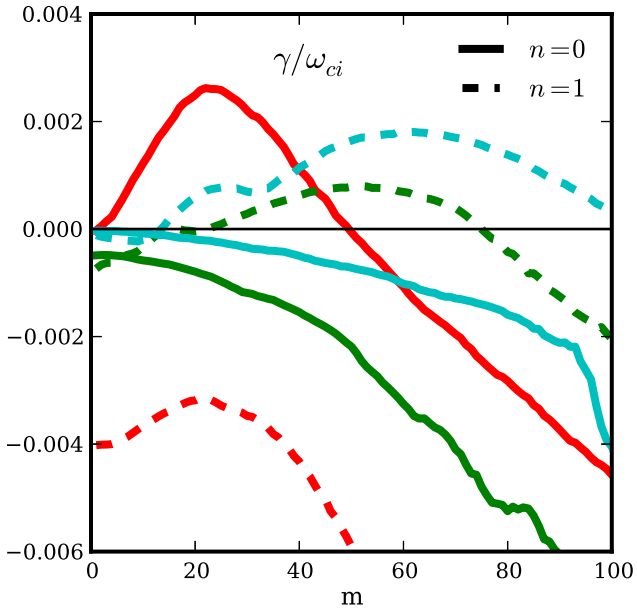

Figure 7.8: Linear vs. nonlinear growth rates

transient growth has ended. The red curves map out γ for the turbulent stage of the Periodic simulation. The $n = 0$ growth rate is *positive* for low m, while the $n = 1$ growth rate is negative for all m. This isn't surprising given the previous section's evidence for $n = 0$ energy injection due to the nonlinear instability, but it is certainly a nice way to show the contrast with the linear growth rate curves. The growth rates in the turbulent stage are consistent with the slopes of the transient growth curves like that shown in Fig. 7.6. Finally, the green curves are the growth rates for the $n = 0$ suppressed simulation during the "turbulent phase" – recall from Fig. 5.8 that the fluctuations remain rather coherent, and the state is only weakly turbulent. These growth rates are somewhat similar to the linear growth rates just as one might expect given the unstable linear eigenmode paradigm.

Now, one may wonder why there is any $n = 0$ growth rate curve at all for the $n = 0$ suppressed simulation. The reason is because I remove the $n = 0$ com-

ponents after they are nonlinearly excited. I allow the nonlinearities to transfer energy into the $n = 0$ components at each time step and then I save the data. The energy, by the way, is transferred from $n = 1$ to $n = 0$ modes in this simulation – consistent with the paradigmatic picture. Then, I remove these $n = 0$ components before the equations are evolved again. So there are small values for these $n = 0$ components that come out in the data, but are not used to evolve the equations. This allows construction of the $n = 0$ growth rate curve. Furthermore, notice that the $n = 0$ suppressed simulation growth rates do not exactly match the linear growth rates. The reason for this is that the nonlinearities change the structures and phases between the fields. Or to put it another way, they excite slower growing or damped eigenmodes that lessen the effect of the most unstable eigenmodes. This is consistent with the linear instability paradigm.

Finally, one might notice that manually removing all of the $n = 0$ fluctuation components means that the zonal flows ($n = 0, m = 0$ component of ϕ) are also removed. Zonal flows are often invoked as being an important saturation mechanism for turbulence by either shearing the turbulent eddies [BDT90] or by exciting stable eigenmodes [MTK12]. They are often considered to provide the most important nonlinear interactions to plasma turbulence. So one might naively think that their removal in the $n = 0$ suppressed simulation causes the removal of the nonlinear instability. I say "naively" because the nonlinear instability mechanism outlined in Fig. 7.5 doesn't depend upon zonal flows. But to prove this and to explore the real effect of the zonal flows, I have rerun the $n = 0$ suppressed simulation without removing the zonal flows. I still remove all of the $n = 0$ components of the density and temperature fluctuations and all of the $n = 0, m \neq 0$ components of ϕ, but I leave the zonal flow component intact. I show some comparisons of the two simulations in Fig. 7.9. In Fig. 7.9 a), I show the k_r spectrum of the two simulations, revealing that the zonal flows cause radial wavenumber transfers from low k_r to medium k_r. This is a simple consequence of a three-wave interaction

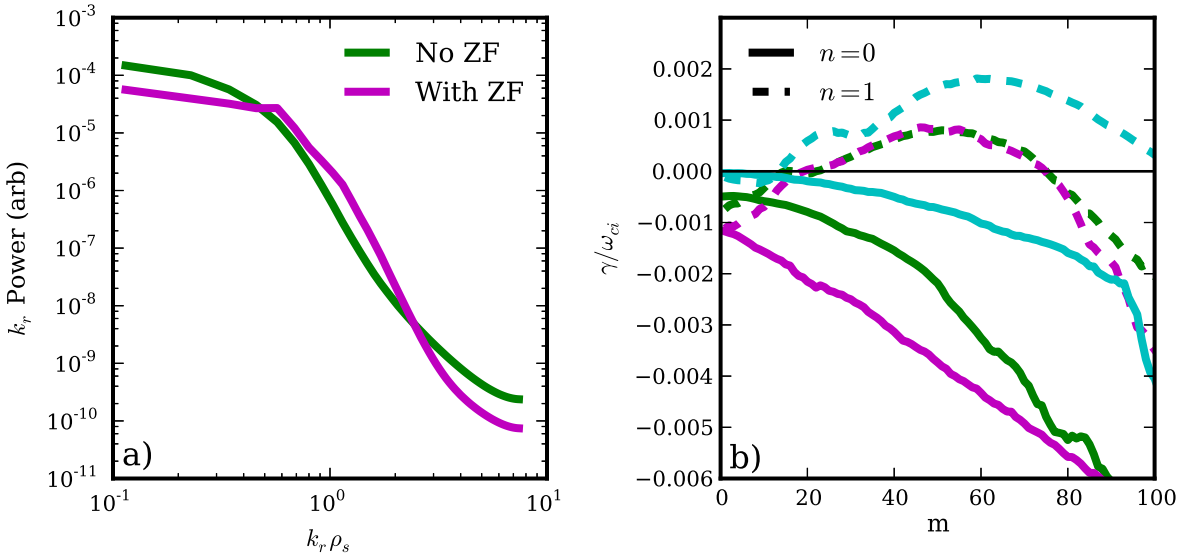

Figure 7.9: Zonal flow affect on spectra and growth rate

between the dominant low k_r structures and the zonal flows which have finite k_r. This interaction causes a slight saturation effect because the medium k_r modes have lower growth rates than the low k_r modes, and the overall saturation level is depressed by about a factor of 2 when I retain the zonal flows.

Nevertheless, the zonal flows don't cause the nonlinear instability, which is evident from Fig. 7.9 b) where the nonlinear growth rates of the two simulations are shown along with the linear growth rates. Recall from Fig. 7.8 how different the growth rates look when the nonlinear instability is active. The simulation with the zonal flows is qualitatively similar to the simulation without the zonal flows, but as expected, the growth rates with the zonal flows are less than or equal to the growth rates without the zonal flows. Interestingly, the zonal flows only affect the $n = 1$ growth rates at very low high m, but they affect the $n = 0$ growth rates mostly at medium m. Anyhow, the zonal flows don't affect the nonlinear instability and have a relatively weak affect on turbulent saturation compared to other types of turbulence like ITG [DBB00, HDC03].

7.3 Nonlinear Instability Literary History

After I found this curious nonlinear instability, I wondered if others had previously found this particular mechanism. After all, the equations and the geometry that I use are not new. In fact, a look at Fig. 7.5 reveals that even simpler models like the 3D Hasegawa-Wakatani equations [HW83] contain the proper components to cause the nonlinear instability. And cylindrical simulations of the Hasegawa-Wakatani equations are three decades old – although the original simulations were 2D. My search of the literature reveals that this nonlinear instability was, in fact, identified in 1995. Actually, going even further back, in 1977-1979, Cheng et al. [CO77, CO79] performed 3D turbulence simulations that may have actually been driven by the nonlinear instability. In their work, they identified a dominance of $k_\parallel = 0$ "convective cells [that] are non-linearly excited as a result of mode-coupling of the drift instabilities." It's unclear what equation set they used and what exactly they meant by this mode coupling, but their results seem similar to mine, and it's reasonable to believe that they at least identified the consequences of the nonlinear instability.

In 1995, Biskamp and Zeiler simulated local cylindrical plasma fluid turbulence in the first published use of the 3D Hasegawa-Wakatani equations [BZ95]. Using an energetics analysis, they in fact, correctly identified the nonlinear instability mechanism that drove the $k_\parallel = 0$ structures in their simulations. So the nonlinear instability mechanism is, in fact, not new. Furthermore, others expanded on this original work. Drake et al. showed that elimination of the linear instability by removing the $k_\parallel \neq 0$ components of the linear drive term had virtually no affect on the turbulence [DZB95]. Furthermore, they showed that adding magnetic shear, which also stabilized the linear drift waves, did not stop the turbulence from sustaining itself. Both of these showed that the nonlinear instability could act as a subcritical instability. A few years later, Camargo iden-

tified the nonorthogonality of the linear eigenmodes in the Hasegawa-Wakatani equations as a possible reason for effects that were previously attributed to nonlinear physics [CTC98]. Additionally, Scott and others have explore nonlinear drift wave turbulence in a number of different models with different physics effects such as magnetic shear and curvature and found that drift wave turbulence with very long parallel structures tends to sustain itself despite the lack of linear instability [Sco90, Sco92, ZBD96, ZDB97, KMN99, Sco02, Sco03, Sco05].

After visually exploring their turbulent simulations, Drake et al. proposed a physical mechanism for the nonlinear instability. The mechanism contains three steps: (1) a radially elongated $k_z = 0$ convective filament – or cell – radially transports density across the equilibrium density gradient, causing a density fluctuation with an azimuthal density gradient. (2) Radially propagating drift waves with $k_z \neq 0$ grow on this density gradient. (3) The flows associated with these drift waves reinforce the original radial flows of the convective filament. They went on to simulate this mechanism in a reduced equation set, using a finely crafted initial state to show the growth of the structures involved in the mechanism. It's not difficult to see that this mechanism is the same one that I described using Fig. 7.5, though my description used modal energy transfer language while Drake's uses the language of flows and drift waves. Furthermore, they lumped together my two middle steps into his single middle step. Nevertheless, our explanations are equivalent.

Drake et al. cleverly used their physical insight to develop a reduced turbulent model, consisting of only three modes: a $k_z = 0$ radially elongated mode, a $k_z \neq 0$ drift wave with finite radial and azimuthal wavenumbers, and a second $k_z \neq 0$ drift wave with higher azimuthal wavenumber with a phase such that its interaction with the other drift wave drives the $k_z = 0$ mode. The electrostatic potential resulting from these modes is given by the expression

$$\phi = \phi_0 \cos(\pi y) + [\phi_1 \cos(\pi y) + \phi_2 \sin(2\pi y)] \times \sin(k_z z) \exp(i k_x x). \tag{7.2}$$

The evolution of these modes can be calculated by insertion of this expression into the evolution equations (such as Eqs. 4.1 and 4.3). Further simplifying the resulting equations, they calculated that the $k_z = 0$ mode would grow with an algebraic time dependence of $t^{4/3}$; they didn't have any dissipation in the model to stop the growth, though. Such an algebraic time dependence is consistent with the notion of non-normal transient growth [Wal95]. They didn't make this connection, but in light of my Fig. 7.6 and general properties of non-normal subcritical turbulence, this isn't a surprising result.

Later, Krommes, noted the similarity between Drake's self-sustainment mechanism and the mechanism of turbulent self-sustainment in subcritical hydrodynamic flows like Poiseuille pipe flow [Kro99]. The self-sustainment mechanism in hydrodynamic flows is the following: (1) advection of mean shear by weak streamwise rolls (vortices) which create streaks (spanwise velocity fluctuations); (2) secondary instability of the resulting streaks; (3) nonlinear self-interaction of the streaks that re-energizes the original streamwise rolls. The streamwise rolls are elongated $k_z = 0$ structures. Furthermore, the first step is a linear interaction, called the 'lift-up' mechanism, which relies on nonorthogonal eigenmodes that grow transiently with algebraic dependence [TTR93, Wal95, Hen96]. This self-sustainment mechanism is analogous to the Drake plasma mechanism with the caveat that a secondary drift wave instability in the plasma case replaces the wake-like instability in the neutral fluid case. Such a correspondence between the two mechanisms led Krommes to suggest using mathematical techniques and conclusions from the neutral-fluid studies to further study the plasma mechanism.

CHAPTER 8

Energy Dynamics for the Non-periodic Simulations

I turn my focus in this chapter to the simulations with non-periodic axial boundary conditions: the Dirichlet, Neumann, and Sheath simulations. I showed in Sec. 5.1 that the linear properties of these simulations are rather different from the Periodic simulation and from one another. However, the statistical turbulent properties of the four simulations are all quite similar (Sec. 5.3). This, combined with the observation that the turbulence in the Periodic simulation self-organizes and drives itself by nonlinear instability, points to the conclusion that the axial boundary conditions have little affect on the nonlinear instability or the energy dynamics in general. Nevertheless, additional supporting evidence for this claim can provide confirmation regarding the robustness of the nonlinear instability. I therefore explore the energy dynamics of the non-periodic simulations in this chapter, attempting to differentiate the nonlinear dynamics from the linear ones.

8.1 Fourier Decomposing Non-periodic Functions

To my knowledge, nobody has considered the affect of non-periodic axial boundary conditions on this nonlinear instability in a straight magnetic field. But this is a critical extension of the topic because in the real world, linear plasma devices don't have periodic boundary conditions. Additionally, the nonlinear instability seems to crucially depend on axial wavenumber dynamics, which should be affected by

the axial boundary conditions. It is perhaps surprising then that nobody has taken up this line of research.

On the other hand, it may not be so surprising given that the non-periodicity can cause interpretation issues regarding the linear vs. the nonlinear instability. In the periodic case, the linear eigenmodes are sinusoidal with integer axial mode numbers, and all of the unstable eigenmodes have $|n| \geq 1$. So any energy injection into $n = 0$ fluctuations from the equilibrium gradients cannot come from the unstable linear eigenmodes. In the non-periodic cases, the linear eigenmodes are not necessarily sinusoidal (see Fig. 5.2 b)) and if they are, they certainly don't have integer mode numbers. Fourier decompositions of the non-periodic unstable eigenmodes yields finite $n = 0$ Fourier coefficients. This can muddle interpretation of energy injection into $n = 0$ fluctuations during the turbulent simulation phase. It seems as though a linear eigenmode decomposition may fix this problem, but as I commented in the last chapter, nonorthogonal eigenmode decompositions are difficult to analyze. Plus, it is difficult to calculate linear eigenmodes with two non-Fourier dimensions. So I proceed with the spectral energy dynamics on non-periodic simulations and show that the results are less clear-cut than those of the Periodic simulation, but nevertheless, rather conclusive in that the nonlinear instability still dominates.

First, however, I raise a related problem with Fourier decompositions of non-periodic data – Gibbs phenomena. Fourier basis functions are continuous and periodic, so Fourier decomposing discontinuous or non-periodic functions leads to Gibbs phenomena. One of the significant results of this is the slow convergence of Fourier reconstructions to the original signal. Mathematically, I can take a discrete signal with the following Fourier decomposition:

$$f(x) = \sum_{k=-Q}^{Q} \hat{f}_k e^{2\pi i k x}, \tag{8.1}$$

where the $\hat{f}_k$ are ordered in the sum by the size of their absolute value with $\hat{f}_0$

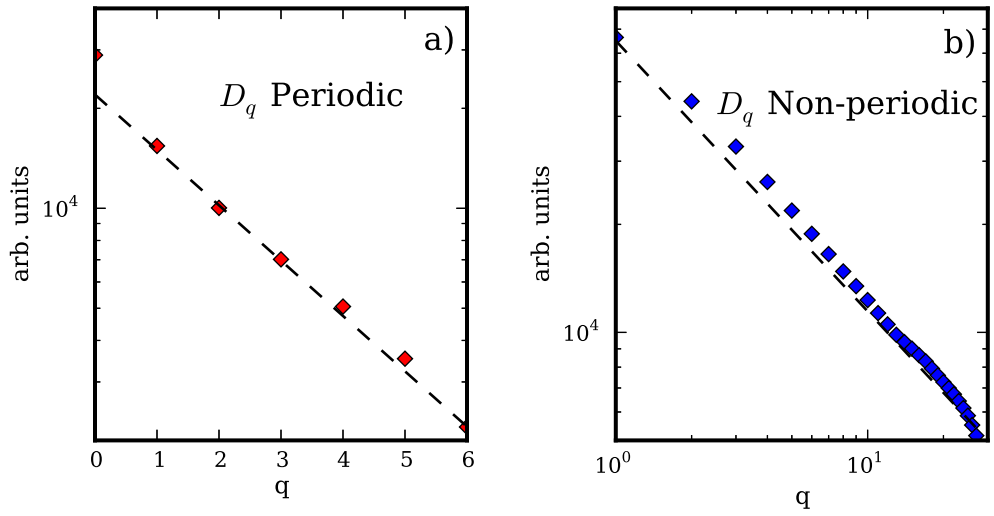

Figure 8.1: Convergence of Fourier reconstructions showing the effect of non-periodicity

being the largest Fourier coefficient. The Fourier reconstruction of rank $q < Q$ is:

$$g^{(q)}(x) = \sum_{k=-q}^{q} \hat{f}_k e^{2\pi i k x} \tag{8.2}$$

Defining the L_1 norm difference between the original signal and the rank q Fourier reconstruction as $D_q = \sum_x |f(x) - g^{(q)}(x)|$, one can study the convergence of D_q as a function of q. For continuous periodic signals, D_q converges geometrically, but it only converges algebraically for non-periodic or discontinuous signals.

As an example, I display D_q for the Periodic and Sheath simulations in Fig. 8.1. The Periodic simulation in Fig. 8.1 a) converges geometrically, while the Sheath simulation in Fig. 8.1 b) converges algebraically. Additionally, even though the x-axis indicates the mode with the q^{th} largest amplitude by construction of Eq. 8.2, it also corresponds to the axial mode number n for all but the last few q. In other words, in both simulations, most of the energy is contained in $n = 0$ modes followed by $n = 1$ modes and so on. So I should still be able to focus on the $n = 0$ and $n = \pm 1$ mode numbers in the energy dynamics data, but they will not

contain as much of the dynamics as they do for the Periodic case.

8.2 Energy Dynamics Results

The simplest way to view the vast quantities of energy dynamics information is through the effective growth rate defined in Eq. 7.1. So in Fig. 8.2, I show the growth rates for all of the simulations. In Fig. 8.2 a), I plot the growth rates during the turbulent phases of all five simulations (see Fig. 5.8 for the color code). Again, I break up the $n = 0$ and $n = 1$ components and don't show the $n \geq 2$ growth rates. Notice that the Periodic, Dirichlet, Neumann, and Sheath simulations all have quite similar growth rates, especially at $n = 0$. Their $n = 1$ growth rates have similar m dependencies, but somewhat different magnitudes, and the $n = 1$ growth rates are all negative except for a small region in the Dirichlet curve, which is marginal. Contrast these with the $n = 0$ suppressed simulation, which recall, is dominated by the linear instability. These growth rates certainly indicate that the same kind of processes occur for the four similar simulations regardless of axial boundary conditions – the nonlinear instability process. This isn't too surprising given the similarity of the turbulent statistics of the four simulations (Fig. 5.8).

It is also instructive to compare the nonlinear turbulent growth rates against the linear growth rates as I did for the Periodic simulation in Fig. 7.8. I do this for the non-periodic simulations in Figs. 8.2 b)-d). The black curves in these figures are the linear growth rates for each respective simulation. For example, the solid black line in Fig. 8.2 b) corresponds to the $n = 0$ linear growth rate of the Dirichlet simulation. The dashed black line in this figure corresponds to the $n = 1$ growth rate of the Dirichlet simulation. Note that the linear growth rates come from the same data as that used in Fig. 5.2, but these are decomposed in m and n, while those were simply decomposed in m.

All three of these simulations (Dirichlet, Neumann, and Sheath) have a lot of

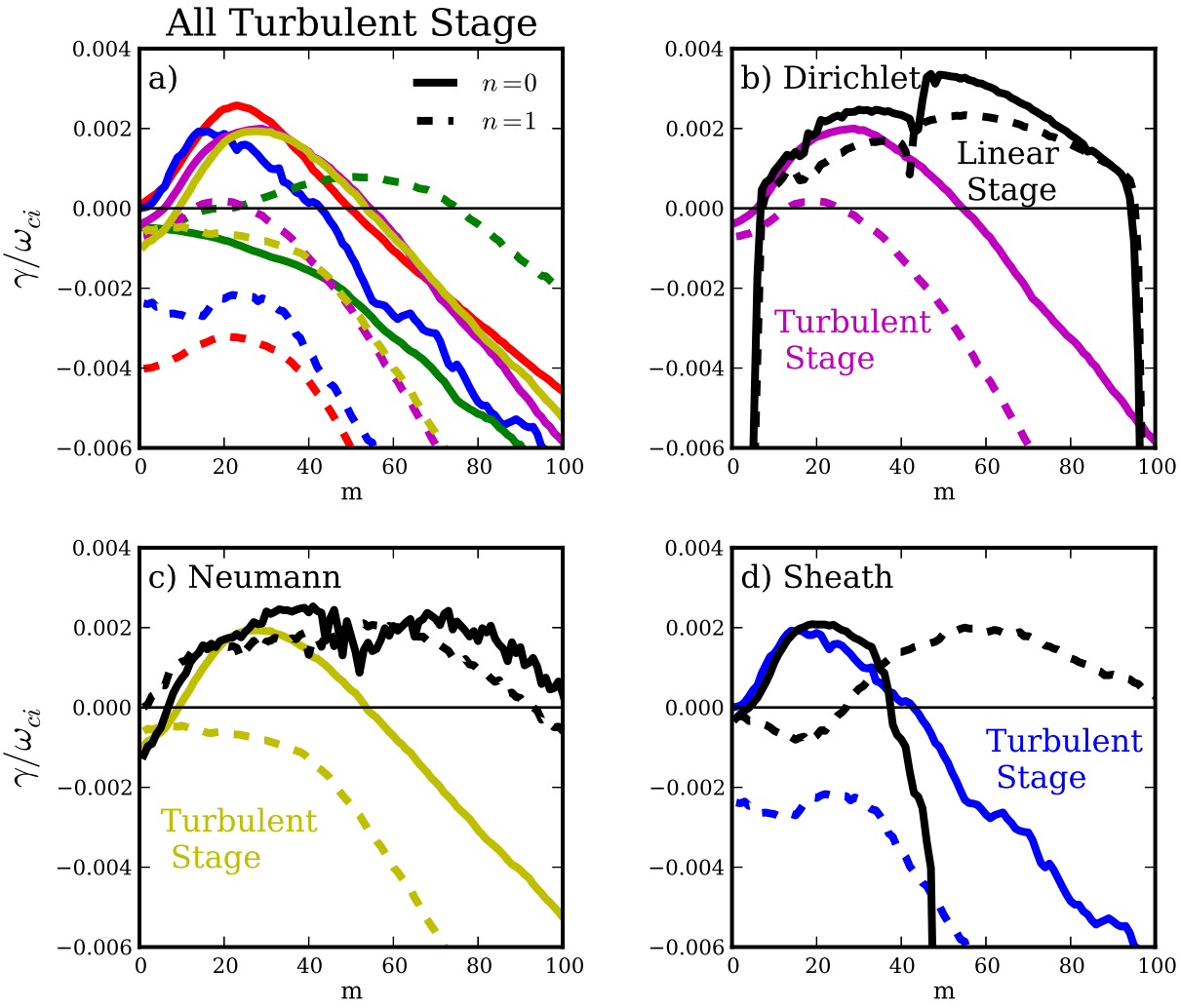

Figure 8.2: Linear and nonlinear growth rates of all simulations

similarity, especially the Dirichlet and Neumann simulations. All three have $n = 1$ growth rate curves that differ qualitatively between the linear and the nonlinear phase. For the most part, the $n = 1$ linear growth rates are always positive, while the $n = 1$ nonlinear growth rates are always negative. The $n = 0$ linear growth rates for the Dirichlet and Neumann simulations are similar to the $n = 1$ linear growth rates because the linear eigenmode structures contain roughly equal parts $n = 0$ and $n = 1$ and the density-potential phases are set by the linear drift-wave physics. The $n = 0$ and $n = 1$ Sheath simulation linear growth rates are quite different because the linear eigenmodes actually undergo a qualitative change at $m \sim 40$. All $m < 40$ Sheath linear eigenmodes have shapes like that in Fig. 5.2 b), which are even about the axial midpoint. However, all $m > 40$ linear eigenmodes have shapes that are odd about the axial midpoint. The CWM has even and odd solution branches whose growth rates cross at $m \sim 40$, causing this change.

In any case, it is interesting that the $n = 0$ linear and nonlinear growth rates for these three simulations are so similar for $m < 50$ but so dissimilar for $m > 50$. Does this low m region of similarity indicate that the linear instability dominates these simulations or is the similarity just a coincidence? To put it another way, is there some optimal axial wavelength that the Periodic simulation can only access by nonlinear instability, but the other simulations can access by linear instability? The difficulty in answering this question lies in my inability to perform a linear eigenmode decomposition energy analysis – due to their nonorthogonality. However, I have found a way around this.

8.3 Linear vs Nonlinear Structure Correlation

To try to sort out the problem of linear versus nonlinear instability in a non-normal linear system, I propose projecting the fastest growing linear eigenmode onto the turbulence and calculating the projection amplitude. If a linear instability is dom-

inant, a large portion of the fluctuation energy should reside in the fastest growing linear eigenmode structure [HTJ11]. It is the presence of the structure, after all, which injects energy into the fluctuation system. In the alternative case where a nonlinear instability is dominant, the linear eigenmode should have little bearing on the structure of the turbulence and therefore little energy should be contained in it. The only complicating piece of this conjecture is the nonorthogonality of the eigenmodes. Recall from Sec. 2.2.3 that the total energy of the system is made up of the energy from each of the individual eigenmodes *plus* cross energies from different eigenmodes. The cross energies may be negative. This, however, isn't a problem, which I now show in detail.

In my model, I fully describe the turbulent state by four independent fields, which I can appended into a single vector of the spatio-temporal field functions: $\boldsymbol{f}_{turb}(\vec{r},t) = \{N(\vec{r},t), T_e(\vec{r},t), \nabla_\perp\phi(\vec{r},t), v_{\|e}(\vec{r},t)\}$. $\boldsymbol{f}_{turb}(\vec{r},t)$ is the state of the system, and this analysis can be generally extended to any dynamical system. The state $\boldsymbol{f}_{turb}(\vec{r},t)$ may be decomposed in a complete basis:

$$\boldsymbol{f}_{turb}(\vec{r},t) = \sum_{i,m} c_{i,m}(t)\boldsymbol{\psi}_{i,m}(r,z)e^{im\theta}, \tag{8.3}$$

where $\boldsymbol{\psi}_{i,m}(r,z)$ are time-independent spatial complex basis functions, which for my system take the form: $\boldsymbol{\psi}_{i,m}(r,z) = \{n_{i,m}(r,z), t_{i,m}(r,z), \nabla_\perp\phi_{i,m}(r,z), v_{i,m}(r,z)\}$. The $c_{i,m}(t)$ are the complex time-dependent amplitudes. I have explicitly imposed a Fourier bases for the θ dependence of the basis functions, which need not be done in general, but it is convenient for my system and any system that possesses a symmetry – a periodic coordinate. Now, $\boldsymbol{\psi}_{i,m}(r,z)$ can be any linearly independent set of functions. The trick in proving the projection conjecture is choosing just the right set of basis functions. So first, I set $\boldsymbol{\psi}_{0,m}(r,z)$ to the fastest growing linear eigenmode. Then, I set the other $\boldsymbol{\psi}_{i\neq 0,m}(r,z)$ to functions that are orthogonal to $\boldsymbol{\psi}_{0,m}(r,z)$ and also orthogonal to each other. It isn't necessary to actually compute these other basis functions, but if I were to compute them, I might start

with all of the linear eigenmodes and perform a Gram-Schmidt orthogonalization procedure, making sure to start with the fastest growing eigenmode in order to preserve it. Hatch et al. [HTJ11] used this orthogonalization procedure explicitly. They found that a significant fraction ($\sim 50\%$) of the energy in a turbulent state of ITG turbulence was contained in the fastest growing linear eigenmode at each perpendicular wavenumber. Such a result, however, doesn't require knowledge of the other basis functions, and thus I don't compute them here.

Now, to compute the fraction of energy in the fastest growing eigenmode to the total energy, I first define an inner product that is energetically meaningful and that defines the orthonormality of the basis functions:

$$\langle \boldsymbol{\psi}_{i,m}, \boldsymbol{\psi}_{j,m} \rangle = \int w \boldsymbol{\psi}^*_{i,m} \cdot \boldsymbol{\psi}_{j,m} dV = \delta_{i,j}. \tag{8.4}$$

The weighting w is such that $\langle \boldsymbol{f}_{turb}, \boldsymbol{f}_{turb} \rangle = E_{turb}$. Now from Eqs. 8.3 and 8.4, $\langle \boldsymbol{f}_{turb}, \boldsymbol{f}_{turb} \rangle = E_{turb} = \sum_{i,m} |c_{i,m}|^2$ and $\langle f_{turb,m}, f_{turb,m} \rangle = E_{turb,m} = \sum_i |c_{i,m}|^2$. Then, the amount of energy contained in the fastest growing mode (for each m) is given by the square of the projection of the mode onto the turbulence: $E_{0,m} = |\langle \boldsymbol{\psi}_{0,m}, f_{turb,m} \rangle|^2 = |c_{0,m}|^2$. The ratio $R_m = E_{0,m}/E_{turb,m}$ is a measure of the fraction of turbulent energy contained in the fastest growing linear eigenmode.

Of course, $E_{turb,m}$ is easily calculated from the turbulent state, but $E_{0,m}$ in the turbulent state can only be found with knowledge of the fastest growing eigenfunction. The fastest growing eigenfunction, though, can be found easily by running a simulation from a random or turbulent state with all of the nonlinearities removed from the model equations. After some time, the fastest growing eigenfunctions will come to dominate the fluctuation structure. Then, a Fourier decomposition in m space will separate the fastest growing eigenfunctions at each m, including the real and imaginary part of the eigenfunctions – up to a time dependent complex constant, which is removed by normalizing the eigenfunction. Then, one can project the eigenfunctions onto the turbulent state with the inner product defined

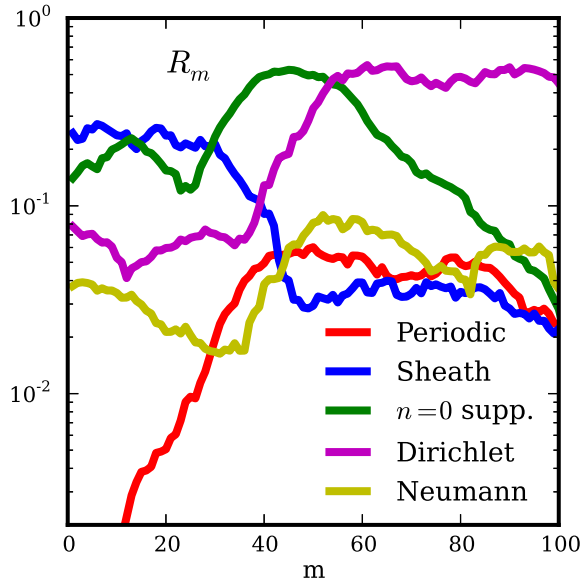

Figure 8.3: The ratio of energy contained in the most unstable eigenmodes to that in the turbulence

in Eq. 8.4, giving $E_{0,m}$.

I do this and show the ratio R_m in Fig. 8.3 for the five simulations. For the most part, the simulations other than the $n = 0$ suppressed one have a small value of the ratio ($R_m < 0.3$) for all m. This confirms that the turbulence largely self-organizes without regard to the linear physics in the four other simulations. The one exception is the Dirichlet simulation for $m > 50$, which has $R_m \sim 0.5$. This is quite the unexpected result, and I can't explain it based on any of the other evidence. Most of the energy in this and the other simulations, however, is at low m (Fig. 7.1), so these larger m eigenmodes don't make a large impact on the overall structure of the turbulence. In fact, R_m is below 0.1 for $m < 40$ for the periodic, Dirichlet, and Neumann simulations, precisely the area where $n = 0$ structures dominate the energy spectrum. This answers the question posed in the previous section regarding the similarity in the $n = 0, m < 40$ linear and nonlinear growth rates for the Dirichlet and Neumann simulations. The fastest

growing linear eigenmodes do not significantly drive the turbulence in this region! The nonlinear instability does.

On the other hand, the fastest growing eigenfunctions make up a significant fraction of the energy in the $n = 0$ suppressed simulation. Where the linear drift wave instability – and the turbulent growth rate – is the strongest (at $m \sim 50$) $R_m \sim 0.5$. The linear physics controls the $n = 0$ suppressed simulation, and the linear eigenmode structure certainly asserts itself in the turbulence, but still only to 50%. So since this is the controlling case, I cannot conclude that the nonlinear instability dominates unless $R_m \ll 0.5$. In that regard, the Sheath simulation is the most difficult to classify because it has significantly more linear eigenmode dominance at low m ($R_m \sim 0.25$) than the other nonlinear instability-dominated simulations, but it isn't at the 50% level. I therefore, refrain from classifying it, saying only that the linear and nonlinear instabilities are both quite active in this simulations. This raises the question of the importance of the CWM in LAPD, although LAPD doesn't have such simple boundary conditions, so I don't take this question further.

8.4 Nonlinear Saturation Levels

The prediction of the saturation level of turbulence is important for predicting transport. Generally, such predictions are based off of linear properties, however, a dominant nonlinear instability should have an effect on the level at which the turbulence saturates. One theory – mixing length theory – based on linear drift waves predicts that the saturation level should be about $\gamma/k_\perp^2$ where γ and $k_\perp$ are the growth rate and perpendicular wavenumber of the fastest growing linear eigenmode [Hor90]. Turbulence driven by a nonlinear instability may saturate at some other level, which seems probable given Fig. 5.8, which shows that the $n = 0$ suppressed simulation saturates at a lower level than the simulations driven by

the nonlinear instability.

Mixing length theory provides an estimate for the turbulence saturation level where only properties of the linear eigenmodes are known. This can be useful for finding scaling relations and allows prediction without direct numerical simulation. Therefore, I develop a corresponding estimate based on the drift wave turbulence driven by the nonlinear instability that I have described. Now, it is quite difficult to predict a saturation level based on a nonlinear mechanism when nonlinear simulation results are not available. However, as suggested in Ref. [CO79], and as seen in Fig. 5.4 b), it appears that the turbulence begins to saturate when the amplitude of the $n = 0$ fluctuations becomes equal to the $n = 1$ fluctuations. At this point, the strongest nonlinear interaction term catches up to the linear terms, bringing about the onset of saturation. However, the nonlinear instability really doesn't become important up until this point, which is why saturation occurs only when values are a few times higher than this point. Therefore, this crossing point can only be seen as a rough approximation for the saturation level, and more work will be needed to improve upon this calculation.

In order to find the crossing point amplitude, notice from Fig. 5.4 b), that before the components become equal, in the linear phase of the simulation, the $n = 0$ components seem to have twice the growth rate of the $n = 1$ components. This indicates that the $n = 0$ components are driven nonlinearly (parametrically). Furthermore, both are exponentially growing in the linear phase. It is possible then to use only linear eigenmode knowledge to compute the level at which the $n = 0$ and $n = 1$ components become equal as long as both start at small amplitudes and experience a few e-foldings before saturating. To find the crossing point, I first derive an expression for the time evolution of the linear eigenmode amplitudes. According to Drazin [DR81], such an evolution for the linear eigenmode A_j should take the form:

$$\frac{dA_j}{dt} = s_j A_j + N_j(A_k) \tag{8.5}$$

where the complex function N_j of the A_k's represents the nonlinear action of all the k modes on the jth – including the self-interaction. I now derive such an equation for my model set, finding the explicit forms for s_j and N_j.

8.4.1 Linear Eigenvector Amplitude Evolution

The linear eigenvectors are fixed composite objects of the independent fields ($N, v_{\|e}, \phi$ and T_e). Each one has a fixed complex-valued spatial structure where the different fields have a certain amplitude and phase relationship between each other. Each one evolves in time under the linear equation set with a fixed frequency and growth rate. Eigenmode structures of global simulations have radial and axial shapes that are not described by well-known functions like sines and cosines or Bessel functions. So to simplify matters, I use a local model in which each linear eigenmode can simply be identified by its wavevector $\vec{k} = (k_r, k_\theta, k_z)$. Then, the number of eigenvectors at each $\vec{k}$ is equal to the number of fields – 4 in my case.

Formally, the local fully spectral version of Eqs. 4.1- 4.4 can be written as

$$\frac{\partial \boldsymbol{\xi}_{\vec{k}}}{\partial t} = \mathbf{M}_{\vec{k}} \cdot \boldsymbol{\xi}_{\vec{k}} + \sum_{\vec{k}'} (k_r k'_\theta - k'_r k_\theta) \boldsymbol{\xi}_{\vec{k}'} \phi_{\vec{k}-\vec{k}'}, \tag{8.6}$$

where

$$\boldsymbol{\xi}_{\vec{k}} = \begin{pmatrix} N_{\vec{k}} \\ v_{\|e\vec{k}} \\ \phi_{\vec{k}} \\ T_{e\vec{k}} \end{pmatrix},$$

$$\mathbf{M}_{\vec{k}} = \begin{pmatrix} -\mu_N k_\perp^2 & -ik_z & -\frac{ik_\theta}{L_N} & 0 \\ -\frac{ik_z m_i}{m_e} & -\nu_e & \frac{ik_z m_i}{m_e} & -1.71\frac{ik_z m_i}{m_e} \\ 0 & \frac{ik_z}{k_\perp^2} & -\nu_{in}\mu_\phi k_\perp^2 & 0 \\ 0 & -1.71\frac{2}{3}ik_z & -\frac{ik_\theta}{L_T} & -\frac{2}{3}\kappa_{\|e}k_z^2 - \frac{2m_e\nu_e}{m_i} - \mu_T k_\perp^2 \end{pmatrix}$$

where I have used $\partial_r N_0 = -1/L_N$ in accordance with the local approximation, and I have neglected the sources, which are only nonzero for $k_r = k_\theta = 0$ in any case. The final term on the RHS represents nonlinear advection. Without this, the system is linear with the form of a linear eigenvalue problem:

$$\frac{\partial \boldsymbol{\rho}_{\vec{k},j}}{\partial t} = -i\omega_{\vec{k},j}\boldsymbol{\rho}_{\vec{k},j} = \mathbf{M}_{\vec{k}} \cdot \boldsymbol{\rho}_{\vec{k},j} \tag{8.7}$$

where $\omega_{\vec{k},j}$ and $\boldsymbol{\rho}_{\vec{k},j}$ are the eigenvalues and eigenvectors of $\mathbf{M}_{\vec{k}}$. j is an index that goes from 1 to 4, since there are 4 linear independent eigenvectors for each $\vec{k}$. I note that the linear matrix $\mathbf{M}_{\vec{k}}$ is not normal; therefore, the eigenvectors are not orthogonal. This can be a problem for eigenvector decompositions. However, the *left* eigenvectors are orthogonal to the right eigenvectors: $\mathbf{l}^T_{\vec{k},i}\boldsymbol{\rho}_{\vec{k},j} = \delta_{i,j}$, where

$$\mathbf{l}^T_{\vec{k},i} \cdot \mathbf{M}_{\vec{k}} = -i\omega_{\vec{k},j}\mathbf{l}^T_{\vec{k},i}. \tag{8.8}$$

Decomposing the spectral vectors $\boldsymbol{\xi}_{\vec{k}}$ with the linear eigenvectors:

$$\boldsymbol{\xi}_{\vec{k}} = \sum_{j=1}^{4} A_{\vec{k},j}\boldsymbol{\rho}_{\vec{k},j} \tag{8.9}$$

where $A_{\vec{k},j}$ are the time-dependent eigenmode amplitude coefficients, I substitute this decomposition into Eq. 8.6:

$$\sum_j \boldsymbol{\rho}_{\vec{k},j}\frac{\partial A_{\vec{k},j}}{\partial t} = \sum_j A_{\vec{k},j}\mathbf{M}_{\vec{k}} \cdot \boldsymbol{\rho}_{\vec{k},j} + \sum_{\vec{k}',j} A_{\vec{k}',j}(k_r k'_\theta - k'_r k_\theta)\boldsymbol{\rho}_{\vec{k}',j}\phi_{\vec{k}-\vec{k}'}. \tag{8.10}$$

Using Eq. 8.7 to simplify the first term on the RHS, then multiplying this equation on the left by the left eigenvector $l_{\vec{k},i}$, and using the eigenvector orthogonality relation:

$$\frac{dA_{\vec{k},i}}{dt} = -i\omega_{\vec{k},i}A_{\vec{k},i} + \sum_{k'} A_{\vec{k}',i}(k_r k'_\theta - k'_r k_\theta)\phi_{\vec{k}-\vec{k}'}. \tag{8.11}$$

This has the Drazin form of Eq. 8.5 where s_j is just the complex linear eigenfrequency, and N_j has the form indicative of a three-wave interaction. With this, I proceed to find the amplitude at which the $n = 0$ eigenmodes cross with the $n = 1$ eigenmodes.

8.4.2 Mixing Length Approximation

To begin, I apply Eq. 8.11 to the fastest growing drift wave in the linear phase of the simulation before the crossing of the $n = 0$ and $n = 1$ modes. The $n = 1$ fastest growing eigenmode curve, which has $m \sim 60$, evolves as:

$$\frac{dA_d}{dt} = -i\omega_d A_d \tag{8.12}$$

where A_d represents the fastest growing $n = 1, m \sim 60$ linear drift wave structure with time-dependent amplitude – d identifies drift wave eigenmode. Note that I have made the assumption that in the linear phase of the simulation, the linear term dominates the nonlinear term, which is quadratic in two small quantities. The solution of this equation is:

$$A_d(t) = A_d(0)e^{-i\omega_d t}. \tag{8.13}$$

On the other hand, the $n = 0$ mode has much smaller amplitude than the linear drift wave during the linear simulation phase, meaning that the nonlinear term can be comparable to or larger than the linear term. Specifically, the evolution equation for the $n = 0$ "flute mode" is:

$$\frac{dA_c}{dt} = -i\omega_c A_c + \sum_{\vec{k'}} (k_{rc}k'_\theta - k'_r k_{\theta c}) A_{\vec{k'}} \phi_{c-\vec{k'}}, \tag{8.14}$$

where I use the subscript c to denote the flute mode eigenmode. Now, the flute modes that grow the fastest under the nonlinear forcing have $m \sim 0$. This is clear by noting that the largest term in the sum should have $\vec{k'} = d$ and $c \sim 0$. Using the symbol M_{cd} for the wavevector difference $k_{rc}k_{\theta d} - k_{rd}k_{\theta c}$ and noting that $\phi_{-d} = \phi_d^* \sim A_d^*$,

$$\frac{dA_c}{dt} \approx -i\omega_c A_c + M_{cd}|A_d|^2. \tag{8.15}$$

Plugging in Eq. 8.13 into the A_d in this equation, and then solving this differential equation for $A_c(t)$ results in:

$$A_c(t) = A_c(0)e^{-i\omega_c t} + \frac{M_{cd}|A_d(0)|^2}{2\gamma_d + i\omega_c}\left(e^{2\gamma_d t} - e^{-i\omega_c t}\right). \tag{8.16}$$

I now make a simplifying approximation that $\omega_c = 0$. I essentially take the linear eigensystem of these flute modes to have zero axial wavenumber, zero frequency and growth rate, near-zero azimuthal wavenumber, and radial wavenumber about twice that of the drift wave radial wavenumber. These assumptions are not arbitrary. I get them by looking at the spectra of the flute modes and drift waves at the point of the simulation in which I'm interested. Furthermore, these assumptions make $k_{rc}k_{\theta d} \gg k_{rd}k_{\theta c}$, so that $M_{cd} \approx k_{rc}k_{\theta d}$ Then,

$$A_c(t) = A_c(0) + \frac{k_{rc}k_{\theta d}|A_d(0)|^2}{2\gamma_d}\left(e^{2\gamma_d t} - 1\right). \tag{8.17}$$

At the time (t_f), when the amplitudes of the drift wave and flute mode equal one another, the initial perturbation $A_c(0)$ is much smaller than the second term on the right hand side of Eq. 8.17 and can therefore be neglected when looking at large times. While this doesn't have to be true in general, it is true if the initial perturbations are set small enough. In fact, if the initial perturbations are not set to be small enough, the flute modes will not necessarily grow nonlinearly before saturating – they could grow transiently due to the nonorthogonality of the linear eigenmodes. So, setting the amplitude of $A_d(t_f)$ from Eq. 8.13 to the amplitude of $A_c(t_f)$ from Eq. 8.17 and performing some algebra, the result is:

$$|A_c(t_f)| = |A_d(t_f)| = \frac{2\gamma_d}{k_{rc}k_{\theta d}}. \tag{8.18}$$

The factor of two probably isn't significant given the approximations that went into this result, but the scaling of the drift wave growth rate, the drift wave azimuthal wavenumber, and the flute mode radial wavenumber are. The result is very similar to the mixing length result except that the wavenumbers of interest are from both the drift waves and the convective cells rather than from just the drift waves. Putting in LAPD values for this relation gives that the crossing level amplitude should be about 0.05. This is consistent with the amplitude at which the simulations begin to saturate, as can be seen in Fig. 5.4 a). Again, though, the ultimate saturation level is somewhat larger than this, and it's not clear if that

ultimate saturation level can be completely predicted prior to direct simulation.

One last point I want to make involves the $n \geq 2$ curves in Fig. 5.4 b). These curves all appear to grow at the same growth rate as the $n = 1$ curve during the linear stage of the simulation. This may seem odd because the linear growth rates of the eigenmodes with these higher axial mode numbers are much less than the growth rate of the fastest $n = 1$ eigenmode. Furthermore, if these modes were to be pumped nonlinearly (parametrically), one might expect them to grow with twice the growth rate of the $n = 1$ curve like the $n = 0$ curve does. In fact, the $n \geq 2$ curves are pumped nonlinearly. A look at the spectra (not shown) reveals that all of the $n \geq 2$ modes have $k_r - k_\theta$ spectra just like that of the $n = 1$ mode. So this means that the nonlinear interaction that drives the $n \geq 2$ modes involves the fastest growing $n = 1$ linear eigenmode beating against an eigenmode that has $k_r \sim k_\theta \sim 0$. This second eigenmode has close to zero growth rate, meaning that the $n \geq 2$ modes will only grow at the same rate as the fastest growing $n = 1$ linear eigenmode and not at twice its growth rate. It's difficult to guess this *a priori* due to the complexity of the nonlinear transfer term, so it seems that simulation results have to provide the evidence for this.

CHAPTER 9

Deterministic Chaos vs. Stochastic Turbulence

In this chapter, I tackle the difficult question regarding the level of determinism of the turbulence in LAPD. Through the previous chapters, I maintained the modern Ruelle and Takens [RT71] viewpoint that the turbulence is governed by a set of deterministic differential equations. That allowed me to simulate the turbulence using a set of differential equations with non-random coefficients. However, I also largely used statistical and structural theory to diagnose the turbulence, assuming as most do, that the large number of degrees of freedom available to the turbulence prevents a simpler diagnosis. In this chapter, I directly explore the assumptions that the turbulence is deterministic and that it has many effective degrees of freedom. I am motivated by the recent work on LAPD by Pace, Shi, Maggs, and Morales [PSM08a, PSM08b, SPM09, MM11, MM12b, MM12a, MM13], which I review below. Their conjecture is that the plasma turbulence in LAPD and a number of other devices is deterministic with a small number of effective degrees of freedom.

9.1 Lorentzian Pulses as an Indicator of Deterministic Chaos

In this section, I apply theoretical findings from work by Pace, Shi, Maggs, and Morales to study my own data. In their work, these authors identified exponential frequency spectra and Lorentzian pulses in the time signals of experimental measurements, which ultimately led them to conclude that the turbulence they were viewing was deterministic chaos. Since they based most of their analysis

and findings on time signals of experimental data rather than spatially resolved simulation data, I restrict myself here to looking at density and I_{sat} time signals, neglecting any simulated spatial structures. While comparing time signals point for point is futile in chaotic systems due to sensitivity to initial conditions, chaotic systems can produce time signals with identifiable visual characteristics. In this regard, Pace et al. discovered that the time signals in LAPD experiments and in the edge of some magnetic confinement devices contain Lorentzian-shaped pulses [PSM08a, PSM08b]. A Lorentzian is simply a function of the form

$$f(t) = A/\left[1 + (t - t_0)^2/\tau^2\right] \tag{9.1}$$

where A is the pulse amplitude, t_0 is its center, and τ is the pulse width. The absolute value of the Fourier transform of a Lorentzian is simply a decaying exponential, so the Lorentzian pulses in the time signals lead to frequency power spectra that have exponential shape, which show up as a straight line in a log-linear plot. In such a plot, the slope of the line is proportional to the Lorentzian width τ. Sometimes, however, the Lorentzian pulses in the time signals have different widths, which cause different spectral slopes, leading to power spectra with non-exponential shape.

To determine whether or not my time signals contain Lorentzian pulses, I first plot the frequency spectra of the experiment, the Periodic simulation, and the $n = 0$ suppressed simulation in Fig. 9.1 a). I don't use any window functions since they can distort any structures in the time signals, and I use only one radial location (30 cm) rather than doing a volume average. More spectra of this type are displayed in Fig. 5.11. Clearly, the spectra are not exponential for either the experiment or the simulations. This doesn't rule out Lorentzian pulses in the time signals, however, as long as the time signals have pulses of varying width. So next, I look directly at the time signals of the experiment and simulations. I show representative signals for the experiment, Periodic simulation, and $n = 0$ suppressed simulation in Figs. 9.1 b), c), and d), respectively. Notice

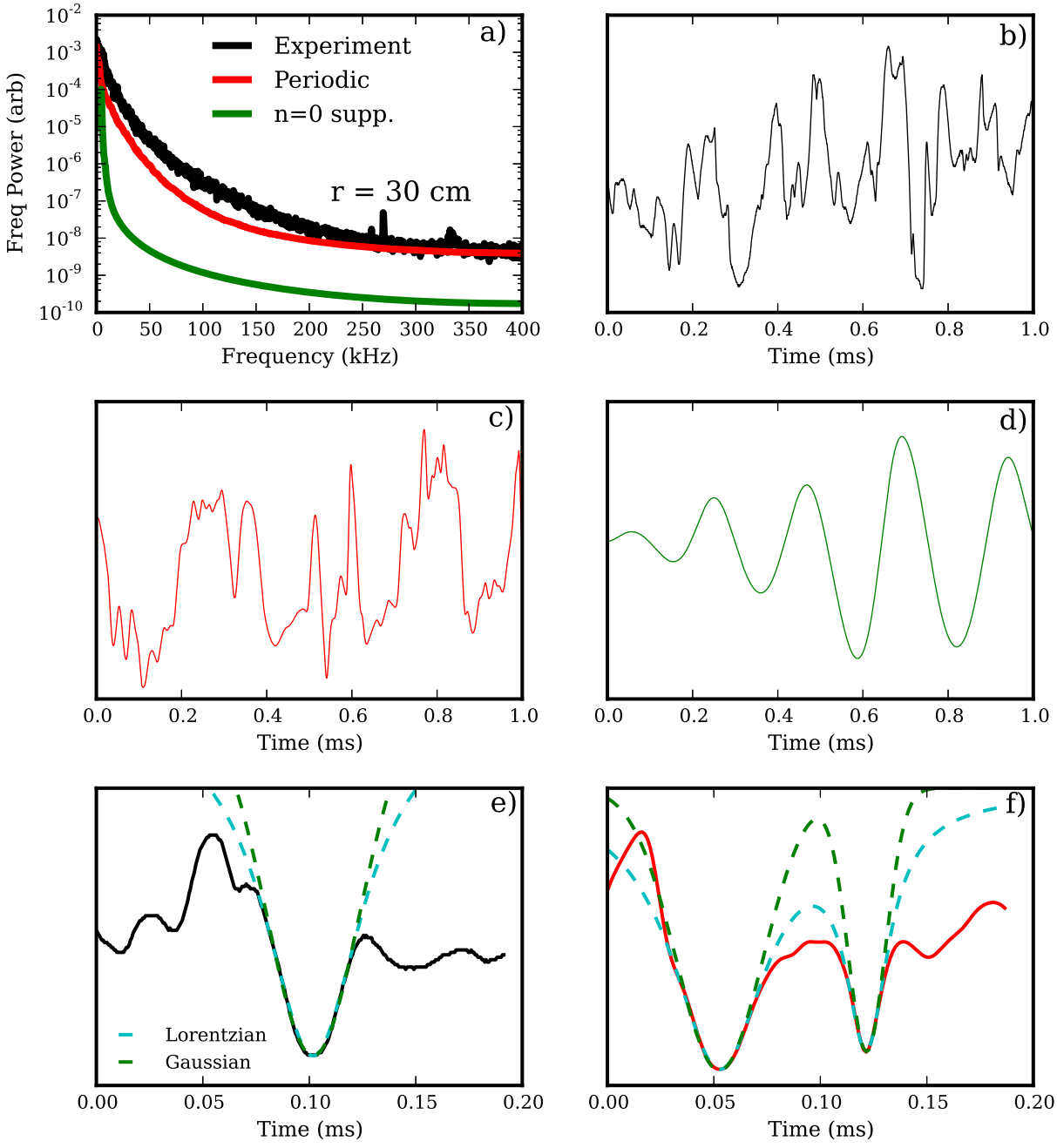

Figure 9.1: Lorentzian-shaped fluctuation pulses in time signals of experimental and simulation data

that the experiment and Periodic simulation appear to have qualitatively similar time signals, while the $n = 0$ suppressed simulation has a much different, simpler looking signal. Furthermore, the experiment and Periodic simulation contain a number of pulse-like features. I take a closer look at some of these pulses in Figs. 9.1 e) (experiment) and f) (Periodic simulation), trying to find times when the pulses are relatively isolated. In Fig. 9.1 e), I fit one of these pulses to a Lorentzian function (the dashed cyan line), proving that this pulse, does in fact have a Lorentzian shape. I confirm that a Lorentzian does provide a better fit than a Gaussian, which doesn't fit the pulse as well for as long of a time range as the Lorentzian, though the difference is quite small. However, Gaussian pulses create spectra that look very different from those in Fig. 9.1 a), supporting the claim that the pulses have Lorentzian rather than Gaussian shape. Finally, in Fig. 9.1 f), I look at a signal snippet from the Periodic simulation with two relatively isolated pulses, and I fit a sum of two Lorentzian functions to this. The fit is excellent, verifying that both of these pulses have Lorentzian shape, and importantly, they have different widths – explaining the non-exponential shape of the spectra. I don't show a fit to the $n = 0$ suppressed simulation signal, but I note that it is quite sinusoidal with seemingly two or so dominant low frequency waves, which is clear from the highly peaked, non-broadband frequency spectra.

Maggs and Morales recently explained the origin of the Lorentzian pulses in terms of phase space trajectories in dynamical systems theory [MM12b]. Specifically, they showed that some chaotic nonlinear systems – including the well-known Lorenz system [Lor63] – have phase space orbits on a strange attractor that circle indefinitely around two (or more) fixed points – think of the butterfly wings of the Lorenz attractor. The trajectory circles around one fixed point with ever changing radius, but eventually jumps and circles around the other fixed point. The jumps between the fixed points have trajectories that – when projected onto one coordinate – have a Lorentzian shape. In a plasma, an $\mathbf{E} \times \mathbf{B}$ flow controlled

by several modes – like drift waves – can have a Lorentzian structure. Since the flow advects the scalar density and temperature, it imprints the Lorentzian shape onto their time signals. Maggs and Morales conclude that since the Lorentzian shape specifically results from deterministic strange attractor orbits, systems that contain Lorentzian pulses are deterministic, not stochastic.

To understand this last point in terms of a real life system like a plasma that has access to an infinite number of degrees of freedom, note that in general solutions to dynamical systems can be controlled by an effective number of degrees of freedom that is less than that available to the system. Dissipative dynamical systems have some control parameter – like the Reynolds number – associated with them that determines their steady state behavior. At low values of the control parameter, the system often has a steady-state laminar solution called a fixed point. As the control parameter increases, the system can undergo a series of bifurcations in which each bifurcation increases the phase space dimension of the attractor solution and the effective degrees of freedom available to the system. For example, a limit cycle is a one-dimensional attractor with two effective degrees of freedom. Strange attractors often have fractional dimension greater than two [Man04]. The bifurcation from a limit cycle attractor to strange attractor then increases the dimension, or similarly increases the effective number of degrees of freedom available to the system. As the bifurcation parameter increases still further, the number of effective degrees of freedom increases, leading to high-dimensional hyperchaos. Therefore, infinite systems like real life fluids and plasmas may be controlled by deterministic motion. On the other hand, it may be the case that systems with extremely high-dimensional attractors may be indistinguishable from stochastic systems and systems with infinite dimension are stochastic.

For LAPD and similar plasma systems, the control parameters ought to be proportional to the equilibrium gradients. For the system to display Lorentzian chaotic dynamics, the conjecture is that the control parameter and thus the gra-

dient must be high enough so that the attractor is chaotic, but low enough so that it still has a Lorentzian trajectory associated with it – assuming the Lorentzians disappear or crowd each other out when the control parameter is too high. Furthermore, such a situation may be a natural consequence of chaotic advection in confinement-like systems because chaos causes transport which relaxes the gradients and prevents them from building up. The control parameter, therefore should not be able to grow much beyond the point where chaos ensues. In other words, the control parameter causes the chaos, but the chaos regulates the the control parameter, preventing the system from straying from the bifurcation point between the limit cycle and the low dimensional strange attractor.

I note, however, that this is less likely to be the case in LAPD than in confinement devices like tokamaks. The reason is that LAPD sustains particle losses through parallel transport to the ends of the machine in addition to radial transport losses. That is, the radial confinement time is on the order of the parallel confinement time in LAPD, which is different than the situation in all but the SOLs of confinement devices. Therefore, the chaotic or turbulent advection does not have a chance to completely relax the profiles to the point where this advection is shut off. That means that LAPD should be able to sustain a control parameter well above the chaotic threshold, allowing for high dimensional chaos, which may even be stochastic. I attempt to determine whether in the next sections whether the turbulence in the zero mean flow experiment is chaotic or stochastic and how high the dimension of its attractor is.

9.2 Permutation entropy as an Indicator of Chaos

While Lorentzian pulses in the time signals of experimental data provided the clue to the possible chaotic nature of the turbulence in LAPD, there are more direct and more conclusive ways to determine how deterministic versus how stochastic

a system is. Therefore, Maggs and Morales set out to test one of their LAPD experiments with one of these more direct methods [MM13], namely a method invented by Bandt and Pompe about a decade ago [BP02]. The Bandt-Pompe method, called permutation entropy, uses a time signal of a single observable to quantify the amount of determinism of the underlying process that creates the time signal. The method has gained better theoretical interpretation over the years, and various researchers have refined its implementation. Recently, Riedl et al. [RMW13] published a review on permutation entropy that provides theory, instructions, and most importantly, practical considerations for using the Bandt-Pompe method.

9.2.1 Trajectory reconstruction by the method of delays

The Bandt-Pompe permutation entropy is – for dynamical systems – based on a standard chaotic time signal analysis technique that is often called the method of delays, first formalized by Takens [Tak81]. The method of delays attempts to reconstruct the attractor that sits on a manifold in the phase space over which the effective dynamics take place. I review the method following Manneville's treatment [Man04], but I note that there is another nice review that is more freely available by Theiler [The90].

First, one can formally write the dynamical system $\dot{\mathbf{X}} = \mathcal{F}(\mathbf{X})$ for the state $\mathbf{X}$ in the phase space $\mathbb{X}$. Furthermore, there is a manifold $\mathbb{M}$ of dimension d_{eff} on which the dynamics lie, where d_{eff} is less than the dimension of the entire space $\mathbb{X}$. The only available information is the time signal W that is measured in an experiment. It is some unknown projection of the state $\mathbf{X}$ onto a single dimension: $W = \mathcal{W}(\mathbf{X})$. For a discrete time signal, the dynamical system may be approximated as

$$\mathbf{X}_{k+1} = \mathcal{F}(\mathbf{X}_k) \tag{9.2}$$

where the subscript denotes a time index. Reconstructing the dynamics amounts to determining an empirical relation between the $\mathbf{X}_k$ in their phase space and the observables $W_k,\ k = 0, 1, \ldots$ Clearly, $W_0 = \mathcal{W}(\mathbf{X}_0)$ is not sufficient to determine $\mathbf{X}_0$ since one coordinate is not enough to define $\mathbf{X}_0$. But, note that W_1 is to the projection of $\mathbf{X}_1$, which evolves from $\mathbf{X}_0$ under the map $\mathcal{F}$. Thus, the second measurement W_1 adds a piece of information about the coordinate $\mathbf{X}_0$ through $W_1 = \mathcal{W}(\mathbf{X}_1) = \mathcal{W}(\mathbf{F}(\mathbf{X}_0))$. The third measurement, W_2 further provides information on $\mathbf{X}_0$ through $W_2 = \mathcal{W}(\mathcal{F}(\mathcal{F}(\mathbf{X}_0)))$. In principle, a sufficiently long array of measurements of length d_{test}, $\{W_0, W_1, \ldots, W_{d_{\text{test}}-1}\}$ should serve to specify $\mathbf{X}_0$. Similarly, $\{W_1, \ldots, W_{d_{\text{test}}}\}$ specifies $\mathbf{X}_1$, etc. Eventually, a whole trajectory $\mathbf{X}_k,\ k = 0, 1, \ldots$ can be reconstructed from the series of vectors, $\mathbf{V}_k = \{W_k, \ldots, W_{k+d_{\text{test}}-1}\}$, existing in $\mathbb{R}^{d_{\text{test}}}$.

The length d_{test} of the reconstruction vectors can be increased until the method produces a reliable reconstruction of the trajectory. d_{test} must be large enough so that one does not lose any useful dynamical information. This means that different states must also have different reconstructions:

$$\mathbf{X}_k \neq \mathbf{X}_{k'} \rightarrow \mathbf{V}_k \neq \mathbf{V}_{k'} \tag{9.3}$$

The tentative number d_{test} of components used to reconstruct the state vectors is more properly regarded as the effective dimension of the space in which the effective phase space can be embedded by means of an injective map. Thus, I change notation from d_{test} to d_e, the embedding dimension. Takens theorem states that the $\mathbf{V}_k$ achieve a reliable reconstruction provided that the d_e are large enough: $d_e \geq 2d_{\text{eff}} + 1$. In chaotic systems, strange attractors often have fractal dimension, d_f, and one can replace d_{eff} by d_f in this inequality. Moreover, the $\mathbf{V}_k$ can actually be any series of d_e measurements, namely, $\mathbf{V}_k = [W_k, W_{k+\kappa_1}, \ldots, W_{k+\kappa_{d_e-1}}]$, where the κ_q can take on any values. It's natural to take the κ_q as multiples of some basic κ so that $\mathbf{V}_k = [W_k, W_{k+\tau}, \ldots, W_{k+(d_e-1)\tau}]$, where τ is the subsampling rate.

In practice, the usefulness of the method of delays relies upon choosing optimal values for the two basic ingredients in the reconstruction: the embedding dimension d_e and the subsampling rate τ (actually a time, not a rate). Optimal values can reduce the effects of noise on results and can minimize required computation and required length of time signals. The generally accepted optimal choice for the subsampling rate τ is the time over which a signal becomes decorrelated with itself [Man04, RMW13]. While the autocorrelation time seems like a natural quantity to use, it doesn't always lead to a satisfactory choice of τ. A better theoretical criterion, in fact, makes use of a quantity called the mutual information, defined as

$$I_{mut}(\tau) = \sum_{W',W''} P_\tau(W',W'')\ln\left(\frac{\mathrm{P}_\tau(\mathrm{W}',\mathrm{W}'')}{\mathrm{P}(\mathrm{W}')\mathrm{P}(\mathrm{W}'')}\right) \tag{9.4}$$

where $W' = W_k$, $W'' = W_{k+\tau}$, $P(W)$ is the probability distribution of the time signal W, and $P(W',W'')$ is the joint probability distribution function of the signals W' and W''. $I_{mut}(\tau)$ is a measure of the redundancy in the signal. When τ is small, the signals W' and W'' are highly correlated and I_{mut} is large, but when τ is large and the signals are uncorrelated, $P_\tau(W',W'')$ is essentially $P(W')P(W'')$, making I_{mut} small.

In Fig. 9.2, I show an example of $I_{mut}(\tau)$ for two time signals. The black curve is the mutual information of the experimental I_{sat} time signal at one radial location. The green curve is the mutual information of the x coordinate of the Lorenz model [Lor63]:

$$\dot{x} = \sigma(y-x) \qquad \dot{y} = x(\rho - z) - y \qquad \dot{z} = xy - \beta z \tag{9.5}$$

where I use the chaos-producing values $\sigma = 10, \rho = 28$, and $\beta = 8/3$. I numerically solve the Lorenz model with an integration time step 0.017 using a Python ODE solver. The Lorenz model has an oscillating and decaying $I_{mut}(\tau)$, while the experiment (and simulation) has a simple decaying mutual information. The optimal value of τ corresponds to the first local minimum of I_{mut}, which for

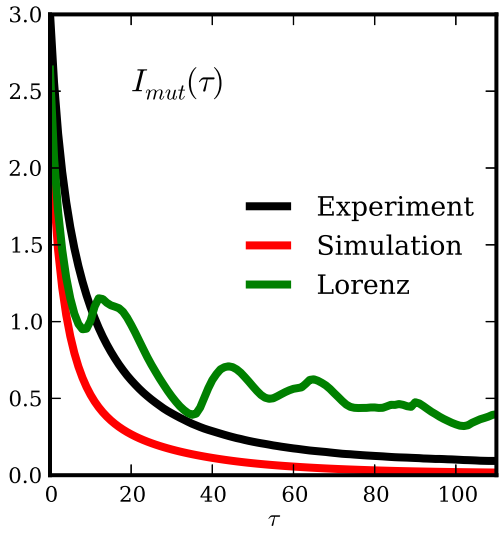

Figure 9.2: Mutual information of the Lorenz model, the experiment, and the simulation as a function of subsampling rate τ

the Lorenz model is at $\tau \approx 10$. The experiment has no local minimum, which can mean that there is either very large noise, the observable has been undersampled, or that too many degrees of freedom are involved [Man04]. All of these can be a problem for using methods of low dimensional deterministic dynamical systems. However, in the next section I review the permutation entropy, which can provide an optimal τ for the experiment. Furthermore, the permutation entropy can provide an optimal value for the embedding dimension d_e. There are other methods for finding the optimal d_e, such as the method of false neighbors [Man04], but I don't use it because it is difficult to analyze.

9.2.2 Permutation Entropy

The permutation entropy invented by Bandt and Pompe [BP02] defines an entropy measure for the time delay trajectory reconstructions based on their ordinal ranks. This means that the time delay embedding vectors $\mathbf{V}_k$ with embedding dimension $d_e = n$ are binned into $n!$ bins based on the order of their elements. For instance,

if $n = 3$ and one of the time delay reconstruction vectors is $\mathbf{V}_0 = (10, 15, 8)$, then this is binned based on its rank representation of $(2, 3, 1)$. The other vectors are binned similarly into the $3! = 6$ bins because that is the number of possible vector rank permutations. The number of vectors of a given ranked representation divided by the total number of embedding vectors produces a series of probabilities p_j that add up to 1. The Shannon permutation entropy is then defined by

$$P_n = -\sum_{j=1}^{n!} p_j \log_2(p_j) \tag{9.6}$$

It is also convenient to define different normalizations for the permutation entropy, such as $h_n = P_n/(n-1)$, which allows for entropy comparison with different n, and $H_n = P_n/\log_2(N)$, which ranges from $0 \leq H_n \leq 1$. More details on the procedure for calculating the permutation entropy may be found in Riedl et al. [RMW13].

Recall that the reconstruction vectors represent points on the attractor. The ranking procedure thus removes detailed information about the attractor. In fact, it partitions or bins the whole phase space, erasing detailed phase space information. Nevertheless, the ranked vector counting provides a good measure of how often a trajectory visits one of the phase space bins, which can provide a good proxy for the attractor's measure – the density of points on the attractor in a given region. In general, the permutation entropy retains broad underlying features of attractor trajectories that can be obtained in other ways. However, permutation entropy is generally much easier to calculate than other methods.

Since the permutation entropy relies on time delay reconstructions of phase space trajectories, it is important to use properly reconstructed vectors in the analysis. That means, one must use optimal values of the subsampling rate τ and the embedding dimension n for the permutation entropy to have any meaning. The strong dependence of the permutation entropy on these parameters makes it meaningless to compare the permutation entropy across different systems if the wrong parameters are used. I illustrate this strong dependence by calculating the

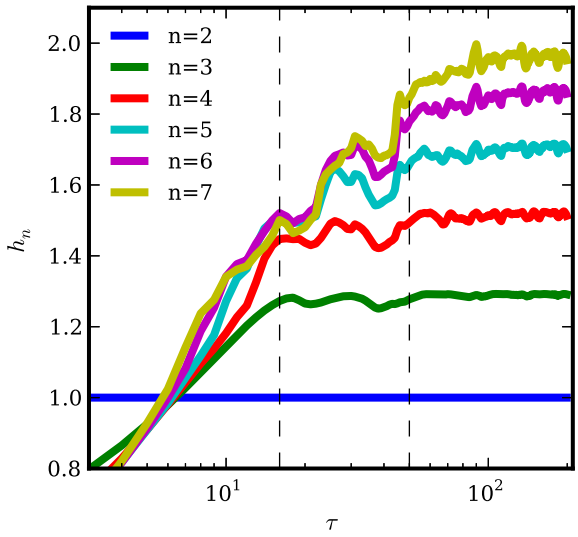

Figure 9.3: Permutation entropy as a function of subsampling rate τ and embedding dimension n for the Lorenz model

permutation entropy for the Lorenz model with varying values of τ and n, shown in Fig. 9.3. For the different curves, I use different embedding dimensions n. The horizontal axis is a function of the subsampling rate τ. I divide the figure domain into three separate regions, which I separate with the vertical dashed lines. The first region, from $1 \leq \tau \leq 16$ is the region where the permutation rises monotonically with τ. This rise is due to the under-subsampling in the reconstructed vectors, which is sometimes called the "redundancy effect" [RMW13]. The components in the reconstructed vectors are too highly correlated, which causes the reconstructed trajectory to visit only limit regions of phase space. The reconstructed trajectories are poor representatives of the original trajectories when the reconstructed vectors are under-subsampled. The region between the two dashed lines $16 \leq \tau \leq 50$ marks where the components of the reconstructed vectors become less correlated. For $\tau > 50$ every component in the vectors is uncorrelated with every other component, and the permutation entropy is relatively flat be-

cause the components cannot become any more decorrelated. This is called the "irrelevance effect."

Riedl et al. propose using the value of τ at the first dashed line, which in this case is 16. Note that this is about double what I found for the optimal value based on the mutual information analysis, but the different values produce permutation entropies that differ by only about 15%, so they do somewhat agree. Furthermore, other chaotic models that I have tested agree better when using the two techniques. As for the embedding dimension, they recommend using the value of n that produces the highest permutation entropy at the location of the first dashed line. For the Lorenz model, this is $n = 6$, although $n = 5$ comes very close. The embedding dimension, as required by Takens theorem [Tak81], which I discussed above, must be $d_e \geq 2d_f + 1$. Since the fractal dimension d_f of the Lorenz model is known to be 2.06, it requires an embedding dimension of 6, just what the permutation entropy analysis suggests. And an embedding dimension of 5 would not do too poorly either.

A final point regarding the calculation of the permutation entropy deals with the total number of time points that are needed to calculate it. The probability distributions that go into Eq. 9.6 of course become steadier as more reconstructed vectors are used, so the more time points the better. Actually, the number of vectors is more important than the number of time points, and since the number of vectors decreases with increasing τ, it is the total time used that's important. In general, Riedl et al. recommend using at least $5n!$ vectors, which puts practical limits on the permutation entropy technique since $n!$ grows so fast with n. In order to reconstruct extra vectors without increasing the total time of the data, one may consider changing the starting location of the reconstructions. For example, reconstructing vectors with time indices $[0, 10, 20, 30, 40]$, $[1, 11, 21, 31, 41]$, etc., where $\tau = 10$, produces more reconstructed vectors than if one throws out the vectors $[1, 11, 21, 31, 41] \ldots [9, 19, 29, 39, 49]$. However, there is little new infor-

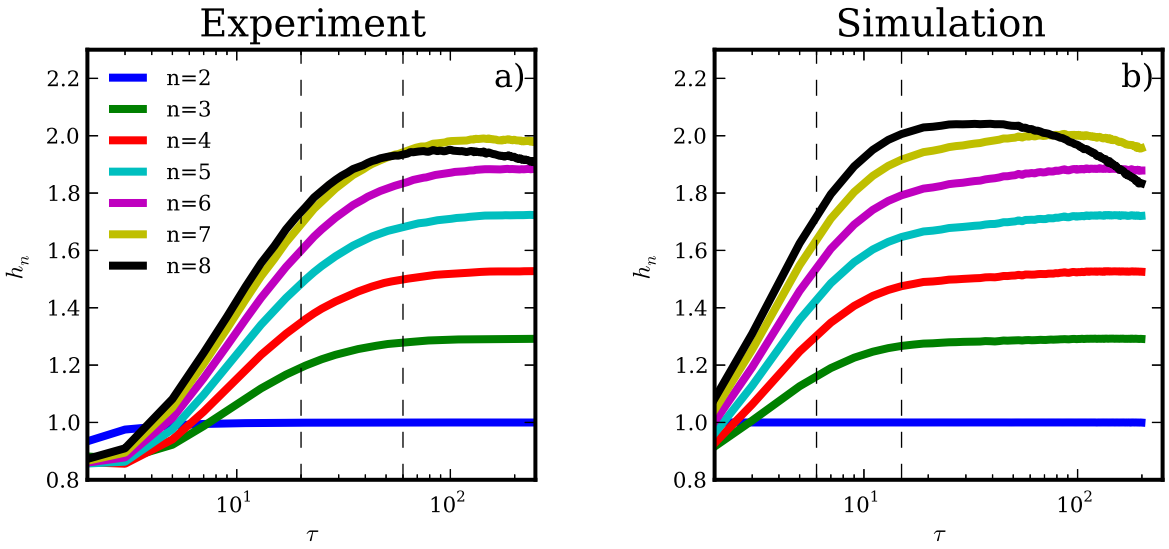

Figure 9.4: Permutation entropy as a function of subsampling rate τ and embedding dimension n for the experiment and simulation

mation from vectors $[1, 11, 21, 31, 41] \ldots [9, 19, 29, 39, 49]$ because they are highly correlated to vector $[0, 10, 20, 30, 40]$. So this doesn't significantly help. The permutation entropy is then quite limited to systems with small attractor dimensions. The same is true for other techniques of low dimensional deterministic chaos.

Moving to the LAPD data, I perform the permutation entropy analysis for the LAPD experiment and the Periodic simulation, which I show in Fig. 9.4. Like the Lorenz model curves, these curves all increase monotonically before eventually saturating and eventually reach an irrelevance point. This alone is a good indication that the experiment is deterministic chaos. Stochastic models don't act this way [RMW13]. The region between the redundancy and irrelevance effects is difficult to identify, but that is not essential. One important new effect, however, is the falloff of the entropy for high τ and high n. This is a result of using too few reconstructing vectors (fewer for the experiment), and it places a practical limit on the analysis at $n \sim 8$ – not to mention the time it takes to calculate the

entropy as n becomes this large. Moreover, the experiment and simulation have different optimal subsampling rates: 20 and 6, respectively, but this is not meaningful since the original sampling is not the same. Essentially, the experiment and simulation have the same permutation entropy curves, further validating the simulation. They both have higher permutation entropies than the Lorenz model: $h_{n,\text{lapd}} > 1.7$ compared to $h_{n,\text{Lorenz}} = 1.5$. However, it is clear that the permutation entropy at the dashed line is still rising as n increases, meaning that the optimal embedding dimension is above 8. And I cannot increase the embedding dimension without significantly increasing the time of the experiment and the simulation. In fact, the total time of the experiment can be limited by the constancy of the underlying dynamical system. In other words, if the equilibrium parameters change during the experiment, the attractor solution will change, invalidating the analysis. The permutation entropy, therefore, cannot be accurately calculated for the turbulence in LAPD. The turbulence simply has too many effective degrees of freedom, indicating that it is high dimensional.

Nevertheless, there are other measures that can differentiate between high dimensional deterministic processes and very high dimensional stochastic ones. One such method makes use of the structural complexity of the time signals. The Jenson-Shannon complexity is defined by [RLM07]

$$C_S^J = -2\frac{P_n(\frac{p+p_e}{2}) - \frac{1}{2}P_n(p) - \frac{1}{2}P_n(p_e)}{\frac{N+1}{N}\log_2(N+1) - 2\log_2(2N) + \log_2(N)}H_n(p) \tag{9.7}$$

where P_n is the Shannon permutation entropy defined in Eq. 9.6. $P_n(p)$ refers to the normal permutation entropy. $P_n(p_e)$ refers to the maximum entropy, which occurs for $p_j = 1/N,\ j = 1, 2, \ldots, N$. H_n stands for the permutation entropy normalized by $\log_2(N)$, which takes on values in the range of 0 to 1. The complexity provides an important additional piece of information that the entropy alone does not, namely, it quantifies the degree of temporal structure correlation in a a signal. And structural correlation indicates determinism. The way in which complexity can be used to differentiate chaos from stochasticity is by plotting the

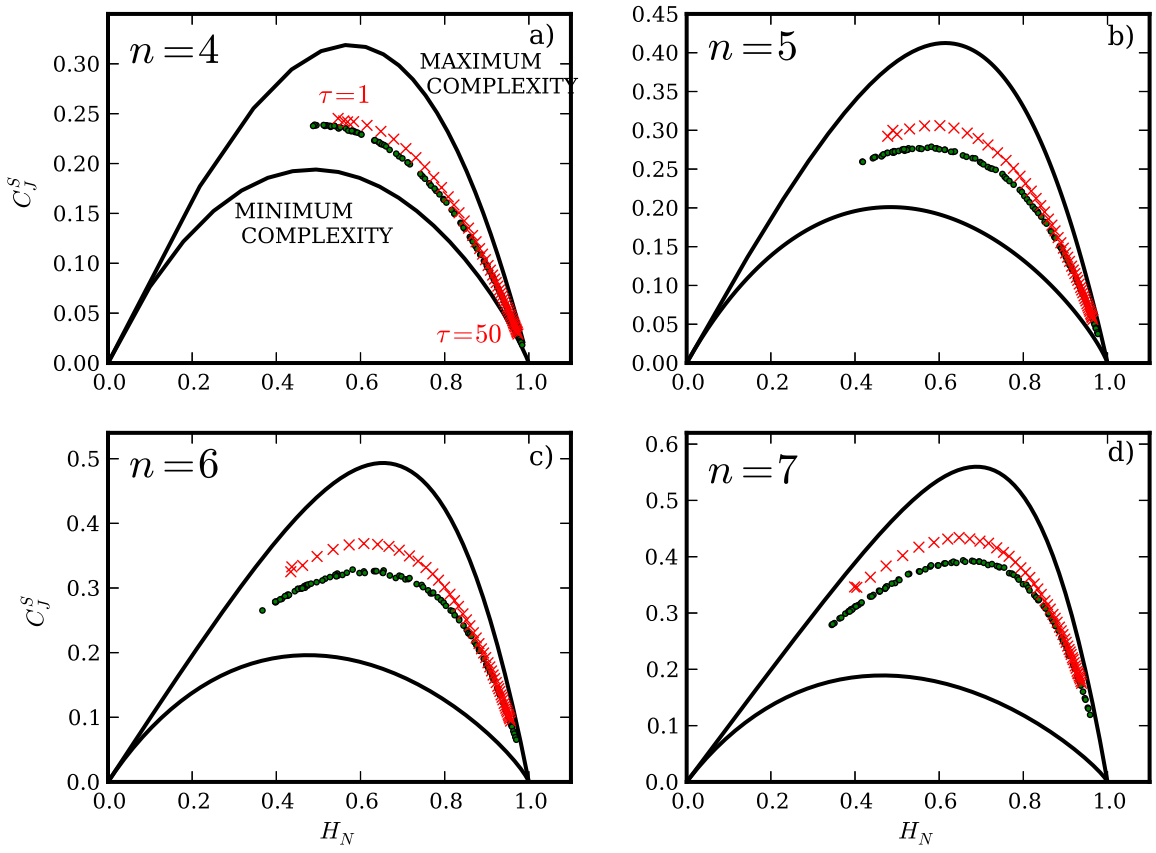

Figure 9.5: Entropy and complexity of the experimental data as a function of time delay and embedding dimension mapped in the CH plane

permutation entropy against the permutation complexity. I do this for the experimental data in Fig. 9.5. The solid black curves in each plot bound all data, and the region between them is called the complexity-entropy (CH) plane. The curves indicate the minimum and maximum possible complexity as a function of entropy for a given embedding dimension. The probability distributions that define these curves are explained by Maggs and Morales [MM13]. The green data points in these plots map out the high complexity, stochastic, fractional Brownian motion curve. Rosso et al. explain fractional Browning motion and how to obtain the time signals that lead to these different data points by varying the Hurst exponent [RLM07]. The curve more or less divides the CH plane into two regions, where the region above consists of deterministic time signals, and the region below, stochastic time signals. The red crosses represent the experimental data at a single radial location of 30 cm. The different crosses correspond to different subsampling rates τ, and as τ increases, the points move left to right, which is clear given the results of Fig. 9.4. The optimal τ for this method is that which gives the maximum complexity, and the optimal embedding dimension is that which produces data with the highest complexity relative to the Brownian motion curve. For the experiment then, $\tau \sim 10$ is optimal, while the $d_e = 6$ is sufficient because the relative complexity levels off at $d_e = 6$. This CH plane method, then, proves to be more useful than the entropy-only method employed above because $d_e = 6$ is sufficient in the CH plane method whereas it was insufficient in the entropy-only method.

One more point to notice is that when τ becomes high, the experimental data points overlap the Brownian motion data points. This means that over-subsampling causes the time signals to look stochastic. Figure 9.6 shows the effect of proper subsampling $\tau = 10$ and over-subsampling $\tau = 50$ on an experimental time signals and frequency spectrum. Proper subsampling maintains most of the structure in the time signal and most of the exponential part of the frequency

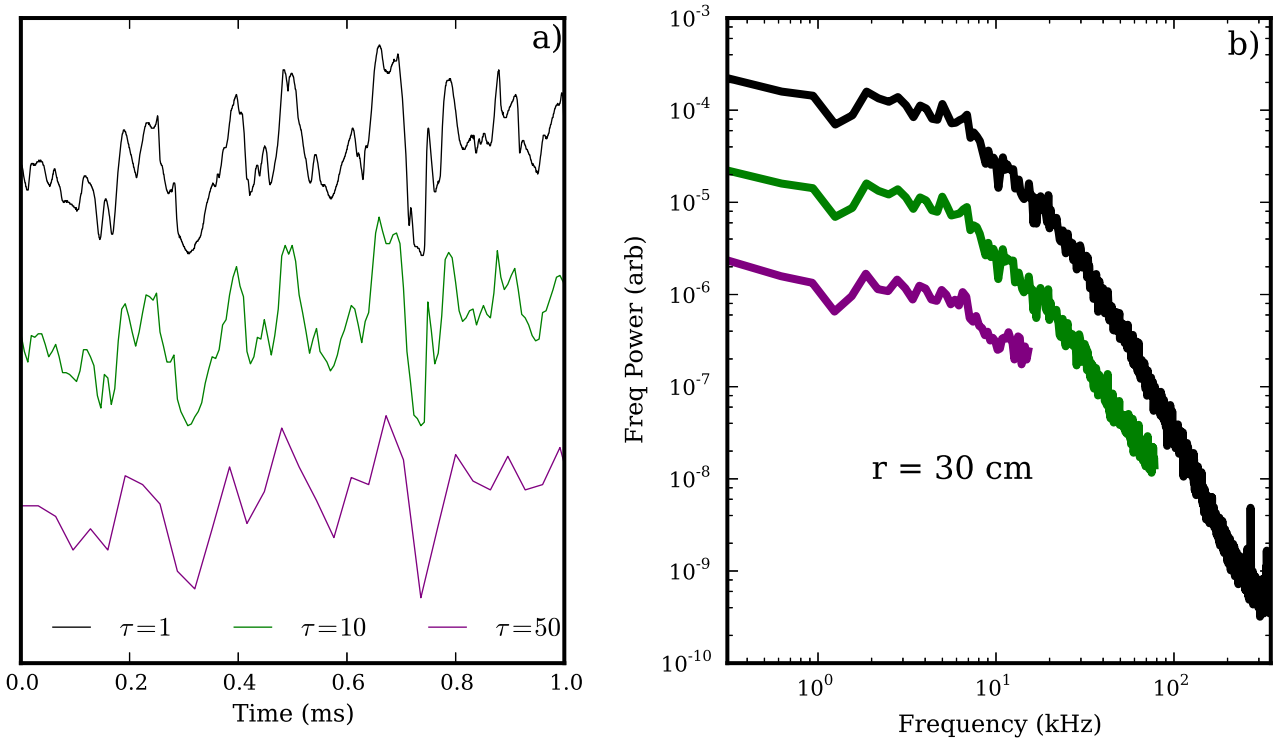

Figure 9.6: The effect of subsampling and over-subsampling on experimental time signals and frequency spectra

spectrum, while improper subsampling does not. The over-subsampled signal cannot be distinguished from a stochastic signal, while the properly subsampled one can.

Again, Rosso et al. showed that chaotic and stochastic processes occupy different locations in the entropy-complexity (CH) plane, which provides a simple way to test whether data is created by a chaotic or stochastic process [RLM07]. Stochastic models have high entropy and low complexity, so they sit in the lower right part of the plane. Chaotic models have medium entropy and high complexity and sit in near the maximum complexity curve, generally near the highest point. In Fig. 9.7, I show the location in the $d_e = 6$ CH plane of different chaotic and stochastic models along with the experimental and simulation data. The stochastic model I use again is that of fractional Brownian motion (fBm). As I said before, it is a high complexity stochastic process that can divide the plane between stochastic and chaotic behavior. I show this explicitly with the yellow shaded region above the fBm curve. The chaotic models that I use are the aforementioned low-dimensional Lorenz model [Lor63] as well as a paradigmatic high-dimensional chaotic model – the Mackey-Glass model [MG77]. The Mackey-Glass model is a differential time-delay equation for blood production:

$$\frac{dx}{dt} = \frac{ax(t-\tau_s)}{1+x^c(t-\tau_s)} - bx \tag{9.8}$$

where τ_s is the delay time. For the parameters of $a = 0.2, b = 0.1, c = 10, \text{and} \tau_\text{s} = 300$ that I use, the equation is known to produce high-dimensional chaos with dimension of about 20 [Fam82]. The greater the time delay, the greater the attractor dimension, so the Mackey-Glass model can produce attractor solutions with low dimension or arbitrarily high dimension. Furthermore, like the Lorenz model, the Mackey-Glass model has an exponential frequency spectrum (see Fig. 9.8). In Fig. 9.7, one sees that both chaotic models sit well into the chaotic region. And although one might conclude from this that the plane may be further divided

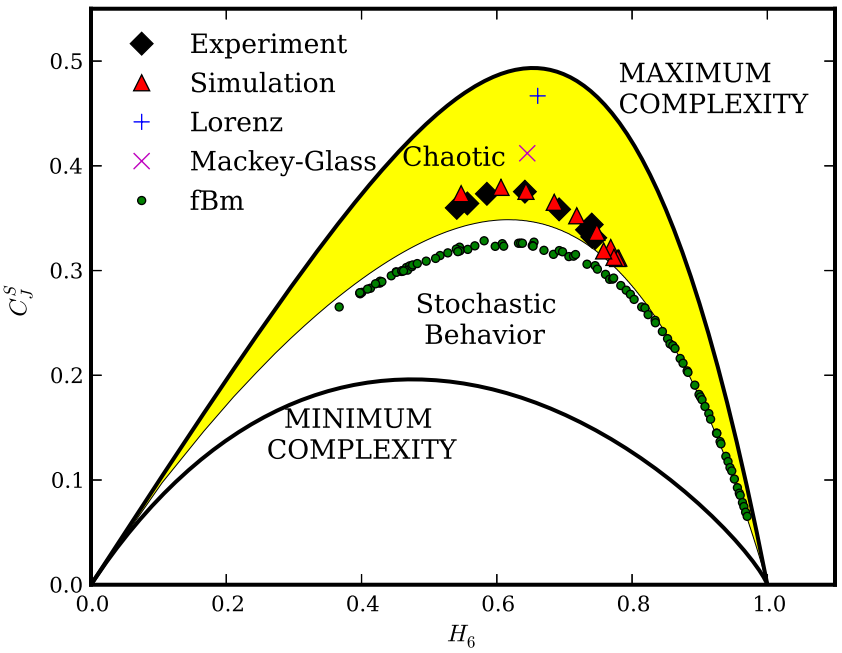

Figure 9.7: Location of chaotic, stochastic, and LAPD data in the entropy-complexity plane

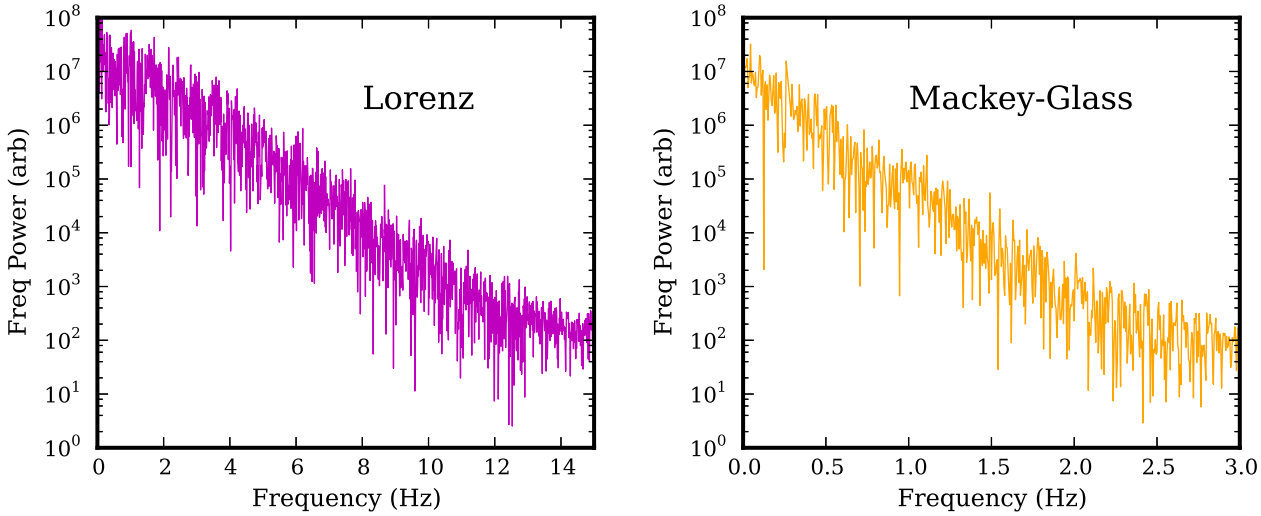

Figure 9.8: Exponential frequency spectra of the Lorenz and Mackey-Glass models

based on dimensionality since the higher dimensional model sits lower in the CH plane than the lower dimensional model, this doesn't seem to be the case. When I use a smaller or larger time delay in the Mackey-Glass model, the point sits in the same place in the CH plane (not shown) despite order of magnitude change in dimension of the attractor. Therefore, according to my albeit limited evidence, the CH plane does not differentiate between low- and high-dimensional chaos. However, this is still an attractive conjecture based on the idea that stochastic processes are infinitely dimensional chaotic processes, so I leave this matter to further study.

Finally, look at the experimental and simulation points in Fig. 9.7. I use $\tau = 10$ for all the experimental points and $\tau = 6$ for the simulation points. The different points correspond to different radial locations, but there is no clear trend between radius and location in the CH plane for the LAPD data. Perhaps the only reason for the slightly different locations is my use of a single subsampling rate rather than using a different subsampling rate for different radii. Also, there is no

significant difference between the simulation and experiment, further validating the simulation. Moreover, the LAPD data are located in the chaotic region of the CH plane, but do not sit as high as the paradigmatic chaotic models. Again, I cannot definitively conclude anything about the dimension of the LAPD attractor from this. I can only speculate that the dimension might be quite high or that there is some kind of more complicated process involved in LAPD that makes the time signals less deterministic. This also may be related to the non-exponential frequency spectra of the LAPD data. The Lorenz and Mackey-Glass models have exponential spectra, meaning that they are controlled by a process with one time scale, while the LAPD data have non-exponential spectra and multiple-time width Lorentzian pulses. It may be the case then, that the lower location of the LAPD data in the CH plane is a manifestation of a multiple-time-scale process, which is a different type of high-dimensional chaos than that of the Mackey-Glass model. This conjecture requires much more supporting evidence, though that is left to future work.

9.3 The Proper Orthogonal Decomposition Entropy

The permutation entropy uses only the time signal of the data because it's based upon time delay attractor reconstruction. This makes it nice to use for experimental data, which is generally restricted to time series data. But in this dissertation, I have presented forms of analysis that require the full spatial information obtained from simulations, which have successfully enhanced understanding of underlying turbulent processes. In the same spirit, I can use the spatio-temporal simulation data to answer the question of low-dimensional versus high-dimensional chaos, and even determinism versus stochasticity. First, it should be clear that I do not need to reconstruct the attractor orbit from a single time series because the spatio-temporal output of the simulation is the attractor orbit. Thus, the primary

difficulty in understanding the chaotic nature of the simulation is finding the effective degrees of freedom in which the attractor is embedded among the large number of available degrees of freedom of the simulation domain.

In my simulation model that has four differential equations for the four independent variables, the number of degrees of freedom is $4 \times N_r \times N_\theta \times N_z$, where N_j corresponds to the number of grid points that I use in each respective direction. In fact, using a finite number of grid points already reduces the number of degrees of freedom from infinity to a finite number. Gridding assumes that the turbulence can be described without an infinite number of degrees of freedom in that very small structures below the grid resolution cannot exist due to diffusive and viscous forces. I can go further by hypothesizing that there are a limited number of "modes" that effectively determine the turbulence. In other words, there exists some manifold in the phase space on which the attractor lies that has dimension less than that of the entire phase space. This, after all, is the assumption behind the time delay embedding that allows for a low embedding number. With the spatio-temporal simulation data available, it must be possible to find the relevant modes that control the turbulence and project the turbulence onto these modes. The POD procedure, which I introduced in Sec. 6.3 is perfect for this task. The reason is that the POD provides the optimal basis for reconstructing the turbulence from the fewest possible modes, as described by Eq. 6.48. The POD procedure can be considered a way of rotating the phase space axes so that the attractor lies in a hyperplane that can be described with as few coordinates as possible.

The way to quantify the number of effective degrees of freedom of the turbulence through the POD is by looking at the POD singular values σ_q. Recall that σ_q^2 is the time-averaged energy contained in POD mode q. If the top 10 POD modes, for example, contain 90% of the energy, then the projection of the turbulence onto the 10 mode POD reconstruction is 0.9. This follows from Eqs. 6.45-6.47.

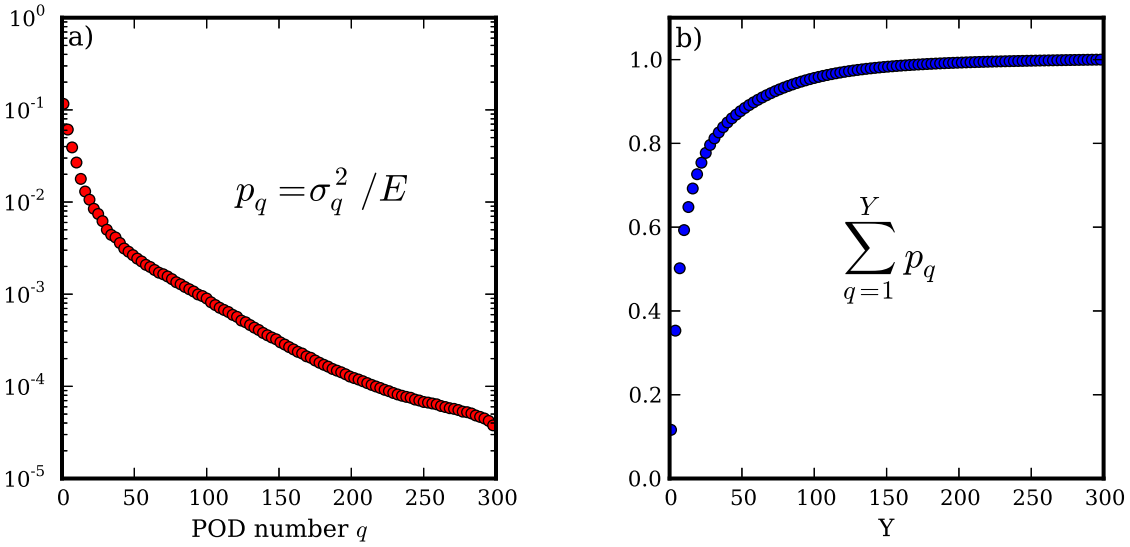

Figure 9.9: Fractional energy content of POD modes

To normalize the singular values to the total energy of the turbulence, I define

$$p_q = \sigma_q^2 / E \tag{9.9}$$

where $\sum_q p_q = 1$. The p_q's then form a probability distribution.

I perform a POD on the turbulent data of the Periodic simulation, using 300 time points in the quasi-steady state stage of the simulation. For the POD, I do not use any Fourier transforms like I did in Sec. 7.1.4. Obviously, that would be inappropriate for my aim here. I plot the p_q's in Fig. 9.9 a), showing only every third p_q. The fairly rapid exponential decay of the POD energy fractions indicates that the turbulence can be relatively well constructed using a limited number of modes and that the turbulence is not stochastic. In Fig. 9.9 b), I plot $\sum_{q=1}^{Y} p_q$ as a function of Y. This indicates how much of the turbulent energy is reproduced by the rank-Y POD reconstruction. From this calculation, I determine that the top 58 POD modes contain 90% of the turbulent energy. One might crudely conclude that the turbulence is governed by something on the order of 100 effective degrees of freedom. This, then, is high-dimensional chaos.

An obvious practical problem with this is that every single POD mode contains at least some energy, so that one may never obtain a definitive value for the number of effective degrees of freedom. Taking the number of modes that contain 90% of the energy is quite arbitrary, as is using any other percentage. It would be convenient if the p_q's became zero at some q, but this is not the case, and to further complicate matters, the σ_q's saturate eventually due to numerical noise of the POD procedure – shown by Professor Paul Terry in unpublished work. The upshot is that it is not possible to conclude exactly how many effective degrees of freedom there are based on the number of finite-energy POD modes. Probably, it is better to get a sense of how deterministic or how stochastic a process and how high the dimensionality is based on the rate of decline of the p_q's. The results in the previous section hint at how one might use this information – that is, with an entropy measure. In fact, Futatani et al. [FBC09] suggested the use of POD entropy as a way to classify turbulence. Turbulence with low POD entropy is dominated by coherent structures, while that with high entropy is stochastic.

The normalized POD entropy, defined similarly to Eq. 9.6, is

$$H_{\mathrm{POD}} = \sum_{q=1}^{N_{\mathrm{POD}}} p_q \log_2(p_q)/\log_2(N_{\mathrm{POD}}). \tag{9.10}$$

It isn't clear if the POD complexity has any meaning, so I will not use it. The value that I obtain for the normalized POD entropy is $H_{\mathrm{POD}} = 0.67$. This entropy is about the same as what I found for the permutation entropy of the chaotic models and the LAPD data in the previous section. For reference, Futatani et. al. found values of 0.20 and 0.93 for decaying and gradient-driven Hasegawa-Wakatani turbulence, respectively [FBC09]. To my knowledge, there are no standard spatio-temporal models that have been classified well enough for me to compare against. Better comparisons may come in future work.

One possible issue with the POD entropy is that it may depend on the total number of POD modes used in the POD procedure, at least for the normalization

that I use in Eq. 9.10. To prove this, I define a rank-T POD entropy as follows:

$$H_{\mathrm{POD}}(T) = \sum_{q=1}^{T} p_q \log_2(p_q)/\log_2(T). \tag{9.11}$$

The proper way to find this, would be to perform the POD with a different number of time points, which would give a different number of POD modes. However, the POD takes a long time to calculate, so this isn't feasible. Rather, by looking at Fig. 9.9 a), I reason that using more time points will simply extend the p_q's along the exponential line. Using this logic, I create series of p_q's with different lengths and calculate the entropy as a function of the total length of the given series. In Fig. 9.10, I plot the POD entropy H_{POD} as a function of the total mode number T used in the POD. The blue curve that I call "Constant Slope" – because I use a constant slope (in log space) to extend the series – is this result. Additionally, I plot the green curve in the same figure. For this curve, rather than extending the p_q's with a constant logarithmic slope, I simply extend them to have the same value as the last POD mode ($q = 300$). I do this under the assumption that all POD modes beyond a certain point are simply due to noise of the POD calculation, so that they all contain the same energy. These results indicate that the entropy is a function of the number of modes used in the POD; however, the entropies appear to level off at high T, suggesting that the actual entropy may be the asymptotic value of ~ 0.5. It is possible that an entropy normalization different from the one used in Eq. 9.10 might fix this problem, although it is also possible that performing the POD with a different number of time points actually does not produce different values of entropy. This matter is left to future study.

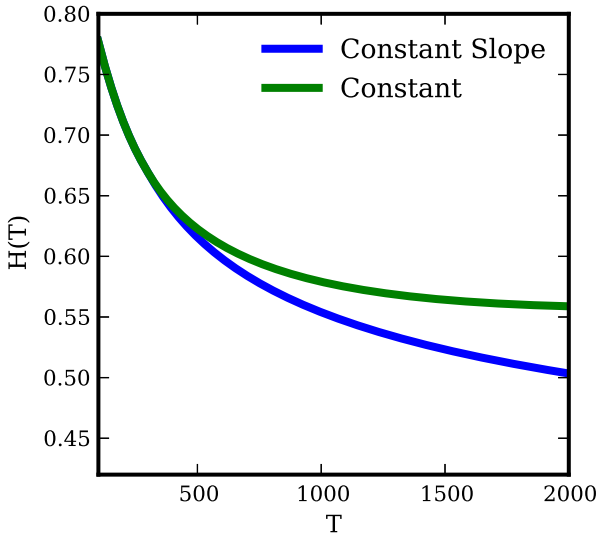

Figure 9.10: POD entropy as a function of total mode number used in the decomposition

CHAPTER 10

Conclusion

In this dissertation, I model, simulate, and analyze the turbulence in a flow varying experiment on LAPD, focusing only on the plasma state in which the mean radial electric field is minimal. The model I use in the simulations is an electrostatic reduced Braginskii two-fluid model that describes the time evolution of density, electron temperature, electrostatic potential, and parallel electron velocity fluctuations in the edge region of LAPD. The spatial domain I use is annular, encompassing the radial coordinates over which a significant equilibrium density gradient exists. I use a few different axial boundary conditions, such as periodic and Bohm sheath, but they have little bearing on the nature of the turbulence. My model breaks the independent variables in the equations into time-independent equilibrium parts and time-dependent fluctuating parts, and I use experimentally obtained values as input for the equilibrium parts.

The simulations start with a small random initial fluctuation, which is evolved in time, growing at first due to a linear drift wave instability. The fluctuations cause density and temperature transport across the equilibrium gradients, leading to relaxation of the profiles. I correct for this with ad hoc sources and sinks, which roughly model the ionization source and recombination sink in LAPD. After the initial exponential growth of the fluctuations due to the linear drift wave instability, the fluctuations saturate and the frequency and azimuthal wavenumber spectra become broadband with no visible coherent peaks, at which point the fluctuations become turbulent. The turbulent fluctuations of both density and

potential in the simulation are very similar to those in the experiment for a wide range of statistical properties – especially when compared as synthetic diagnostics. Specifically, the frequency spectra are similar at all radii, the PDFs have the similar mean, standard deviation, skewness, and kurtosis, and the radial dependence of the RMS amplitudes and the amplitudes themselves are very similar. On the other hand, the simulation has a steeper m_θ spectrum than the experiment along with a smaller spatial correlation length as well as a more structured and broader autocorrelation. These differences, however, are not large; at most, differences are a factor of two. The qualitative and quantitative agreement between the simulation and experiment is quite remarkable compared to all other cases in magnetically confined plasma systems that I have seen. This level of validation authorizes me to make strong conclusions regarding the nature of the turbulence in the experiment based on detailed analysis of the simulations, especially conclusions pertaining to the spatial structure of the turbulence.

The spatially resolved turbulence in the simulations develops intermittent pressure and flow filamentary structures that grow and dissipate, but look much different than the unstable linear drift waves. The difference is most easily seen in the long axial wavelengths that these structures possess. Their wavelengths are much longer than the machine length, which is in contrast to the linear drift waves, whose axial wavelengths are equal to or on the order of the machine length depending on boundary conditions. An energy dynamics analysis that I derive reveals the mechanism that drives these structures, which dominate the turbulent energy. These long $k_\parallel \sim 0$ potential filaments convect equilibrium density across the equilibrium density gradient, setting up local density filaments. These density filaments, also with $k_\parallel \sim 0$, produce azimuthal density gradients, which drive radially propagating secondary drift waves. These finite $k_\parallel$ drift waves have pressure and electrostatic components associated with them, which are coupled by the adiabatic response. The potential component of these drift waves nonlinearly

couple to one another and reinforce the original convective filament, allowing the process to bootstrap itself, at least intermittently. The growth of these structures is by nonlinear instability because they require a finite amplitude to start, and they require nonlinear terms in the equations to sustain their growth.

The reason why $k_\parallel \sim 0$ structures can grow and support themselves at all in a dynamical system with no $k_\parallel = 0$ linear instability is because the linear eigenmodes of the linear dynamical system are nonorthogonal. Nonorthogonal eigenmodes that individually decay under linear dynamics can, in fact, produce transient energy growth, which is always responsible for subcritical instability in conservative dynamical systems. The instability, however, can only occur when the fluctuations are given some finite threshold amplitude, and nonlinearities are able to mix energy between different eigenmodes. In my simulations, the linear drift wave instability kick-starts the fluctuations, but noise may provide the impetus in real systems or in linearly stable systems.

Additionally, I analyze the experiment and simulations in regards to their deterministic character. In other words, I attempt to figure out how many effective degrees of freedom control the turbulence. Using two different methods – permutation entropy analysis by means of time delay trajectory reconstruction and Proper Orthogonal Decomposition – I determine that more than a few degrees of freedom, possibly even dozens or hundreds, are all active. The turbulence, though is still deterministic, not stochastic, meaning it is high-dimensional chaos.

It seems that one can always understand more about a particular experiment or phenomenon or add more physics to a model, but eventually the problem of diminishing returns sets in. So barring any problems with my results or methods, future efforts will best be directed toward analyzing different experiments or determining how certain results change with changing parameters. I have two ideas in mind, which based on my results, may present interesting avenues of research. The first idea is to change some parameter – maybe plasma radius – that changes

the chaotic nature of the experiment. Bifurcation theory rests on the idea that a control parameter – or set of parameters – changes the nature of the attractor solutions of the system, especially the attractor dimension. Can one see this in experiments? If so, what are the implications for magnetic fusion? Second, experiments on LAPD that vary the mean radial electric field have already been done, and simulations based on these experiments need to be properly performed and analyzed to help uncover some important physics. While I have made some progress on these simulations and their analysis, which I describe in Appendix B, I have not yet achieved a sufficient level of validation or analyzed the results in depth. These are two paths of exploration that await future research. There is still much to be done in LAPD experiments and simulations to uncover the nature of plasma turbulence.

APPENDIX A

The BOUT++ Code

I use the BOUT++ [DUX09] code to solve the model equations of Chapter 4. This is a free open-access code available at https://github.com/bendudson/BOUT. In this appendix, I briefly describe this code and my specific implementation of the model equations. I cannot simply paste the entire code here and explain it line for line because the code is on the order of 10^6 lines and quite complicated. Rather, I provide an overview of the BOUT++ framework and focus on describing and discussing details that are specific to my code implementation so that readers should be able to understand how to reproduce the simulations that I describe in this dissertation.

A.1 The Object-Oriented Fluid Framework

BOUT++ is an object-oriented C++ extension of BOUT. BOUT, short for Boundary Turbulence, was written by X. Q. Xu and M .V. Umansky [XC98, UXD09]. BOUT, written in C, evolves a set of drift-reduced Braginskii fluid equations in 3D tokamak geometry. P. Popovich and Umansky modified BOUT to solve the equations in cylindrical geometry for simulation of LAPD turbulence [PUC10b]. BOUT++ is much more, however, than a C++ Braginskii solver. It is a C++ framework for writing single or multi-species fluid simulations with an arbitrary number of equations in 3D curvlinear coordinates. The framework allows input of a grid file, which contains information regarding the magnetic field geometry, the metric tensor, and axisymmetric equilibrium profiles and parameters if de-

sired. Users may simulate fluids and plasmas in slabs, sheared slabs, cylinders, or tokamaks. The input equilibria have only one restriction in that they must be two-dimensional, having one axisymmetric coordinate.

The inner workings of the code take care of many of the difficult coding and numerical issues associated with writing fluid simulations. For example, users may run parallelized simulations that are spread onto multiple processors simply by specifying a number in an input file. Furthermore, users can specify specific implicit or explicit numerical schemes to solve the equations as well as specific finite difference schemes to approximate spatial derivatives in the equations. None of the numerical schemes need to be written by the user, although the framework also provides relatively simple ways that the user can implement his own finite difference schemes. Derivatives in the axisymmetric coordinate may be solved spectrally, but BOUT++ is not a spectral code in general.

Moreover, the user specifies the equation set to be solved in a "physics module." The equation set can be the Braginskii equations, MHD equations, Navier-Stokes equations, gyro-fluid equations, etc. Finally, BOUT++ evolves variables from initial conditions with boundary conditions applied at every time step. It cannot solve the eigensystem of a linear equation set. Overall, BOUT++ is easily adaptable to solving many different hydrodynamic and plasma physics models. More information can be obtained in the various reference manuals included in the downloaded working tree.

I have implemented a specific LAPD turbulence model in the BOUT++ framework using the equations, sources, profiles, and parameters outlined in Chapter 4. In the next section, I explain the specific choices of numerical schemes that I use for the time evolution and the spatial differential operators.

A.2 Numerical Schemes

A.2.1 Spatial Finite Differences

In my BOUT++ LAPD turbulence implementation, the code solves Eqs. 4.1-4.4 for the fields $N, T_e, \phi, v_{\|e}$. In order to do this, it must calculate the RHS of the equations using my prescribed equilibrium profiles, transport coefficients, and stored values of $N, T_e, \phi, v_{\|e}$. Since the RHS of the equations involve spatial derivatives, they must be approximated before the solution can be found. The approximations involve a number of differential operators for the different terms. First, I explicitly write out the linear advection terms such as $\mathbf{v_E} \cdot \nabla N_0$ into an azimuthal derivative of ϕ times a radial derivative of N_0. Then, I use simple first-derivative central 4^{th} order finite difference schemes for each of the derivatives.

For the perpendicular Laplacian operators, I use Fourier transforms, which is the standard BOUT++ scheme for this. For the parallel Laplacian operator, I use a second-derivative central 4^{th} order finite difference scheme. For the parallel gradient operators, I use a quasi-staggered method to prevent grid-sized oscillations on top of the solution that are called grid modes. For the explanation of why non-staggered numerical schemes can cause unphysical grid modes, see Appendix C in Popovich et al. [PUC10b]. In the quasi-staggered method, I use a first derivative first or third order one-sided finite difference scheme for the parallel gradients. I use a right-sided scheme for the derivatives when they are applied to the flux variables ($v_{\|e}$ and $j_\|$) and a left-sided scheme when applied to the state variables (N, T_e, and ϕ). BOUT++ now has the capability to use real staggered grids in which the flux and state variables exist on different grids that are shifted by half a grid-spacing from one another, but this capability wasn't present when I started the work, so I had to use the quasi-staggered method. I implemented the third-order schemes myself in the physics module, so the one-sided third order schemes are not part of the standard BOUT++ internal code. I generally use the third

order schemes, but I sometimes use the first order schemes, and the statistical solution doesn't significantly vary between the two different schemes.

Finally, for the nonlinear advection terms in the Poisson brackets, I generally use an Arakawa advection scheme that I have written into the physics module, which is not part of the BOUT++ internal code. The Arakawa advection scheme [Ara66] is useful for my purposes because it exactly conserves fluctuation energies of the type I have written in Chapter 6. I have used this advection scheme for all of the simulations that I describe in the dissertation – but not for the simulations I describe in Appendix B. The Arakawa advection scheme can cause overshoots or spurious fluctuations at steep gradients, which is one of the reasons why I use artificial diffusion and viscosity in the equations. Another problem with the Arakawa advection scheme is that it is not a positivity-preserving scheme. The advection equation:

$$\frac{\partial A}{\partial t} + \mathbf{v} \cdot \nabla A = 0, \tag{A.1}$$

for any normal flow field $\mathbf{v}$ preserves the positivity of the variable A. This is easy to see because anytime A becomes very small at a certain location not on the boundary, it becomes a local minimum there and its gradient goes to zero. This prevents A from decreasing any further. When dealing with finite differences, however, the gradient of A at a local minimum may be different from zero due to finite grid spacing effects. This can cause A to become negative at that point on a subsequent time step. Some finite difference advection schemes take this into account and do not allow A to become negative. Arakawa schemes do not. This can be a problem because the total density and electron temperature are physically positive quantities in my model. They should not become negative at any time at any spatial location. Otherwise, the results become unphysical, invalidating the simulation. As long as the fluctuations are not too large, the total density and temperature remain positive when I use Arakawa advection. But I found that in some simulations – including those described in Appendix B – the fluctuations can

become large enough that the total density and/or temperature become negative when I use the Arakawa scheme. In those cases, I use a first-order upwind (U1) advection scheme. In this scheme, the component $\left(v_x \frac{\partial A}{\partial x}\right)_{U1}$ is approximated as:

$$\begin{aligned} v_{x,i}\frac{A_i - A_{i-1}}{\Delta x} \quad &\text{for} \quad v_{x,i} > 0, \\ v_{x,i}\frac{A_{i+1} - A_i}{\Delta x} \quad &\text{for} \quad v_{x,i} < 0. \end{aligned} \tag{A.2}$$

It is easily confirmed that any local minimum must grow in amplitude from this formula because A is always advected into the local minimum. Also note that a local maximum must shrink. Because of these properties, solutions tend to numerically smooth out, indicative of diffusive action. To show this explicitly, Eq. A.2 can be rewritten in an interesting way:

$$\left(v_x \frac{\partial A}{\partial x}\right)_{U1} = v_{x,i}\frac{A_{i+1} - A_{i-1}}{2\Delta x} - \frac{\Delta x}{2}|v_{x,i}|\frac{A_{i+1} - 2A_i + A_{i-1}}{(\Delta x)^2}. \tag{A.3}$$

The first term on the RHS is simply the expression for central second order advection, while the second term on the RHS is $\frac{\Delta x}{2}|v_{x,i}|$ times the expression for the central second order second derivative:

$$\left(v_x \frac{\partial A}{\partial x}\right)_{U1} = \left(v_x \frac{\partial A}{\partial x}\right)_{C2} - \frac{\Delta x}{2}|v_{x,i}|\left(\frac{\partial^2 A}{\partial x^2}\right)_{C2}, \tag{A.4}$$

meaning that the one dimensional advection equation with a first order upwind advection scheme is equivalent to the advection-diffusion equation with a second order central advection scheme and a diffusion coefficient of $\frac{\Delta x}{2}|v_{x,i}|$. This generalizes to the 3D advection equation as well. The diffusion is numerical diffusion, and when I use U1 advection, I make sure to add this numerical diffusion to the artificial diffusion in my energy analyses to correctly obtain the energy dissipation.

Using a U1 advection scheme helps maintain positivity of the total density and temperature, but Eqs. 4.1 and 4.4 are not simple advection equations or even advection-diffusion equations. The density equation is close to an advection-diffusion equation, but since I partially linearize it, it doesn't preserve the concept

of evolving the total density. And more importantly, the source term makes it a different equation altogether. Physically, the source is an ionization source and a recombination sink at the end plates, but in the model, it is much simpler. It's simply a term that corrects the equilibrium by essentially removing the flux-surface averaged density fluctuation component (Eq. 4.5). Such a source is clearly not positivity-preserving since it averages over an entire flux surface and has no knowledge of the local total density. When positivity preservation becomes an issue in the simulations, I multiply the source terms in Eqs. 4.1 and 4.4 by N_t and T_{et} respectively whenever the sources are negative. Therefore, when N_t or T_{et} become small, if the sources are negative, they become weaker so that they can't drive N_t and T_{et} negative. Physical sources must have this property, so it's not unreasonable to do this with the model sources.

A.2.2 Time Integration Technique

Perhaps the real power of BOUT++ lies in its time integration procedures. While a few simple explicit methods such as Euler and Runge-Kutta 4^{th} order methods come with the BOUT++ code, some much more sophisticated solver packages can be compiled with the code and used with simple commands. The solver that I use is the CVODE package that comes in the Sundials suite of codes. CVODE is a parallel solver that can solve stiff or non-stiff ODE initial value problems of the form [CVO]:

$$\frac{du}{dt} = f(t, u). \tag{A.5}$$

Plasma simulations tend to be stiff due to the large range of time scales involved. Simple explicit schemes are generally too inefficient or too inaccurate to use, and only some implicit schemes work with stiff systems. For stiff problems, CVODE uses the Backward Differentiation Formula (BDF). This formula approximates u

at time n as

$$u_n = \sum_{i=1}^{q} \alpha_{n-i} u_{n-i} + h_n \beta_0 f_n, \tag{A.6}$$

where $f_n \equiv f(u_n, t_n)$, h_n is the time step at time n, q is the order of the BDF method, and α_{n-i} and β_0 are coefficients determined by the order of the BDF method. Since, f_n is unknown, CVODE uses a Newton formula to approximate it as

$$f_n \approx f_{n-1} + \frac{\partial f}{\partial u}(u_n - u_{n-1}). \tag{A.7}$$

$\frac{\partial f}{\partial u} \equiv J$ is the Jacobian. This allows Eq. A.6 to be written as

$$(1 - h_n \beta_0 J) u_n = \sum_{i=1}^{q} \alpha_{n-i} u_{n-i} + h_n \beta_0 f_{n-1} - h_n \beta_0 J u_{n-1}. \tag{A.8}$$

The process is actually more complicated as the Eq. A.7 approximation actually uses a Newton iteration[CVO], so that the solution can be computed more accurately. The user supplies error tolerances and CVODE iterates the solution until the tolerance is met. If the tolerance is not met after a certain number of iterations, CVODE changes the order of the implicit method. If this doesn't produce a tolerable error, CVODE reduces the time step and starts the procedure again. These tolerance steps are not necessarily all done in this order. Again, CVODE is an efficient, yet complicated code.

APPENDIX B

Finite Mean Flow Simulations

In the main text, I focused on one particular LAPD experiment, which contained little mean $\mathbf{E} \times \mathbf{B}$ flow and flow shear. Focusing on this null flow experiment allowed me to model the system with a smaller number of linear terms in the equation set than if the experiment had contained significant $\mathbf{E} \times \mathbf{B}$ flow. Furthermore, neglecting mean flow and flow shear eliminated linear instabilities such as Kelvin-Helmholtz and Rotational Interchange, which are both flute-like ($k_\parallel = 0$). With these present, it can be difficult to differentiate between the nonlinear instability and these linear instabilities, though careful energetics analysis can do so. Furthermore, the low flow experiments have proven to be easier to successfully simulate than the high flow experiments, and the null flow experiment and simulations contain so much interesting physics that they deserve study in their own right.

In this appendix, I review preliminary results of simulations and analysis of finite mean flow experiments recently performed in LAPD. I choose to present this in an appendix rather because it is preliminary, highly unpolished work. Moreover, mean flow shear suppression is somewhat off topic and wouldn't necessarily add to the main points that I developed in the main text. But I cannot emphasize enough how important well-validated, well-analyzed mean flow simulations would be to the understanding of these experiments and the important effects that they were designed to illuminate. Because of that, I present here my preliminary results of some mean flow simulations so that others can build upon this work.

B.1 Biasing Experiment Profiles

As I discussed in Sec. 4.3.1, Schaffner et al. conducted an $\mathbf{E} \times \mathbf{B}$ flow and flow shear variation experiment on LAPD [SCR12]. In the main text, I simulated only a single experimental realization – that in which the plasma had minimum mean azimuthal flow. The study, however, really stressed the higher flow states because they are relevant to tokamak research, specifically research into the High Confinement Mode (H-mode) and the transition to the H-mode. Researchers have long realized that H-mode is associated with strong toroidal rotation of the tokamak plasma and that the shear associated with this rotation is the likely cause of the decrease in energy transport. The particular physical mechanism of turbulent-shear interaction that causes the flux suppression is still an area of intense research. Although here I do not address the question of shear suppression, future work using LAPD simulations may be able to do so. Rather, I focus here on accurately simulating the turbulence in a few of the finite flow plasma realizations in the experiment and partially analyzing them.

First, I show the equilibrium density, electron temperature, and potential profiles for the three experiments that I will simulate. The first, corresponding to the unbiased plasma – the 0 V potential profile in Fig. 4.2 – is in Fig. B.1 a). Furthermore, in Fig. B.1 b), I plot the azimuthal $v_{E\times B}$ profile and its radial derivative, the shear. Both are normalized by the same potential as ϕ_0. I do the same for two other cases: a medium flow case – corresponding to the 100 V bias in Fig. 4.2 – and a high flow case – corresponding to the 150 V bias.

As documented in Schaffner et al. [SCR12, SCR13] and is clear from Fig. B.1, the mean flow inside of the 26 cm limiter radius points in the ion diamagnetic direction for the unbiased case, but then nulls out and changes direction. Furthermore, the radial flow shear also changes with changing bias, with the shear rate γ_s ranging from zero to about five times the autocorrelation time τ. Schaffner's analysis

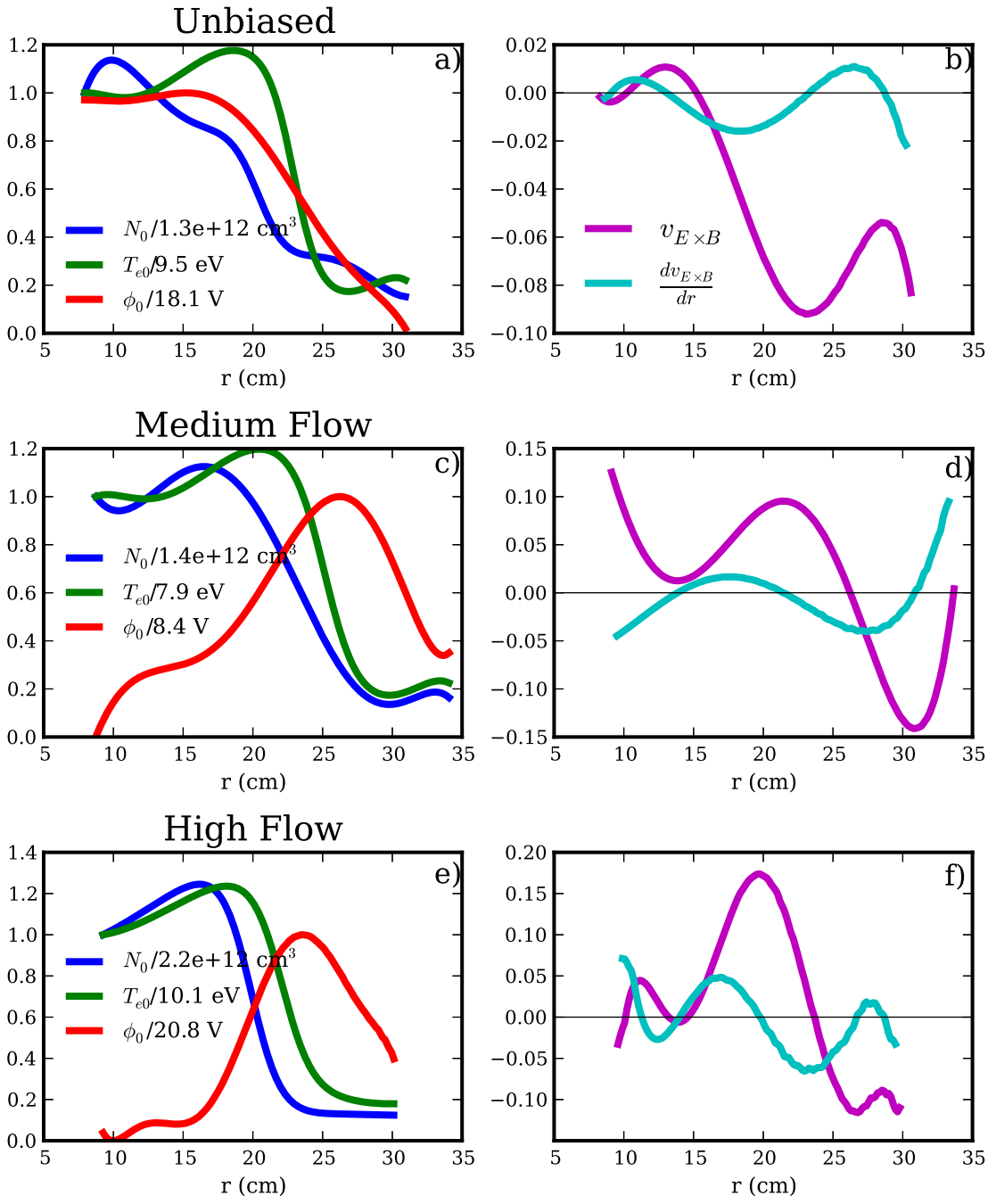

Figure B.1: Fitted equilibrium profiles for different biases

showed that the radial particle flux and the density scale length were inversely proportional to the flow shear regardless of the flow direction [SCR12]. The experiments clearly showed that flow shear suppresses radial particle flux through suppression of turbulent density fluctuations. The mechanism that causes this, however, is less obvious, and they tried to answer this by comparing shear scaling properties to various theoretical predictions [SCR13]. Simulations with highly resolved spatial features may eventually help this effort.

Other interesting findings in the biasing experiment include a change in the shape of the frequency spectra with biasing. As the flow and flow shear become large, a coherent feature, seen as a sharp peak at the low end of the frequency spectra, emerges. Furthermore, the spectra become more exponential at high frequency as the flow and flow shear increase. These signal possible changes in the nature of the turbulence. The coherent feature, for instance, indicates the presence of a coherent mode, possibly due to a flow instability. The exponential spectra might indicate a change in the chaotic properties of the turbulence, namely, a decrease in the attractor dimension. This speculation can likely be sorted out with the help of well-validated numerical simulations. Therefore, I have attempted to simulate a few of the different biased cases and analyze the results using the tools I used in the main text on the null flow experiment and simulations.

B.2 Simulation Model

The simulation model that I use is the same that I use in the main text (See Chapter 3) with mostly obvious and straight forward additions to account for the mean potential profiles in the experiments that I simulate in this appendix. I treat the potential the same way that I treated the density and temperature in the main text – by dividing it into a time-independent equilibrium part and a

time-dependent fluctuating part. With this, the model equations become:

$$\partial_t N = -\mathbf{v_E} \cdot \nabla N_0 - \mathbf{v_{E0}} \cdot \nabla N - N_0 \nabla_\parallel v_{\parallel e} + \mu_N \nabla_\perp^2 N + S_N + \{\phi, N\}, \quad \text{(B.1)}$$

$$\partial_t v_{\parallel e} = -\mathbf{v_{E0}} \cdot \nabla v_{\parallel e} - \frac{m_i}{m_e}\frac{T_{e0}}{N_0}\nabla_\parallel N$$
$$-1.71\frac{m_i}{m_e}\nabla_\parallel T_e + \frac{m_i}{m_e}\nabla_\parallel \phi - \nu_e v_{\parallel e} + \{\phi, v_{\parallel e}\}, \quad \text{(B.2)}$$

$$\partial_t \varpi = -\mathbf{v_E} \cdot \nabla \varpi_0 - \mathbf{v_{E0}} \cdot \nabla \varpi - \frac{1}{r}\frac{\partial \phi_0}{\partial r}\left(\frac{\partial N_0}{\partial r}\frac{\partial^2 \phi}{\partial r \partial \theta} - \frac{\partial^2 \phi_0}{\partial r^2}\frac{\partial N}{\partial \theta}\right)$$
$$-N_0 \nabla_\parallel v_{\parallel e} - \nu_{in}\varpi + \mu_\phi \nabla_\perp^2 \varpi + S_\phi + \{\phi, \varpi\}, \quad \text{(B.3)}$$

$$\partial_t T_e = -\mathbf{v_E} \cdot \nabla T_{e0} - \mathbf{v_{E0}} \cdot \nabla T_e - 1.71\frac{2}{3}T_{e0}\nabla_\parallel v_{\parallel e} + \frac{2}{3N_0}\kappa_{\parallel e}\nabla_\parallel^2 T_e$$
$$-\frac{2m_e}{m_i}\nu_e T_e + \mu_T \nabla_\perp^2 T_e + S_T + \{\phi, T_e\}. \quad \text{(B.4)}$$

I simulate three different biasing experiments – those corresponding to the profiles that I showed in Fig. B.1. I use a potential source S_ϕ in the same way that I use density and temperature sources (see Sec. 4.1.1). However, while it is clear that the turbulent flux will cause the total radial density and temperature profiles – equilibrium plus flux-surface averaged fluctuating component – to relax over time, it is not obvious what affect if any the turbulence should have on the total potential profile. The reason is that the turbulent Reynolds Stress, which comes from the flux-surface average of the $\{\phi, \varpi\}$ term in Eq. B.3 can drive time-dependent zonal flows and time-independent mean flows – the Reynolds Stress is a three-wave transfer in the terminology of the energy dynamics. Generally, however, radially non-oscillatory mean flows require an external torque due to angular momentum conservation.

When I simulated the null flow experiment and even the unbiased experiment without a potential source, no noticeable mean flow developed. However, when I simulated the medium flow and high flow experiments, a mean flow did form, presumably because my radial boundary conditions apply a significant torque to the plasma. In any case, this means that I do have to use a potential source to maintain the physically relevant total potential profile. In most cases it would

probably be best to use a fixed potential source because the source that I use (see Sec. 4.1.1) largely removes the zonal flows as well as the mean flows. I don't think the zonal flows are that important, as I showed in Fig. 7.9, but they might be in the higher flow cases.

Additionally, I use periodic axial boundary conditions for these simulations because the boundary conditions didn't seem to have much affect on the turbulence in the null flow simulations. As for the artificial diffusion and viscosity levels – which I use as a free parameter to match the level of turbulence between the simulations and experiment – I use values of 1.2×10^{-3}, 2×10^{-3}, and 0 for the unbiased, medium flow, and high flow simulations respectively. Also, as I discussed in Appendix A, I use a first order upwind advection scheme for the advective nonlinearities in these equations, which introduces a lot of numerical diffusion.

B.3 New Linear Instabilities

The addition of an equilibrium potential profile introduces two new linear instabilities into the picture. First, the Kelvin-Helmholtz (KH) instability, which is a fluid instability – as opposed to a plasma-specific instability – is caused by the radial gradient in the azimuthal $\mathbf{E_0} \times \mathbf{B}$ velocity. Second is the rotational interchange instability (RIC), which is caused by the bulk rotation of the plasma in the presence of the magnetic field.

The KH instability is a convective vorticity instability, meaning it can be described by the simple equation

$$\frac{\partial \varpi}{\partial t} = -\mathbf{v} \cdot \nabla \varpi. \tag{B.5}$$

The instability occurs when there is a shear in the velocity gradient. Diagrams of the mechanism can be found in Manneville p. 227 [Man04], Drazin and Reid p.15 [DR81], and in other hydrodynamic instability books. Their treatments all follow Batchelor's [Bat67]. I summarize the mechanism as follows. Imagine a

boundary layer separating two flows that have equal speeds but velocities going in different directions. Since the vorticity is just the curl of the velocity, this boundary layer is a vortex sheet. Now a sinusoidal vorticity perturbation on this sheet causes a sinusoidal ripple in the elevation of the sheet. This ripple brings parts of the sheet into regions where the background flow is positive and other parts of the sheet into regions where the flow is negative. The vorticity on the sheet is then advected by this background flow in such a way that it reinforces the initial sinusoidal vorticity perturbation, thus causing instability. This instability is 2D and requires only a velocity gradient. In the LAPD plasma, the mean flow is in the azimuthal direction and its gradient is in the radial direction. Since the instability is 2D, it need not have a finite wavelength in the axial direction, potentially making it a flute mode. In Eq. B.3, the terms that cause the KH instability are $-\mathbf{v_E} \cdot \nabla \varpi_0$ and $-\mathbf{v_{E0}} \cdot \nabla \varpi$.

The RIC instability is analogous to the more commonly known interchange instability in magnetic confinement devices like tokamaks. That interchange instability is a result of a curved magnetic field that causes particles to feel a centrifugal force as they travel along the field. The RIC instability in LAPD is not caused by magnetic field curvature (there is none), but by the centrifugal force on particles as they are rotated around the cylinder by the azimuthal mean flow. The force on the particles is $\mathbf{F} = mv_\theta^2/r\ \hat{\mathbf{r}}$. Forces on particles in magnetic fields cause drifts:

$$v_d = \frac{1}{q}\frac{\mathbf{F} \times \mathbf{B}}{B^2}. \tag{B.6}$$

Since the centrifugal force due to rotation is independent of charge, the electron and ion fluids drift in different azimuthal directions. If there is a density perturbation, this drift will cause a spatial charge separation, which causes azimuthal electric fields and thus, radial $\mathbf{E} \times \mathbf{B}$ velocities. These radial velocities advect fluid of different density into this charge-separated region in such a way to enhance the original density perturbation. In this instability, unlike the drift wave instability,

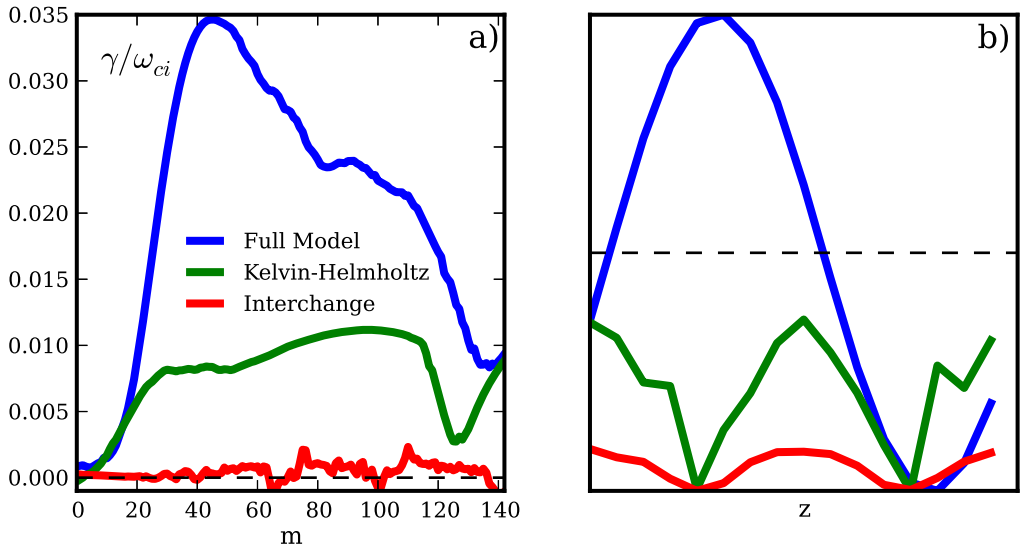

Figure B.2: Linear growth rates and axial structures for the high mean flow linear simulation

the density and potential perturbations are 90^o out of phase, meaning that the instability grows but does not propagate – if the electrons are adiabatic. In other words, this instability does not require the adiabatic response, and it is 2D, so it can have infinite axial wavelength. And unlike in the KH instability, the density is not a passive scalar in the RIC instability. The new term in Eq. B.3 that is responsible for the RIC instability is $-\frac{1}{r}\frac{\partial\phi_0}{\partial r}\left(\frac{\partial N_0}{\partial r}\frac{\partial^2\phi}{\partial r\partial\theta} - \frac{\partial^2\phi_0}{\partial r^2}\frac{\partial N}{\partial\theta}\right)$.

I show the growth rates as a function of m number for the high flow simulation in Fig. B.2 a). The Full Model curve is the linear growth rate for the full equation set. The growth rates are much higher than for the null flow case due primarily to the steep density and temperature gradients. For the Kelvin-Helmholtz and Interchange curves, I have simulated only subsets of the equations. For both, I have removed the adiabatic response terms, which eliminate the drift wave drive. And for the KH simulation, I disregarded the RIC term and vice versa for the IC simulation. From these results, it appears that the linear drift wave is most dominant with the KH instability also having significant positive growth rate.

The RIC instability is only marginally unstable. I note that the RIC and KH growth rate curves may be inaccurate, and that I need to confirm them with an independent calculation. I also note that the growth rates might be very sensitive to the profiles, especially the potential profile, which I also must check.

In in Fig. B.2 b), I show the axial structure of the potential for the linear simulations that I used to calculate the growth rate. The Full Model curve has the shape of a single $n = 1$ Fourier component, indicative of the linear drift wave that dominates the linear dynamics in this simulation. The KH and RIC axial structures have large $n = 0$ and $n = 2$ Fourier components, and no significant $n = 1$ Fourier component. The $n = 2$ component is quite surprising and warrants further investigation.

B.4 Statistical Comparisons to Experiment

In Fig. B.3, I compare a few statistical quantities of the density fluctuations – I_{sat} for the experiment – between the flow experiments and the simulations corresponding to the profiles in Fig. B.1. The top row of plots – a), b), and c) – are based on the unbiased experiment and simulation, the middle row – d), e), and f) – derive from the medium flow experiment and simulation, while the bottom row – g), h), and i) – come from the high flow experiment and simulation. The first column plots – a), d), and g) – show the frequency power spectrum, the middle column shows the probability distribution function of the fluctuations, while the last column displays the radial RMS values of the fluctuations.

For the unbiased case, the simulation matches the experiment quite well – at about the same level as the null flow experiment and simulation in the main text. Moreover, the statistical quantities for the unbiased simulation and experiment closely resemble those of the null flow experiment (see Fig. 5.8) except for the fluctuation peak at ~ 26 cm in the unbiased case, which isn't present in the null

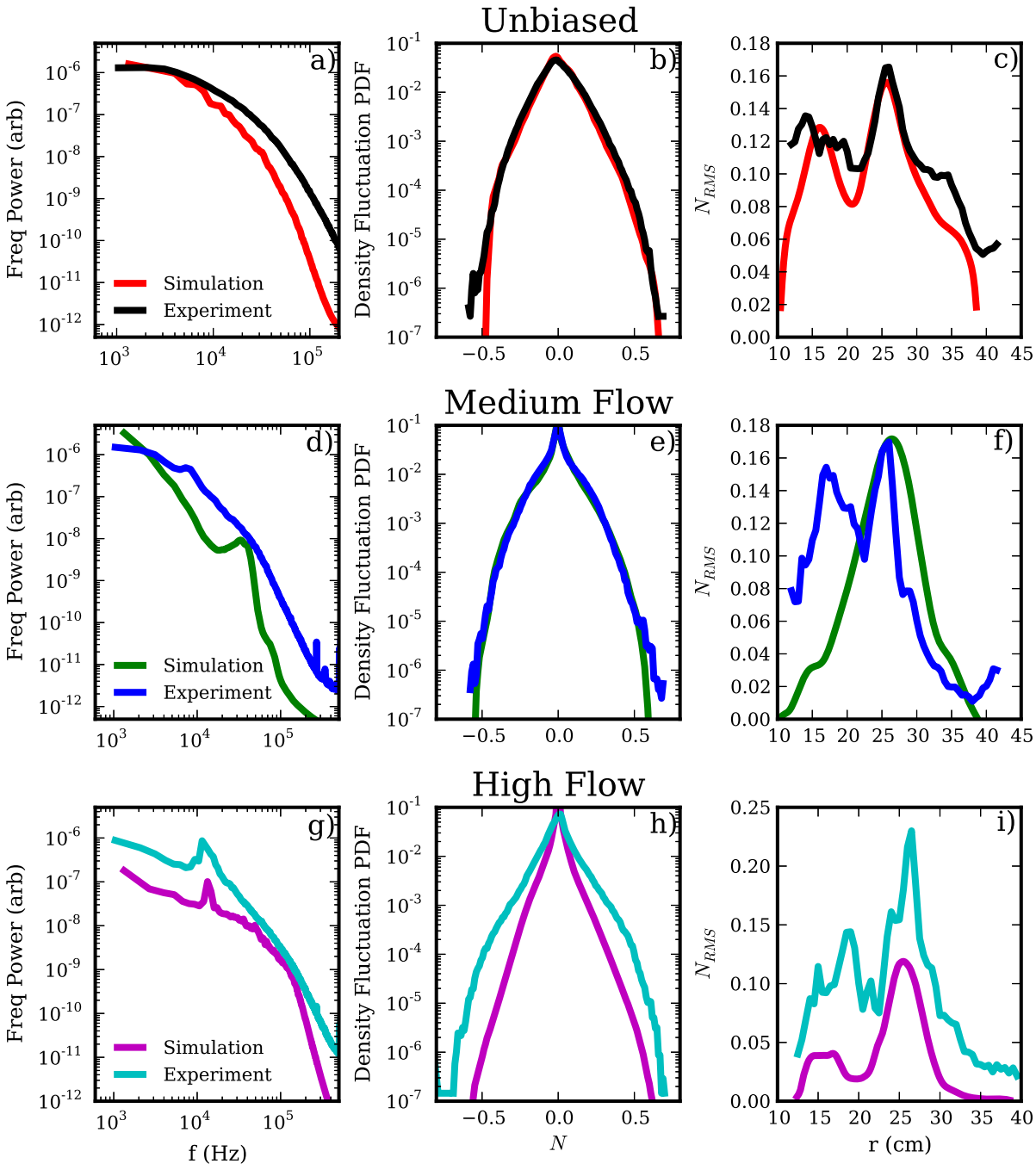

Figure B.3: Finite mean flow experimental and simulation statistical comparisons

flow statistics. The medium and high flow simulations, on the other hand, leave much to be desired with regards to their match against experiment. The medium flow simulation PDF matches the experimental PDF very well, although I use my free parameter – artificial diffusion and viscosity coefficient – to match the standard deviation of the PDF of the simulation with the experiment. The skewness and kurtosis, however, are similar, and I do not control them. Furthermore, the medium flow simulation and experiment both have a strong fluctuation level at ~ 26 cm, but the experiment has another peak at ~ 16 cm that the simulation does not. Also, the simulation frequency spectra is qualitatively different than that of the experiment. The simulation frequency spectra has a strong coherent peak that is lacking in the experiment. I notice that this is a common feature of the simulations when I use a high level of artificial diffusion. Presumably, then, this feature would disappear when I lower the diffusion. However, this would cause a mismatch in the fluctuation level. I presume that I would be better served by lowering the diffusion and finding the cause of the then unphysically large fluctuation levels. Obviously, the simulation model has some issue in this case. Perhaps my profiles have some unphysical feature in them, or maybe the zonal flows play a more important role in saturating this case than in the unbiased case. This requires investigation.

For the high flow simulation, the qualitative match to the experiment is actually very good, including the match of the location of a coherent feature in the frequency spectrum at about 12 kHz. However, the level of fluctuations is obviously too low in the simulation. Now I claimed that I use the PDF standard deviation to set the free parameter, and in this instance, it appears that I should lower the free parameter to better match the fluctuation level. However, I have already lowered the free parameter to *zero* in this simulation, so I cannot lower it further. I note, though, that in addition to the artificial diffusion and viscosity that I put in these simulations, there is also numerical diffusion and viscosity from

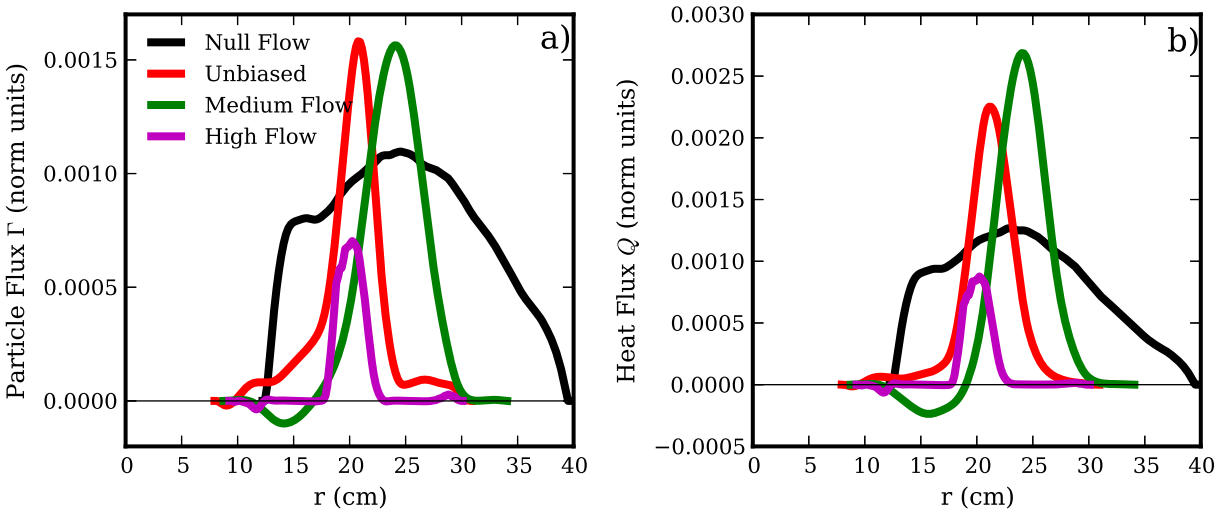

Figure B.4: Particle and heat flux for finite flow simulations

the finite difference schemes, particularly from the first order upwind scheme that I use for the nonlinear advection terms in the flow simulations. Therefore, the grid spacing that I use also acts like a tunable parameter for the diffusion and viscosity levels. In light of this, I have tried using finer grids, but I cannot use too fine of grids because it increases simulation time, and more importantly, the very low level of diffusion leads to density positivity problems as I discuss in Appendix A. It appears then, that my partial linearization of the model equations, which is responsible for the lack of strict density and temperature positivity, may be an issue for this simulation. But for now, I note that there is at least good qualitative agreement between this simulation and experiment. Nevertheless, due to my inability to fully validate the simulations, all conclusions that I present are subject to change in the future.

Next, in Fig. B.4, I display the particle flux $\Gamma = \langle N v_r \rangle$ and heat flux $Q = \langle N T_e v_r \rangle$. One of the first things one may notice in this figure is that the high flow simulation has much lower overall flux than the other simulations. This isn't a physical result because of the fluctuation level shortfall in the high flow simulation.

Additionally, the fluxes of the finite flow simulations are all much more peaked than they are in the null flow simulation. The peaks have radial locations similar to where the flow profiles are peaked and where the shear profiles are at inflection points (see Fig. B.1). For instance, the flux in the high flow simulation peaks at 20 cm. From Fig. B.1 f), at 20 cm, the flow is at its largest absolute value, while the flow shear is about 0. Additionally, the width of the flux peak is on par with the width of the shear inflection curve (from 17-23 cm). The same holds for the other two simulations, but to a lesser extent. These simulations seem to capture local shear suppression, although it's not clear from this one figure if the flux is suppressed by the shear or if it is merely following the peaks in the density and/or temperature gradients. Simulations that evolve the equilibrium gradients rather than taking them as input may be better suited to answering this question.

B.5 Energy Dynamics Results

B.5.1 The Broadband View

The addition of the mean flow terms in Eqs. B.1-B.4 – those that contain $\mathbf{v}_{e0}$ or ϖ_0 – only change the energy dynamics expressions slightly from their form in Chapter 6. In fact, only two terms – both in Eq. B.3 – actually contribute to the energy dynamics: $-\mathbf{v_{E0}} \cdot \nabla \varpi$ and $-\frac{1}{r}\frac{\partial \phi_0}{\partial r}\left(\frac{\partial N_0}{\partial r}\frac{\partial^2 \phi}{\partial r \partial \theta} - \frac{\partial^2 \phi_0}{\partial r^2}\frac{\partial N}{\partial \theta}\right)$. Mean flow advection terms such as $-\mathbf{v_{E0}} \cdot \nabla N$ in Eq. B.1, perhaps surprisingly, do not contribute to the energy dynamics. This can be seen by recalling the procedure for calculating the dynamics, which begins with multiplying Eq. B.1 by $T_{e0}/N_0 N$ and integrating over the volume. This term becomes

$$-\int_V \left(\frac{T_{e0}}{N_0} N \mathbf{v_{E0}} \cdot \nabla N\right) dV = -\frac{1}{2}\int_r v_{E0}\frac{T_{e0}}{N_0}\int_{\theta,z}\frac{\partial N^2}{\partial \theta} r d\theta dz dr. \tag{B.7}$$

Then, it is easy to see that the inner integral is zero due to the natural θ periodicity of N. The same holds for the mean flow advection terms in Eqs. B.2 and B.4. The

fluctuations are Doppler shifted by the mean flow, and even though the Doppler shift is a function of radius, the shift does not feed or dissipate the fluctuations as a whole. This also holds true for each individual (m, n) mode. These terms can, however, change the radial structures of the fluctuations, and this could be captured in different decompositions that do use radially decomposed modes, but I don't focus on any of those here.

The linear mean flow advection of the vorticity ($-\mathbf{v_{E0}} \cdot \nabla\varpi$) actually does provide a non-zero contribution to the energy dynamics because I obtain the perpendicular kinetic energy by multiplying Eq. B.3 by $-\phi$ rather than by ϖ. In fact, this leads the $-\mathbf{v_E} \cdot \nabla\varpi_0$ term in Eq. B.3 to give zero energy contribution instead, for the same reason as the term in Eq. B.7. Consequentially, only the $-\mathbf{v_{E0}} \cdot \nabla\varpi$ and $-\frac{1}{r}\frac{\partial\phi_0}{\partial r}\left(\frac{\partial N_0}{\partial r}\frac{\partial^2\phi}{\partial r\partial\theta} - \frac{\partial^2\phi_0}{\partial r^2}\frac{\partial N}{\partial\theta}\right)$ terms in Eq. B.3 contribute to the energy dynamics that I formulated in Sec. 6.2. I identify the first of these terms as the contribution from the linear KH mechanism, and the second as the contribution from the linear RIC mechanism. These are energy injection terms that take energy from the mean flow and deposit it into the perpendicular kinetic energy fluctuations (ϕ fluctuation energy).

It should not be surprising that the addition of the mean flow does not change the nonlinear instability picture that I developed in Chapter 7, especially for the unbiased and medium flow cases. I do not show results from these two simulations here. Rather, I focus only on the high flow simulation energy dynamics since they are the most interesting, and the others can simply be seen as intermediate cases of the null and high flow cases. First, I show the (m, n) energy spectra for the high flow case in Fig. B.5, which can be compared to the null flow energy spectra in Fig. 7.1. Overall, the spectra of the two simulations are somewhat similar, but differences are visible. The first clear difference is that the high flow simulation has a local energy peak at $|m| = 1, |n| = 2$ in all four fields, which is not present in the null flow case. Second, E_N has more relative energy at $|n| = 1$ for the

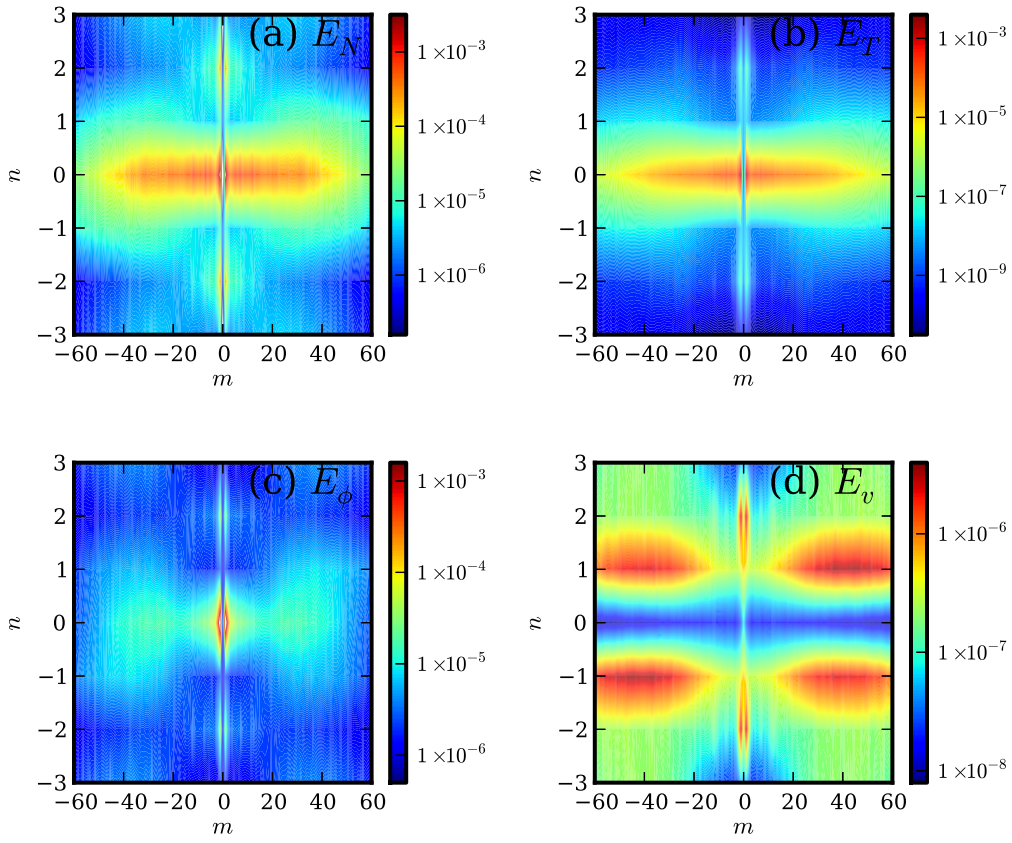

Figure B.5: Energy spectra for the high flow simulation

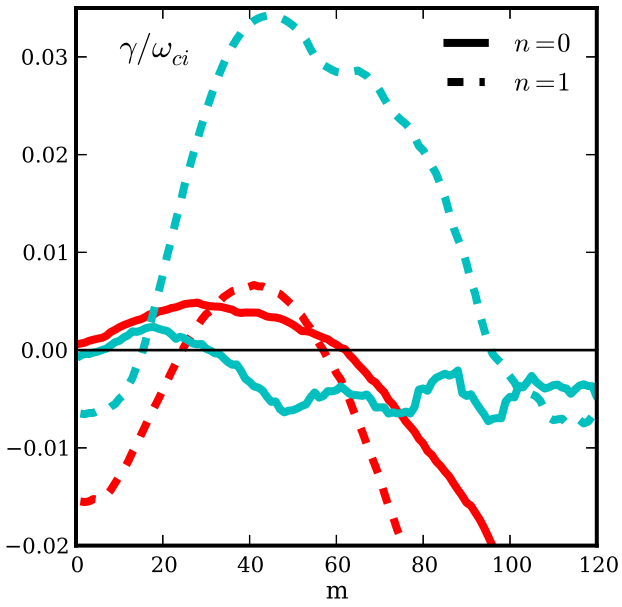

Figure B.6: High flow linear vs. nonlinear growth rates

high flow simulation, and this energy is peaked at about $|m| = 40$. The same is not true for E_ϕ, where the null flow case seemingly has more relative energy at $|n| = 1$, but the high flow case does have a local energy peak at $|n| = 0, |m| = 40$. Clearly, the high flow case has more spectral features than the null flow case.

To compactly describe some of the energy dynamics, I show the linear and nonlinear (turbulent) growth rates (explained in Sec. 7.2) in Fig. B.6. The red curves represent the nonlinear growth rates, while the cyan curves represent the linear growth rates. Note that I previously showed the linear growth rates of the different linear instabilities in Fig. B.2. Here, I am not breaking up the curves in terms of linear instabilities, but rather in terms of n number. The $n = 1$ curve, however, pretty closely corresponds to the Full Model curve in Fig. B.2 a), but they are different because here, I have added a precise amount of artificial diffusion and viscosity in order to better compare to the nonlinear growth rate curves, which have numerical diffusion and viscosity due to the finite difference

advection scheme. That is the reason for the sharper falloff at high m for the $n = 1$ curve in Fig. B.6 compared to the Full Model curve in Fig. B.2 a). Likewise, the $n = 0$ curve here corresponds to the KH curve in Fig. B.2 a), except here there is artificial viscosity. Now like for the null flow case, for which I showed the linear and nonlinear growth rates in Fig. 7.8, the high flow simulation nonlinear growth rates are much different from the high flow linear growth rates. This is a result of the same nonlinear instability mechanism that controlled the null flow case. Fig. B.6, by itself, doesn't prove that the nonlinear instability mechanism is active because it is possible that the KH or RIC instabilities could be responsible for the positive $n = 0$ growth rate. But a deeper look at the energy dynamics reveals that this isn't the case, and that the nonlinear instability mechanism still dominates. On the other hand, the high flow case does have a positive nonlinear growth rate for $n = 1$, which is just as strong as the $n = 0$ growth rate. Presumably, the linear drift wave instability is so strong for this high flow case – which has a high localized density gradient – that it can compete with the nonlinear instability mechanism. Overall, despite the high mean flow, the KH and RIC instabilities are not wholly significant, though they cannot be ruled out as factors for the coherent mode.

B.5.2 The Coherent Mode

In Sec. B.1, I mentioned that Schaffner et al. [SCR12] identified a coherent mode that grows within the broadband turbulence when the mean flow becomes large due to high biasing. In fact, I reproduce in the simulation a signature of the coherent mode, namely the peak at about 12 kHz in the frequency spectrum (Fig. B.3 g)). That means that the simulation data can be used to figure out the cause of this coherent mode.

In order to understand the coherent mode better, I first look at the frequency spectra as a function of radius, which I show in Fig. B.7. Figure B.7 a) is the spectrum of the density fluctuations, while Fig. B.7 b) is the spectrum of the

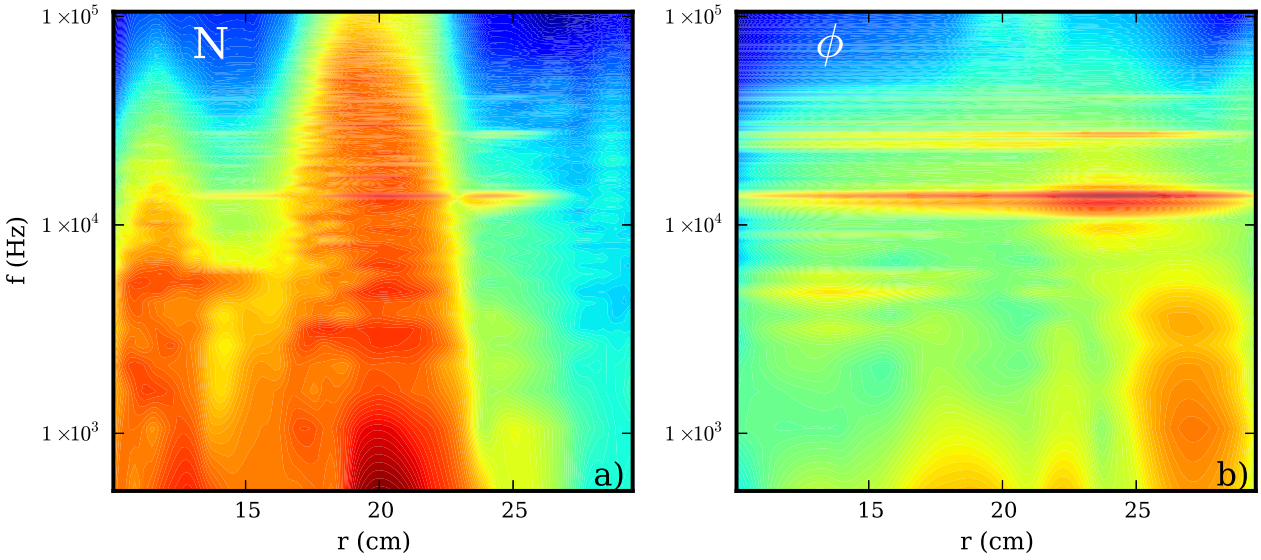

Figure B.7: Radial frequency power spectra for the high flow simulation

potential fluctuations. The difference between the spectra of the two fields is remarkable, with the potential having a coherent spectra and the density having a broadband spectra. While the 12 kHz coherent mode shows up in both fields, it is far more significant in the potential field. This indicates that the coherent mode is a flow-driven mode as opposed to a drift wave, which shouldn't be too surprising given that the mode emerges only when the flow becomes large. Furthermore, the coherent mode is somewhat localized at a radial position around $23 - 26$ cm. By comparing this to Fig. B.1 f), one sees that this mode peaks where the flow shear peaks, but where the flow magnitude is small, which provides evidence that the mode is KH-driven rather than RIC-driven. To further test this, I run two more simulations – one removing the KH term in Eq. B.3, the other removing the RIC term. I display the radial frequency spectra of these two simulations in Fig. B.8. The results of these simulations are not that straight-forward. When I remove the KH term, the coherent mode at 12 kHz disappears, and the frequency spectrum of the potential changes significantly, somewhat validating the idea that

the coherent mode is KH-driven. However, removal of the RIC term also has an effect on the coherent mode. It shifts its frequency. While there is still a sharp peak in the spectrum at about 12 kHz, there is a more significant peak at about 7 kHz, meaning that the 12 kHz peak is probably just a side-band of this. Likely, the coherent mode is KH-driven, but the RIC term shifts the frequency of the mode, though it's not obvious why it would do so.

To further test the KH-driven coherent mode hypothesis, I look at the energy dynamics of the full simulation with both the KH and RIC terms included. However, in order to try to isolate the coherent mode, I volume average over only the annulus in the $23 - 26$ cm radial domain, which should eliminate the background that is still largely controlled by the nonlinear instability. I do not show any specific results of the energy dynamics, but qualitatively in this domain, the KH mechanism injects energy into the system, primarily at $n = 0$ and at $m = 1, 2$. The RIC, on the other hand, is not active here, and the nonlinear instability is also not strong here. The evidence, then, points to a KH-driven coherent mode where the RIC only affects its frequency.

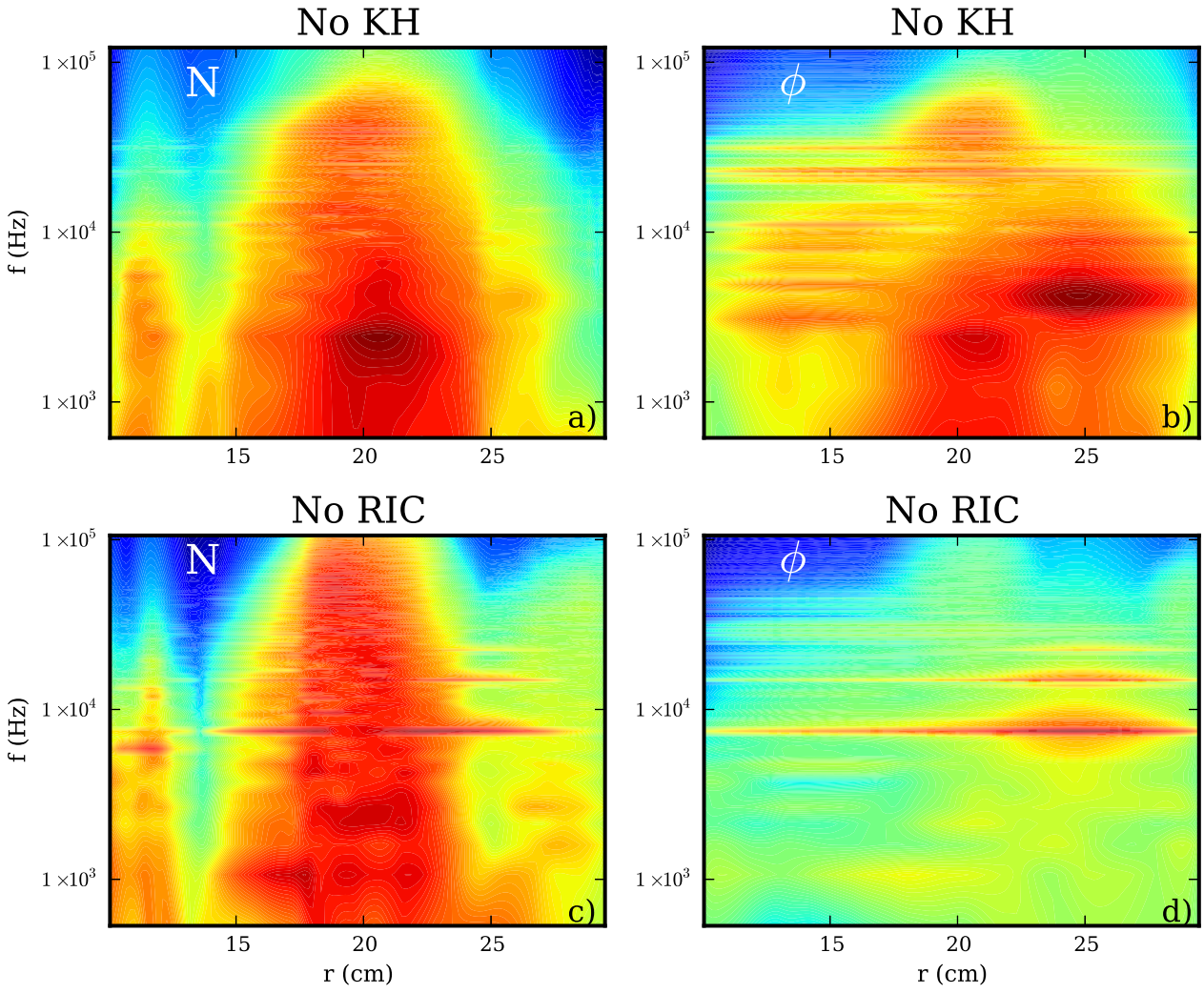

Figure B.8: Frequency power spectra without KH or RIC term

References

[Ara66] A. Arakawa. "Computational Design for Long-Term Numerical Integration of the Equations of Fluid Motion." *J. Computational Physics*, **1**:119–143, 1966.

[Bat67] G. K. Batchelor. *An Intorduction to Fluid Dynamics*. Cambridge Univ. Press, 1967.

[BCR93] H. L. Berk, R. H. Cohen, D. D. Ryutov, Yu. A. Tsidulko, and X. Q. Xu. "Electron temperature gradient induced instability induced in tokamak scrape-off layers." *Nuclear Fusion*, **33**:263, 1993.

[BDT90] H. Biglari, P. H. Diamond, and P. W. Terry. "Influence of sheared poloidal rotation on edge turbulence." *Phys. Fluids B*, **2**:1, 1990.

[BF92] K. M. Butler and B. F. Farrell. "Three-dimensional optimal perturbations in viscous shear flows." *Phys. Fluids A*, **4**:1637, 1992.

[BHL93] G. Berkooz, P. Holmes, and J. L. Lumley. "The proper orthogonal decomposition in the analysis of turbulent flows." *Annu. Rev. Fluid Mech.*, **25**:539, 1993.

[BK85] D. Biskamp and H. Kaifen. "Three-drift-wave interaction at finite parallel wavelength: bifurcations and transition to turbulence." *Phys. Fluids*, **28**:2172, 1985.

[BP02] C. Bandt and B. Pompe. "Permutation Entropy: A Natural Complexity Measure for Time Series." *Phys. Rev. Lett.*, **88**:174102, 2002.

[Bra65] S. I. Braginskii. "Transport processes in a plasma." In M A Leontovich, editor, *Reviews of Plasma Physics*, volume 1, pp. 205–311. Consultants Bureau, New York, 1965.

[BRT91] H. L. Berk, D. D. Ryutov, and Yu. A. Tsidulko. "Temperature-gradient instability induced by conducting end walls." *Phys. Fluids B*, **3**:1346, 1991.

[BZ95] D. Biskamp and A. Zeiler. "Nonlinear Instability Mechanism in 3D Collisional Drift-Wave Turbulence." *Phys. Rev. Lett.*, **74**:706, 1995.

[CBS95] S. J. Camargo, D. Biskamp, and B. D. Scott. "Resistive drift-wave turbulence." *Phys. Plasmas*, **2**:48, 1995.

[Che06] F. F. Chen. *Introduction to Plasma Physics and Controlled Fusion*. Springer, 2006.

[CO77] C. Z. Cheng and H. Okuda. "Formation of convective cells, anomalous diffusion, and strong plasma turbulence due to drift instabilities." *Phys. Rev. Lett.*, **38**:708, 1977.

[CO79] C. Z. Cheng and H. Okuda. "Theory and numerical simulations on collisionless drift instabilities in three dimensions." *Nuclear Fusion*, **18**:587, 1979.

[CTC98] S. J. Camargo, M. K. Tippett, and I. L. Caldas. "Nonmodal energetics of resistive drift waves." *Phys. Rev. E*, **58**:3693, 1998.

[CVO] `https://computation.llnl.gov/casc/sundials/documentation/cv_guide/node3.html`. [Online; accessed 9-May-2013].

[DBB00] A. M. Dimits, G. Bateman, M. A. Beer, B. I. Cohen, W. Dorland, G. W. Hammett, C. Kim, J. E. Kinsey, M. Kotschenreuther, A. H. Kritz, L. L. Lao, J. Mandrekas, W. M. Nevins, S. E. Parker, A. J. Redd, D. E. Shumaker, R. Sydora, and J. Weiland. "Comparisons and Physics Basis of Tokamak Transport Models and Turbulece Simulations." *Phys. Plasmas*, **7**:969, 2000.

[DR81] P. G. Drazin and W. H. Reid. *Hydrodynamic Stability*. Cambridge University Press, 1981.

[DUX09] B. D. Dudson, M. V. Umansky, X. Q. Xu, P. B. Snyder, and H. R. Wilson. "BOUT++: A framework for parallel plasma fluid simulations." *Computer Physics Communications*, pp. 1467–1480, 2009.

[DZB95] J. F. Drake, A. Zeiler, and D. Biskamp. "Nonlinear Self-Sustained Drift-Wave Turbulence." *Phys. Rev. Lett.*, **75**:4222, 1995.

[Fam82] J. D. Famer. "Chaotic attractors of an infinite-dimensional dynamical system." *Physica*, **4D**:366, 1982.

[FBC09] S. Futatani, S. Benkadda, and D. del Castillo-Negrete. "Spatiotemporal multiscaling analysis of impurity transport in plasma turbulence using proper orthogonal decomposition." *Phys. Plasmas*, **16**:042506, 2009.

[FCU12] B. Friedman, T. A. Carter, M. V. Umansky, D. Schaffner, and B. Dudson. "Energy dynamics in a simulation of LAPD turbulence." *Phys. Plasmas*, **19**:102307, 2012.

[FCU13] B. Friedman, T. A. Carter, M. V. Umansky, D. Schaffner, and I. Joseph. "Nonlinear instability in simulations of Large Plasma Device turbulence." *Phys. Plasmas*, **20**:055704, 2013.

[FUC12] B. Friedman, M. V. Umansky, and T. A. Carter. "Grid Convergence Study in a Simulation of LAPD Turbulence." *Contrib. Plasma Phys.*, **52**:412–416, 2012.

[GPL91] W. Gekelman, H. Pfister, Z. Lucky, J. Bamber, D. Leneman, and J. Maggs. "Design, Construction and Properties of the Large Plasma Research Device - The LAPD at UCLA." *Rev. Sci. Inst.*, **62**:2875, 1991.

[Gus91] L. H. Gustavsson. "Energy growth of three-dimensional disturbances in plane Poiseuille flow." *J. Fluid Mech*, **224**:221, 1991.

[HDC03] C. Holland, P. H. Diamond, S. Champeaux, E. Kim, O. Gurcan, M. N. Rosenbluth, G. R. Tynan, N. Crocker, W. Nevins, and J. Candy. "Investigations of the role of nonlinear couplings in structure formation and transport regulation: experiment, simulation, and theory." *Nuclear Fusion*, **43**:761, 2003.

[Hen96] D. Henningson. "Comment on "Transition in shear flows. Nonlinear normality versus non-normal linearity" [Phys. Fluids 7, 3060 (1995)]." *Phys. Fluids*, **8**:2257, 1996.

[Hor90] W. Horton. *Nonlinear drift waves and transport in magnetized plasma*. North-Holland, 1990.

[HR94] D. S. Henningson and S. C. Reddy. "On the role of linear mechanisms in transition to turbulence." *Phys. Fluids*, **6**:1396, 1994.

[HTJ11] D. R. Hatch, P. W. Terry, F. Jenko, F. Merz, and W. M. Nevins. "Saturation of Gyrokinetic Turbulence through Damped Eigenmodes." *Phys. Rev. Lett.*, **106**:115003, 2011.

[Hut02] I. H. Hutchinson. *Principles of Plasma Diagnostics*. Cambridge University Press, 2002.

[HW83] A. Hasegawa and M. Wakatani. "Plasma Edge Turbulence." *Phys. Rev. Lett.*, **50**:682–686, 1983.

[KMN99] S. B. Korsholm, P. K. Michelsen, and V. Naulin. "Resistive drift wave turbulence in a three-dimensional geometry." *Phys. Plasmas*, **6**:2401, 1999.

[Kol41] A. N. Kolmogorov. "The local structure of turbulence in incompressible viscous fluid for very large Reynolds numbers." *Dokl Akad. Nauk SSSR*, **30**:301–305, 1941.

[Kro99] J. A. Krommes. "Recent results on analytical plasma turbulence theory: realizability, intermittency, submarginal turbulence and self-organized criticality." *Plasma Phys. Control. Fusion*, **41**:A641–A652, 1999.

[KT10] J.-H. Kim and P. W. Terry. "Energetic study of the transition to nonlinear state in two-dimensional electron temperature gradient fluid turbulence." *Phys. Plasmas*, **17**:112306, 2010.

[Lan44] L. D. Landau. "On the problem of turbulence." *C.R. Acad. Sci. U.R.S.S.*, **44**:311, 1944.

[LL59] L. D. Landau and E. M. Lifshitz. "Fluid mechanics." In *Course of theoretical physics*, volume 6. London: Pergamon Press, 1959.

[Lor63] E. N. Lorenz. "Deterministic nonperiodic flow." *J. Atmos. Sci.*, **20**:130, 1963.

[LRH12] J. Loizu, P. Ricci, F. Halpern, and S. Jolliet. "Boundary conditions for plasma fluid models at the magnetic presheath entrance." *Phys. Plasmas*, **13**:122307, 2012.

[Man04] P. Manneville. *Instabilities, Chaos and Turbulence*. Imperial College Press, 2004.

[McD04] J. M. McDonough. "INTRODUCTORY LECTURES on TURBULENCE Physics, Mathematics and Modeling.", 2004.

[MCT07] J. E. Maggs, T. A. Carter, and R. J. Taylor. "Transition from Bohm to classical diffusion due to edge rotation of a cylindrical plasma." *Phys. Plasmas*, **14**:052507, 2007.

[MG77] M. C. Mackey and L. Glass. "Oscillation and Chaos in Physiological Control Systems." *Science*, **197**:287, 1977.

[MM11] J. E. Maggs and G. J. Morales. "Generality of Deterministic Chaos, Exponential Spectra, and Lorentzian Pulses in Magnetically Confined Plasmas." *Phys. Rev. Lett.*, **107**:185003, 2011.

[MM12a] J. E. Maggs and G. J. Morales. "Exponential power spectra, deterministic chaos and Lorentzian pulses in plasma edge dynamics." *Plasma Phys. Control. Fusion*, **54**:12041, 2012.

[MM12b] J. E. Maggs and G. J. Morales. "Origin of Lorentzian pulses in deterministic chaos." *Phys. Rev. E*, **86**:015401, 2012.

[MM13] J. E. Maggs and G. J. Morales. "Permutation entropy analysis of temperature fluctuations from a basic electron heat transport experiment." *Plasma Phys. Control. Fusion*, **55**:085015, 2013.

[MTK11] K. D. Makwana, P. W. Terry, J. H. Kim, and D. R. Hatch. "Damped eigenmode saturation in plasma fluid turbulence." *Phys. Plasmas*, **18**:012302, 2011.

[MTK12] K. D. Makwana, P. W. Terry, and J. H. Kim. "Role of stable modes in zonal flow regulated turbulence." *Phys. Plasmas*, **19**:062310, 2012.

[PSM08a] D. C. Pace, M. Shi, J. E. Maggs, G. J. Morales, and T. A. Carter. "Exponential frequency spectrum and Lorentzian pulses in magnetized plasmas." *Phys. Plasmas*, **15**:122304, 2008.

[PSM08b] D. C. Pace, M. Shi, J. E. Maggs, G. J. Morales, and T. A. Carter. "Exponential Frequency Spectrum in Magnetized Plasmas." *Phys. Rev. Lett.*, **101**:085001, 2008.

[PUC10a] P. Popovich, M. V. Umansky, T. A. Carter, and B. Friedman. "Analysis of plasma instabilities and verification of BOUT code for linear plasma device." *Phys. Plasmas*, **17**:102107, 2010.

[PUC10b] P. Popovich, M. V. Umansky, T. A. Carter, and B. Friedman. "Modeling of plasma turbulence and transport in the Large Plasma Device." *Phys. Plasmas*, **17**:122312, 2010.

[RH93] S. C. Reddy and D. S. Henningson. "Energy growth in viscous channel flows." *J. Fluid Mech*, **252**:209, 1993.

[RLM07] O. A. Rosso, H. A. Larrondo, M. T. Martin, A. Plastino, and M. A. Fuentes. "Distinguishing Noise from Chaos." *Phys. Rev. Lett.*, **99**:154102, 2007.

[RMW13] M. Riedl, A. Muller, and N. Wessel. "Practical considerations of permutation entropy." *Eur. Phys. J. Special Topics*, **222**:249, 2013.

[RR10] B. Rogers and P. Ricci. "Low-frequency turbulence in a linear magnetized plasma." *Phys. Rev. Lett.*, **104**:225002, 2010.

[RSH93] S. C. Reddy, P. J. Schmid, and D. S. Henningson. "Pseudospectra of the OrrSommerfeld operator." *SIAM J. Appl. Math.*, **53**:15, 1993.

[RT71] D. Ruelle and F. Takens. "On the Nature of Turbulence." *Commun. math. Phys.*, **20**:167, 1971.

[SC03] A. N. Simakov and P. J. Catto. "Drift-ordered fluid equations for field-aligned modes in low-β collisional plasma with equilibrium pressure pedestals." *Phys. Plasmas*, **10**:4744, 2003.

[Sco90] B. D. Scott. "Self-Sustained Collisional Drift-Wave Turbulence in a Sheared Magnetic Field." *Phys. Rev. Lett.*, **65**:3289, 1990.

[Sco92] B. D. Scott. "The mechanism of self sustainment in collisional drift wave turbulence." *Phys. Fluids B*, **4**:2468, 1992.

[Sco02] B. D. Scott. "The nonlinear drift wave instability and its role in tokamak edge turbulence." *New J. Physics*, **4**:52.1–52.30, 2002.

[Sco03] B. D. Scott. "Computation of electromagnetic turbulence and anomalous transport mechanisms in tokamak plasmas." *Plasma Phys. Control. Fusion*, **45**:A385–A398, 2003.

[Sco05] B. D. Scott. "Drift wave versus interchange turbulence in tokamak geometry: Linear versus nonlinear mode structure." *Phys. Plasmas*, **12**:062314, 2005.

[SCR12] D. A. Schaffner, T. A. Carter, G. D. Rossi, D. S. Guice, J. E. Maggs, S. Vincena, and B. Friedman. "Modification of Turbulent Transport with Continuous Variation of Flow Shear in the Large Plasma Device." *Phys. Rev. Lett.*, **109**:135002, 2012.

[SCR13] D. A. Schaffner, T. A. Carter, G. D. Rossi, D. S. Guice, J. E. Maggs, S. Vincena, and B. Friedman. "Turbulence and transport suppression scaling with flow shear on the Large Plasma Device." *Phys. Plasmas*, **20**:055907, 2013.

[SG81] H. L. Swinney and J. P. Gollub. *Hydrodynamics Instabilities and the Transition to Turbulence*. Springer-Verlag, 1981.

[SPM09] M. Shi, D. C. Pace, G. J. Morales, J. E. Maggs, and T. A. Carter. "Structures generated in a temperature filament due to drift-wave convection." *Phys. Plasmas*, **16**:062306, 2009.

[Sta00] P. C. Stangeby. *The plasma boundary of magnetic fusion devices*. Institute of Physics Publishing, 2000.

[Tak81] F. Takens. "Detecting strange attractors in turbulence." *Lect. Notes Math.*, **898**:366, 1981.

[The90] J. Theiler. "Estimating the Fractal Dimension of Chaotic Time Series." *The Lincoln Laboratory Journal*, **3**:63, 1990.

[TL72] H. Tennekes and J. L. Lumley. *First Course in Turbulence*. The MIT Press, 1972.

[TTR93] L. N. Trefethen, A. E. Trefethen, S. C. Reddy, and T. A. Driscoll. "Hydrodynamic Stability Without Eigenvalues." *Science*, **261**:578, 1993.

[UPC11] M. V. Umansky, P. Popovich, T. A. Carter, B. Friedman, and W. M. Nevins. "Numerical simulation and analysis of plasma turbulence the Large Plasma Device." *Phys. Plasmas*, **18**:055709, 2011.

[UXD09] M. V. Umansky, X. Q. Xu, B. Dudson, L. Lodestro, and J. Myra. "Status and verification of edge plasma turbulence code BOUT." *Phys. Plasmas*, **180**:887, 2009.

[Wal95] F. Waleffe. "Hydrodynamic Stability and Turbulence: Beyond Transients to a Self-Sustaining Process." *Studies in Applied Mathematics*, **95**:319, 1995.

[Wes11] J. Wesson. *Tokamaks*. Clarendon Press, 2011.

[XC98] X. Q. Xu and R. H. Cohen. "Scrape-Off Layer Turbulence Theory and Simulations." *Contrib. Plasma Phys.*, **36**:158, 1998.

[XRD93] X. Q. Xu, M. N. Rosenbluth, and P. H. Diamond. "Electron-temperature-gradient-driven instability in tokamak boundary plasma." *Phys. Fluids B*, **5**:2206, 1993.

[ZBD96] A. Zeiler, D. Biskamp, J. F. Drake, and P. N. Guzdar. "Three-dimensional fluid simulations of tokamak edge turbulence." *Phys. Plasmas*, **3**:2951, 1996.

[ZDB97] A. Zeiler, J. F. Drake, and D. Biskamp. "Electron temperature fluctuations in drift-resistive ballooning turbulence." *Phys. Plasmas*, **4**:991, 1997.